# NUCLEAR PHYSICS AT PEP
# RECENT RESULTS USING THE TIME PROJECTION CHAMBER

S. O. Melnikoff
Lawrence Livermore National Laboratory
University of California
P.O. Box 808 L-421
Livermore, Calif. 94550

## Abstract

A preliminary result on Bose-Einstein correlations is reported using the *PEP-4* Time Projection Chamber facility. The data, from scattering 14.5 GeV electrons on nuclei, was taken at the Stanford Linear Accelerator Center positron-electron (*PEP*) storage ring. Bose-Einstein (BE) correlations were measured from events having identified like-sign pion pairs. The particle identification and tracking capability of the Time Projection Chamber (TPC) was used to select like-sign pion pair events. The resulting correlation function for the data was fitted to a gaussian form $R(q) = 1 + \lambda exp(-q^2\sigma^2)$ where $q$ is the relative four-momentum difference of the pions. The fitted value to the chaoticity is $\lambda = 0.37 \pm 0.19$ and $\sigma = 1.37 \pm 0.41$ *fermi*. This result agrees with that from $e^+e^-$ annihilation data taken with the TPC.

We explain the operation of the TPC and the analysis of the data used. The feasiblity of similiar detectors for doing high energy electron scattering on nuclei at *PEP* is briefly discussed.

## Introduction

During the past year we have initiated a small program to study the feasibility of nuclear physics experiments at the PEP colliding beam facility[1]. As part of this LLNL study small amounts of deuterium, or argon or xenon gas were infused into the PEP ring, in the vicinity of the TPC-2$\gamma$ interaction region. The data from the dedicated gas-bleed and that as a result of electron scattering from residual gases already present in the ring (from previous run cycles) was analyzed to obtain a first look at possible physics topics that could be studied at a future nuclear physics facility. Such a facility could address the interest in looking at exclusive final states in inelastic electron scattering. Experiments at PEP can run at energies up to 14.5 GeV, well into the region of Bjorken scaling.

While our major concern is with the data from the TPC-2$\gamma$ detector, for future experiments, a second important topic is in the area of detector design. The general feasibilty of any proposed detector facility must be addressed first, before a detailed design study based on the particulars of the physics. The advantage the nuclear physics community has at PEP is that a generation of working detectors have been in operation for more than five years. A study of these detectors, in particular the TPC-2$\gamma$ facility, provides first answers to the questions of what works at PEP and what is unrealistic.

Our Bose-Einstein correlation result, which uses all the major components of the TPC-2$\gamma$ facility, makes two important points. First that despite being optimized for high energy physics running, a TPC-like detector works well in a nuclear physics environment. Secondly the scale of any proposed future experiment will be closer to that of high energy physics than traditional nuclear physics experiments.

## The Time Projection Chamber

All of our data and resulting measurements presented are from the *PEP-4* detector. We will summarize the design and operation of the detector facility with respect to those features relevent to our results. More complete reviews are available elsewhere[2-5], along with a good summary of the *PEP-9* or forward spectrometer[6].

## Goal and Objectives

The *PEP-4* facility has been designed and built with three definite objectives:

1. Efficient charged particle detection and momentum measurement over a large fraction of the entire solid angle.
2. Identification of charged particles by means of energy loss measurements over the accepted momentum range.
3. Detection of energetic photons over a comparable solid angle with capabilities for reconstrution of neutral pions.

The forward detector system, or *PEP-9* , was design to observe or *tag* the outgoing electrons (positrons) in photon-photon or *two–gamma* interactions. These generally scatter at small angles with respect to the beam axis and are outside the *PEP-4* detector volume. We used the *PEP-9* system to tag the scattered electron from nuclei.

## Geometry of the System

To achieve the design objectives listed above and to promote modularity during the construction phase of the facility, the *PEP-4* detector is divided into six subsystems. The entire central detector system is cylindrically symmetric about the $e^+e^-$ beam axis; the forward spectrometer is symmetric about the interaction midplane perpendicular to the beam axis. Figure (1) is a schematic of the facility showing one arm of the forward spectrometer. Radially outward from the $e^+e^-$ interaction point the six subsytems are:

1. An inner drift chamber (IDC) which wraps around the beam pipe, used as a fast pretrigger chamber.
2. The central detector, the *Time Projection Chamber* or *TPC* .
3. A solenoidal 13.25 KGauss superconducting magnet. The momentum resolution achieved was $(\sigma p/p)^2 = (1.5\%)^2+(0.65\%p)^2$ $(p\ in\ GeV)$.
4. A second cylindrical outer drift chamber (ODC) which encircles the magnet. The spatial resolution of the two drift chambers was 150–250 microns.
5. A set of electromagnetic calorimeters, surrounding and capping the magnet. These are follwed in radius by an iron superstructure forming the flux return yoke and hadron absorber layers for the muon detection system. The *rms* energy resolution of the calorimeter using 14.5 GeV Bhabha events was $\sigma_E = 14\%\sqrt{E}$ $(E\ in\ GeV)$.
6. A muon detection subsystem consisting of proportional drift tubes layered between sections of iron absorber material. The spatial resolution of the muon chambers was 700 microns.

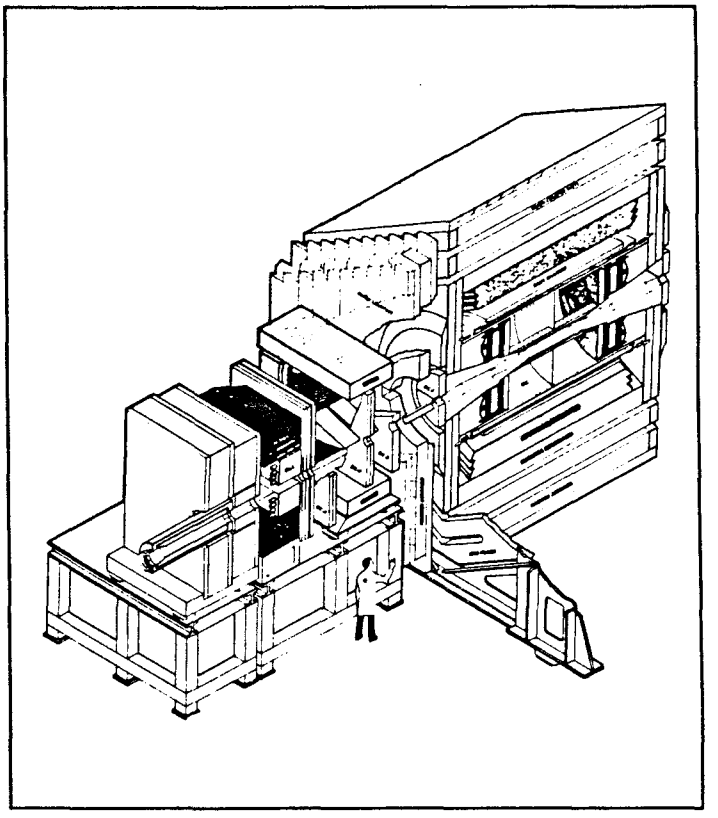

Fig. 1.1 *Artist schematic view of the TPC-2γ facility. One arm of the forward spectrometer is shown here.*

## Operation of the TPC

The central detector of the TPC-2$\gamma$ system is the time projection chamber. The device is a large cylinder two meters long and two meters in diameter. The chamber is filled with a gas mixture of 80% Argon and 20% Methane and has operated at 8.5 atmospheres of pressure.

The volume is divided into symmetric halves by a conducting mesh membrane which is held at – 75 Kilovolts with the endplanes at ground voltage. A series of conductive rings at the inner and outer radii of the chamber are the components of the high-voltage *field cages* which produce a very uniform axial electric drift field, while a solenoidal magnet introduces a four kilogauss uniform magnetic field in the same direction. The ends of the cylindrical volume, the *endcaps*, are the detection planes for the *TPC* .

The uniform electric field in the drift volume is achieved by the field cages which step down the central membrane potential for a constant velocity drift field throughout the *TPC* volume. This is done by a set of $G-10$ fiberglass cylinders at the inner and outer radius on which $0.5mm$ wide conductive rings are etched. Design tolerances maintained a precision of better than 0.01% in the resulting electric field.

As pictured in Figure (2) each endcap is physically divided into six identical multiwire proportional chambers, the *sectors*. Each sector reads out information on a wedge of space formed by its boundaries in $r$ and $\phi$ and the central membrane along the beam axis, a detection volume of approximately $0.51m^3$.

During operation, charged particles from an $e^+e^-$ interaction will pass through the *TPC* volume. These particles will ionize the gas along their track length. On the average 200 primary ion pairs per $4mm$ of track are produced. The ionization electrons will drift in the direction of the electric field to the endplane detectors. The endplanes simultaneously do both the spatial tracking and energy loss measurement.

A sector detects incoming drift electrons with a set of 185 twenty micron diameter gold plated tungsten sense wires (of which 183 are read out). These are alternating with $75\mu m$ field shaping wires. Four millimeters underneath the sense wires, the copper clad endplane has been etched to form fifteen $7.5mm$ wide rows. The centers of the rows are spaced approximately equal distances apart, the first and last at 23.6 and $95.2cm$ from the interaction point. Each row is segmented into $7.5mm$ squares, called *pads*. These will see an induced signal from the sense wires. Figure (3) illustrates the layout of the wires and pads. An additional shielding plane of wires $7.5mm$ above the cathode plane is held at ground voltage.

Arriving clusters of ionization in the neighborhood of a wire will undergo charge avalanching which in turn induces a signal on some of the pads directly under the particular wire. Signal gains are typically $10^3$ with sense wire voltages of $3.4kV$ and field wire voltages of +700 volts.

From the pads two coordinates, $xy$ (in the sector frame), of tracking information are determined. The $xy$ coordinates come from the center of a parabolic fit to the pads having signals. A third coordinate along the beam axis, Z, is determined by measuring the time it takes for the electrons to drift to a sense wire. Knowing this time and the constant drift velocity of the electrons in the uniform electric field in the gas mix allows us to *project* back in Z to find the original creation position of the electron-ion cluster. The term Time Projection Chamber originates from being able to use the available drift time information.

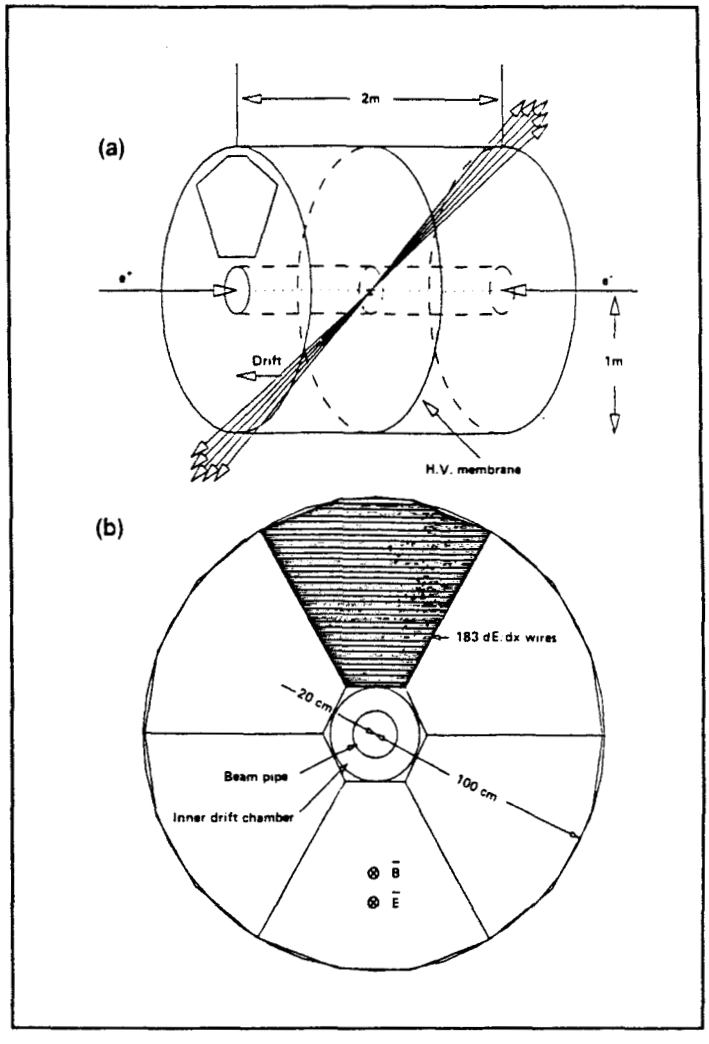


Fig. 1.2 *(a) Schematic of the TPC volume. (b) View of one TPC endcap showing the sectors and the dE/dx wires. The magnetic bending and electric drift fields are parallel (into the page).*

Particle Identification with the *TPC*

The *TPC* identifies a particle by measuring its ionization energy loss (proportional to the sense wire signal amplitude) through the gas volume and its momentum through the magnetic field's curvature of the track The average energy loss per unit length, $dE/dx$ , is a well-defined function of a particle's velocity, given by the Bethe-Heitler relation[7]

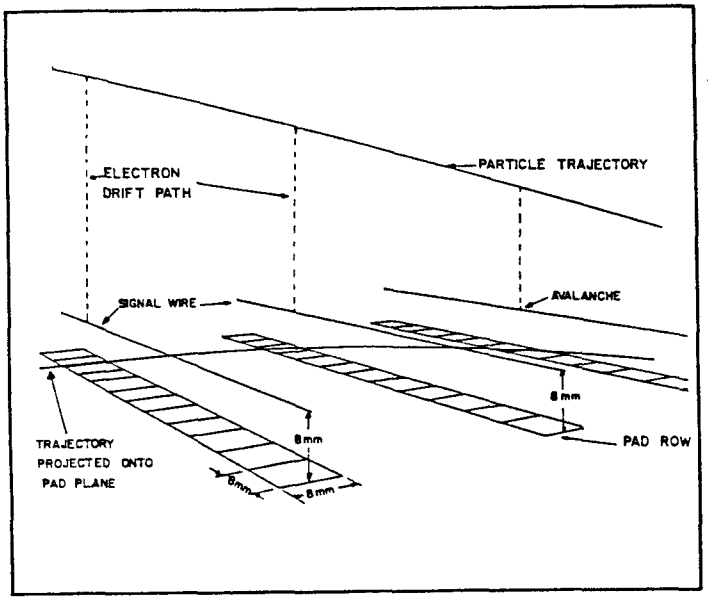


Fig. 1.3 *Detail of the TPC endcap wire/pad geometry showing placement of the cathode pads and the central wire over the pad rows. Pictured is one particle trajectory and its projection onto the pad plane.*

$$< dE/dx > \approx \frac{4\pi\eta Z^2 e^2}{m_e c^2 \beta^2} \left\{ ln\left( \frac{2m_e\beta^2\gamma^2}{I^2 + (\hbar\omega)^2\beta^2\gamma^2} \right) - 2\beta^2 \right\} \quad (01)$$

where

$m_e$ is the mass of the electron

I is the effective ionization potential for the material

$\eta$ is the electron density of the material

$\omega$ is the plasma frequency of the material.

For a $< dE/dx >$ resolution of better than 4% the TPC samples a track's ionization energy loss up to a maximum of 185 times. In practice a 'truncated mean' is used, being the mean for 65% of the sample having the smallest energy loss. Figure (4) shows the experimental energy loss curves as a function of momentum. The minimum of the curve is called minimum ionizing (and the momentum around this point the minimum ionizing region). Seen are the different mass bands corresponding to electrons, pions (and muons), kaons and protons along with ambiguous *crossover* regions between particle types. Pion and muon bands were not resolvable due to the momentum resolution obtained and their small (33.9 MeV) mass difference. The high and low momentum regions with respect to minimum ionizing are referred to as the one–over–beta–square and relativistic–rise regions respectively.

To quantify the probability of identifying a specific particle type, a dE/dx $\chi^2$ is defined. For a measured track momentum $P_x$ the $\chi^2_x$ is the distance squared between the measured dE/dx point and the theoretical curve for the x particle type. The lowest $\chi^2_x$ determines the identification of the particle.

Since TPC particle identification is dependent on conditions in the device that are time dependent (for example the Argon-Methane gas pressure) calibration plays an important part in the detector's performance. To calibrate the sectors, before final assembly a complete gain map of each was done. Later, run-time three point calibrations are used to correct it for any variations. Calibration of the absolute gain from the wires is done *in situ* at three points along a wire with $Fe^{55}$ sources. These were located underneath the endplanes and switchable, irradiating the wires through holes drilled in the endplanes.

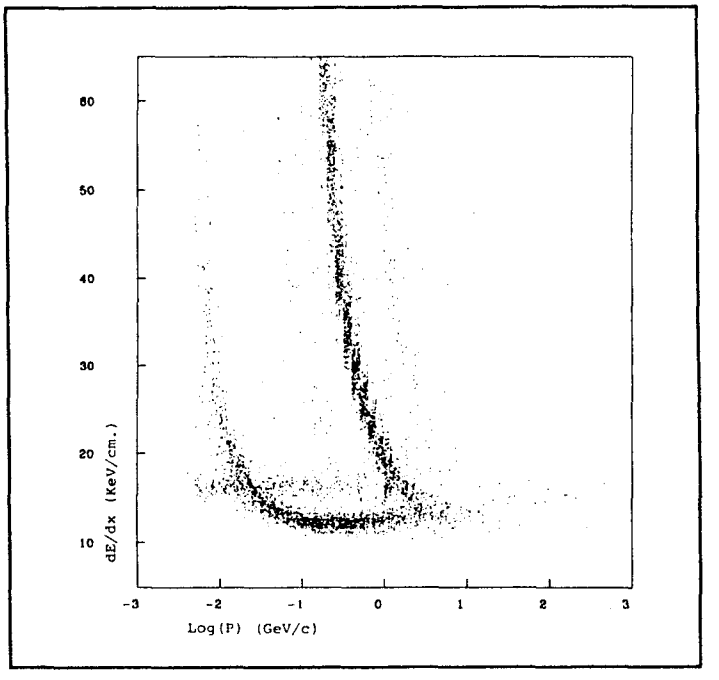


Fig. 1.4 *Plot of energy loss (dE/dx) vs. momentum for our data sample. Energy loss curves showing the presence of electrons, pions, kaons and protons are seen.*

## First Test Run

Our first test of the gas-bleed system was done in March 1986. This was a live test of gas injection at PEP with beams and all detectors on. The first segment of the test was a 24 hour run with $D_2$, raising the pressure in the PEP beamline in the neighborhood of the TPC from $10^{-9}$ to $(3.0)10^{-7}$ *torr*. This was followed by a 16 hour run using Argon followed by an 8 hour run with Xenon. The neighborhood pressure in the ring for the two heavier gases was

raised to $(2.0) - (5.0)10^{-8}$ *torr*.

To trigger the detector during this test we required the following. An identified electron *tag* in the forward spectrometer along with a track in the IDC and a set of ionization clusters or *ripple* in the TPC forming a track. Lacking a charged track trigger in the TPC we also accepted as a trigger hits in the $2\gamma$ muon chambers or 2 *GeV* of energy deposited in the TPC poletip calorimeter. The event rate using this set of trigger configurations was $6-8$ $sec^{-1}$.

We collected approximately 30 tapes of raw data for further analysis or around $10^5$ events. In addition to this data exists around 2000 tapes of raw data taken during past run cycles of high-energy $e^+e^-$ physics running. About 10–20% of this data are events with electrons or positrons scattering from the residual gas in the PEP beamline. These tapes were separately analyzed from what we call the *dedicated* runs where gas was injected into the beampipe.

## Data Analysis and Scanning

### Data Selection

In order to filter out internal target (nuclear) physics from the $e^+e^-$ or 2-$\gamma$ processes also present in the data a set of offline selections were imposed:

1. The event had to have a associated $e^{\pm}$ tag
2. The event vertex had to be offset from the $e^+e^-$ interaction point. We required $80.0 > Z_{vertex} > 6.0$ *cm*.
3. The tracks in the event had to cluster around the event vertex. This filtered out events that triggered the detector but had a second interaction occur shortly afterwards (during the TPC detector sensitivity time), where both were readout and written to tape as a single event.
4. Any event was also kept even if $Z_{vertex}$ was inside the offsets when there were protons present in the event. These cuts left us with around $(3.0)10^4$ events for scanning and full analysis from the test run.

### Event Scanning

As an introduction to the TPC-2$\gamma$ data analysis system OASIS (originally OASYS for Offline Analysis SYStem), we did a selection and event-by-event hand scan of a selected sample. OASIS is a software interrupt driven program allowing for single event analysis/reanalysis applying different physics cuts to the data. A sampler of interesting events was compiled. This sampler included examples of quasielastic scattering, $\Delta$ production, associated strangeness production, deep-inelastic scattering and a unique example of massive target fragmentation from a Xenon nucleus.

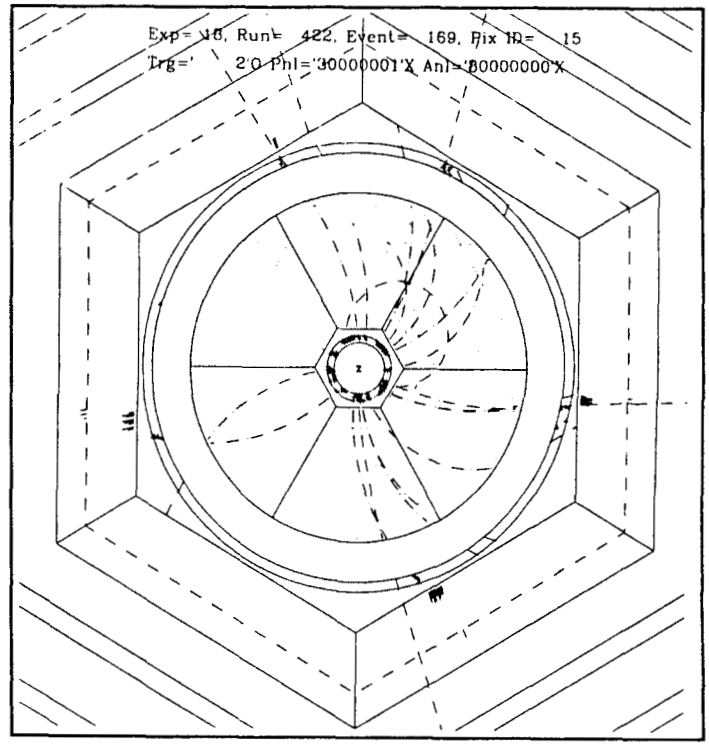


Fig. 1.5 *Example of an event as seen by the PEP-4 system. In this case, possible target fragmentation of an electron on a Xenon nucleus.*

Figure (5) shows an end-on and radial view of the high multiplicity xenon target fragmentation event. Figure (6) shows a plot of DeDx vs. momentum for the same event. In this figure each track is labeled by its track number and enclosed by a $2\sigma$ error ellipse. The theoretical DeDx curves for different particle masses are also plotted.

What is clear from this event is that to study such phenomena (*i.e.* looking at different exclusive final states) will require detectors capable of tracking and particle identification like a TPC.

## Bose Einstein Correlations

The renewed interest in Bose-Einstein correlations has prompted recent investigations in $e^+e^-$ an-

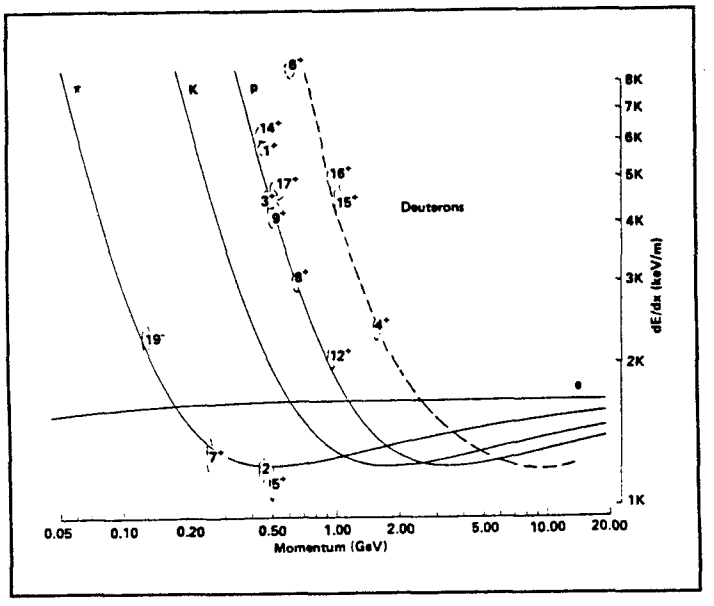


Fig. 1.6 *The dE/dx vs. Log(p) plot for the particles in the above Xenon event. Along with numerous protons, four deuterons are seen.*

nihilations and hadronic reactions[8-9] . The general ideas as applied to particle physics are an outgrowth of the formulation by Hanbury-Brown and Twiss (HBT) in radio astronomy. In high energy particle physics the acronym GGLP (Goldhaber-Goldhaber-Lee-Pais) is used to reference this correlation phenomena, along with the terms intensity interferometry or second-order interferometry.

BE correlation analysis is a tool to study the space-time development of particle emitting souces in high-energy interactions. Since boson wave functions are symmetrized according to Bose-Einstein statistics, a boson source (for instance emitting pions) will exhibit an enhancement for pions with small relative momenta. Quantitatively a two particle correlation function $R(p_1, p_2)$ is defined:

$$R(p_1, p_2) = \rho(p_1, p_2)/\rho_o(p_1, p_2)$$

where $p_1$ and $p_2$ are the pion four momenta and $\rho$, $\rho_o$ are the pion densitiess for a correlated and uncorrelated (no BE statistics) sample respectively. The parameter $q = p_1 - p_2$ $GeV$, the relative four momenta of the pions, is defined so that $R(q)$ is proportional to the fourier transform of the emitting source's space time distribution. For sources that have a lifetime $\tau$ and have a gaussian distribution in space $S(\bar{r}) \propto exp(-r^2/2\sigma^2)$ then $R(\bar{q}) = 1 + exp(-\bar{q}^2\sigma^2)/[1 + (q_o\tau)^2]$. Here $\bar{q} = \bar{p}_1 - \bar{p}_2$ $GeV/c$ is the pion three momenta difference and $q_o = |E_1 - E_2|$ $GeV$. In our analysis an exponential form $R(Q^2) = 1 + \lambda exp(-Q^2\sigma^2)$ where $Q^2 = \sqrt{p_1 - p_2)^2}$ $GeV$ was used.

Analysis Procedure

For our study the higher statistics sample of beam-residual gas events was used. We required

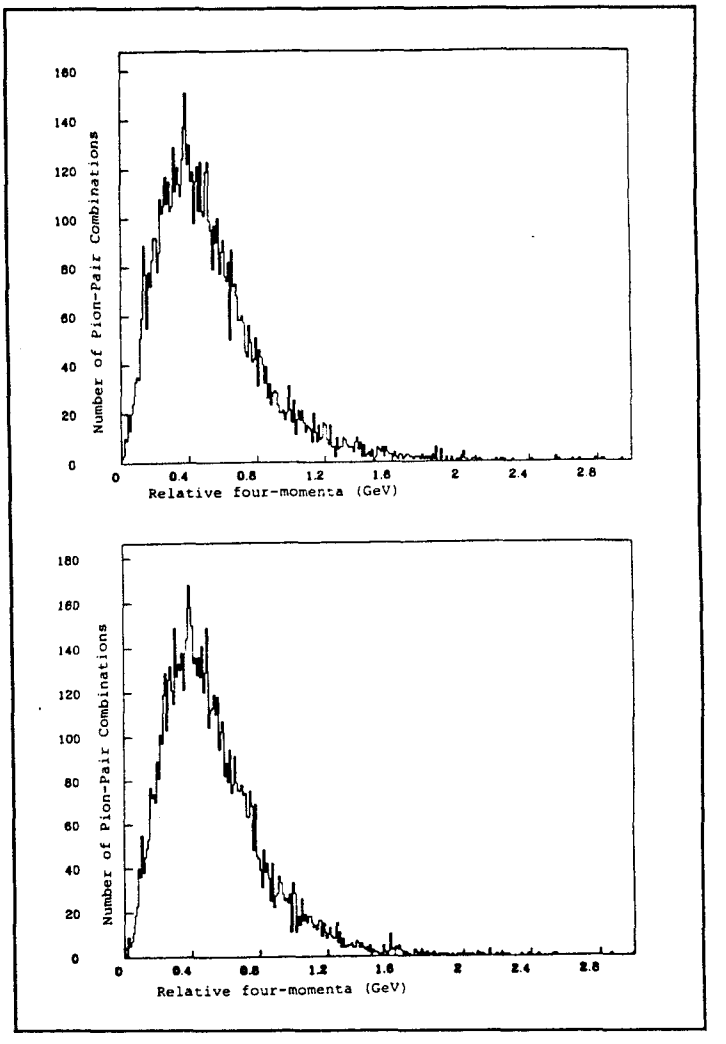


Fig. 1.7 *The pion density $\rho(\bar{p}_1, \bar{p}_2)$ as a function of $Q^2$ GeV. The top plot is for the correlated sample, the bottom for the uncorrelated sample.*

events having at least two like-sign pions identified in the TPC. A minimum momentum of 150 $MeV/c$ was required, the cutoff for pions to track into the TPC volume. This helped filter out low momenta conversion pairs where an electron was misidentified as a pion. The sample thus obtained was scanned for failures in the track pattern recognition progam. Any *bad* events where, for example, a single track was divided into two (hence forming a pair of tracks having very small relative momenta and introducing a bias into our results) are rejected. Figure (7) is a plot of $\rho(\bar{p}_1, \bar{p}_2)$.

For $\rho_o(\bar{p}_1, \bar{p}_2)$ the pion density in the absence of BE correlations, event mixing was used. Event mix-

ing uses a pion from one event combined with a pion from a different (and independent) event, insuring no correlations between the pions. The correlation function $R(\bar{q})$ is then the ratio of the correlated to uncorrelated pion densities.

Results

Figure (8) is a plot of the correlation function $R(Q^2)$ An enhancement is seen at $Q^2 < 0.25$. Fitting to the exponential form above we get $\lambda = 0.37 \pm 0.19$ and $\sigma^2 = 1.37 \pm 0.41$ *fermi*. However even with our larger data sample this result is still statistics limited. We also looked at $R(Q^2)$ as a function of $P = |\bar{p}_1 + \bar{p}_2|$ $GeV/c$ and as a function of the mediating virtual photon's momentum transfer $-q^2$ $(GeV/c)^2$. The results for both were consistant with no variations, again the statistics of our data sample limiting what we could do.

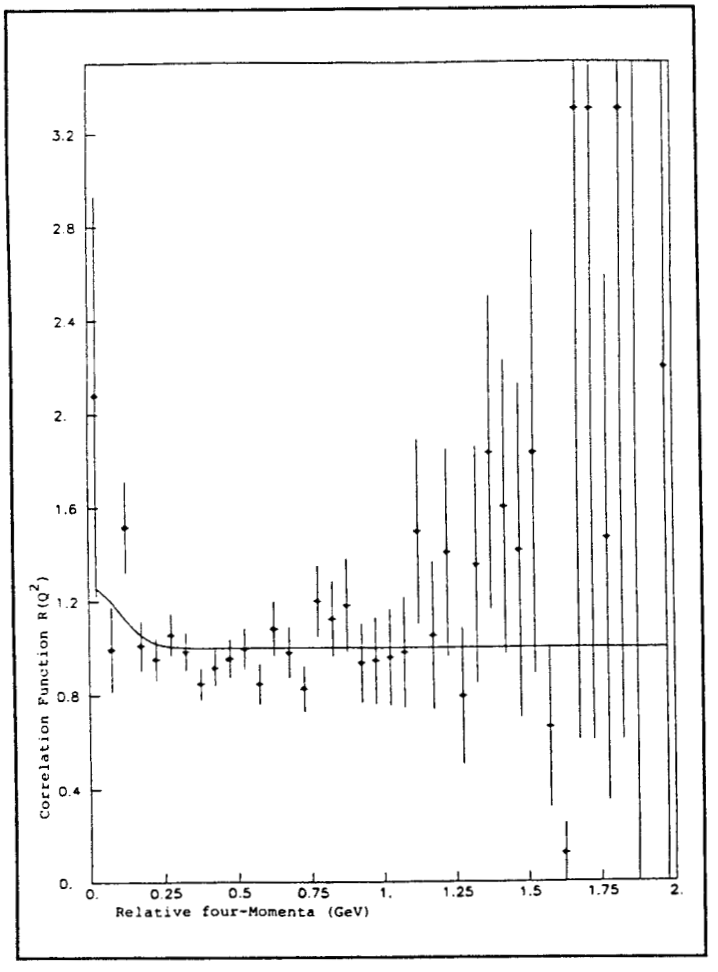


Fig. 1.8 *The fitted two-pion correlation function. The fitted data shows an enhancement at small relative four-momenta.*

Summary

We have briefly presented a preliminary result of a gas target test run at PEP. For this test and for subsequent data analysis the TPC-2$\gamma$ facility was used. The combined three-dimensional tracking and particle identification capabilities of the TPC allow study of a number of processes of interest in nuclear physics. The success of the TPC at PEP indicates that a future nuclear physics facility at PEP should be of similiar capability. However the size and complexity of the TPC-2$\gamma$ facility means that any future nuclear physics detector will be much larger that what has been traditional. In any case the feasibility of such a detector is very good.

## REFERENCES


1. F.S. Dietrich *et. al.*, *An Exploratory Gas-Target Experiment at PEP using the TPC/2$\gamma$ Facility;* Submitted to the 2nd conference on Intersections between Particle and Nuclear Physics Lake Louise, Canada (1986).
2. M.D. Shapiro, University of California Ph.D. Thesis, Berkeley (1985).
3. J. Marx and D. Nygren, *The Time Projection Chamber,* Physics Today, **46**, October (1978).
4. R. Madaras and P. Oddone, *Time-Projection Chambers,* Physics Today, **36**, August (1984).
5. H. Aihara, *et. al.*, IEEE Trans. Nucl. Sci. **NS-30**, a series of articles devoted to the different PEP-4 subsystems, (1983).
6. A. Buijs, University of Utrecht, Netherlands Ph.D. Thesis, Utrecht (1986).
7. D. Ritson, *Proceedings of the Summer Institute on Particle Physics,* edited by A. Mosher, SLAC Report **239,** 177, (1981).
8. H. Aihara, *et. al.*, Phys. Rev. **D31**, 996, (1985).
9. A. Breakstone *et. al.*, Phys. Lett. **162B**, 400 (1985).

# A Nuclear Physics IR for PEP – Issues and Conceptual Design

K. Van Bibber
Lawrence Livermore National Laboratory
University of California
P.O. Box 808 L-421
Livermore, Calif. 94550

## Abstract

A conceptual design for a nuclear physics interaction region at PEP is presented. The design is based on components of the $2\gamma$ (PEP-9) detector, configured as a large acceptance forward angle spectrometer suited for asymmetric fixed target kinematics. The system is evaluated with a prototype experiment in mind, namely pion production in quasielastic kinematics, $(e, e'\pi)$. Issues and open questions particular to internal target work are discussed.

## Introduction

Most of the 'Work' of this Workshop has concerned identifying the unique physics potential of the MIT-Bates stretcher-storage ring and the PEP storage ring for nuclear physics, and rightly so. Nevertheless, the experimental conditions and beam parameters are sufficiently unlike those of fixed target operation that it is worthwhile giving some preliminary thought to the hardware – targetry and detectors – in order to realistically constrain physics proposals being developed for these facilities.

Presented here is a conceptual design of a small angle, large acceptance forward spectrometer for PEP. It is intended as a multiparticle spectrometer, which would record both the inelastically scattered electron, and resulting hadrons within $20^o - 25^o$ of the beam axis. As is, it is may be most suited for, among others: (*i*) inclusive electron scattering (*e.g.* from polarized targets); (*ii*) semi-exclusive measurements in hadronization studies (where the inelastically scattered electron and one or more hadrons normally will be detected); and (*iii*) vector meson production, *e.g.* $(e, e'\phi)$, $\rho \rightarrow K^+ + K^-$. The suitability *as is* for quasielastic scattering, *e.g.* $(e, e'p)$, $(e, e'2p)$ is less clear in view of the wide angle at which the struck nucleons normally go. Nevertheless, such a downstream spectrometer could be viewed as the first most essential piece of a comprehensive IR, with either a central tracker (solenoidal magnet, wire chambers, *etc.*), or a movable small solid angle spectrometer arm to cover wider angles.

A brief description of the IR environment will be given, followed by a discussion of how an existing detector, the PEP-9 $2\gamma$ spectrometer could be reconfigured for fixed-target kinematics. Space does not permit a detailed description of all the components, but relevant parameters will be mentioned. Estimates of rates, resolution and acceptance will be presented. Finally, very preliminary considerations concerning data acquisition will be discussed. The gas jet target for unpolarized work will not be dealt with at all, as it will be described in detail in the paper of J. Molitoris[1] . However, the question of luminosity monitoring will be addressed, and a proposal to use Moller electrons (analogously to Bhabha scattering in $e^+e^-$ physics) will be put forward.

## The Interaction Region

A likely location for nuclear physics at PEP (at least initially) will be IR-8, shown in Figure 1. Four of six of the PEP interaction regions are nearly identical, and alternative siting would not change any important details. The beam line is 4 meters off the floor, and is 5.7 m and 9.9 m from the outer shielding wall and inner wall respectively. The distance from the $e^{\pm}$ interaction point to the first quadrupole magnet in either direction is approximately 6.4 m. The house for electronics and computer have been added to the figure. There is one interesting feature to be commented on in IR-8, which is the proton alcove downstream of the IR in the electron-going

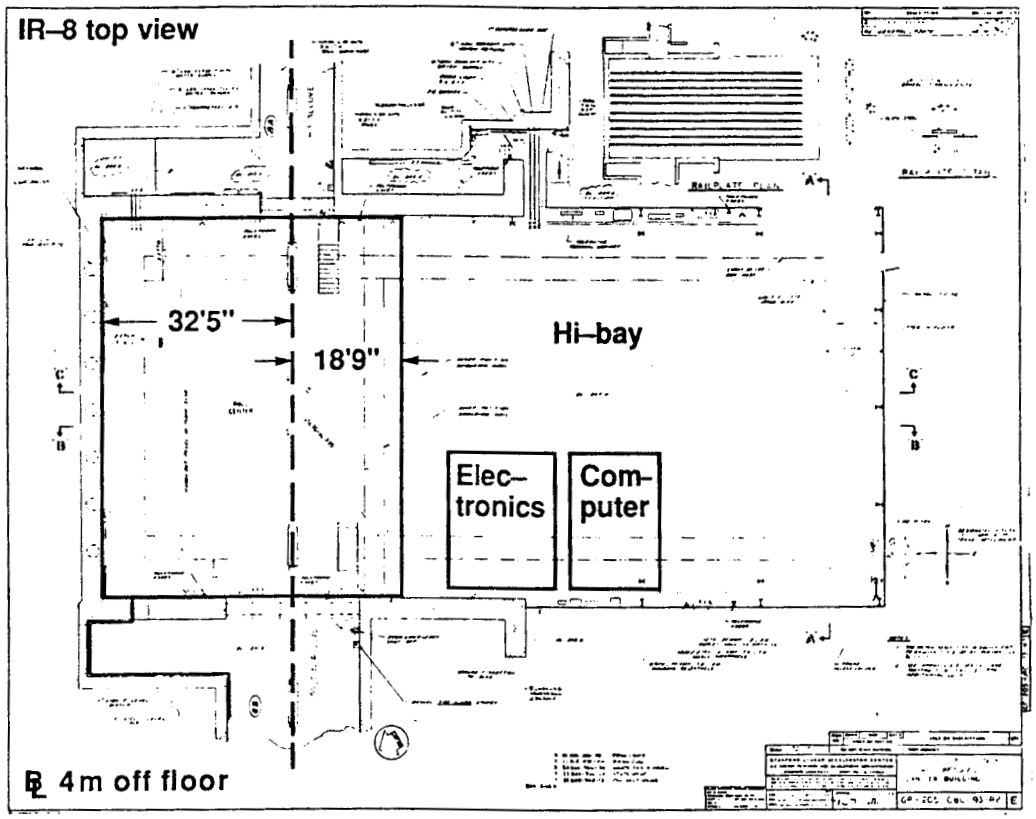


Fig. 1 *Top view of PEP Interaction Region 8. The electron direction is from top to bottom in the figure.*

direction. This feature was added to the design for PEP when it was anticipated that it might become an *ep* collider at some later date. Such an alcove would permit detectors at very small angles, should that be desirable in the future.

For fixed target physics, the gas target need not be located at the $e^{\pm}$ interaction point, and in any case the electron and positron beams will be separated everywhere except at IR-2 (this separation being $\approx 1\ cm$). Figure 2 shows the $10\sigma_{x,y}$ beam envelope and the horizontal and vertical 'beam stay clear' ($\equiv 10\sigma + 1\ cm$). Since it is anticipated that the gas jet target will be directed vertically, it is seen that even at $z = 4m$, a jet of radius $0.5 - 1\ cm$ will handily intercept the whole beam.

## The PEP-9 2$\gamma$ Spectrometer

The PEP-9 2$\gamma$ Spectrometer is part of the TPC-2$\gamma$ Detector, which is described in detail in the paper of S. Melnikoff[2] . The 2$\gamma$ spectrometer actually consists of two symmetric low angle spectrometers at the 'North' and 'South' ends of the Time Projection Chamber (TPC). Each end is comprised of a Cerenkov detector, drift chambers, a magnetic volume, a time-of-flight hodoscope, calorimetry and muon identifiers. Subtending 20-200 msr, their chief function is to tag inelastically scattered $e^{\pm}$ in two-

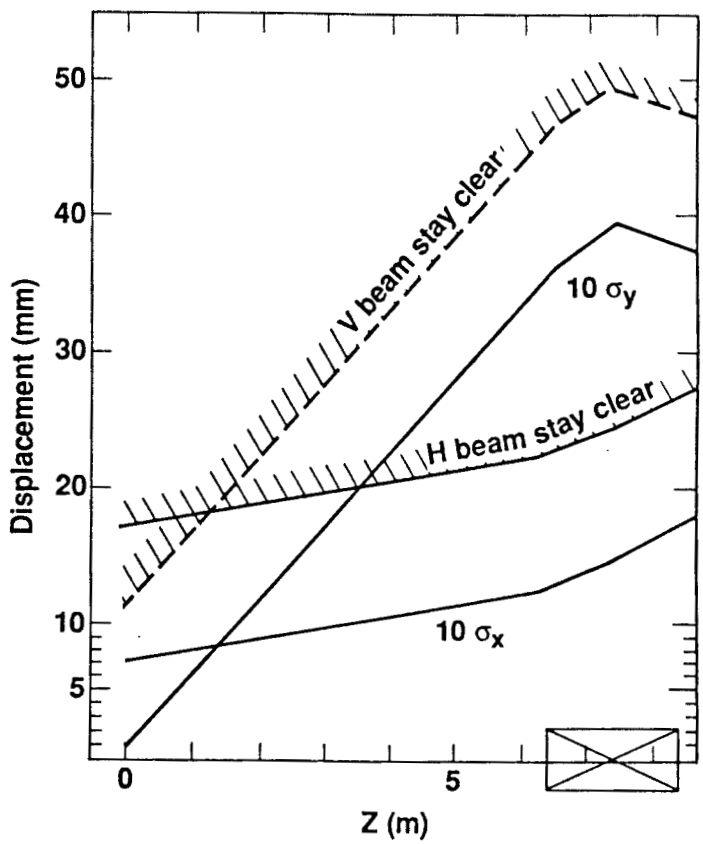


Fig. 2 *PEP beam profile for non-interacting IR's during high-luminosity era. Not final.*

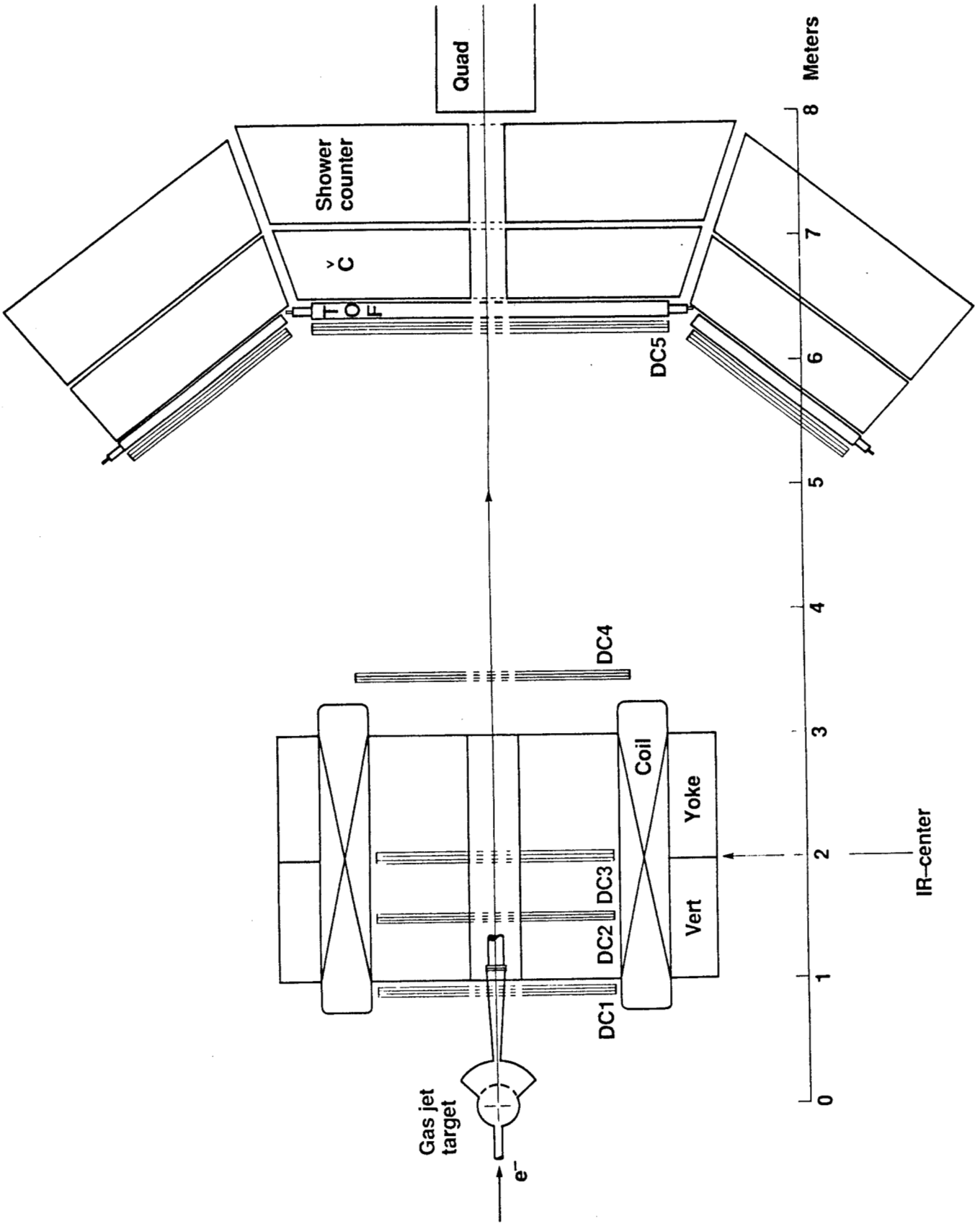


Fig. 3 *Conceptual design of a fixed target interaction region for PEP (top view).*

photon physics. Here the electron and positron do not annihilate, but rather each radiates a virtual photon which fuse to produce a hadronic or leptonic final state with the quantum numbers of two photons. It was the low-angle spectrometer system which made the TPC-2$\gamma$ detector attractive for the nuclear physics test of 1986.

The development which permits us to think about PEP-9 for the future nuclear physics program at PEP is that the TPC-2$\gamma$ collaboration has been approved for several years of high luminosity running at PEP. Under the high luminosity upgrade, the two final quadrupoles in IR-2 will be moved in much closer to the TPC, and most of the 2$\gamma$ detector will need to be relinquished. Most of the collaborating institutions in PEP-9 have been extremely gracious in permitting us future use of their components.

## A Spectrometer for Fixed Target Physics

The features of a spectrometer for nuclear physics generally desired for many of the experiments proposed at this Workshop are *(i)* large solid angle coverage for multiparticle final states; *(ii)* an angular range starting as close to the beam axis as possible; *(iii)* at least moderate momentum resolution ($\leq 10^{-2}$); and *(iv)* good particle identification $(e, \pi, K, p, d)$ up to 5 $GeV$. Of particular importance is excellent $\pi - e$ discrimination for processes where the inclusive hadron production cross section in relation to the inelastic electron cross section may be severe.

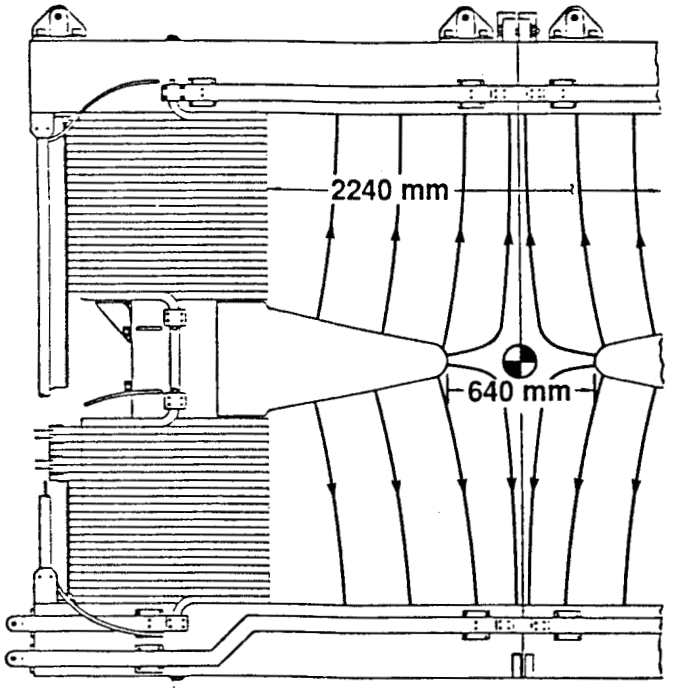


Fig. 4 *View from beam axis of existing PEP-9 Septum Magnet. Magnetic field lines are indicated.*

A conceptual design for a large acceptance forward spectrometer is shown in Figure 3, assembled partially from components of the PEP-9 spectrometer.

## The Septum Magnet

Each half of the *PEP-9* spectrometer contains a septum magnet shown in Figure 4. The active area is approximately 2.2 $m$ on a side, with a depth of 1 $m$. The coils around the vertical yoke are wound with the sense such that flux lines emerge from the septum or 'nose' of the magnet and are directed upwards in the top half and downwards in the lower half. The resulting field at the beam axis is zero as required; an air-core quadrupole cancels out higher multipoles to a large degree. An unfortunate characteristic of the magnets at present is that the $\int Bdl = 1.8\ kG - m$ only. The reason for this is twofold: *(i)* half of the amp-turns are outside of the vertical yoke and cause flux loss to the exterior region; and *(ii)* saturation of the iron, particularly in the nose. Our intention is to use the magnets back-to-back, but additionally to consider modifications that will increase the magnetic field strength. A study has been made using the two-dimensional code POISSON of various options involving addition of iron, and rewinding the coil. (Obviously as the coil will be rewound, the two yokes will be first joined before the mounting of the coil.) Figure 5 *top* shows the field lines for the magnet as is, where the maximum field strength is 4.9 $kG$. Figure 5 *bottom* shows the proposed modification. The equivalent number of amp-turns (762,000) is now wound around the nose, rather than the vertical yoke. The nose itself has been made wider, and the vertical and horizontal yoke-pieces have been moved outwards to preserve the active area of the spectrometer. The resulting maximum magnetic field is predicted to be 7.6 $kG$, and the average $\int Bdl \approx 12\ kG - m$. The three heavy lines indicate cuts along which the magnetic field is plotted in Figure 6.

## Drift Chambers

The existing *PEP-9* detector consists of five drift chambers per arm termed DC1-5. The total number of planes per arm (*e.g.*, the North arm) is 15, as each DC basically consists of $u$, $v$, $y$ stereo planes whose wire pitch is $\pm 5^{\circ}$ and $90^{\circ}$ from vertical respectively. Each plane consists of roughly 60 drift cells per plane, and each drift cell by itself resolves the 'left-right ambiguity' as instead of a single sense

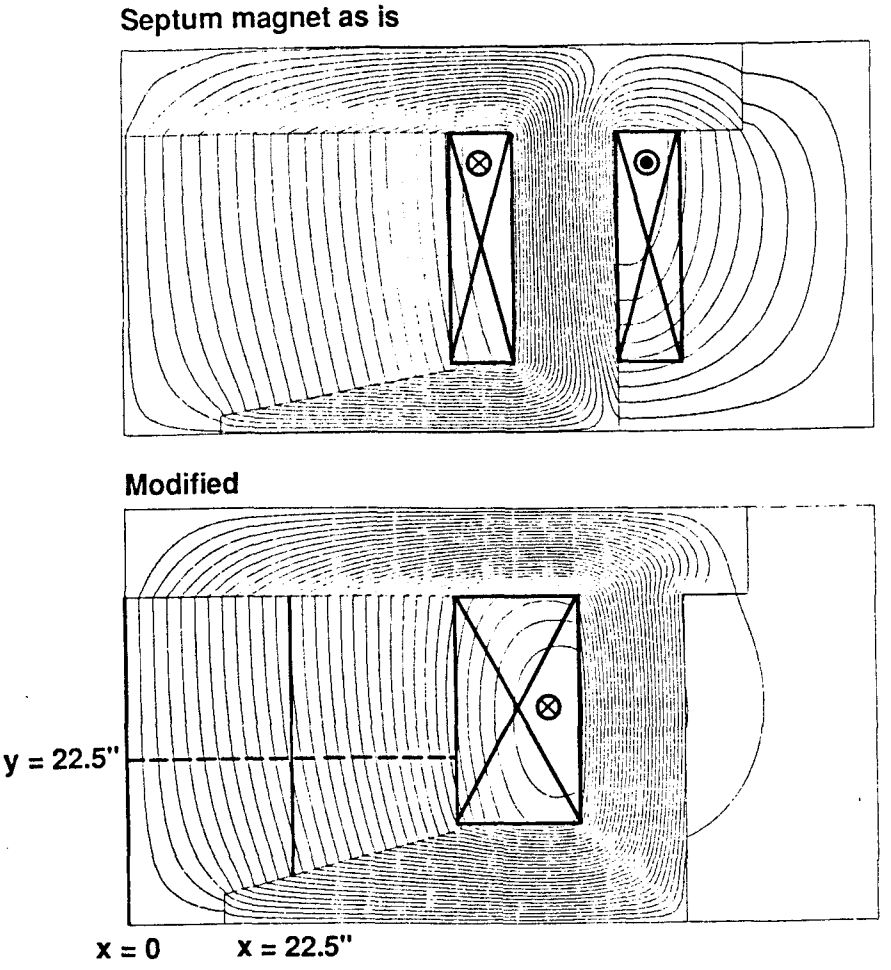


Fig. 5 *Quadrant field map for the present configuration of the septum magnet (top), and a possible modification (bottom). In the modified case, the coil return is made around the magnet nose. From 2-d code POISSON.*

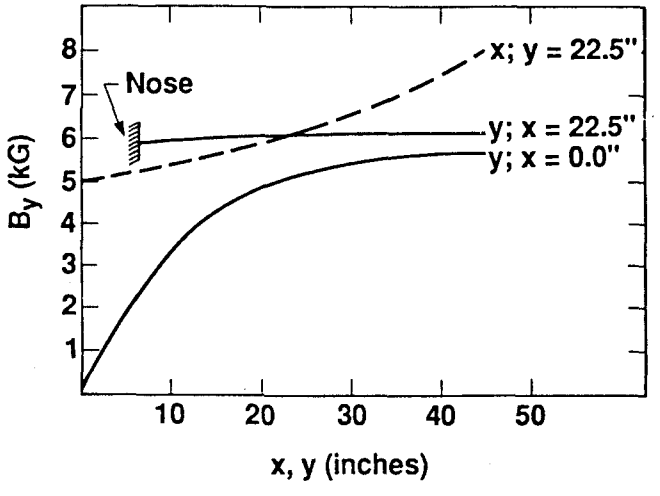


Fig. 6 *Profiles of vertical magnetic field component ($B_y$), vs. $x, y$. Cuts refer to dashed, and heavy solid lines in Figure 5.*

wire per cell, there is a double sense wire spaced by 250 $\mu$.

The sense and cathode wires for DC2-5 are 38 $\mu$ and 250 $\mu$ respectively, and the gas mixture is $Ar - CO_2$ (16.4%) at one atmosphere. Windows for DC2-5 are aluminized mylar 25 $\mu$ thick. The typical resolution is $\sigma = 125$ $\mu$. The most comprehensive document on the *PEP-9* drift cells is that of White[3] .

The TOF Hodoscope

The TOF hodoscope of each arm of *PEP-9* is a lattice of 50 horizontal and 62 vertical scintillator strips, assembled in four quadrants. Each strip is 8.5 *cm* wide, and is read out by a single photomultiplier tube (PMT).

Corrections are made in analysis for time slewing due to amplitude variations (for which 15% improvements were reported in test beam measurements), and for propogation time through the scintillator ($\approx 14$ $cm/nsec$). The resulting time resolu-

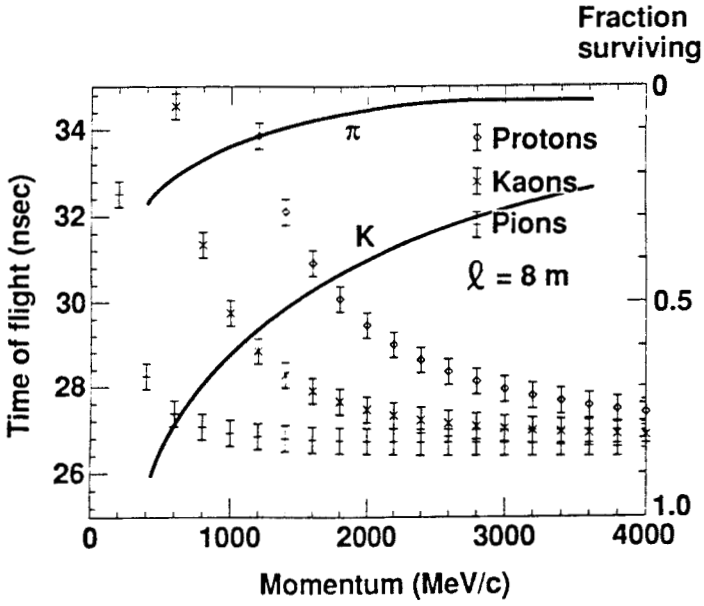


Fig. 7 *Time-of-Flight for $\pi$, $K$, $p$ vs momentum left ordinate; $\pi$, $K$ fraction surviving right ordinate.*

tion is found to be $\sigma = 0.47$ *nsec* for horizontal or vertical strips alone, and $\sigma = 0.30$ *nsec* where the average is taken between a coincident horizontal and vertical strip.

The particle identification by TOF that can be expected with this hodoscope in the spectrometer proposed is shown in Figure 7. (Note that the TOF wall in Figure 1 is actually at 6 $m$ rather than at 8 $m$ for which this calculation was performed.) Also included in the figure are the fraction of $\pi$, $K$ surviving decay in flight for an 8 $m$ flight path.

One intact TOF wall and electronics have been designated for future use in the nuclear physics interaction region, the other TOF wall was cut in half for use as a fast offline cosmic ray trigger for the TPC. When it has completed its function there, its use as lateral extensions to the downstream detector package could be negogiated.

The Calorimeter

The calorimeter is a critical component of the detector package as clean electron identification depends heavily on it. A suitable candidate appears to be the novel lead-liquid scintillator design of the Santa Barbara group used at FNAL[4] . Their detector consisted of 60 layers, each $1/3X_0$ thick. Each layer was made of an Al-Pb-Al laminate, plus a rectangularly corrugated teflon-coated aluminum sheet. The corrugations space the layers from one another, and are filled with liquid scintillator. Light emitted from the scintillator is thus confined to a strip of 3.17 *cm* width and is transmitted in either direction to its end. The layers are arranged to give $u$, $v$, $y$ stereo views of $\pm 20.5^o$ and $90^o$ respectively. Channels emerging on any side of the calorimeter with a common $(x,y)$ coordinate are ganged together in the readout; a lightguide containing a wavelength shifter is mounted above the common ends with a small airgap and a single PMT reads out each lightguide. The resolution for the full scale detector $(2.44m \times 4.88m)$ was $12\%/\sqrt{E}$, and position resolution was about 3 $mm$. One practical difficulty which inhibited this group from adopting this design for the TPC was the difficulty of introducing a hole for the beam pipe through the device; this difficulty would obviously have to be countenanced in this spectrometer as well.

The Cherenkov Detector

The area where least progress has been made is the issue of Cherenkov detector(s). Cherekov detectors are possibly required for two purposes: to improve the $\pi/e$ separation, and second, to improve the $K/\pi$ separation. For the former case, the solution is straightforward. A threshold detector with atmospheric or sub-atmospheric pressure can be made handily with a range of gases to choose any threshold momentum $p_t^\pi$ desired. The only complication is the very non-paraxial trajectories at the back end of the spectrometer that will result when the septum magnet is upgraded. The issue of $K/\pi$ separation (indistinguishable above 1.5 $GeV/c$ by time-of-flight alone) is more difficult. A combination of a heavy gas Cerenkov (*i.e.* neopentane) and silica-aerogel is certainly an option. Concerning aerogel, its range of index of refraction in manufacture is limited to $1.02 \leq n \leq 1.1$, and we are not aware of any commercial vendors at present. For $n = 1.02$, $p_t^\pi = 0.71$ $GeV/c$, whereas $p_t^K = 2.5$ $GeV/c$.

A ring imaging Cerenkov detector is also under study for particle identification, motivated by the design of Fermilab experiment E-665.

## Performance of the System

Rates

In designing a large solid angle forward spectrometer, the inclusive rates must be well understood in order to select the appropriate instrumentation with the requisite granularity so the sytem will not be overwhelmed. Furthermore, it must be considered whether it will be possible to trigger on all of the categories of events of interest while minimizing useless triggers.

Rates have been estimated assuming a $D_2$ target, a luminosity $\mathcal{L} = 10^{32}$, and an effective coverage

in polar angle for the spectrometer of $4^o \leq \theta \leq 20^o$. Numbers below refer to incident energies of 14.5 (4) GeV.

Inclusive Electron Rate

The rate of inelastically scattered electrons from nuclei have been estimated using parameterized structure functions for deep inelastic scattering ($E_{min} = 0.1\ GeV$), and the assumption of $y$-scaling for the quasielastic part. This yields 40 $Hz$ (400 $Hz$), the factor of 10 increase in going down in energy being due to quasielastic scattering.

Inclusive Hadron Rate

Useful parameterizations of inclusive hadron production at high energies are almost non-existent. Based on the data of Boyarski[5] using a 0.3 radiation length Be target at 18 $GeV$, the hadron singles rates should be less than 40 $kHz$.

Moller Electrons

The Moller electron spectrum diverges with increasing lab angle out to the maximum angle of $90^o$, but the electron energy falls rapidly. (Wide angle electrons in the lab frame correspond to 'grazing' collisions in the center-of-mass frame.) Within the spectrometer's angular acceptance, the *total* Moller rate is $6 \times 10^7\ Hz$ ($1.7 \times 10^7\ Hz$); however the fringe field of the septum magnet should pin the softest part of the spectrum preventing these electrons from hitting the first plane of wire chambers. Cutting off the spectrum (somewhat arbitrarily) at $E_{min} = 30\ MeV$ results in a much lower rate: $8.5 \times 10^5\ Hz$ ($2.3 \times 10^5\ Hz$).

Resolution

The momentum resolution of the spectrometer is limited by multiple scattering of particles in the drift chambers and the air, the finite position resolution of the drift chambers, and the uncertainty of the exact trajectory through the magnet (as the field is inhomogeneous, particularly so at smaller angles). In the region where the field is fairly strong (and where the inhomogeneous nature of the field may be neglected), the resolution is estimated to be $\delta p/p = [(2.5 \times 10^{-5}) + 10^{-6}p^2]^{1/2}$ (see Figure 8). This resolution is predicated upon an average $\int Bdl = 10\ kG - m$, two sets of drift chambers (6 planes comprising 0.03 cm mylar for multiple scattering) separated by 1 meter before the magnet, and likewise after it, and a drift chamber resolution of $\sigma = 150\ \mu m$. (It is easy to see that only the inner two drift chamber planes contribute to the momentum uncertainty, and not the outer two.) It is a general property of non-focussing spectrometers that their low-momentum resolution is limited by multiple scattering, and it is difficult to achieve much better than $5 \times 10^{-3}$.

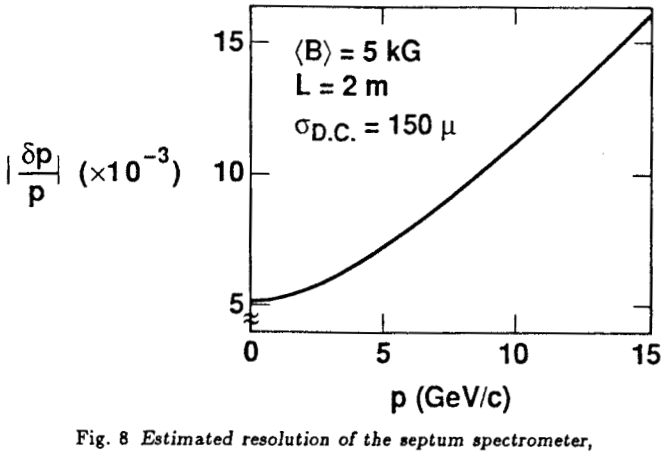


Fig. 8 *Estimated resolution of the septum spectrometer, not including effect of field inhomogeneity.*

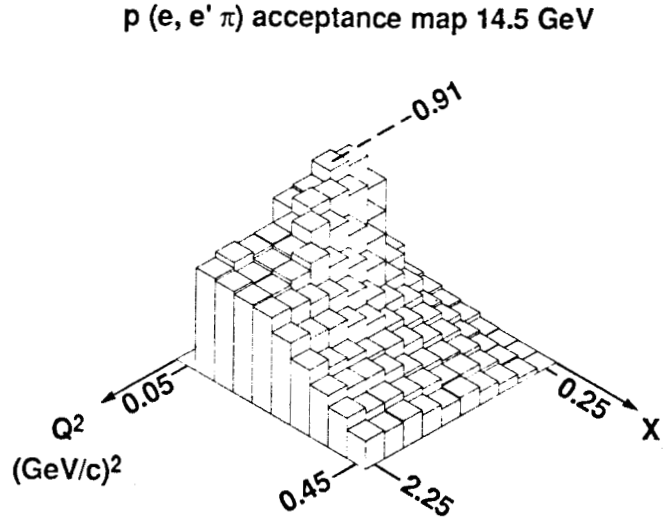


Fig. 9 *Acceptance map for the reaction $p(e,e'\pi)n$ at 14.5 GeV. The angular distribution for the pions was taken to be $e^{(10t)}$.*

Acceptance

The concept of a forward spectrometer is to detect the inelastically scattered electron, and at least part of the hadronic final state in the same detector. This will preferentially be the maximum rapidity part of the final state. With the gas jet target 100 cm in front of the septum magnet entrance, the magnet exit defines a square of $\theta_{x,y} = 18^o$. The acceptance surface for detecting both the electron and pion in the reaction $p(e,e'\pi)n$ at 14.5 GeV as a function of $x$, $Q^2$ has been calculated by Monte Carlo, and is shown in Figure 9. (The angular distribution of the pion about the momentum transfer vector q was taken to be $e^{10t}$, where $t = (p_\pi - q)^2$ in the usual

way). The acceptance is significant throughout $x$, and for all but the lowest $Q^2$. The corresponding map for quasielastic scattering from nucleons would be much worse, as the heavy mass of the nucleon implies a large momentum transfer angle, typically $50^o$ or so. The dead solid angle that the vertical yoke represents is one of the most unsavory aspects of a spectrometer built around a septum magnet.

## Data Acquisition

The total number of channels of data the spectrometer represents will be at least 3000, and could easily double if a conventional Cerenkov detector is forsaken in favor of a ring-imaging device. (The number of channels requiring readout with zero-suppression is estimated to be 50 per track, leading to a total of 100-250 per event typically.) The collaboration forming about such an interaction region for PEP (American / ANL / CalTech / LLNL / Massachusetts / RPI / SLAC / Virginia / Washington) has defined as a necessity a data acquisition rate of 30 $Hz$, and a realistic goal of 100 $Hz$. The former should be achievable within conventional VAX-based systems, the latter would require either multiple tape drives or the new WORM technology combined with a multiple processor system for data logging and analysis[6] . Nevertheless, at this stage it must be said that plans concerning computers and software are still at a fairly primitive level.

## Luminosity Monitoring and Calibrations

Perhaps the chief unanswered issues for an internal target facility at PEP concern luminosity monitoring and calibration of the various detector components. The situation for $e^+e^-$ physics is more felicitious in that Bhabha scattering provides both luminosity monitoring and monoenergetic (*e.g.* 14.5 $GeV$) electrons and positrons with a meaningful rate at wide angles (in spite of the $Q^{-4}$ angular distribution) for running calibrations of calorimeters, TOF hodoscopes, DC's, *etc.*. The analog of Bhabha scattering for fixed target experiments, Moller scattering from atomic electrons in the gas target, holds out hope for luminosity monitoring. Figure 10 (a) and (b) shows that while the cross section rises steeply for larger angles, the energy drops precipitously; particles emitted at angles less than $5^o$ will be occluded by the beam pipe within almost any spectrometer design. Nevertheless, electrons in the 100 $MeV$ range should be cleanly identified with a combination of magnetic analysis and shower energy in a small NaI detector.

Calibration is a different matter; Moller scattering is of no use here to keep detectors calibrated even at small angles. Perhaps the only possibility is to intersperse actual data collection with periodic hydrogen target runs in order to collect sufficient *ep* elastic scattering pairs throughout the acceptance of the spectrometer.

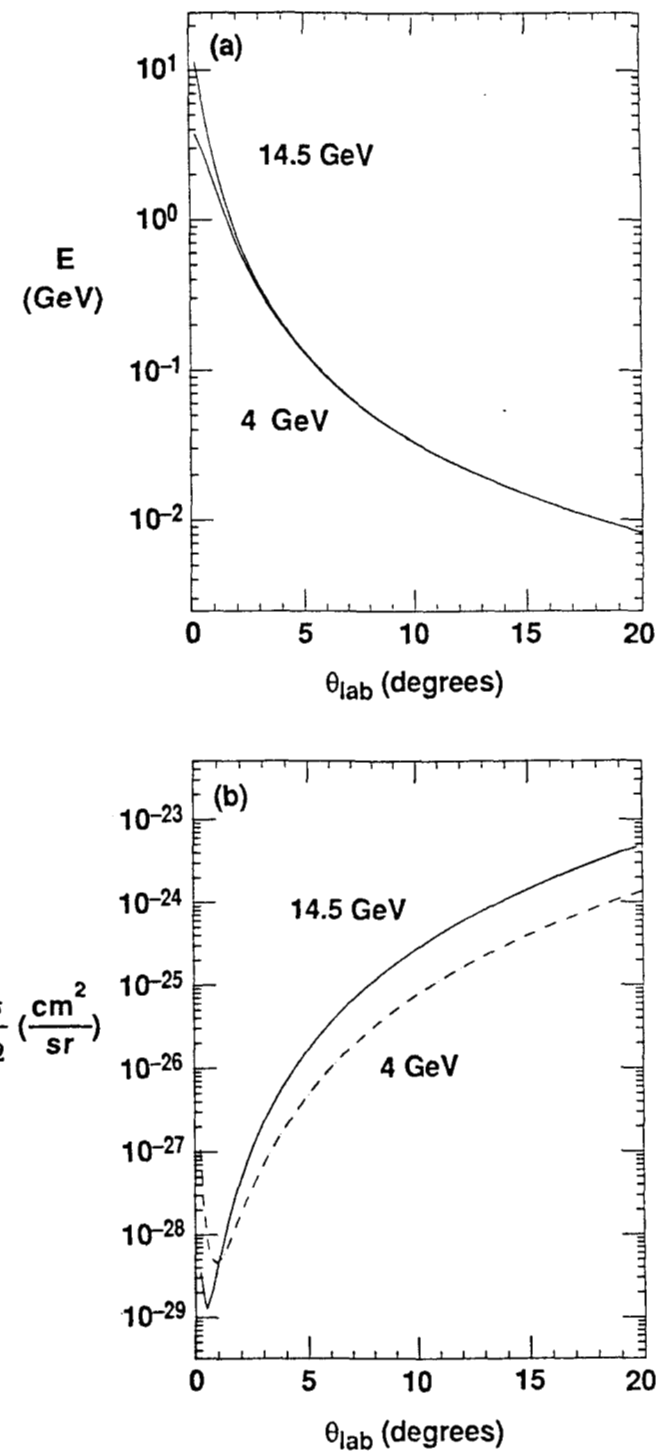


Fig. 10 *(a) Energy of Moller electrons vs. angle; (b) Differential cross section of Moller electrons vs. angle.*

Acknowledgements

The cooperation of S. Melnikoff and J. Molitoris has been invaluable in this work. I thank R. Early for assistance with the magnetic field calculations. We are very grateful to the member institutions of PEP-9 who have made their components of the $2\gamma$ spectrometer and their counsel available to us freely.

## REFERENCES

1. J.D. Molitoris, K. Van Bibber, *Development of a Warm Gas Jet Target for PEP*, Proceedings of this Workshop.
2. S.O. Melnikoff, *High Energy Nuclear Physics at PEP Recent Results using the Time Projection Chamber*, Proceedings of this Workshop.
3. J. White, *PEP-9 Drift Cells*; PEP-9 Technical Memo TG-311 DRF-015 (June 20, 1984).
4. V.K. Bharadwaj, Nucl. Instr. and Meth. **155**, 411 (1978) and Nucl. Instr. and Meth. in Phys. Res. **228**, 283 (1985).
5. A.M. Boyarski §C.2 *SLAC USERS MANUAL*, (1968).
6. W.J. Langeveld, *Optical Storage and its possible use in High Energy Physics*; Asilomar Conference on Computing in High Energy Physics (1986).

# KAON ELECTROPRODUCTION FROM THE PROTON AND DEUTERON†

Stephen R. Cotanch and Shian S. Hsiao

Department of Physics, North Carolina State University
Raleigh, North Carolina 27695-8202

## Abstract

Calculations for the electroproduction reactions $p(e,e'K)Y$ ($Y=\Lambda,\Sigma$) and $d(e,e'K)YN$ are reported to motivate future experiments using different facilities at SLAC. Study of the elementary production processes $p(e,e'K)\Lambda$ and $p(e,e'K)\Sigma$ will provide important information about KNY coupling constants, the kaon form factor, and possible differences between Quantum Hadrodynamic and Chromodynamic formulations. Inclusive measurements for $d(e,e'K)YN$ will permit unique investigations of YN interactions as well as a search for strange dibaryons which are predicted to occur at energies near the $\Sigma N$ threshold.

## Introduction

As evidenced by the Nuclear Physics at SLAC (NPAS) and Continuous Electron Beam Accelerator Facility (CEBAF) projects, as well as several other GeV electron accelerators under development outside of the U.S., interest in high energy electro-nuclear physics is clearly expanding. Much of this interest is motivated by the growing awareness that a complete understanding of the photon's electromagnetic coupling to hadrons provides an unique, theoretically "clean" handle for studying individual and composite hadron structure and hadronic interactions. Investigating kaon electromagnetic production is perhaps the most appropriate example of this philosophy since the $K^+$ meson has the simplest hadronic reaction mechanism. Further, photo, $(\gamma,K)$, and electroproduction, $(e,e'K)$, studies directly address several fundamental issues in both nuclear and particle physics. These issues are detailed in the next two sections which describe kaon production from the proton and deuteron, respectively.

## Production From The Proton

Unfortunately, the quantity of data for the elementary reaction is not significantly greater than it was twenty years ago. The quality of existing data also needs improvement as cross sections are only accurate to about 10% and polarizations are only determined to within 25 to 50%. Additional, more accurate, measurements will provide new information and insight into: the fundamental production mechanism; the quark structure of the participating hadrons (i.e. static properties, form factors, etc.); tests of various SU(N) symmetry predictions including the usefulness of kaon PCAC; the vector meson hypothesis; and the important issue of distinguishing between theoretical formulations based on Quantum Hadrodynamics (QHD, only baryons and mesons) and Quantum Chromodynamics (QCD, explicit color degrees of freedom).

Figure 1 shows a recently published[1] electroproduction calculation for the virtual photoproduction process $p(\gamma_V, K)\Lambda$. Complete details of the calculation are given in ref. 1. As indicated in the figure, the different curves correspond to various combinations of coupling constants (labeled set I and II, obtained from a phenomenological photoproduction analysis[2]) and kaon form factors. Notice that set I coupling constants provide a better description of the $K\Lambda$ production data (asterists denotes experimental points). Enigmatically, however, set II coupling constants are favored for $K\Sigma^0$ production which is shown in Figure 2. It should be stressed that flavor SU(3) symmetry was assumed in transforming the coupling constants from $\Lambda$ to $\Sigma^0$ production. Using vector dominance, the kaon form factor is represented by a simple monopole term, (1 - Q**2/M**2), where M is the mass of the vector meson mediating the process. A detailed examination of both figures suggests that the phi meson (M = 1.02 GeV) generated form factor provides a slightly better description of the overall data than the rho which is more appropriate for $\pi$ electroproduction (this conclusion appeared much more dramatic in ref. 1, however, the first figure in that work contained an error which is corrected in this paper). The dotted line in both figures represents the result using a kaon form factor computed within the quark model[3]. This form factor

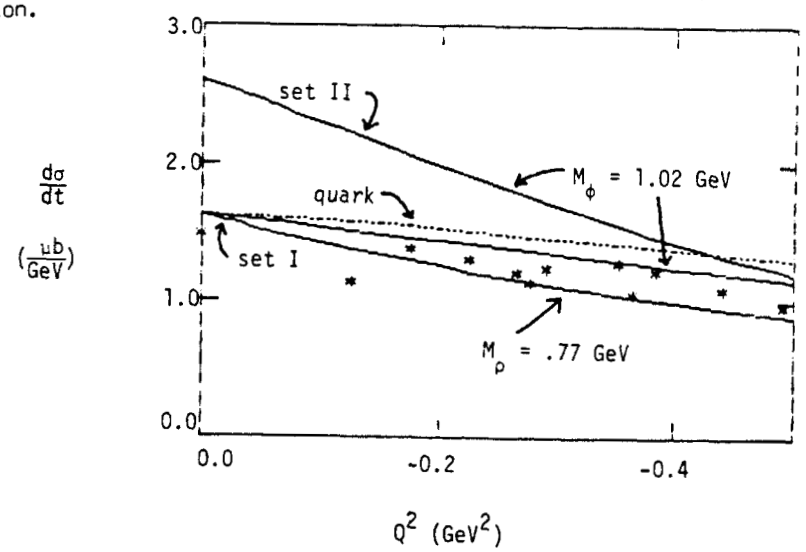


Fig. 1 Experiment and theory for $\gamma_V + p \rightarrow K^+ + \Lambda$.

†Supported in part by the U.S. Department of Energy and the Research Corporation.

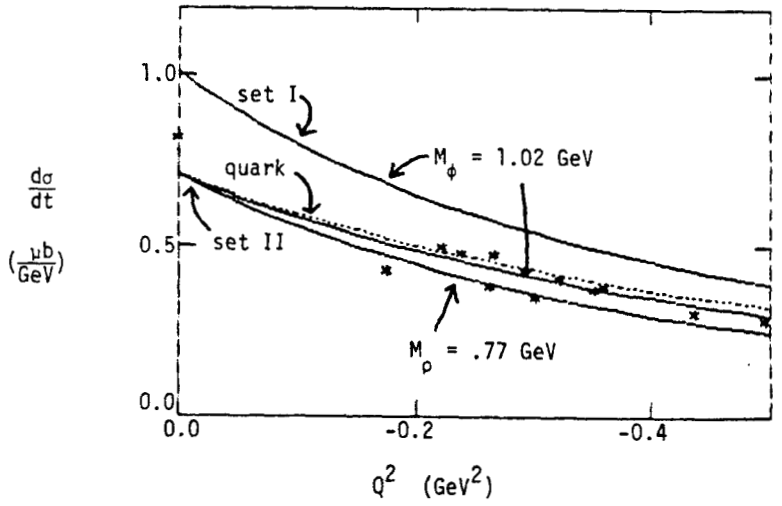


Fig. 2 Experiment and theory for $\gamma_v + p \rightarrow K^+ + \Sigma^\circ$.

seems to over predict the cross sections but when combined with the rho meson prediction does provide useful lower and upper theoretical cross section bounds. Because the current uncertainty in the data (error bars are shown in ref. 1) precludes extracting more detailed form factor information, more exacting theoretical constrains will have to await future precision measurements.

In addition to form factor studies and the determination of coupling constants, it is also of interest to understand the rapid Q**2 fall off of $\Sigma^0$ production relative to $\Lambda$ production. Arguments have been given[4,5] which relate the $\Sigma/\Lambda$ ratio decrease to the decrease of the neutron to proton structure function ratio which approaches .25 as the Bjorken scaling variable approaches 1. The implication is that the u and d quarks predominantly couple to isospin 0 which, with the addition of an isospin 0 s quark, favors $\Lambda$ formation over the isospin 1 $\Sigma$ production. Another related and important study is the high Q**2 behavior of kaon electroproduction. According to QHD the leading diagrams involve kaon exchange (t channel) and the cross section should scale like the kaon form factor squared (Q**-4 dependence). This prediction is completely different from the perturbative QCD results[6] which become more reliable at high Q**2. Accordingly, this may be a useful signature for delineating the two approaches as well as determining energy regions of applicability for each theory. Clearly, for these and the above reasons it is paramount that additional and more accurate KY electromagnetic production data be obtained.

### Production From the Deuteron

The reactions $d(e,e'K)YN$ and $d(\gamma,K)YN$ afford an unique method for studying $\Lambda N$ and $\Sigma N$ interactions. This is of timely importance as the existing $\Lambda p$ data is both meager and imprecise and the future of $\Lambda$ beams is not optimistic. The interesting physics centers around the cross section cusp region which is near the $\Sigma N$ threshold and is displayed in Figure 3. This curve represents the $\Lambda n$ theoretical total elastic cross section generated by solving a coupled channels problem (see ref. 7 for full details) for the three mass partitions $\Lambda n$, $\Sigma^0 n$, and $\Sigma^- p$ using potential D provided by Nagels and de Swart[8]. This interaction, which contains hard core, tensor, and antisymmetric spin-orbit components, provides a reasonable comprehensive description of limited $\Lambda p$ elastic and inelastic, $\Lambda p \rightarrow \Sigma N$, data. This cusp is due to an enhancement in the triplet s wave sigma channel which is the strange analogue of the deuteron. Since $\Lambda n$ measurements are not possible the only direct way to investigate this system is through

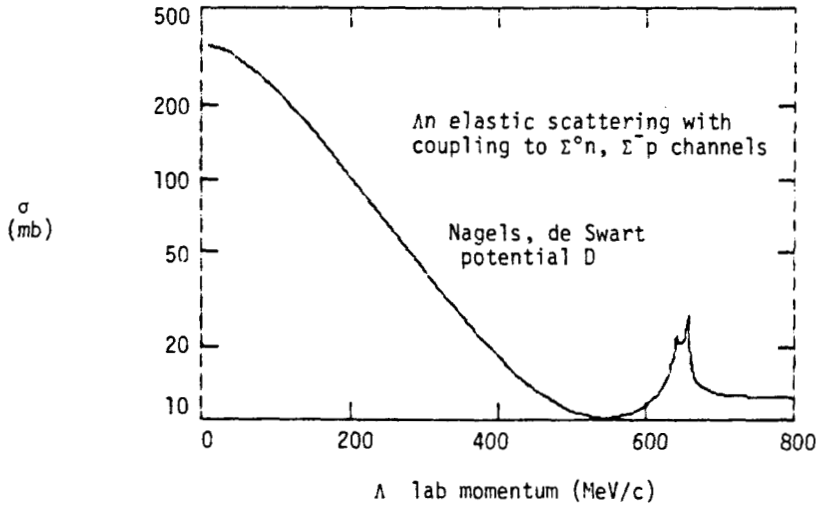


Fig. 3 Theoretical $\Lambda n$ total elastic cross section.

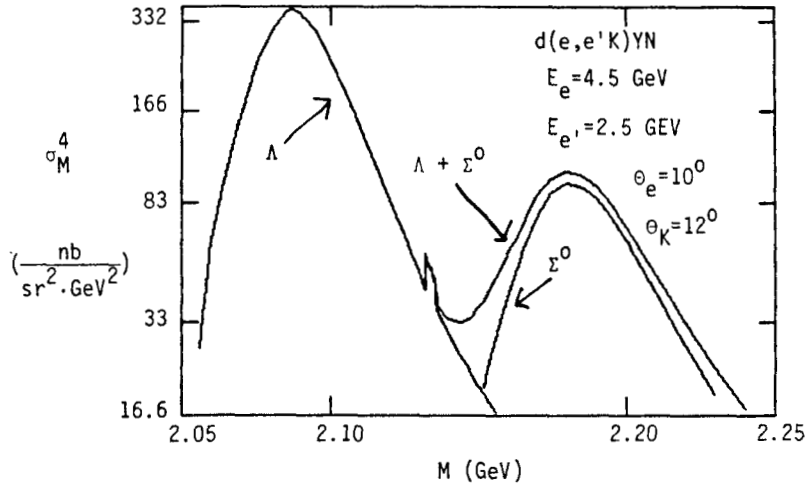


Fig. 4 Inclusive lab cross section for d(e,e'K)(Λn + $\Sigma^0$n).

final state interaction studies of the reaction d(e,e'K)Λn. In Figure 4 the predicted inclusive cross section (Λ is unobserved, only the three-momentum of the final electron and kaon are detected) is plotted versus the Λn invariant mass. Again notice the presence of the ΣN cusp near the sigma threshold (M = 2.13 GeV). Because this is an inclusive process it is not possible to resolve Λ and $\Sigma^0$ production hence, the upper curve represents the sum of the theoretical cross sections (the lower curves at low and high invariant masses represent pure Λ and Σ production, respectively). Accurate measurements of this reaction will provide firm constraints for YN potentials and will determine the unknown relative phase between Λ and Σ elementary production amplitudes (this calculation assumed +1 phase; a -1 phase generates a destructive dip instead of a peak in the cusp region). Further and of fundamental importance, such measurements would enable the search for strangeness -1 dibaryons which are predicted[9] to have mass values spanning the ΣN threshold (the singlet spin 0, $D_0$, has a calculated mass between 20 and 40 MeV below the cusp while the triplet spin 1, $D_1$, is expected to have a mass 20 to 40 MeV above the cusp). These six quark composite objects, which are distinct from a partial wave resonance between two three quark structures, have a predicted p wave internal configuration and also couple to p wave ΛN channels[10]. Consequently, the kaon angular distribution from d($\gamma_v$,K)YN should be markedly different for strange dibaryon formation than for the cusp excitation which is predominantly s wave. This is demonstrated, in part, in Figure 5 where the cusp in Figure 4 is isolated and decomposed into components. Note that the dominant contribution to the total cross section (top curve) is from including only the triplet s wave final state YN distortions (next curve from the top). Piekarz[11] has used this signature to argue for the formation of the triplet $D_1$ dibaryon using the reaction d($\pi^-$,$K^-$)Λp. He reports observing a maximum about 10 MeV above the ΣN threshold. Ideally, a search for the singlet $D_0$ should also be conducted since the experimental signature is clearer because at energies below the Σ threshold the inclusive measurement is free from the complexities of the sigma channel. This is illustrated in Figure 5 where the cross section for pure sigma production is shown to be relatively small at threhold (bottom curve is pure $\Sigma^0$ production). Unfortunately the ($\pi^-$,$K^-$) reaction is not effective in exciting the singlet state because the participating mesons have spin 0 and the elementary hadronic amplitudes have a small spin-flip component. However, the ($\gamma_v$,K) excites both spin states as shown in Figure 5. Kaon electromagnetic production is therefore not only an attractive, alternative process for triplet dibaryon

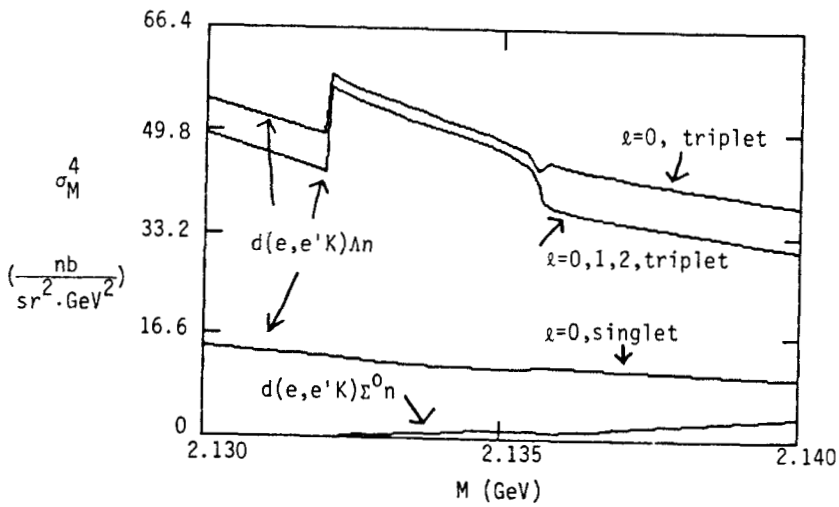


Fig. 5 Same as Fig. 4 for cusp region.

studies but also an unique way of searching for singlet dibaryon production from the deuteron.

Finally, it is also possible to study $K^+n$ final state interactions using $d(\gamma_V,K)YN$. In contrast to $K^+p$ the $K^+n$, or isospin 0, interaction is not well known. Improving our understanding of the KN amplitudes would further enhance the utility of the kaon as a scattering probe and provide important information concerning the exotic Z* strangeness +1 baryon resonances. Because the current experimental evidence is weak the existence of the Z* is highly controversial, however this resonance has also emerged from recent Skyrme model calculations[12].

## Experimental Considerations At SLAC

The luminosity available to the Nuclear Physics Interaction Region project at PEP for proton and deuteron targets, 10**33/(cm**2·s), appears to be quite suitable for elementary production studies and, depending on spectrometer design, perhaps even adequate for Yn final state interaction investigations. For example, a conventional two arm coincidence experiment involving a kaon and electron spectrometer each have 50 and 10 msr solid angle acceptance, respectively, and ± 5% momentum acceptance could anticipate 2 counts per hour for $d(e,e'K)\Lambda N$. If a large acceptance $4\pi$ detector is used the count rate would be increased by at least an order of magnitude. These count rate predictions assume a 50% kaon detection efficiency and are based on the cross section value near the cusp regions of about 50 nb/(GeV·sr)**2. Because the background for this experiment is low it should be possible to obtain accurate cross sections even without a large number of counts. Even higher counting rates, however, could be obtained using the primary SLAC beam and end station A. Although these spectrometers have much smaller acceptances (use the 1.6 GeV detector for the kaon with $\Delta\Omega$ = 3 msr, $\Delta p/p$ = ±5%; use the 8 GeV spectrometer for the electron with $\Delta\Omega$ = .75 msr, $\Delta p/p$ = ± 2%) the effective luminosity is significantly higher, about 10**37. Predicted count rates for a double coincidence, inclusive measurement of $d(e,e'K)YN$ in the cusp region are about 1 every 2 minutes.

## Conclusion

In summary, several important issues affecting both nuclear and particle physics could be resolved by performing more accurate measurements of the two reactions $p(e,e'K)Y$ and $d(e,e'K)YN$. More specifically, the elementary production studies would provide a decisive comparative test of QHD and asymptotic QCD while the final state interaction investigations would permit a clear search for strange dibaryons. Because much of the necessary equipment is already in place serious proposals to perform such experiments should receive high priority.

## References


1. S. R. Cotanch and S. S. Hsiao, Nucl. Phys. A450, 419 (1986).
2. H. Thom, Phys. Rev. 151, 1322 (1966).
3. W. Polyzou and P. L. Chung, private communication.
4. O. Nachtmann, Nucl. Phys. B74, 422 (1974).
5. J. Cleymans and F. E. Close, Nucl. Phys. B85, 429 (1975).
6. S. J. Brodsky and C. R. Ji, SLAC-PUB-3745 (1985) and S. J. Brodsky private communication.
7. S. R. Cotanch and S. S. Hsiao, Proceedings of the International Symposium on Hypernuclear Physics, Tokyo (1986, in press).
8. M. M. Nagels, T. A. Rijken and J. J. de Swart, Phys. Rev. D15, 2547 (1977).
9. R. L. Jaffe, Phys. Rev. Lett. 38, 195 (1977).
10. C. B. Dover, Nucl. Phys. A450, 95 (1986).
11. H. Piekarz, Nucl. Phys. A450, 85 (1986).
12. D. O. Riska, private communication.

# HOW GOOD IS VECTOR-MESON DOMINANCE IN THE DESCRIPTION OF E.M. FORM FACTORS OF HADRONS?

Manfred F. Gari

Institut für Theoretische Physik
Ruhr Universität Bochum
D-463 Bochum, W-G
and
Institut für Kernphysik
Kernforschungsanlage Jülich
D-5170 Jülich, W-G

Abstract

We discuss the quality of the vector-meson dominance approach in the description of electromagnetic form factors of nucleon and pion. A generalisation of this approach is given which includes the constraints at high $Q^2$ as obtained from perturbative quantum chromodynamics. An interesting possibility in the interpretation of the analysis is that nucleon and pion are very different in their quark-gluon structure. The importance for measurements of the electric form factors of neutron and proton as well as the pion form factor is emphasized.

---

The determination and understanding of the electromagnetic form factors of hadrons belongs to the fundamental problems in hadron physics. It is needless to say that with the knowledge of the form factors over a wide range of momentum transfer, important information on the underlying quark-gluon structure of the hadrons is obtained. As nucleon and pion are the simplest quark, resp. quark-antiquark systems they play a very special role. The simultaneous understanding of these bound states is of outstanding importance.

In the present discussion we investigate the quality of the vector-meson dominance (VMD) approach[1] in the description of the e.m. form factors of nucleon and pion. The connections to the quark-gluon description of the form factors is indicated together with the necessary modifications of the form factor description in view of the constraints obtained from perturbative QCD[2,3,4].
We follow the description of refs.5,6.

According to our understanding of a physical photon, the interaction of a virtual photon with a hadron consists of two different pieces: (i) a direct contribution which describes the interaction of the bare photon, and (ii) a contribution which is associated with the hadronic structure of the photon. This second part can be visualized by the interaction of the neutral vector mesons $\rho,\omega,\phi,J/\psi$ with the hadron.

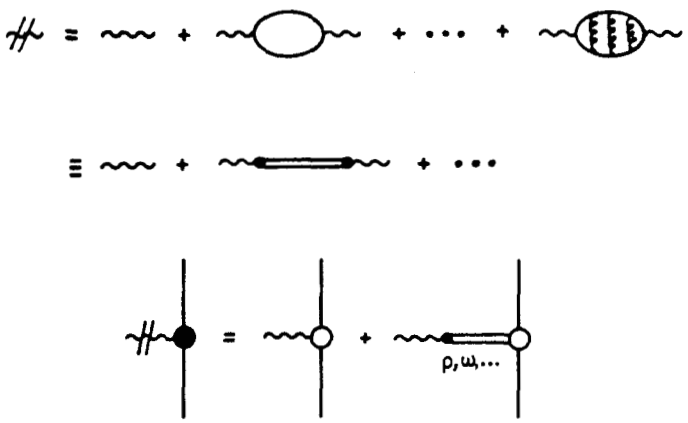


Fig.1

Hadronic (quark-gluon) structure of the photon and the interaction of a physical photon with a hadron.

Assuming that the vector meson contributions (Fig.1b) to the form factor, which dominate for momentum transfers close to the masses of the vector mesons, also dominate the form factor far away from these poles, the form factors can be described totally by the vector-meson contributions. This is the origin of the vector-meson dominance model. In the simplest version of this model, where one assumes a point-like interaction of the vector mesons with the hadron, the e.m. form factors are described completely by the vector meson propagators. For example, the nucleon isovector, as well as the pion e.m. form factor is given by the $\rho$-propagator:

$$F_\pi(Q^2) = m_\rho^2/(m_\rho^2+Q^2) = F_1^{IV}(Q^2) = G_M^p(Q^2)/\,G_M^p(0)$$

It is interesting to see the quality of such a simple description in the space-like region for the e.m. pion and nucleon magnetic form factor. A comparison with the available experimental information is shown in the following Fig.2.

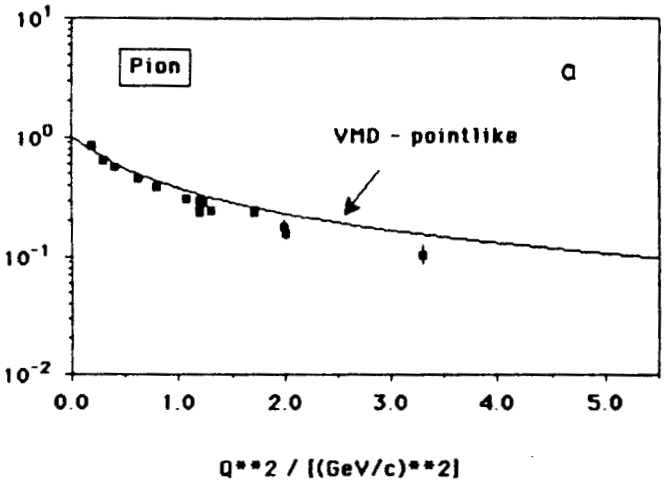


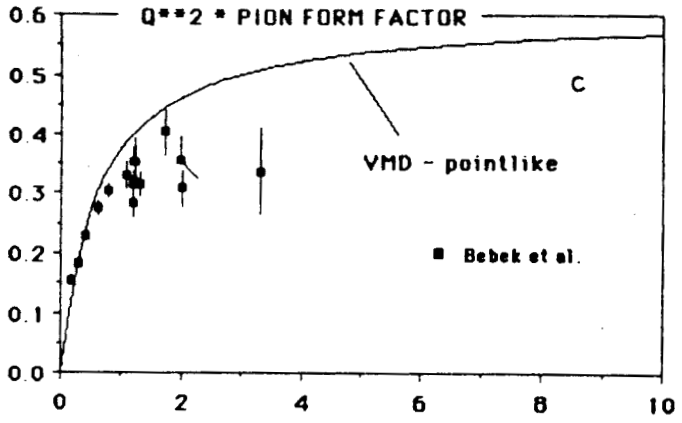


We realize that VMD, assuming point-like ρ - nucleon interaction, gives remarkable differences in the form factor description for nucleon and pion. While for the pion VMD gives a rough description of the data - showing very large deviation from the experiment only at high $Q^2$ - in the case of the nucleon the description is completely insufficient already at low $Q^2$.

How can we understand this difference? Does this finding already tell us that VMD is not a good way to describe hadron form factors?

Actually this is not the case as can be seen by considering structured particles. In a meson picture this seems to be rather an indication for a different importance of the meson cloud contribution of nucleon and pion. Consider the interaction of a photon with a hadron in the case of nucleon and pion. The emission probability for a virtual meson seems to be very different for nucleon and pion. The energy violation due to the uncertainty principle is very different in both cases. While ΔE is small for the nucleon, it is rather large for the pion, indicating a strong variation of the γ - nucleon interaction with momentum, while no such effect is expected for the pion. A similar effect is to be expected if we replace the photon by a ρ-meson. Compare Fig3 (V= γ , ρ, ω, φ, J/ψ).

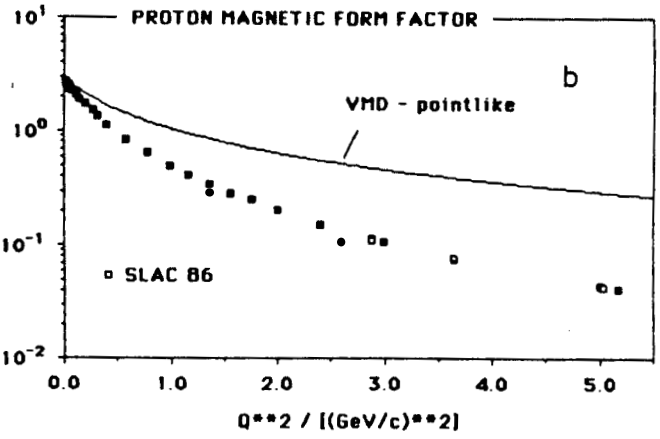


Fig.2

The e.m. form factors of pion and nucleon in the vector-meson dominance approach assuming point-like particles. Data are from refs.(7-10) for the nucleon and ref.(11) for the pion.

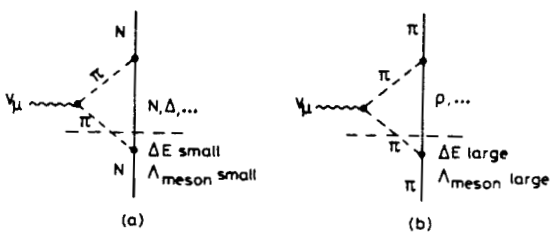


Fig.3

Illustration of the importance of meson cloud contributions to the interaction of the photon with nucleon and pion in a 'meson picture'.

This indicates that the strong disagreement of VMD with the data in the case of the nucleon disappears when we introduce a momentum dependence of the ρ - nucleon interaction:

$$G_M^p(Q^2)/\,G_M^p(0) = m_\rho^2/(m_\rho^2+Q^2) * \Lambda_1^2/(\Lambda_1^2+Q^2)$$

Here we denoted by $\Lambda_1$ a meson scale parameter giving the variation of the ρ - nucleon interaction with momentum transfer. This is the simplest possible assumption as long as we are only interested in the low $Q^2$ behavior. With $\Lambda_1 \sim m_\rho$ this corresponds roughly to the dipole form $F_D = [\Lambda^2/(\Lambda^2+Q^2)]^2$ with $\Lambda=\sqrt{0.71}$ GeV, which is the optimal one parameter fit to the nucleon data.

For the pion we do not expect such a large effect according to the above discussion. Thus a small modification of the simple VMD picture gives a rough description of the experimental data - both for nucleon and pion - at least at low momentum transfer.
A closer look at the comparison of theory with experiment however shows that in order to obtain a satisfying description of the data several deficiencies have to be cured. First of all the parameter $\Lambda$ in the best fit dipole form is not exactly the $\rho$-$\omega$ mass, a fact which is disturbing; $\Lambda$ is slightly larger than 0.84 GeV.
A more severe point is the failure of this simple picture to describe the experiments for momentum transfer larger than 1 GeV/c - for all form factors under consideration.

In the following we will see that taking into account **(i) the direct interaction of the photon with the hadron - and (ii) the form factor predictions from perturbative QCD** - a satisfactory description of all available nucleon and pion experimental data is possible. For more details see also refs.(5,6).

Applying the factorization approach of Brodsky and Lepage, perturbative QCD predicts the following high $Q^2$ behaviour of pion and nucleon form factors:

Pion

$$Q^2 \to \infty : \qquad F_\pi(Q^2) \to 16\pi\alpha_s(Q^2) f^2_\pi / Q^2 \qquad (1)$$

Note that as the pion decay constant $f_\pi$=93 MeV is measured, the asymptotic form factor is known in form and magnitude[4].

Nucleon
Here we have different asymptotic forms for Dirac and Pauli form factors, namely:

$$\text{Dirac} \quad Q^2 \to \infty : \qquad F_1^N(Q^2) \to \alpha_s(Q^2)^2 / Q^4 \qquad (2)$$

$$\text{Pauli} \quad Q^2 \to \infty : \qquad F_2^N(Q^2) \to F_1^N(Q^2)/Q^2 \sim Q^{-6}$$

The Pauli form factor is power suppressed as compared to the Dirac form factor reflecting the suppression of helicity changing amplitudes in QCD.

Considering the vector mesons in a one-field approximation we can consider a universal vector-particle nucleon vertex function, which strongly simplifies the picture. We see that **VMD contradicts the high $Q^2$ prediction from perturbative QCD**. This is due to the additional power suppression originating from the vector-meson propagators and emphasizes the need for additional corrections to the form factors. The vector-meson contributions to the e.m. form factors die out with increasing $Q^2$ as compared to the direct interaction contribution.

Nucleon form factors

Using the known information on the vector meson nucleon interaction which we have from pion-nucleon scattering, $SU(3)_F$ and the Zweig rule ( $g_{\varphi NN} \approx 0$ ), the nucleon isoscalar, isovector form factors are reduced to universal Dirac and Pauli vector-particle nucleon vertex functions $F_1(Q^2)$, $F_2(Q^2)$. Correspondingly, we have the following expressions for the isoscalar, isovector e.m. nucleon form factors:

$$F_1^{IV}(Q^2) = [\, \Delta_\rho\, c + (1-c)\,]\; F_1(Q^2)$$

$$\kappa_V\, F_2^{IV}(Q^2) = [\, \Delta_\rho\, c\kappa_\rho + (\kappa_V - c\kappa_\rho)\,]\; F_2(Q^2)\,, \qquad (3)$$

with $\Delta_\rho = m_\rho^2/(m_\rho^2+Q^2)$ and $c = g_{\rho NN}/f_\rho = g_{\omega NN}/f_\omega$. $m_{\rho(\omega)}^2/f_{\rho(\omega)}$ denotes the $\gamma$-$\rho(\omega)$ coupling constant. $m_\rho$=0.776 GeV, $m_\omega$=0.784 GeV, $\kappa_V$=3.706, $\kappa_S$= -0.12.

The isoscalar form factors $F_1^{IS}(Q^2)$, $\kappa_S F_2^{IS}(Q^2)$ are obtained from eq.(3) for $\rho \to \omega$ and $\kappa_V \to \kappa_S$.

The crucial information on the meson, resp. quark-gluon dynamics is hidden in the universal intrinsic Dirac- and Pauli-vertex functions $F_1$ and $F_2$. These functions have also to fulfill the requirements from meson physics[12] at low $Q^2$ and PQCD at asymptotic $Q^2$, as illustrated in the following Fig.4.

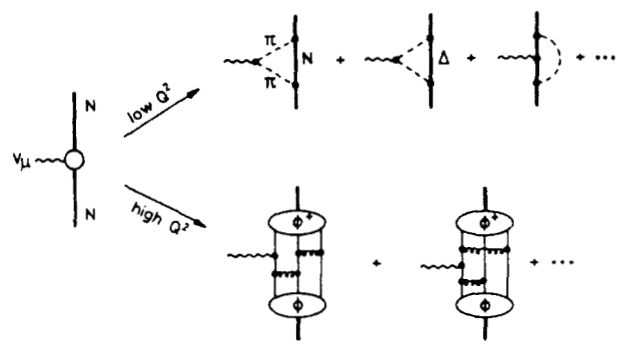


Fig.4

Illustration of the low $Q^2$ - high $Q^2$ constraints as incorporated in the present analysis. Low $Q^2$: meson dynamics; high $Q^2$: perturbative QCD. Some of the leading meson cloud contributions are shown, as well as the leading gluon exchanges.

Introducing meson and quark-gluon scale parameters $\Lambda_1$ and $\Lambda_2$ respectively, very simple forms for both $F_1$ and $F_2$, which fulfill the above requirements are:

$$F_1(Q^2) = \Lambda_1^2/(\Lambda_1^2 + \hat{Q}^2) * \Lambda_2^2/(\Lambda_2^2+\hat{Q}^2)$$

$$F_2(Q^2) = F_1(Q^2) * \Lambda_2^2/(\Lambda_2^2+\hat{Q}^2) \qquad (4)$$

with

$$\hat{Q}^2 = Q^2 \log((\Lambda_2^2+Q^2)/\Lambda^2_{QCD}))/\log(\Lambda_2^2/\Lambda^2_{QCD})$$

Note that for $Q^2 \gg \Lambda_2^2$ the form factors have the asymptotic form required from PQCD. Thus $\Lambda_2$ tells us something about the range of applicability of PQCD.

The magnetic and electric form factors $G_M$, $G_E$ are defined as usual by:

$$G_M^{p(n)} = F_1^{p(n)} + F_2^{p(n)}; \qquad G_E^{p(n)} = F_1^{p(n)} - Q^2/4M^2 F_2^{p(n)}$$

where $F_1^{p(n)}, F_2^{p(n)}$ denote Dirac and Pauli nucleon form factors:

$$F_1^{p(n)} = 1/2[F_1^{IS} +(-) F_1^{IV}]; F_2^{p(n)} = 1/2[\kappa_S F_2^{IS} +(-) \kappa_V F_2^{IV}$$

An analysis of the world nucleon cross section data in terms of the above form factor description yields with c=0.342, $\kappa_\rho$=6.61 and $\kappa_\omega$=0.32 the following scales: $\Lambda_1$=0.785 GeV, $\Lambda_2$=2.22 GeV and $\Lambda_{QCD}$ = 0.287 GeV.

Interested in a precise determination of the scale $\Lambda_{QCD}$ one has to take into account also the contributions from the anomalous dimensions of the three-quark component[6]. This we will not discuss here. The parametrization from above gives already a satisfactory description of the data. The inclusion of the anomalous dimensions in the analysis leads to $\Lambda_{QCD}$ = 180 MeV and very small changes in the other parameters; see ref.(6 ) for details of this analysis.

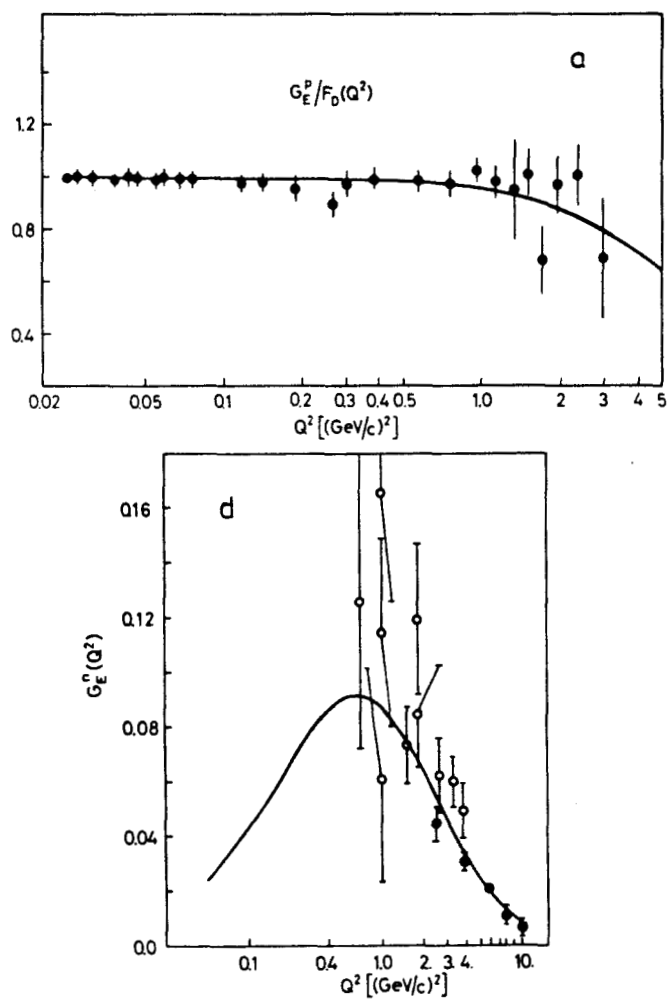


Figs. 5 a-d

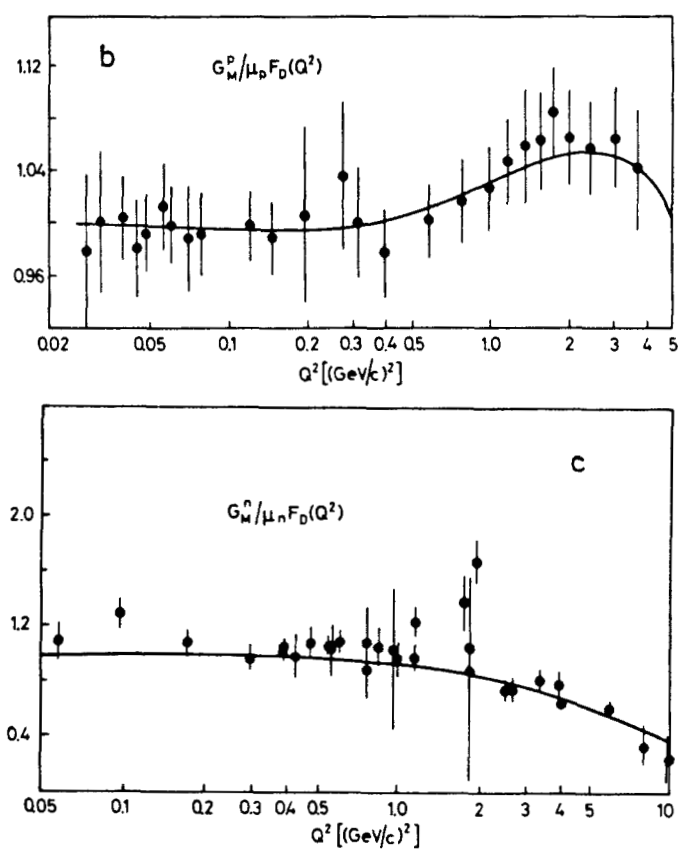


Results of the form factor analysis in comparison with the analysed data. The deviation from the common dipole form $F_D(Q^2) = [1/(1+Q^2/0.71)]^2$ is shown, except for the electric neutron form factor $G_E^n$: a) $G_E^p/F_D$, b) $G_M^p/\mu_p F_D$, c) $G_M^n/\mu_n F_D$, d) $G_E^n$. Data points are from the analysis of the cross sections of refs.(7-10).

One has a clear splitting between meson and quark-gluon scale. While the meson scale is about the mass of the vector mesons ($\rho,\omega$) as expected from meson physics, the quark-gluon scale is rather large $\Lambda_2 \approx 3\Lambda_1$. Note that $\Lambda_2$ is the only parameter in this picture where we have no information from other sources.

In view of the constraints on the model we realize a remarkable description of the data ( $\chi^2$/data $\approx$ 0.5). It is interesting to note that the proton data already determine the form factors. An interesting finding of the QCD-VM model is the fact that the electric neutron form factor turns out to be very large at high $Q^2$ in contrast to the general belief . It even exceeds the magnetic neutron form factor for $Q^2 > 4M^2$. In view of the fact that the neutron form factor turns out - in this model - to be dominated by the Pauli contribution, direct measurements of the electric and magnetic nucleon form factors are of great importance and will yield important information on the spin-flip parts of the form factor ( see also refs.3,5,6 for details).

As can be seen from the above equations ( 3&4 ), the Pauli form factor- for both neutron and proton - is dominated by the isovector part. This means that the electric neutron form factor is strongly related to the Pauli form factor of the proton. Therefore measurements of the electric neutron form factor as well as the Pauli form factor of the proton will give us valuable information on the quark spin flip contributions. In the following Fig.6 we show the importance of the Pauli contribution to the magnetic form factor of the proton.

Within the present model, which takes care of direct and vector-meson contributions to the form factor, we can now answer the question of importance of the vector-meson pole piece. A measure for this part at $Q^2 = 0$ is the constant c in eq.3. For the above given analysis we have c=0.342 showing that the vector meson contribution is rather small, 34 % at $Q^2 = 0$.

It is interesting to see what replaces the dipole form at low $Q^2$. For $Q^2 << \Lambda_2^2$ the isovector part has the following form:

$$F_1^{IV}(Q^2) = [\,\Delta_p\, c + (1-c)\,]\;\Lambda_1^2/(\Lambda_1^2+Q^2)$$

$$\sim [\, m_\rho^2/(m_\rho^2+Q^2)]^2 * 0.34 + 0.66\; m_\rho^2/(m_\rho^2+Q^2)$$

Instead of a moving of the rho-meson mass to higher values, a superposition of a monopole and dipole gives the desired structure.

Note that the presented formulas are only thought for a description of the space-like momentum transfer region! It is is only an effective form factor description and not suited for any continuation into time-like momentum transfer.

The vector-meson contribution to the magnetic form factor is shown in Fig.7.

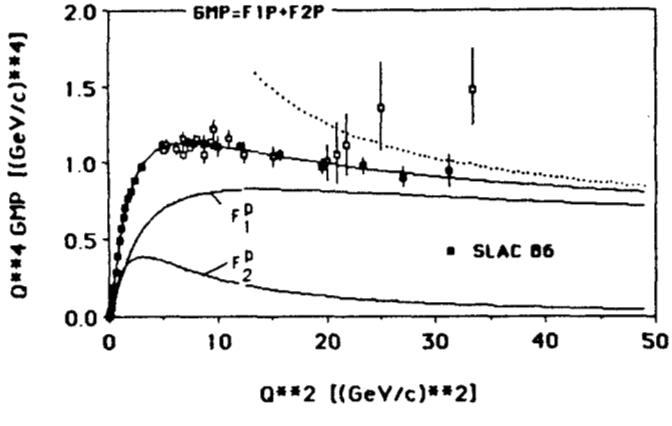


Fig.6

High $Q^2$ behavior of the proton magnetic form factor $Q^4 G_M^p$. The relative importance of Dirac and Pauli contribution is shown. The dotted line corresponds to the asymptotic form as obtained from PQCD .

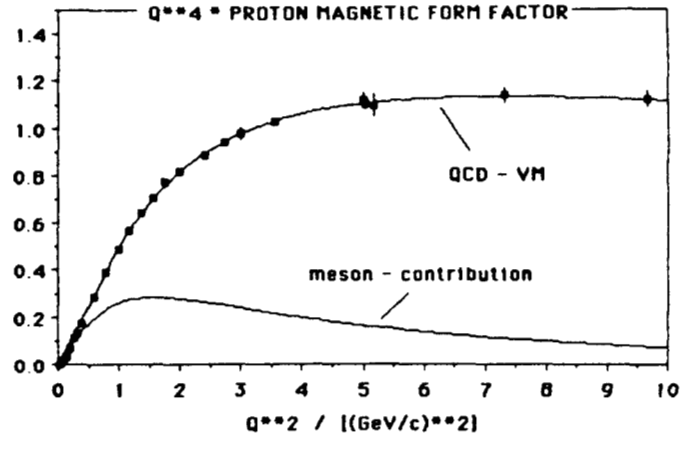


Fig.7

The magnetic form factor in the QCD-VM model. The part which originates from the $\rho,\omega$ contribution is indicated.

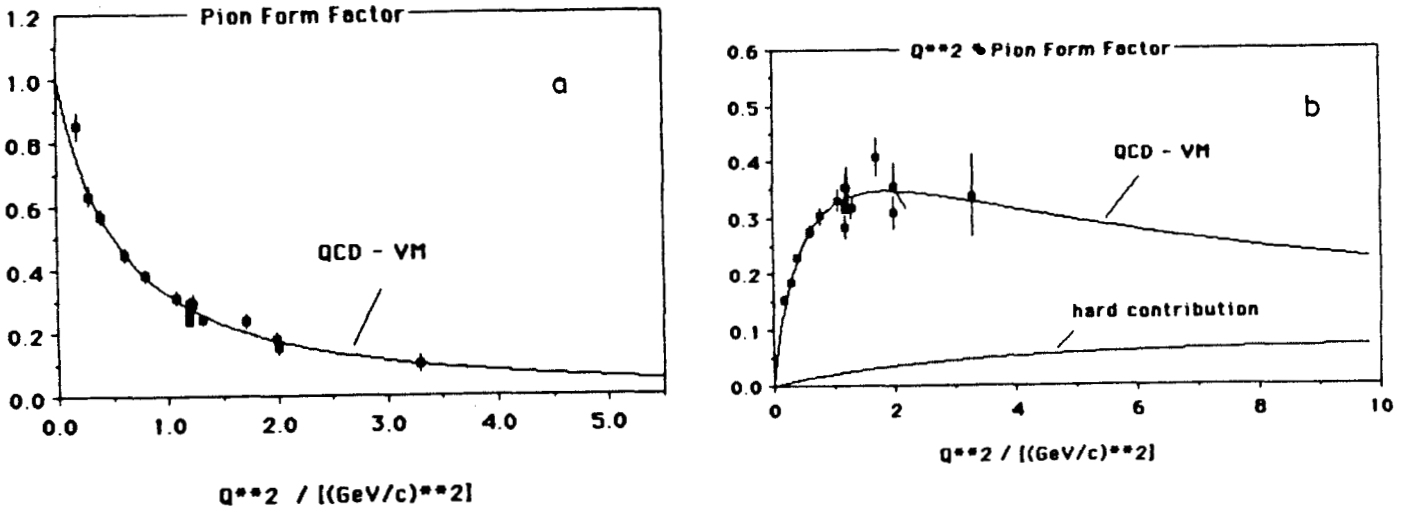


Fig.8

Pion form factor eq.(5), in comparison with the available experimental information. $F_\pi(Q^2)$ and $Q^2 F_\pi(Q^2)$ is shown. To stress the high momentum region, also the non-vector meson part, i.e. the part of the pion form factor which approaches the asymptotic form obtained in PQCD is shown ( hard contribution).

Due to the additional power suppression originating from the vector-meson propagator, the vector-meson contribution dies out with increasing $Q^2$ and becomes less and less important. This is an important finding in connection with the reliability of perturbative QCD calculations of the magnetic form factor. Associating the vector meson contribution with the gluon part of the proton wavefunction it might give us some hint about the importance of the leading Fock states. We shall come back to this point later in connection with the pion form factor where just the opposite behavior is found.

Pion form factor

An analysis equivalent to the one for the nucleon, suggests a form factor for the pion of the type:

$$F_\pi(Q^2)=[\Delta_\rho c_\pi + (1-c_\pi)]\,\Lambda_2^2/(\Lambda_2^2+\hat{Q}^2)\,;$$

$$c_\pi = g_{\rho\pi\pi}/f_\rho \qquad (5)$$

For $Q^2 \to \infty$ : $F_\pi(Q^2) \to (1-c_\pi)\,\Lambda_2^2/\hat{Q}^2$

$\hat{Q}^2$ as defined in eq.4

An optimal description of the data is obtained for $c_\pi = 0.975$, $\Lambda_{QCD} = 180$ MeV and $\Lambda_2 = 2.19$ GeV.

The result of such an analysis is shown in Fig .8 .

In contrast to the nucleon case, the analysis of the pion form factor data reveals a dominant contribution of the vector-meson part up to high momentum transfer. What is usually called the hard contribution and is very large in the case of the nucleon, plays here a minor role.

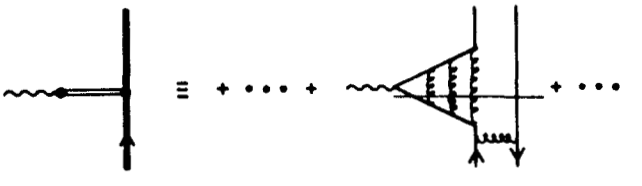

Fig.9

Interpretation of the vector meson part of the form factor as a gluon contribution of the pion wavefunction.

If the vector meson contribution can be associated with the part of the form factor connected with the gluon part of the wavefunction this might be a hint that in the case of the pion form factor the gluon part plays a dominant role, while for the nucleon the situation is reversed and the valence quarks dominate.

We note that the discussed analysis is the most simple one which actually can be performed. However because of the clear dominance of the vector-meson contribution, the situation in comparison with the nucleon is not likely to be changed qualitatively. In view of the importance of these questions, measurements of the pion form factor at high momentum transfer are highly desireable.

Kaon form factor

There are interesting consequences concerning the $K^+$ form factor. Using $SU(3)_F$ and a universality condition $c_\pi = c_\rho = c_\varphi$ ,we have according to the quark assignement of $K^+ = u\bar{s}$ , the following prediction for the Kaon form factor:

$$F_{K^+}(Q^2) =$$

$$[(1/2\,\Delta_\rho + 1/6\,\Delta_\omega + 1/3\Delta_\varphi)c_\pi + (1-c_\pi)]\Lambda_2^2/(\Lambda_2^2+\hat{Q}^2)$$

Comparison with VMD form factor models

In the case of the nucleon there exist a variety of vector-meson dominance models. We have seen that the point-like vector meson dominance model including only the established mesons does not give a reasonable form factor description. Most of the models therefore used generalisations in the direction of including heavier vector mesons as $\rho',\rho'',\rho''',\omega',\omega'',\omega'''$ and $\varphi',\varphi'',\varphi'''$, still with point-like meson nucleon interactions. Although the coupling constants of these hypothetical particles are determined by a fit to the nucleon data no satisfactory description could be obtained. Examples for these type of form factor descriptions are given in Figure 10 where we show the magnetic form factor of the proton, which is the most important form factor as it is best known experimentally.

It is noticeable that the strict point-like vector meson dominance pictures of KK and ZB are not able to give the magnetic form factor, not even at low $Q^2$. The model of Höhler et al. includes the information from pion nucleon scattering which gives additional information beyond VMD for the isovector case. The model of IJL includes a direct coupling of the photon to the nucleon as discussed above, however only in the case of the Dirac form factor. The Pauli form factor is treated in VMD. In addition, a parametrized $\rho$-propagator was necessary to explain $G_M^p$. Although both Höhler et al. and IJL give a good description of the proton magnetic and electric data at low momentum transfer, they fail at high $Q^2$ and in the description of the neutron form factors.

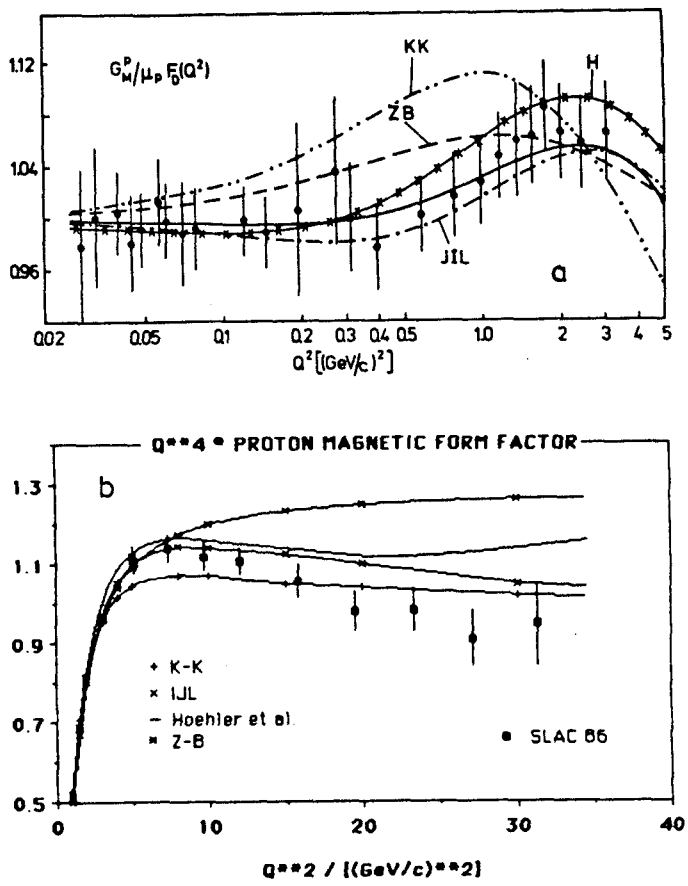


Fig.10

Comparison of different types of form factor descriptions in the case of the magnetic proton form factor ; a) low$Q^2$: $G_M^p/\mu_p F_D$ is shown: KK[13], IJL[14] , Höhler et al.[15] , ZB[16] and QCD-VM b) high $Q^2$: $Q^4 G_M^p$ for KK[13], IJL[14] , Höhler et al.[15] , ZB[16].

In summary we note that combining the information from meson physics at low $Q^2$ and the perturbative QCD predictions at high $Q^2$, a satisfactory description of the present experimental data is achieved. The vector-meson pole contributions dominate at low $Q^2$ only in the case of the pion . They play a minor role for the nucleon. Relating the vector-meson contributions to those arising from the higher Fock state contributions of the hadron wavefunction one would expect that nucleon and pion wavefunctions[17] are very different in their nontrivial structure. In view of the importance of these problems for the understanding of the hadronic interactions[18,19], extended measurements of the nucleon as well as of the pion form factors are necessary. Especially the measurement of the electric proton form factor, which is presently known only up to $Q^2 \sim 2$ GeV$^2$/c$^2$, will give important insight into the underlying quark-gluon structure.

Thanks are due S.J. Brodsky and N.G. Stefanis for discussions.

REFERENCES

1. For a review see M. Gourdin , Phys. Rep. **11C**, 29 (1974); J.J. Sakurai, Currents and Mesons, The University of Chicago Press(1969).
2. G. P. Lepage and S.J. Brodsky, Phys. Rev. **D22**, 2157 (1980); S. J. Brodsky and G. P. Lepage, Phys. Scr. **23**, 945 (1981).
3. C.E. Carlson, in Proceedings of the NATO Advanced Study Institute on New Vistas in Electro-Nuclear Physiscs,Banff Canada, 22Aug. (1985).
4. S.J. Brodsky and G. Farrar, Phys. Rev. **D11**,1309 (1975).
5. M.F. Gari and W. Krümpelmann, Z. Phys. **A322**, 689 (1985); Phys.Lett. **B173** (1986)10.
   M.F. Gari, International Conference and Symposia on Unified Concepts in Many Body Problems, State University of New York at Stony Brook, Sept. 1986
6. M.F. Gari and N.G. Stefanis , RUB-TPII-86-21, Phys.Lett.B, to be published.
7. S. Rock,R.G. Arnold,P. Bosted, B.T. Chertok, B.A. Mecking, I. Schmidt, Z.M. Szalata, R.C. York, R. Zdarko, Phys. Rev.Lett. **49**, 1139 (1982).
8. F. Borkowski, G.G. Simon, V.H. Walther, R.D. Wendeling, Z. Phys. **A275**, 29 ( 1975); Nucl. Phys. **B93**, 461 (1975). G.G. Simon, F. Borkowski, Ch. Schmitt,V.H. Walther,Z. Naturforsch. **35a**,1 (1980).
9. R. Arnold et al. Phys.Rev.Lett. **57** (1986) 174
10. W. Albrecht, H.J. Behrend, H. Dorner, W. Flauger, H.Hultschig, Phys. Lett. **26B**, 642 (1968).
11. C.J. Bebek et al., Phys.Rev. **D17** (1978) 1693.
12. U. Kaulfuß and M. Gari, Nucl. Phys. **A408**, 507 (1983) ; M. Gari and U. Kaulfuß, Phys. Lett. **136B**, 139 (1984)
13. J.G. Körner and M. Kuroda,Phys.Rev.D16,2165(1977)
14. F. Iachello, A.D. Jackson and A. Lande, Phys. Lett. **43B**,191 (1973).
15. G. Höhler et al.,Nucl.Phys.**B114** (1976) 505.
16. S. Blatnik and N. Zovko, Acta Physica Austr. **39**, 62 (1974).
17. S.J. Brodsky, "Quarks and Nuclear Forces", Springer Tracts Vol. 100 (1982).
    F.E. Close,R.G. Roberts and G.G. Ross, RAL-86-083.
18. V.L. Chernyak and I.R. Zhitnitsky, Nucl.Phys. **B246**(1984) 52 ;
    V.L. Chernyak and A.R. Zhitnitsky, Phys.Rep. **112**(1984) 173.
19. M.F. Gari and N. Stefanis, Phys. Lett.**157B** (1986) 462. and Phys.Rev.**D35** (1987) 1074.

# BARYON RESONANCES WITHOUT QUARKS: A CHIRAL SOLITON PERSPECTIVE*

MAREK KARLINER

*Stanford Linear Accelerator Center*
*Stanford University, Stanford, California, 94305*

## ABSTRACT

In many processes involving low momentum transfer it is fruitful to regard the nucleon as a soliton or "monopole-like" configuration of the pion field. In particular, within this framework it is possible to obtain detailed predictions for pion-nucleon scattering amplitudes and for properties of baryon resonances. One can also derive model-independent linear relations between scattering amplitudes, such as $\pi N$ and $\overline{K}N$. A short survey of some recent results is given, including comparison with experimental data.

## 1. INTRODUCTION

This talk describes the application of chiral soliton ideas to the meson-baryon $S$-matrix. Most of the original work reported here was done in collaboration with Michael Mattis at SLAC.[4,8,9]

How can the chiral soliton picture of the nucleon be put to a quantitative test? The flow chart in Fig. 1 illustrates two potentially productive approaches to the problem. Both will be described in some detail in the course of this talk. For now, I will just summarize the two alternatives.

One possibility is to take the simplest realization of this picture, i.e. the simplest mesonic Lagrangian admitting soliton solutions with the right quantum numbers and then calculate the properties of baryons in that model. The simplest model satisfying such criteria is the Skyrme model. In that model the pion-nucleon scattering matrix can be computed explicitly and it is in good agreement with experiment. The Skyrme Lagrangian is of course only a very crude approximation to the true low-energy effective Lagrangian of QCD. In addition, the results obtained from the Skyrme model might therefore depend on the details of the action. Hence the second approach for testing the chiral soliton picture: it turns out that one can derive model independent predictions, valid for all models in which the baryon corresponds to a soliton of a hedgehog form. In all such models the static soliton is not an eigenstate of the isospin $\mathbf{I}$, nor of the angular momentum $\mathbf{L}$. Instead it is invariant under the action of $\mathbf{K} = \mathbf{I} + \mathbf{L}$. Therefore the meson-baryon $S$-matrix has well-defined transformation properties under $\mathbf{K}$. This property of the $S$-matrix yields new and somewhat surprising relations between the various meson-baryon scattering matrix elements. Some of these model-independent relations are satisfied remarkably well in Nature. Let me now describe the two approaches in some detail, addressing first the Skyrme model calculation. I will begin with a very brief review of some basic results in Ref. 3. The Skyrme Lagrangian with a chiral-symmetry breaking mass-term is given by

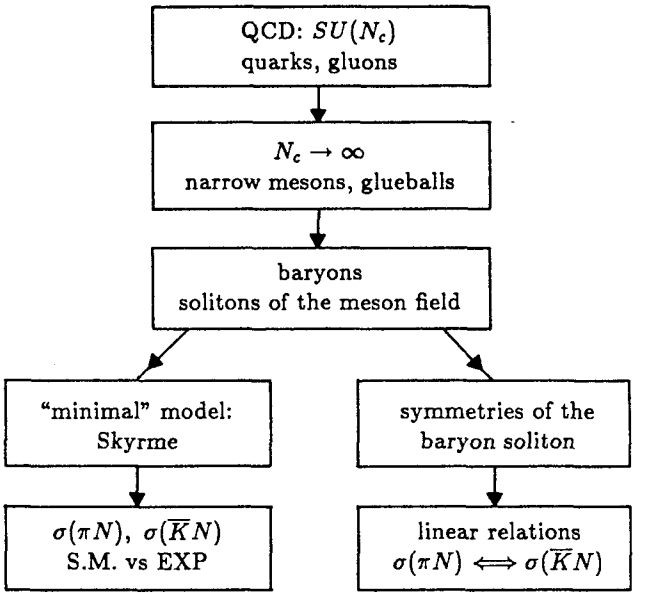


Fig. 1. Flow chart illustrating two possible ways of putting the chiral soliton ideas to a quantitative test: a model-dependent and a model-independent one.

$$\mathcal{L} = \frac{f_\pi^2}{16}\mathrm{Tr}\left(\partial_\mu U\,\partial_\mu U^\dagger\right) + \frac{1}{32e^2}\mathrm{Tr}\left[(\partial_\mu U)\,U^\dagger, (\partial_\nu U)\,U^\dagger\right]^2 + \frac{f_\pi^2 m_\pi^2}{8}\left(\mathrm{Tr}\,U - 2\right). \tag{1}$$

Here $f_\pi$ is the pion decay constant (186 MeV in the real world), $m_\pi$ is the pion mass, and $e$ is a new, dimensionless coupling constant peculiar to the model. The "small parameter" $1/N$ enters the Lagrangian through $f_\pi$ and $e$, which behave like $N^{\frac{1}{2}}$ and $N^{-\frac{1}{2}}$ in the large-$N$ limit, respectively.

The chirally invariant vacuum is $U(x) \equiv 1$ and pions are usually thought of as small fluctuations around this state, hence the standard notation:

$$U = \exp\left[\frac{2i}{f_\pi}\vec{\pi}(\vec{x},t)\cdot\vec{\tau}\right]$$

For small $\vec{\pi}/f_\pi$ we have $U \approx 1 + 2i\vec{\pi}(\vec{x},t)\cdot\vec{\tau}/f_\pi$ and then the first term in Eq. (1) becomes just the kinetic term for free pions, as expected:

$$\frac{f_\pi^2}{16}\mathrm{Tr}\left(\partial_\mu U\,\partial_\mu U^\dagger\right) \quad\to\quad \frac{1}{2}\left(\partial_\mu\vec{\pi}\cdot\partial_\mu\vec{\pi}\right) \quad + \quad \ldots \tag{2}$$

In addition to the vacuum solution, (1) has static soliton solutions which break the chiral symmetry and carry one unit of baryon number. They can all be obtained by an isospin rotation from the canonical "hedgehog" solution:

$$U_0 = \exp\left[F(r)\hat{\mathbf{r}}\cdot\vec{\tau}\right] \quad \text{and} \quad U_A = A\,U_0\,A^{-1} \tag{3}$$

* Work supported by the Department of Energy, contract DE-AC03-76SF00515.

where $A$ is a constant $SU(2)$ matrix. When $A$ is treated as a collective coordinate, one finds that the nucleon corresponds to a superposition of the $U_A$-s. Schematically we can write this as

$$|N\rangle = \int dA\, \chi(A)\, |A\rangle$$

where $\chi(A)$ is the wave-function in the space of collective coordinates. While $|A\rangle$ corresponds to a state pointing in a well-defined direction in the internal space, it has an ill-defined isospin and angular momentum. On the other hand, the state $|N\rangle$ has well-defined spin and isospin, but does not point in any specific direction in the internal space. The situation here is completely analogous to the problem of a particle constrained to move on a circular ring, as shown in Fig. 2.

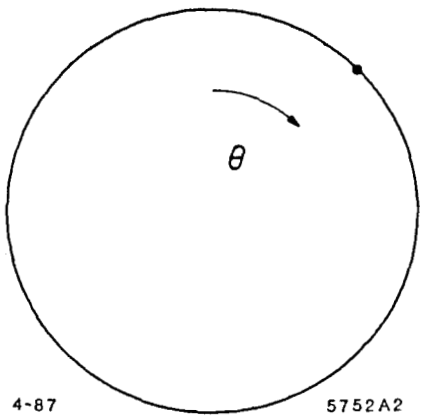


Fig. 2. A one-dimensional analogue of the collective coordinate $A$: particle constrained to move on a circular ring. Classical ground state corresponds to a particle at rest at some fixed angle $\theta$. In quantum mechanics this is no longer true and we must have an eigenstate of the angular momentum operator $L_\theta = -i\frac{\partial}{\theta}$.

Classically, a particle at rest at any angle $\theta$ is a ground state of the system. In quantum mechanics the eigenstates of the hamiltonian no longer are localized at a fixed angle $\theta$. Instead, they are eigenstates of the angular momentum operator $L_\theta = -i\frac{\partial}{\theta}$. Using this analogy, we see that a nucleon with a well-defined spin and isospin corresponds to a *rotating* soliton.

Static properties of the nucleon in the Skyrme model obtained in Ref. 3 were based on treating $f_\pi$ and $e$ as free parameters, to be adjusted for the best fit to nucleon and $\Delta$ masses. All other static quantities were obtained as functions of $e$ and $f_\pi$. Some properties of the nucleon turned out very well, but some others were in serious disagreement with experiment. Most notably, the values of $f_\pi$ and $g_A$ had errors of about 30% and 50%, respectively. At this point it is worth reminding ourselves that the Skyrme Lagrangian is in principle an equally good approximation to an underlying $SU(N)$ gauge theory with $N = 3$ or $N = 5$, etc. In the real world $N = 3$ and it is therefore very unlikely that the Skyrme Lagrangian can reproduce experimental quantities which explicitly depend on $N$. Typically the most we can hope for is to reproduce experimental quantities which do not depend on $N$ in the leading order of the $1/N$ expansion. For example, while $f_\pi \sim N^{\frac{1}{2}}$ and $g_A \sim N$, the ratio $f_\pi^2/g_A \sim N^0$ and in contrast to $f_\pi$ and $g_A$ taken separately, it reproduces experiment to 3%. As shown in Table I, similar statements can be made about some other $N$-independent ratios.

The purpose of this example is *not* to suggest that *all* $N$-independent quantities should agree well with experiment, for this is hardly the case. The results in Table I suggest however that the $N$-independent quantities stand a better chance of reproducing the real world data. If our guiding principle is to look for such quantities, it is natural to examine the pion-nucleon $S$-matrix, since meson-baryon scattering amplitudes are independent of $N$ in the large-$N$ limit.[1]

The first step towards the computation of the $\pi N$ $S$-matrix is the realization that small fluctuations around the soliton can be identified with physical mesons. This is schematically illustrated in Fig. 3.*

Once that identification is made, it is clear that in order to obtain the pion-nucleon $S$-matrix, we should in principle find the eigenmodes of small fluctuations around a rotating soliton. This is a very difficult problem. Fortunately enough, in the large-$N$ limit there is an important simplification: in that limit the soliton rotates very slowly, with angular velocity $\omega_s \sim 1/N$. The reason is as follows. The spin of the nucleon is $\frac{1}{2}\hbar$, independent of $N$. It is the product of the Skyrmion angular velocity $\omega_s$ and its moment of inertia $I_s$. The Skyrmion radius $R_s$ is independent of $N$ and its mass $M_s$ scales like $N$.[1] Consequently

$$I_s \sim M_s R_s^2 \sim N \qquad \text{while} \qquad I_s\, \omega_s = \frac{1}{2}\hbar \sim N^0$$

therefore

$$\omega_s \sim 1/N$$

The characteristic time scale $t_{rot}$ associated with the Skyrmion rotation is large, $t_{rot} \sim 1/\omega_s \sim N$. It is much greater than the time $t_\pi$ that a pion moving with the speed of light spends in the vicinity of the nucleon:

$$R_s \sim N^0; \qquad R_s/c \sim N^0 \sim t_\pi \ll t_{rot} \sim N$$

A pion will therefore not observe the rotation, but rather will take a "snapshot" of the soliton in one of its possible orientations. The probability of any given orientation is proportional to $|\chi(A)|^2$. This justifies the impulse approximation: first obtaining the scattering amplitude for scattering of a pion by a soliton *pointing in a fixed orientation* and then superimposing such amplitudes, according to their weight in $\chi(A)$.

In addition to neglecting the rotation, as described above, we can neglect the nucleon recoil, since in the large-$N$ limit the pion kinetic energy in the domain of interest is independent on $N$, while $M_s \sim N$. In order to obtain the Lagrangian describing scattering of mesons by a static soliton, we write the chiral field $U$ in the form:

$$U = \exp\left[F(r)\hat{\mathbf{r}}\cdot\vec{\tau} + \frac{2i\vec{\pi}}{f_\pi}\right]. \tag{4}$$

This form of $U$ is then plugged back into the original

* This identification breaks down for fluctuations which do not change the energy of the system. Such fluctuations correspond to the translational and rotational zero modes of the soliton. In our treatment this subtlety is neglected, spoiling the agreement with experiment in the low partial waves.

TABLE I
STATIC PROPERTIES OF THE NUCLEON IN THE SKYRME MODEL AND THEIR DEPENDENCE ON $N$.

| Quantity | $N$-dependence | Prediction | Experiment | Error |
|---|---|---|---|---|
| $\langle r^2\rangle^{1/2}_{I=0}$ | $\sim N^0$ | 0.59 fm | 0.72 fm | 18% |
| $\langle r^2\rangle^{1/2}_{M,I=0}$ | $\sim N^0$ | 0.92 fm | 0.81 fm | 14% |
| $\mu_p$ | $\sim N$ | 1.87 | 2.79 | 33% |
| $\mu_n$ | $\sim N$ | -1.31 | -1.91 | 31% |
| $\mu_p/\mu_n$ | $\sim N^0$ | 1.43 | 1.46 | 2% |
| $g_A$ | $\sim N$ | 0.61 | 1.23 | 50% |
| $f_\pi$ | $\sim N^{\frac{1}{2}}$ | 129 MeV | 186 MeV | 31% |
| $f_\pi^2/g_A$ | $\sim N^0$ | 27,280 MeV$^2$ | 28,127 MeV$^2$ | 3% |
| $g_{\pi NN}$ | $\sim N^{\frac{3}{2}}$ | 8.9 | 13.5 | 34% |
| $g_{\pi N\Delta}$ | $\sim N^{\frac{3}{2}}$ | 13.2 | 20.3 | 35% |
| $g_{\pi N\Delta}/g_{\pi NN}$ | $\sim N^0$ | 1.5 | 1.5 | $\lesssim 1\%$ |

The predictions are from Ref. 3. Skyrme model is *a priori* an equally good effective Lagrangian for $N_c = 3$ and $N_c = 5$. So it does not reproduce well the quantities which depend on $N$ in the leading order of the $1/N$ expansion. On the other hand, as demonstrated by the table above, it typically does much better for ratios in which the $N$-dependence cancels out.

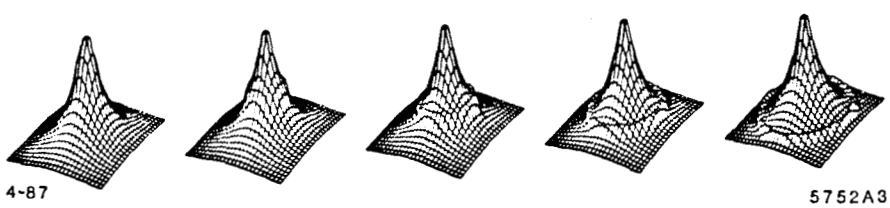


$$U_0 = \exp\left[F(r)\hat{\mathbf{r}}\cdot\vec{\tau}\right]$$

$$U = \exp\left[F(r)\hat{\mathbf{r}}\cdot\vec{\tau} + \frac{2i\vec{\pi}(\vec{x},t)}{f_\pi}\right]$$

Fig. 3. A two-dimensional example showing how fluctuations around the classical soliton profile should be identified with the physical mesons. Time flows from left to right and the fluctuation corresponds to an outgoing spherical wave.

Lagrangian (1) and the action is expanded in powers of $\vec{\pi}/f_\pi$:

$$\mathcal{L}(U) \quad \rightarrow \quad \mathcal{L}(\vec{\pi}) = \frac{1}{2}\vec{\pi}\,\square\,\vec{\pi} + \mathcal{O}\left(\vec{\pi}^3/f_\pi^3\right) \qquad (5)$$

where $\square$ is a second-order linear differential operator depending on $U_0$. For $r \rightarrow \infty$, $U_0 \rightarrow 1$ and then $\square$ becomes just the free four-Laplacian, as in (2). The term linear in $\vec{\pi}$ vanishes, since $U_0$ is an extremum of the classical action. In addition, in the $N \rightarrow \infty$ limit we can formally neglect the $\mathcal{O}\left(\vec{\pi}^3/f_\pi^3\right)$ terms, since $f_\pi \sim N^{\frac{1}{2}}$, and such terms are suppressed relative to the quadratic one. We are left with a quadratic Lagrangian and therefore with linear equations of motion, which can be schematically written as:

$$\square\,\vec{\pi} = 0 \quad .$$

These equations describe the motion of a meson in a potential provided by the soliton background.* Since the potential is invariant under **K**, $K$ plays the role of the angular momentum in the usual partial wave decomposition. The equations can be explicitly solved for each value of $K$, yielding the eigenmodes of $\vec{\pi}$ as functions of energy. For $|\vec{x}| \gg R_s$, $F(r) \rightarrow 0$ (*cf.* Eq. (3)), the potential vanishes, and up to a phase, the $\vec{\pi}$ wave function is that of a free particle. This phase is just the scattering phase-shift defining the $S$-matrix element in a given pion-Skyrmion channel. We shall refer to the latter as *reduced* matrix elements. The reason for this name will become clear in a moment.

* The explicit expression for $\square$ is rather complicated and will not be given here. Interested reader is referred to the original literature Refs. 4, 6, 8 and 9.

In order to obtain the pion-nucleon $S$-matrix from the pion-Skyrmion one, we need to project the Skyrmion onto states with well-defined isospin and spin. This projection is carried out as follows. First, given the T-matrix† $\mathrm{T}_{U_0}$ for scattering off $U_0$, the corresponding T-matrix for scattering off $U_A$ (*cf.* Eq. (3)) is given by:

$$\mathrm{T}_{U_A} = \hat{D}(A)\,\mathrm{T}_{U_0}\,\hat{D}(A)^\dagger \tag{6}$$

where $\hat{D}$ is the adjoint representation of $A$. Next we superimpose the $\mathrm{T}_{U_A}$-s according to their weight in the nucleon wave function $\chi(A)$. The complete expression for the physical T-matrix is then:

$$\mathrm{T}_{PHYS} = \int_{SU(N_f)} dA\; \chi_f^\dagger(A)\,\hat{D}(A)\,\mathrm{T}_{U_0}\,\hat{D}(A)^\dagger \chi_i(A) \tag{7}$$

where $SU(N_f)$ is the flavor group and $\chi_{i(f)}$ is the wave function of the baryon in the initial (final) state. Integration over the flavor group can be carried out in closed form (see Appendix B of Ref. 9 for details.) The final result has a very simple structure:

$$\mathrm{T}_{PHYS} = \sum_i C_i \boldsymbol{\tau}_i^{\mathrm{RED}} \tag{8}$$

where $\boldsymbol{\tau}^{\mathrm{RED}}$ are the T-matrix elements in the pion-Skyrmion system and the $C_i$-s are group-theoretical factors. The structure of Eq. (8) explicitly demonstrates two ingredients on which the physical answer depends: symmetry and dynamics. $C_i$-s reflect only the symmetry and are independent of the details of the Lagrangian. They are determined by the flavor group and by the fact that the soliton is invariant under $\mathbf{K}$; all dynamics is contained in the reduced matrix elements. We are all familiar with this type of division into group theory and dynamics. For example, isospin conservation dictates that the T-matrix for $\pi N \to \pi N$ is given by

$$\mathrm{T}_{\pi N} = C_{\frac{1}{2}}\mathrm{T}_{\frac{1}{2}} + C_{\frac{3}{2}}\mathrm{T}_{\frac{3}{2}} \tag{9}$$

where $C_{\frac{1}{2}(\frac{3}{2})}$ are $SU(2)$ Clebsch-Gordan coefficients and $\mathrm{T}_{\frac{1}{2}(\frac{3}{2})}$ are the $I = \frac{1}{2}(\frac{3}{2})$ reduced matrix elements.

In the foregoing discussion we have focused on the 2-flavor Skyrme model. Extension to 3-flavors is in principle straightforward. The embedding of the $SU(2)$ hedgehog inside $SU(3)$ is done by setting

$$U_0 \to \left(\begin{array}{c|c} U_0 & \\ \hline & 1 \end{array}\right) \tag{10}$$

Technical details for $SU(3)$ are however much more complicated. The interested reader is again referred to the original literature, especially Ref. 9.

At this point we can summarize the prescription for computing the meson-baryon $S$-matrix in the Skyrme model:

- identify small fluctuations around the soliton with mesons
- meson wave function $\Longrightarrow$ phase shifts, $\boldsymbol{\tau}_i^{\mathrm{RED}}$
- **K** symmetry $\Longrightarrow \mathrm{T}_{PHYS} = \sum_i C_i \boldsymbol{\tau}_i^{\mathrm{RED}}$
- Approximations:
  - ▷ $m_u = m_d = m_s = 0 \Longrightarrow$ massless pseudoscalar mesons, exact $SU(3)_f$
  - ▷ Large-$N$ $\Longrightarrow$ no recoil, linear eq's of motions
  - ▷ Zero modes for $L = 0, 1, 2$; neglected

We are ready to compare the Skyrme model T-matrix with the experiment. It is customary to decompose the experimental data into channels with well-defined isospin $I$, angular momentum $J$ and orbital angular momentum $L$. Such channels are denoted by $L_{2I,2J}$ where $L$ is denoted by an appropriate letter: $S, P, D, F, G, H, I, K$ for $L = 0, 1, 2, 3, 4, 5, 6, 7$, respectively. The T-matrix for each $L_{2I,2J}$ channel is plotted as a function of the energy, on the so-called Argand plots (*cf.* Fig. 4).

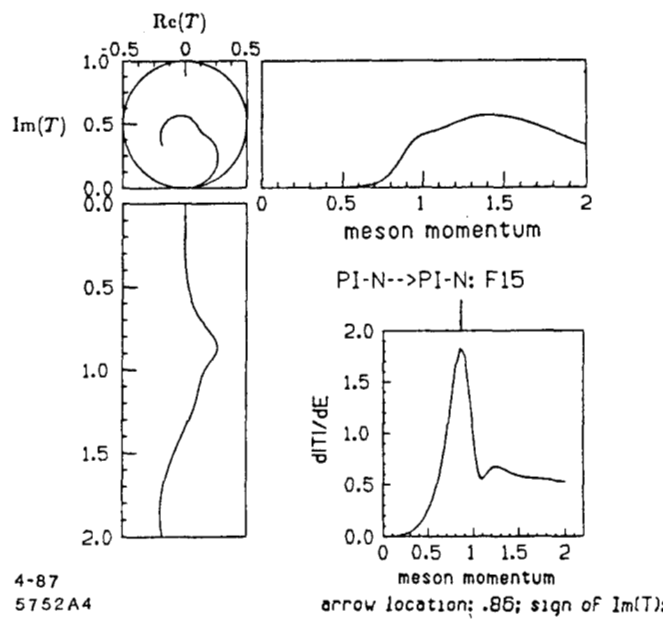


Fig. 4. Sample Argand diagram. A resonance corresponds to the maximum velocity of $d|\mathrm{T}|/dE$ ( here denoted by an arrow ). In the Skyrme model the plot in the unitarity circle, ImT *vs.* ReT, is independent of $e$ and $f_\pi$.

The part of the diagram bounded by the unitarity circle, ImT *vs.* ReT is independent of $e$ and $f_\pi$ and therefore provides the most stringent test of the model. Fig. 5 compares the experimental results for $\pi N \to \pi N$ $S$-matrix with those of the 3-flavor Skyrme model.

I'd like to stress again that the Skyrme model calculation as shown in Fig. 5 *contains no adjustable parameters.* The parameters of the model determine the energy scale, but not the *shape* of the Argand plots. Apart from the $S$, $P$ and $D$ partial waves, containing the spurious zero modes, overall agreement with experiment is quite good.

The most conspicuous feature of Fig. 5 is the fact that the $L_{I=1/2,J=L-1/2}$ channel is much larger than $L_{I=1/2,J=L+1/2}$ for all $L$'s. This is true for both experiment and the Skyrme model. A similar, albeit less pronounced pattern holds for

† We interchange freely between the $S$-matrix and T-matrix, using the one which is the most convenient. The two are related by $\mathbf{T} = (\mathbf{S} - \mathbf{1})/2i$.

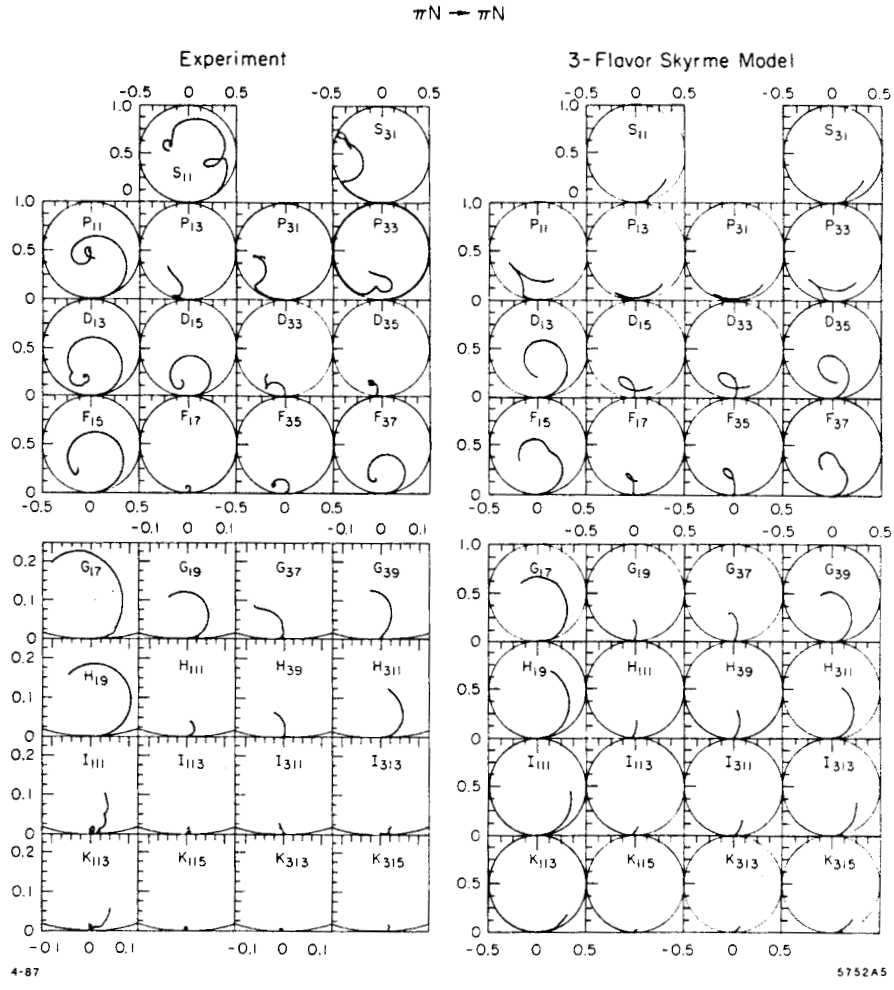


Fig. 5. $\pi N \to \pi N$ : comparison between the 3-flavor Skyrme model and experiment (from Ref. 9). The plots show $\mathrm{Im}(T)$ *vs.* $\mathrm{Re}(T)$ for each channel. Channels are labeled by $L_{2I\,2J}$, where $L$ is the pion orbital angular momentum, $I$ is the total isospin and $J$ the total angular momentum.

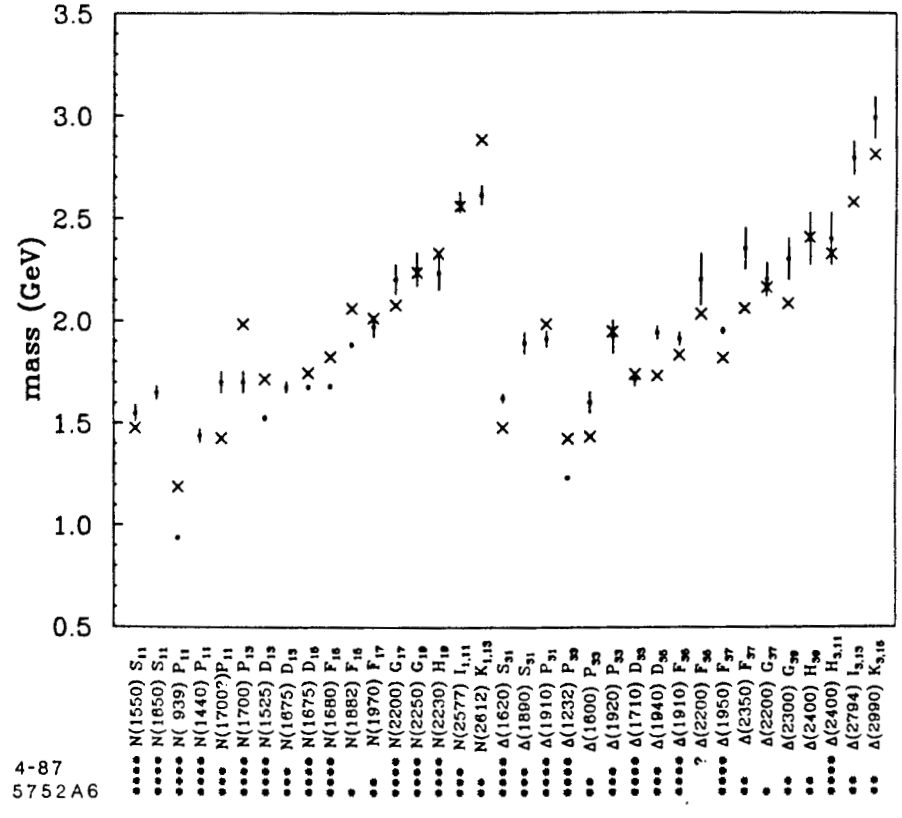


Fig. 6. Spectrum of $N$ and $\Delta$ resonances: 3-flavor Skyrme model (crosses) *vs.* experiment (points with error bars) (from Ref. 9). Resonances are assigned stars according to the Particle Data Book. The Skyrme-model values for $m_N$ and $m_\Delta$ are obtained from Eq. (9) of Ref. 3, using the "best fit" parameters of Ref. 9 ($e$ =4.79, $f_\pi$ =150 MeV.)

$L_{I=3/2,J=L+1/2}$ and $L_{I=3/2,J=L-1/2}$ channels. In the chiral soliton framework this phenomenon has a very simple explanation: there are eight reduced amplitudes entering Eq. (8) for $SU(3)_f$. Out of these, five turn out to be very small and only three are significant, with roughly the same magnitude. The magnitude of the *physical* amplitudes is therefore determined by group theory, *i.e.* the relative strength of the $C_i$-s multiplying the three principal reduced amplitudes.

Having obtained the complete set of partial-wave channels, we can compute the resonance masses from the maxima of $d|\mathrm{T}|/dE$. The resulting spectrum of $N$ and $\Delta$ resonances is displayed in Fig. 6. With over 30 resonances and two adjustable parameters, masses are predicted with an average of about 7%. While all of the 4-star resonances appear in the same place in 2- and 3-flavor calculation, the 1- and 2-star resonances in the $F_{15}$ and $F_{37}$ channels supply a surprise: as demonstrated by Fig. 7, these weak resonances appear only when the third flavor is introduced. It is somewhat puzzling that the appearance of non-strange resonances should be sensitive to the existence of the strange quark. A possible explanation is that they couple to the strange quark sea in the proton.

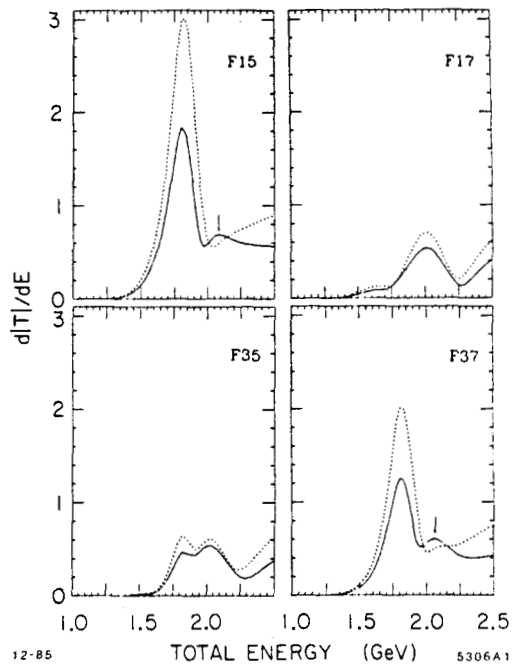


Fig. 7. Speed diagrams for the four $F$-wave amplitudes in the 2- and 3-flavor Skyrme models (dotted and solid lines, respectively).

Fig. 8. $\pi N \to \pi\Delta$ : comparison between the 3-flavor Skyrme model and the experimental solution of Ref. 13 (from Ref. 9). Channels are labeled by $LL'_{2I,2J}$, with $L$ and $L'$ the incoming and outgoing pion angular momenta, respectively. An asterisk denotes amplitudes which were found to be small and/or poorly determined by the available data, and were therefore not included in the experimental solution. The partial-wave analysis of the experimental data is not as unambiguous as in $\pi N \to \pi N$ , but in all cases the Skyrme model correctly reproduces the sign of $\mathrm{Im}(T)$, which is a crucial test for theory.

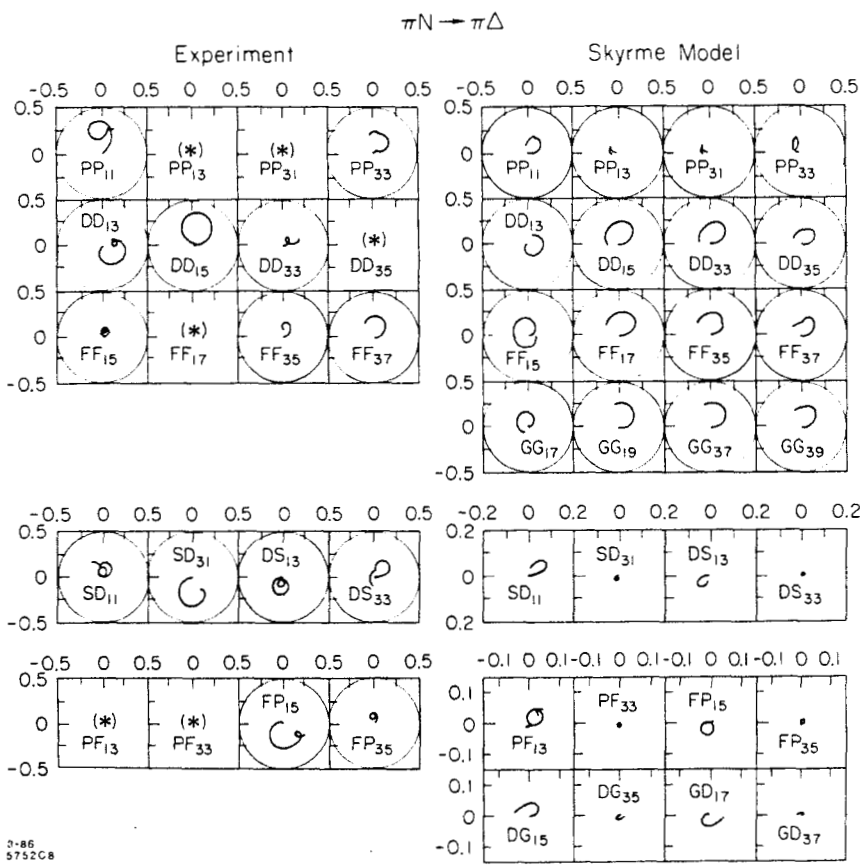

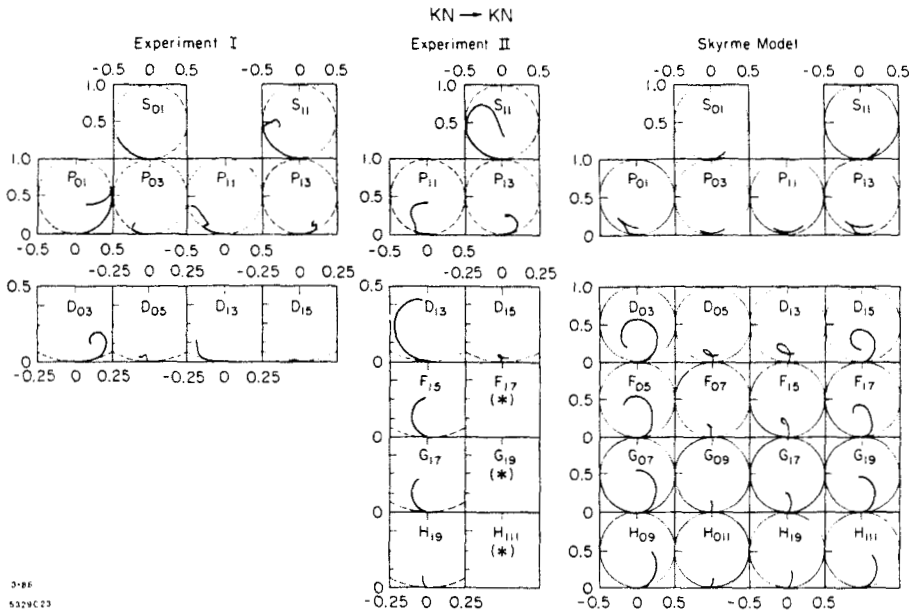


Fig. 9. $KN \to KN$ : comparison between the Skyrme model and two experimental solutions (from Ref. 9): "Experiment I" from Ref. 14 and "Experiment II" from Ref. 15. Channels are labeled by $L_{I,2J}$. Note that experimental and Skyrme-model plots for $L \geq 2$ are shown on different scales. The resonance-like behavior in some of the experimental channels is evident.

In addition to the elastic $\pi N \to \pi N$ processes, we can also consider inelastic processes, such as $\pi N \to \pi \Delta$ . The only change with respect to $\pi N \to \pi N$ is that $\chi_f$ stands now for the $\Delta$, instead of the nucleon wavefunction. The results are shown in Fig. 8. The experimental partial-wave analysis of $\pi N \to \pi \Delta$ is somewhat less clear-cut than $\pi N \to \pi N$ , since a $N\pi\pi$ final state may represent $N\rho$, as well as $\Delta\pi$. The sign of Im(T) is however unambiguous in most cases and wherever it is known experimentally, the Skyrme model yields the correct answer. This is highly non-trivial: the only other theoretical scheme which passes this test is the quark model.

The results discussed so far were obtained in the 3-flavor model, but did not involve strange particles. We will now review two processes with open strangeness, beginning with $KN \to KN$ . That reaction is rather different from $\pi N \to \pi N$ , because any resonances in the $KN$ channels must be exotics, involving more than three quarks. The question whether such resonances exist experimentally has long been a controversial subject.* The Skyrme model has no built-in bias of this kind and therefore it is interesting to compare its predictions with experiment, as shown in Fig. 9. In general, the predictions contain *too many* resonances, compared to the data. Of particular interest are the $F$-waves, where the model typically works best. The theory predicts a clean resonance in the $F_{05}$ channel, similar to the one observed in $D_{03}$. This channel has not yet been analyzed experimentally and thus provides an interesting prediction. Contrary to the $KN$ channel, there is nothing exotic about $\overline{K}N \to \overline{K}N$ . The partial-wave analysis of experimental data is of good quality, although not as precise as $\pi N \to \pi N$ , especially in the higher partial waves. The theory reproduces most of the essential features of the experiment, as shown in Fig. 10. Since we work in the chiral limit, $m_K = 0$, there is no point in attempting to extract the spectrum of the strange resonances.

It is possible to study many more inelastic, strange and non-strange processes. Details may be found in Ref. 9. At this point I would however like to move on to the model-independent tests of the chiral soliton picture, as outlined at the beginning of this talk. Let me invoke the isospin analogue once more. If we consider elastic scattering of charged pions on nucleon, *a priori* there are *four* different amplitudes to consider: $T(\pi^+p)$, $T(\pi^-p)$, $T(\pi^+n)$ and $T(\pi^-n)$. From Eq. (9) we learn that they can all be obtained from *two* reduced amplitudes:

$$T_{\pi N} = C_{\frac{1}{2}} T_{\frac{1}{2}} + C_{\frac{3}{2}} T_{\frac{3}{2}}$$

Only two out of the four can be independent, and so there is a *linear relation* between any three of the four. This is a rather generic phenomenon, with an interesting counterpart in the chiral soliton framework, valid for all models in which the nucleon corresponds to a soliton invariant under the **K** symmetry: with three flavors any elastic meson-baryon T-matrix element is given by a linear superposition of the eight reduced amplitudes. In the Skyrme model five reduced amplitudes are negligible and the other three make the dominant and roughly equal contributions to the physical amplitudes. Even though we cannot compute the reduced amplitudes in Nature, it is natural to make the dynamical assumption that this hierarchy exists in the real world as well:

$$T_{PHYS} \approx \sum_{i=1}^{3} C_i T_i^{\mathrm{RED}} \qquad (11)$$

* Some of our colleagues even refuse to be confused by data, as is perhaps best illustrated by the 1984 Particle Data Book: "... *The general feeling, supported by prejudice against baryons not made up of three quarks, is that the suggestive counterclockwise movement in the Argand diagram of some of the partial waves is not real evidence for true Breit-Wigner resonances...*" (p. S243).

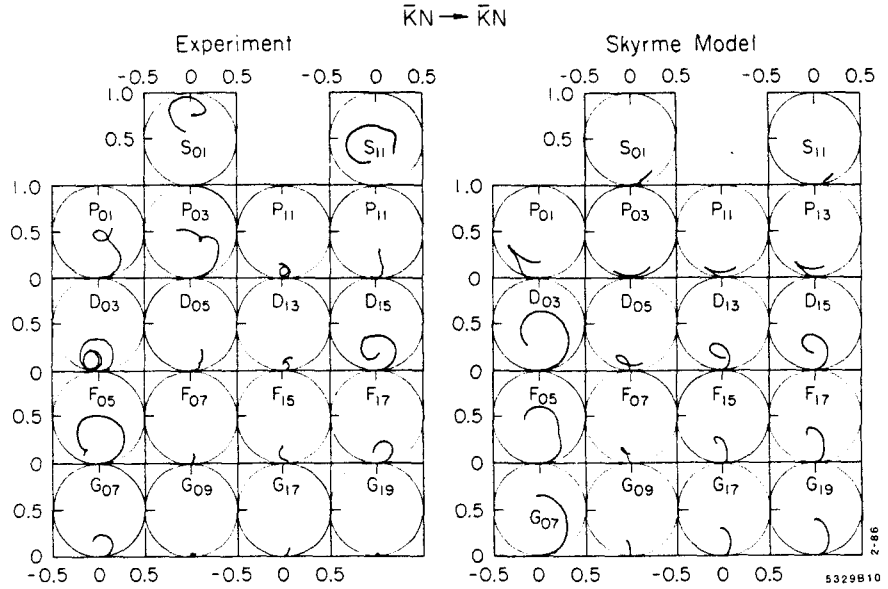


Fig. 10. $\overline{K}N \to \overline{K}N$ : comparison between the Skyrme model and the experimental solution of Ref. 16 (from Ref. 9). Channels are labeled by $L_{I,2J}$.

Such an assumption not only explains why for $\pi N \to \pi N$ $L_{I=1/2,J=L-1/2} \gtrsim L_{I=1/2,J=L-1/2}$, etc., but also yields some quite new and interesting predictions. For a given value of $L$ there are many experimental amplitudes, all determined in terms of the three unknown reduced amplitudes. Consequently, there are linear relations among the experimental amplitudes. Such relations are almost model independent, relying only on the $K$-symmetry group theory and on the assumption that scattering is dominated by the three reduced amplitudes.

First, there are rather accurate linear relations between $\pi N \to \pi N$ and $\pi N \to \pi \Delta$ . Very similar relations can be derived in the 2-flavor case, as was originally done in Ref. 5. In that case there are only 3 reduced amplitudes and no dynamical assumptions are necessary. In order to test the predictions inherent to 3-flavors, it is however necessary to consider relations between strange and non-strange amplitudes.[17] One such relation reads

$$a_1 F_{15}^{\pi N} + a_2 F_{37}^{\pi N} = b_1 F_{05}^{\overline{K}N} + b_2 F_{07}^{\overline{K}N} \quad . \qquad (12)$$

where $a$-s and $b$-s are purely group-theoretical coefficients obtained from $C_i$-s in Eq. (11), and $F_{15}^{\pi N}$, $F_{37}^{\pi N}$, $F_{05}^{\overline{K}N}$ and $F_{07}^{\overline{K}N}$ are the experimental partial-wave amplitudes.

As shown by Fig. 11, the prediction contained in Eq. (12) is satisfied with remarkable accuracy. It is also possible to derive similar predictions for $G$-waves. At present the partial wave analysis for the $G$-wave $\overline{K}N$ is not yet reliable enough. The $G$-wave linear relation is therefore a real prediction for what the $\overline{K}N$ $G$-waves should look like. I very much hope that this prediction will be put to a test sometime in the near future, perhaps with the advent of the $K$-factories. It is important to note that Eq. (12) *cannot* be obtained from $SU(3)_f$ by itself. While $SU(3)_f$ is part of the symmetry used to derive Eq. (12), it is clear that $SU(3)_f$ alone cannot produce such a relation, since it mixes amplitudes with different total angular momenta. A more detailed argument shows that even

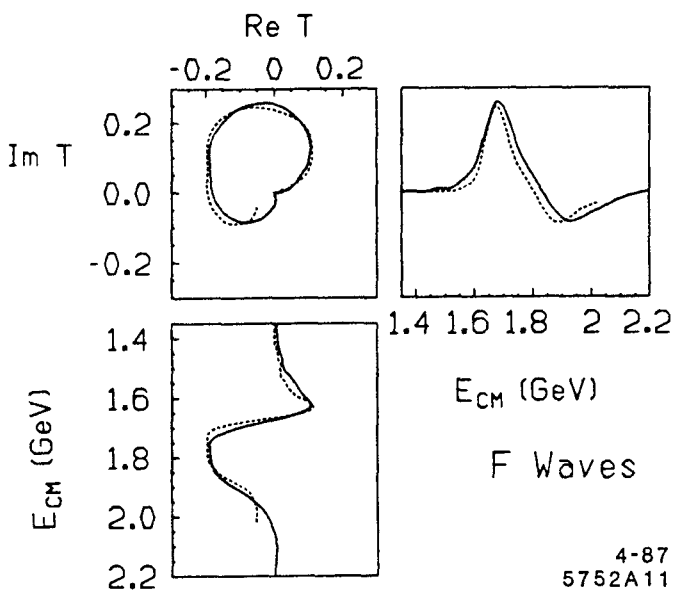


Fig. 11. Test of the prediction for a linear relation between $\pi N \to \pi N$ and $\overline{K}N \to \overline{K}N$ , Eq. (12). The scattering matrix $T$ is plotted both as function of energy and in Im($T$) *vs.* Re($T$) representation. Continuous lines: linear combination of the experimental $F_{15}$ and $F_{37}$ $\pi N \to \pi N$ amplitudes. Dotted lines: linear combination of the experimental $F_{05}$ and $F_{17}$ $\overline{K}N \to \overline{K}N$ amplitudes. $\overline{K}N$ amplitudes are shifted by the strange quark mass $\approx$ 150 MeV.

the more elaborate "conventional" symmetries, such as $SU(6)$ are also incapable of reproducing Eq. (12).[17] That being the case, the very precise experimental confirmation of the $F$-wave linear relations should be regarded as another strong testimony in favor of the view that the nucleon indeed can be regarded as a soliton of the meson field.

In closing, I would like to mention that the same ideas which make it possible to obtain the pion-nucleon $S$-matrix can be applied to the photoproduction of pions on nucleons. This is done by coupling the photon field to the chiral field $U$ and then proceeding as in pion-nucleon scattering. An explicit calculation of the photoproduction helicity amplitudes was recently carried out along these lines in Siegen University.[18]

I hope that this brief review has convinced you that the chiral soliton picture of the nucleon is not only valid on a qualitative basis, but also can be used to study details of low energy hadronic phenomena in a way complementary to and on a par with the quark picture.

## REFERENCES


1. E. Witten *Nucl. Phys.* **B160,** 57 (1979).
2. E. Witten, in Lewes Workshop Proc.; A. Chodos *et al.*, Eds; Singapore, World Scientific, 1984.
3. G. Adkins, C. Nappi, and E. Witten, *Nucl. Phys.* **B228,** 552 (1983).
4. M. P. Mattis and M. Karliner *Phys. Rev.* **D31,** 2833 (1985) and references therein.
5. M. P. Mattis and M. Peskin *Phys. Rev.* **D32,** 58 (1985).
6. A. Hayashi, G. Eckart, G. Holzwarth, and H. Walliser, *Phys. Lett.* **147B,** 5 (1984).
7. H. Walliser and G. Eckart, *Nucl. Phys.* **A429,** 514 (1984).
8. M. Karliner and M. P. Mattis, *Phys. Rev. Lett.* **56,** 428 (1986).
9. M. Karliner and M. P. Mattis, *Phys. Rev.* **D34,** 1991 (1986).
10. M. Karliner and M. P. Mattis, SLAC-PUB-3991, to be published in proceedings of the 2nd Conference on the Interaction Between Particles and Nuclear Physics, Lake Louise, Canada.
11. G. Höhler, F. Kaiser, R. Koch, and E. Pietarinen, *Handbook of Pion-Nucleon Scattering* (Fachinformationszentrum, Karlsruhe, 1979), Physik Daten No. 12-7. Reproduced in Review of Particle Properties, *Rev. Mod. Phys.* **56,** part II (1984). ($\pi N \to \pi N$ )
12. R. E. Cutkosky *et al.*, in *Baryon* 1980 (conference proceedings), ed. N. Isgur; reproduced in Review of Particle Properties, *op. cit.* ($\pi N \to \pi N$ )
13. D. M. Manley, R. A. Arndt, Y. Goradia, and V. L. Teplitz, *Phys. Rev.* **D30,** 904 (1984). ($\pi N \to \pi \Delta$ )
14. K. Hashimoto, *Phys. Rev.* **C29,** 1377 (1984). ($KN \to KN$ )
15. R. A. Arndt and L. D. Roper, *Phys. Rev.* **D31,** 2230 (1985). ($KN \to KN$ )
16. G. P. Gopal *et al.*, *Nucl. Phys.* **B119,** 362 (1977). Reproduced in Review of Particle Properties, *op. cit.* ($\overline{K}N \to \overline{K}N$ )
17. M. Karliner *Phys. Rev. Lett.* **57,** 523 (1986).
18. G. Eckart and B. Schwesinger, *Photoproduction of Baryon Resonances in the Skyrme Model;* Siegen University preprint, SI-86-3, Feb. 1986.

# A $H_2$ GAS JET AS INTERNAL TARGET

R704 Collaboration at CERN, Geneva, Switzerland
J. Fay
IPN, Lyons, France
M. Macri
INFN, Genoa, Italy

**Abstract**: Experiment R704, the last to be performed at the CERN Intersecting Storage Rings, has successfully applied a new method to studying ($\bar{c}c$) states formed directly in antiproton-proton annihilations. The novelty of the method lies in the capability of building a highly performing annihilation source by letting a cold antiproton beam, coasting inside ring 2 at the ISR, continuously interact with a dense internal $H_2$ target. Details of the characteristics of the source are given in this paper.

## 1. Introduction

The possibilities offered by the availability of an intense antiproton source for the study of ($\bar{c}c$) states are now well established [1]. The scheme adopted for the R704 experiment required the use of an internal target (a molecular hydrogen jet) continuously intersecting a cold antiproton beam coasting inside the vacuum pipe of ring 2 at the CERN Intersecting Storage Rings (ISR).

The RF system and cooling equipment of ring 2 at the ISR provided great flexibility of beam-control operations, while the well-localized, high-density target permitted the small-size, high-luminosity source required for charmonium formation studies. The method allows for an absolute calibration in the centre-of-mass energy to a fraction of a MeV.

The luminosity of the annihilation source was continuously monitored by measuring, with a solid-state silicon telescope, the yield of protons from small-angle $\bar{p}p$ elastic scattering. The coupled measurement of energy and angle in the silicon detector provided an essentially background-free sample of elastic events.

## 2. The Beam-Target System

In a formation experiment with antiprotons interacting on a stationary hydrogen target, the energy of the beam is related to the value ($m_r$) of the mass of the resonance by the equation

$$E_{\bar{p}} \approx m_r^2/2m_p - m_p .$$

To study charmonium states we operated ring 2 at the ISR in the range of momentum from 3.5 to 6.5 GeV/c. The unbunched antiprotons coasted inside the ring with a revolution frequency of $\nu \approx 3.1 \times 10^5\ s^{-1}$, crossing, at each turn, an internal target mounted in the straight section upstream of the intersection region I7. The maximum beam current reached was 5.5 mA corresponding to $N = 1.1 \times 10^{11}$ circulating antiprotons. The target, a $H_2$ gas jet, had a density of $\varrho = 10^{14}$ atoms per $cm^3$ and a diameter, at the intersection with the beam, of $d \approx 0.9$ cm.

To summarize, the features of the source were:

i) High luminosity, up to a maximum value:

$$L_0 = \varrho_{H_2} d_{H_2} N \nu = 3 \times 10^{30}\ s^{-1} \cdot cm^{-2} .$$

ii) Long beam lifetime: $T_{beam} \approx 100$ h at the maximum jet density, almost entirely accounted for by beam losses caused by nuclear interactions in the jet.

iii) Small momentum bite, at best:

$$\Delta p/p \approx \pm 4 \times 10^{-4} ,$$

corresponding to an incertitude in the centre-of-mass energy of $\Delta\sqrt{s} \approx 0.5\ MeV/c^2$.

iv) Small source volume:

height × width × depth = 0.5 × 0.8 × 0.9 $cm^3$ (for 90% containment).

v) No energy drift during data taking.

The techniques by which the required performance of the operation of ring 2 at the ISR was achieved are described elsewhere [1], while a description of the target system is given in the following section.

## 3. The Jet Target

The optimal thickness of the internal target for this type of experiment lies in the range of 1 to 3 × $10^{14}$ atoms per $cm^2$. A much thicker target would perturb the beam to an uncontrollable level, while a thinner one would, given the limited supply of antiprotons, lead to an unacceptably low luminosity. The target, intersecting an unbunched beam, must operate continuously to minimize the ratio of instantaneous rate on detectors to integrated luminosity, and have small transverse dimensions, with maximum beam overlap.

A target in the required density range and with the appropriate geometry can be built by letting molecular hydrogen at high pressure and low temperature expand through a narrow throat injector of suitable shape [2]. At a short distance from the nozzle throat, the flow field of the gas is similar to that from a point source (Fig. 1). Stream lines are almost straight with the stream core clustering in large agglomerates of molecules which can move at supersonic speed (hence the name 'jet') over long distances in high vacuum, without absorption or diffusion by the residual gas.

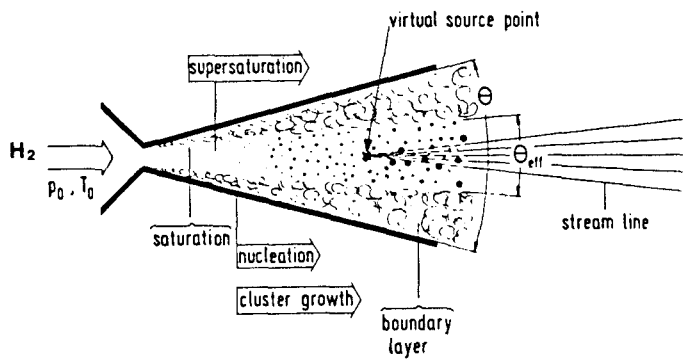


**Fig. 1** Converging-diverging nozzle: schematic localization of phases in the gas expansion [2].

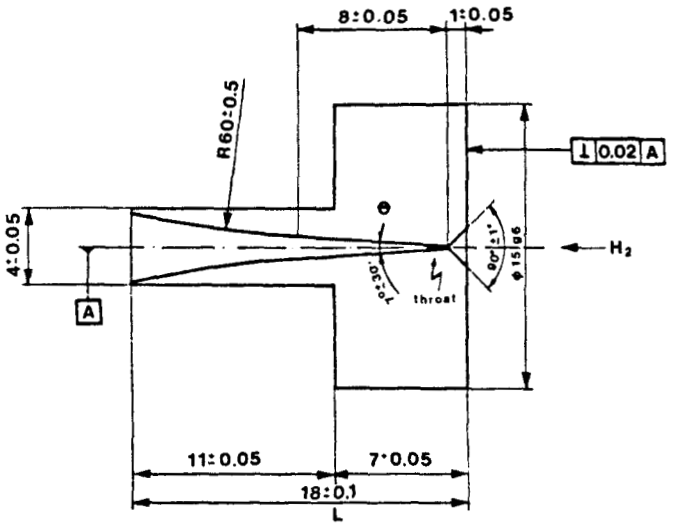


**Fig. 2** Cross-section of the nozzle.

For experiment R704 we built a target with a trumpet-like injector (Fig. 2). This shape maximizes the density of the jet core [2]. The values of the nozzle parameters were: D = 30 $\mu$m, the throat diameter: $\theta$ = 3.5°, the angular half-acceptance; and L = 18 mm, the total length. It was manufactured from copper in the CERN workshop [3].

We choose to operate at liquid $N_2$ temperature to simplify the construction of the temperature-control system and for reliability of operation over long periods.

Figure 3 schematizes the target system. The expansion took place in chamber 1. Typical operating conditions were at $p_0$ = 10 bar and $T_0$ = 77 K. A three-collimators system ($C_1, C_2, C_3$) (Fig. 4) selected the central, denser part of the jet which, after crossing the ISR ring 2, was absorbed by the sink pumps.

The injector was mounted on a movable mechanism to allow for the possibility of optimizing its position relative to the collimation system.

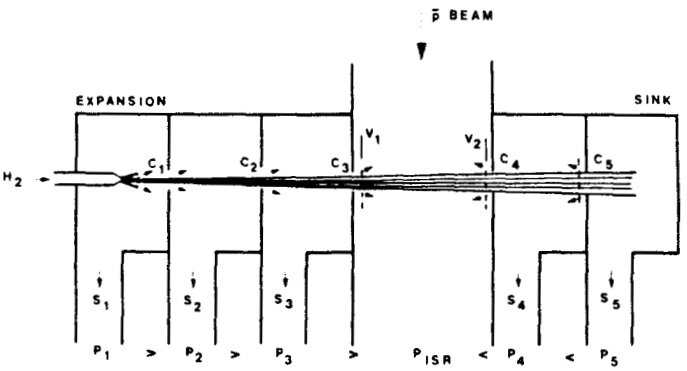


| Stage | S (1/s) | C (1/s) |
|---|---|---|
| 1 | 7000 | 0.7 |
| 2 | 4000 | 3.0 |
| 3 | 4000 | 7.0 |
| ISR | 2000 | 80.0 |
| 4 | S4=8000 | 1100.0 |
| 5 | S5=120000 | |

**Fig. 3** Schematic of the target system: chambers 1, 2, and 3 constitute the production stage, and chambers 4 and 5 the sink stage. The gas jet intersects the antiproton beam at 90°. Listed are pumping speeds (S) for each stage and conductances (C) between chambers.

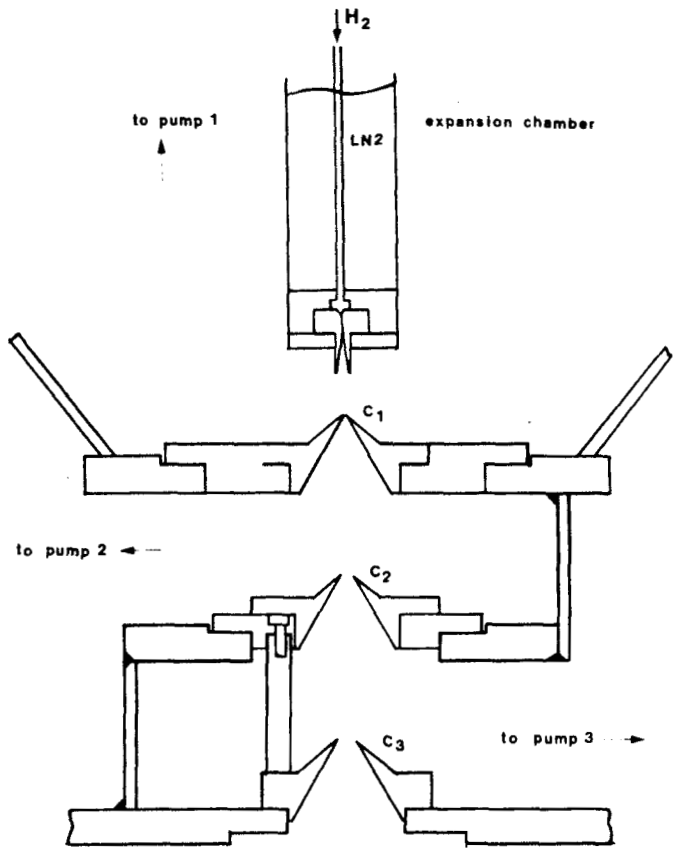


**Fig. 4** System of collimators. The diameters are: 1.4 mm for $C_1$, 2.4 mm for $C_2$, 5.6 mm for $C_3$.

Out of a total flux of 10 Torr · l · $s^{-1}$ expanding from the nozzle, the collimation system selected 0.15 Torr · l · $s^{-1}$ = $10^{19}$ atoms per second. This corresponded to a density of $10^{14}$ atoms per $cm^3$, at the interaction point (26 cm downstream from the nozzle throat), as can be calculated from the speed of the clusters (1290 m · $s^{-1}$) and the dimensions of the jet (d = 9 mm).

A major concern in the target design arose from the need to limit the pressure increase in the ISR vacuum pipe to an acceptable level. As a consequence, both the expansion and the sink chambers were separated from the ISR vacuum pipe by the maximum number of pumping stages compatible with the available space.

On the production side, the collimators, $C_1$, $C_2$, $C_3$, which defined the dimensions of the jet at the intersection with the antiproton beam, connected three different chambers that were evacuated by the successive stages of a differential pumping system. The pumping speeds acting on each chamber and the conductances between chambers are listed in Fig. 3.

On the sink side the jet was dumped on a cryogenic pump of high speed (120,000 l · $s^{-1}$). A differential pumping system, formed by two cryogenic pumps of 4,000 l · $s^{-1}$ each, separated the vacuum pipe from the dump.

A pressure rise to about $10^{-7}$ Torr in the vacuum pipe, around the target region, was mainly due to clusters which hit the edges of the last collimator on the production side and did not reach the sink system. Backstreaming gas from the sink accounted for a negligible fraction of the pressure increase in the vacuum pipe.

Two additional pumps, acting on the ISR ring section where the target was mounted, limited to 1.5 m the region where the pressure was larger than $10^{-9}$ Torr. The pressure rise in the vacuum pipe corresponded to only 1.5% of the target thickness spread over a length of a few metres.

In order to avoid machine vacuum contamination in the case of breakdown of the target system, two fast-acting ultra-high-vacuum valves were installed to separate the production and sink systems from the vacuum pipe of ISR ring 2.

To avoid blockage of the nozzle throat by impurities, high-purity $H_2$ was used and the injection line was provided with mechanical filters (2 $\mu$m), a condensation trap at liquid $N_2$ temperature, and an active charcoal trap.

A system to monitor the jet intensity was mounted in front of the large sink cryogenic pump. It consisted of a plate of stainless steel (6 × 100 $mm^2$) which could scan across the jet. A pressure rise was then produced by the gas backscattered from the plate. A typical profile of the jet is shown in Fig. 5; the measured pressure rise has been converted into thickness traversed by the antiproton beam.

The operations of the target were controlled by two microprocessor-based systems which performed all tasks related to start up, the jet on/off procedure, bookkeeping of the measurements, and safety checks.

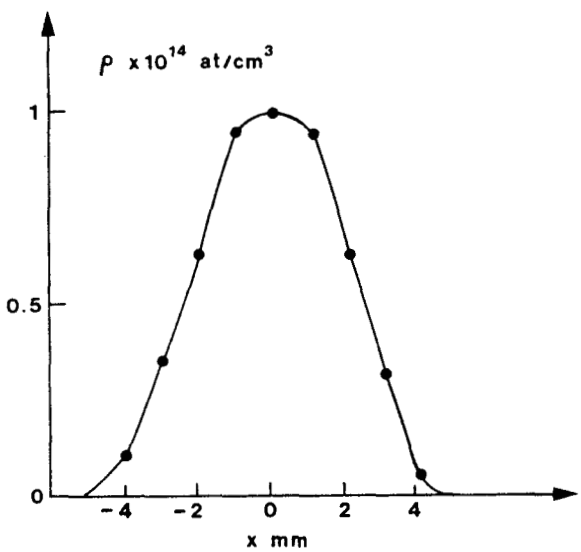


**Fig. 5** Target-thickness profile as obtained from measurements with the monitor described in the text.

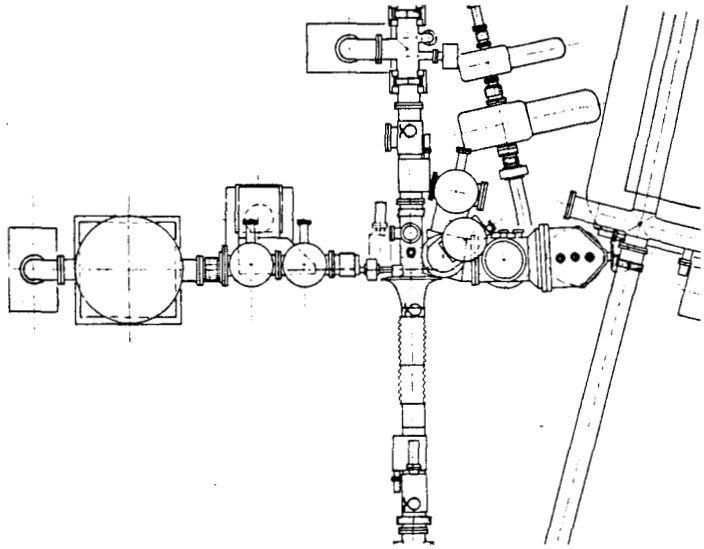

**Fig. 6** Target system layout: top view.

A top view of the complete target system mounted on ring 2 at the ISR is shown in Fig. 6.

## Conclusion

The $H_2$ internal target described in this contribution has been successfully operated in the R704 experiment.

The same novel technique will be used at the FERMILAB $\bar{p}$ Accumulator and at the CERN Low-Energy Antiproton Ring (LEAR).

## References


1. C. Baglin et al., CERN-EP Internal Report 85-01 (1985)
   C. Baglin et al., Phys. Lett. **163B** (1985), 400.
   C. Baglin et al., Phys. Lett. **171B** (1986), 135.
   C. Baglin et al., Phys. Lett. **172B** (1986), 455.
2. W. Obert, Properties of cluster beams formed with supersonic nozzles, Proc. 11th Symposium on Rarefied gaz Dynamics, Cannes, 1978 (CEA, Paris, 1978), p. 118.
3. J.C. Brunet et al., CERN-ISR-GE/82-20 (1982), A different method has been developed at KfK Karlsruhe by W. Obert.

# NUCLEAR EFFECTS IN ELECTROPRODUCTION OF HADRONS

A. Harindranath and J. P. Vary

W. K. Kellogg Radiation Laboratory
California Institute of Technology, Pasadena, CA 91125
and
Physics Department, Iowa State University, Ames, IA 50011

K. E. Lassila

Physics Department, Iowa State University, Ames, IA 50011

We evaluate the possibility of observing nuclear effects in semi-inclusive electroproduction of hadrons(h) from nuclei. We assume factorization and nuclear independence of fragmentation functions in the current fragmentation region. Hence it is shown that the production ratio of oppositely charged hadrons $h^+/h^-$ for the same nucleus is quite insensitive to nuclear effects and the ratio of cross sections for the production of the same sign hadron from different nuclei exhibit the same behaviour as the inclusive ratio which is sensitive to nuclear effects.

## I. INTRODUCTION

Recent inclusive electroproduction experiments on nuclear targets[1] have received considerable attention because of the evidence they provide for the importance of nuclear effects on quark distributions in nuclei. It is reasonable to examine other high energy lepton-nucleus and hadron-nucleus reactions for the consequences of nuclear effects. For example, nuclear effects in lepton pair production in hadron-nucleus interactions have received attention recently. In this work we consider the nuclear effects in electroproduction of hadrons from nuclei.

This paper is organized as follows. In Sec. II we review the conventional assumptions and resulting cross section expressions for the electroproduction of hadrons. Details regarding the fragmentation functions and quark distribution functions used in this work are given in Sec. III. In Sec. IV we evaluate the nuclear effects of quark distribution functions in various cross sections and cross section ratios. Sec. V contains our conclusions.

## II. INCLUSIVE HADROPRODUCTION

First let us review the inclusive process e N $\rightarrow$ $e'$ X. The cross section is given by[2]

$$\frac{d^2\sigma}{dxdy} = \frac{4\pi\alpha^2}{Q^4} 2M_N E[(1-y)F_2(x,Q^2) + xy^2 F_1(x,Q^2)]$$

where $x$ is the usual Bjorken scaling variable, $y = \nu/E$ where $\nu$ is the energy transfer and $E$ is the incident energy, $M_N$ is the mass of the target and $Q^2$ is the negative of the four-momentum squared of the virtual photon. $F_1$ and $F_2$ are the inelastic structure functions. In the above expression we have neglected $\frac{M_N}{2E}xy$ with respect to $1-y$ in the coefficient of $F_2$. In the scaling region $F_{1,2}(x,Q^2) \rightarrow F_{1,2}(x)$ and further $F_1$ and $F_2$ are related by the Callan-Gross relation $2xF_1(x) = F_2(x)$. Thus we have,

$$\frac{d^2\sigma}{dxdy} = \frac{4\pi\alpha^2}{Q^4} 2M_N E \frac{1+(1-y)^2}{2} F_2(x).$$

In the quark parton model we have $F_2(x) = \sum_i e_i^2 q_i(x)$ where $q_i$(x) is the quark distribution function and $e_i$ is the charge of the quark i.

For the semi-inclusive process[3] e N $\rightarrow$ $e'$ h... (see Fig. 1) we define the variables $\epsilon$=h.p, $\kappa$=h.q, u=$\kappa$/p.q and z=$\epsilon$/p.q. Here p, q and h are the 4-momenta of the target, virtual photon and the hadron respectively. The target fragmentation region is defined by $\epsilon$ finite, $\kappa \rightarrow +\infty$, u finite. The current fragmentation region is defined by $\epsilon$ finite, $\kappa \rightarrow -\infty$, u and z finite. In the lab frame current fragmentation corresponds to the detected hadron moving in the direction of the current (with allowance for a bounded transverse momentum $h_t$). In the lab frame z= $E_h/\nu$ where $E_h$ is the energy of the hadron.

In the present work we restrict ourselves to the current fragmentation region and further neglect the transverse momentum of the hadron.

In the parton model, the cross section for inclusive hadron production is given by

$$\frac{d^2\sigma}{dxdydz} = \frac{4\pi\alpha^2}{Q^4} 2M_N E \frac{1+(1-y)^2}{2} \sum_i e_i^2 x q_i(x) D_i^h(z)$$

where the fragmentation function $D_i^h$ represents the probability for the quark of flavor i to break up with the production of hadron h carrying momentum fraction z. Factorization (seperation of the cross section in x and z variables) and scaling ($q_i$(x)

FIG. 1

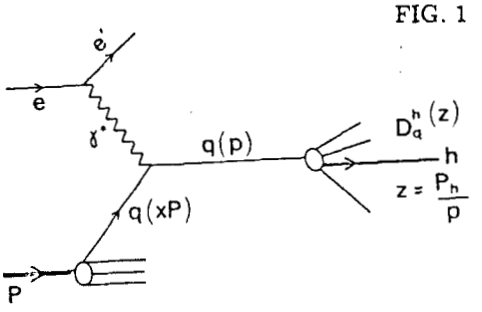


*Inclusive hadron production in deep inelastic electron scattering with nuclear targets. Here thick lines represent hadrons, a wavy line represents the virtual photon and thin lines represent electrons or quarks.*

and $D_i^h(z)$ do not depend on $Q^2$) are characteristic assumptions of the parton model. In reality both $q_i(x)$ and $D_i^h(z)$ depend on $Q^2$ due to QCD scaling violations. These scale breaking effects can be possibly seen by comparing the data at different values of $Q^2$. At low values of $Q^2$ we expect a breakdown of factorization, due to finite strong coupling corrections. Due to these complications that arise in the low $Q^2$ region we restrict ourselves to the deep inelastic region.

## III. FRAGMENTATION FUNCTIONS AND QUARK DISTRIBUTION FUNCTIONS

For the calculation of cross section we need models for the quark distribution functions and fragmentation functions. For the fragmentation process there are hadronization models motivated by QCD. In the present work, however, we employ simple parametrizations deduced from experiment. For simplicity we further assume that the detected hadron is the lightest one, the pion.

Using isospin invariance, charge conjugation and the equality of unfavored functions, we need only two independent fragmentation functions $D_u^{\pi^+}(z)$ and $D_u^{\pi^-}(z)$. Neglecting sea quark distributions ($x \simeq .2$) and using an isoscalar target (deuteron), these functions have been extracted[4] recently up to z=0.8. A simple parametrization

$$zD_u^{\pi^+}(z) = 0.7(1-z)^{1.75},$$

$$zD_u^{\pi^-}(z) = \frac{1-z}{1+z} zD_u^{\pi^+}(z)$$

fits the data reasonably well. We use this parametrization in this work. It is worth noting that this parametrization tends to fall faster with z than that[5] of the data at lower $Q^2$ (See Fig. 2) which is consistent with QCD evolution of the valence fragmentation function.

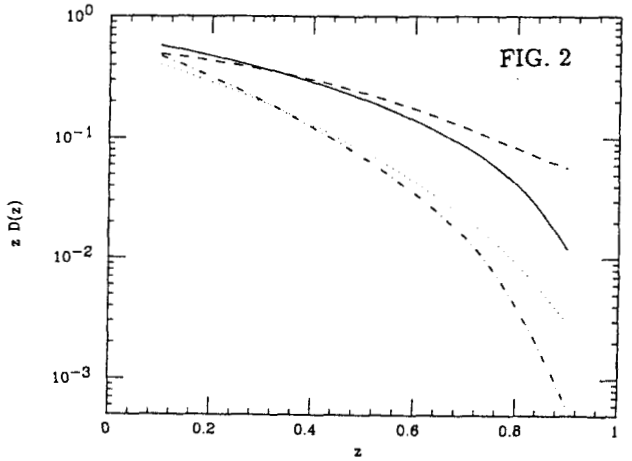


*Fragmentation functions extracted from experiments. Solid line and dot-dash line represents $zD_u^{\pi^+}(z)$ and $zD_u^{\pi^-}(z)$ respectively (taken from Ref. 4). Dashed line and dotted line represents $zD_u^{\pi^+}(z)$ and $zD_u^{\pi^-}(z)$ respectively (taken from Ref. 5 ).*

For the quark distribution functions we use the quark cluster model (QCM)[6-8] which was proposed to explain the deep inelastic $^3He$ scattering results from SLAC[9]. In the QCM one assumes the nucleus at all times is organized into color singlet clusters. The clusters are labelled by their leading Fock space component in the infinite momentum frame as three-quark (3-q), six-quark (6-q), etc., clusters. Larger clusters are assumed to form by the overlap of smaller clusters. As is customary in parton phenemenology, we assume that the participating quark or antiquark is quasifree. Second we assume that the cluster is also quasifree. We also neglect quark exchange processes between clusters. Since we are interested in qualitative behaviour of cross sections and cross section ratios we have further adopted the following simplifying assumptions in this work. All clusters larger than 6-q clusters are approximated as 6-q clusters and Fermi motion is neglected. The quark distribution function in a nucleus is $q_i(x) = p_3 n_{3_i}(x) + p_6 n_{6_i}(x)$ where $p_3$ and $p_6$ are 3-q and 6-q cluster probabilities. In this work we use the quark distribution functions $n_i(x)$ for various clusters from Ref. 7.

## IV. NUCLEAR EFFECTS

From the expression for the cross section given in Sec. II we have,

$$\frac{1}{d\sigma/dx}\frac{d^2\sigma}{dxdz} = \frac{\sum_i e_i^2 q_i(x) D_i^h(z)}{\sum_i e_i^2 q_i(x)}.$$

Denoting the quantity on the r.h.s of the above equation by $N^h$ we can form the charged particle ratio

$$\frac{N^{h^+}}{N^{h^-}} = \frac{\sum_i e_i^2 q_i(x) D_i^{h^+}(z)}{\sum_i e_i^2 q_i(x) D_i^{h^-}(z)}.$$

Explicitly we have,

$$\frac{N^{\pi^+}}{N^{\pi^-}} = \frac{4q_u(x)\eta(z) + q_d(x) + s(x)[7+5\eta(z)]}{4q_u(x) + q_d(x)\eta(z) + s(x)[7+5\eta(z)]}$$

where

$$\eta(z) = \frac{D_u^{\pi^+}(z)}{D_u^{\pi^-}(z)} = \frac{1+z}{1-z}.$$

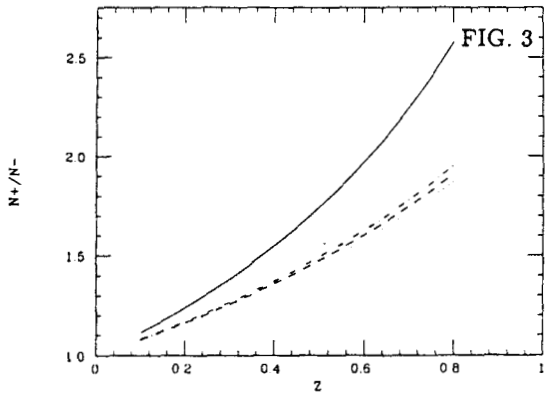


*The ratio $\frac{N^{h^+}}{N^{h^-}}$ (for definition see text) plotted versus z for constant x (=0.1) for the nuclei, proton (solid line), $^{12}C$ (dot-dash line), $^{56}Fe$ [$p_6 = 0.0$] (dashed line) and $^{56}Fe$ [$p_6 = 0.3$] (dotted line).*

In Fig. 3 we plot $\frac{N^{\pi^+}}{N^{\pi^-}}$ as a function of z (at x=0.1) for proton, $^{12}C$ and $^{56}Fe$ targets. Introduction of six quark clusters barely

changes the ratio for $^{12}$C and $^{56}$Fe since the same nucleus occurs in the numerator and the denominator. The difference between the proton and the $^{12}C$ curves, for example, comes simply from the presence of neutrons in $^{12}C$. We expect similar predictions for other models proposed to explain the nuclear effects in deep inelastic lepton scattering.

Next let us examine what we can learn by studying the normalized cross section ratios for different nuclei. Let us define

$$R(x) = \frac{e_i^2(x) q_i^{Fe}(x) D_i^{\pi^-}(z)/56}{e_i^2(x) q_i^{D}(x) D_i^{\pi^-}(z)/2}.$$

In Fig. 4 we plot R(x) at z=0.1. It is readily seen that R(x) exhibits the same qualitative behaviour as the inclusive cross section ratio. Within the QCM the behavior of R in the region x greater than 1 will exhibit steps just as the inclusive cross section ratio[10].

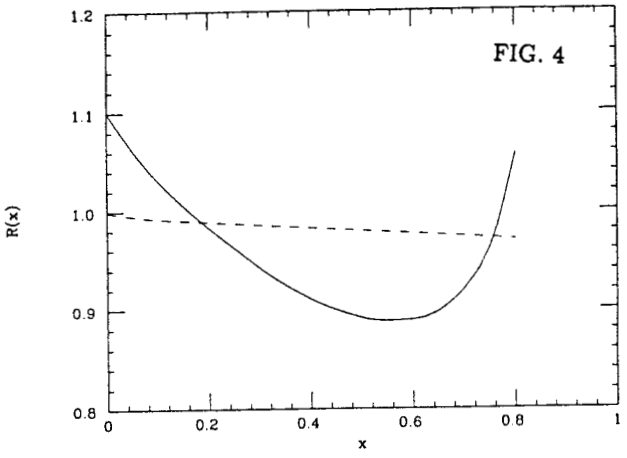


*The ratio R (for definition see the text) calculated in the QCM plotted versus x for z=0.1. The dashed line corresponds to $p_6(D)$=0.0 and $p_6(Fe)$ =0.0. The solid line corresponds to $p_6(D)$=0.0 and $p_6(Fe)$=0.3.The small deviation from unity of the dashed line originates from the non-isoscalar nature of $^{56}Fe$.*

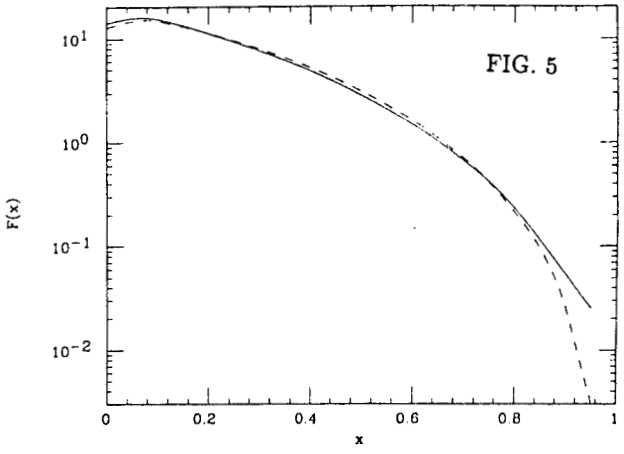


*The quantity F (for definition see the text) plotted versus x for z=0.1. The target nucleus is $^{56}Fe$. Dashed line and solid line correspond to $p_6$=0.0 and 0.3 respectively.*

To get an estimate of the magnitude of the cross section to be expected let us write

$$\frac{d^2\sigma}{dxdydz}\Big|_z = \frac{4\pi\alpha^2}{Q^4} 2M_N E \frac{1+(1-y)^2}{2} F(x).$$

We plot F(x) in Fig. 5. As can be seen the presence of 6-q clusters produces an order of magnitude enhancement in the $x \to 1$ region over the result if there are no quark clusters.

## V. CONCLUSION

Assuming factorization and nuclear target independence for fragmentation functions we have shown that the semi-inclusive hadron production cross section ratio for oppositely charged hadrons with the same target nucleus is quite insensitive to nuclear effects. On the other hand the ratio of cross sections for the *same* hadron produced off *different* nuclei is seen to exhibit the same striking behavior as the inclusive ratio.

## ACKNOWLEDGEMENTS

This work is supported in part by the National Science Foundation grants PHY85-05692 and PHY-04197 and by the U.S.Department of Energy under contract Nos. DE-AC02-82ER40068 and W-7405-ENG-82, Division of High Energy and Nuclear Physics.

## REFERENCES

1. J. J. Aubert *et al.*, Phys. Lett. **123B**, 275 (1983); A. Bodek *et al.*, Phys. Rev. Lett. **50**, 1431 (1983), **51**, 534 (1983); R. G. Arnold *et al.*, Phys. Rev. Lett. **52** 727 (1984); See also G. N. Taylor in *Intersection Between Particle and Nuclear Physics*, Lake Louise, Canada 1986, AIP Conference Proceedings 150, edited by D. F. Geesaman. For recent review of theoretical models see E. L. Berger, *ibid.*
2. F. E. Close, *An Introduction to Quarks and Partons*, (Academic, New York, 1979).
3. Ref. 2; M. Gronau, F. Ravndal and Y. Zarmi, Nucl. Phys. **B51**, 611 (1973); E. Reya in *Perturbative Quantum Chromodynamics*, edited by M. Jacob, Physics Reports reprint book series- Volume 5 (North Holland Publishing Company, Amsterdam, 1982); F. Janata in *1986 CEBAF Summer Workshop Proceedings*, June 23-27, 1986, CEBAF, Newport News, Virginia.
4. J. J. Aubert *et al.*, Phys. Lett. **160B**, (1985) 417.
5. L. M. Sehgal in *Proceedings of the VIII International Symposium on Lepton and Photon Interactions*, edited by F. Gutbrod (Hamburg, 1977).
6. H. J. Pirner and J. P. Vary, Phys. Rev. Lett. **46**, 1376 (1981); H. J. Pirner in *Progress in Particle and Nuclear Physics*, edited by A. Faessler (Pergamon, Oxford, 1985), p.361; J. P. Vary, Nucl. Phys. **A418**, 195c (1984).
7. C. E. Carlson and T. J. Havens, Phys. Rev. Lett. **51**, 261 (1983).
8. M. Sato, S. A. Coon, H. J. Pirner, and J. P. Vary, Phys. Rev. **C33**, 1062 (1986).
9. D. Day *et al.*, Phys. Rev. Lett. **43**, 1143 (1979).
10. J. P. Vary in *Proceedings of the VII International Seminar on High Energy Physics Problems, Multiquark Interactions, and Quantum Chromodynamics*, edited by V. V. Burov, Dubna pub. no. D-1, 2-84-599 (1984) p.186; J. P. Vary, Nucl. Phys., *op. cit.*.

# CAN PION ELECTROPRODUCTION PLUMB THE PION SEA?

R.S. HICKS

Department of Physics and Astronomy
University of Massachusetts
Amherst, MA 01003

## Abstract

An outline is given of the proposal that the nuclear pion field can be determined by coincidence electropion production. Experimental requirements for the measurement of $(e, e'\pi)$ cross sections are discussed, with particular regard to the properties of the PEP storage ring.

## Introduction

The meson field representation of the nuclear force provides the basis for our most detailed, yet tractable, model for calculating nuclear properties. Although the roles of heavy and multiple meson exchanges remain open questions at present, there is some evidence to suggest that the principal process, involving one-pion exchange, is understood. The first such evidence came from calculations of the thermal np capture $(n + p \rightarrow d + \gamma)$ rate. When only the neutron and proton were considered the computed rates were about 10% lower than the observed value.[1]

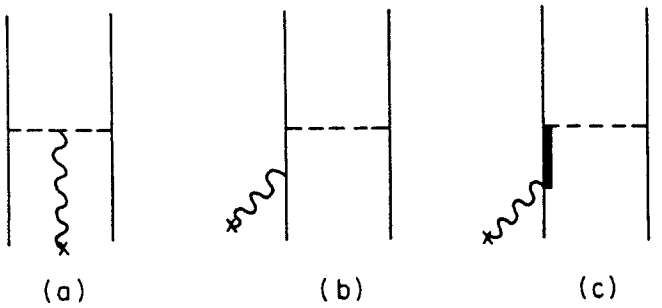


FIG. 1. One-pion exchange current diagrams: (a) pionic current, (b) pair current, and (c) nucleon resonance current.

This discrepancy was subsequently removed by the evaluation of the three one-pion exchange currents shown in Fig. 1, with the pion-nucleon coupling constants being taken from measured $\pi$-N scattering cross sections. More dramatic evidence for the contribution of one-pion exchange currents is found in the cross section for the electrodisintegration of the deuteron at threshold, shown in Fig. 2. Calculations for nucleons only produce a deep diffraction minimum near squared four-momentum transfer $Q^2 = 12$ fm$^{-2}$, in blatant disagreement with the data. Again, consideration of the three one-pion exchange currents of Fig. 1 is crucial for resolving this disagreement.[2] Compelling evidence for the role of pion exchange currents is also found in the cross sections measured for the break-up of the deuteron by 100 – 500 MeV photons,[3] as well as in the magnetic moments[4] and elastic M1 form factors[5] of $^3$H and $^3$He. There is, however, little evidence to confirm our understanding of the meson field in $A \geq 4$ nuclei, where the nuclear force is closer to saturation.

The lack of definitive data on the pionic content of heavy nuclei has impeded the understanding of the EMC effect, where a difference is observed between the cross sections per nucleon for deep inelastic lepton scattering from the deuteron and from heavier nuclei. Various theories, based on diverse ideas, purport to account for this observation. Some theories explain the difference by postulating an enhancement of the pion field in massive nuclei. Other theories do not. Without clear experimental information on the meson field in $A \geq 4$ nuclei, there exists no means of identifying the correct ideas. One experimental investigation that has been made is that of Carey *et al.*,[6] who measured the scattering of polarized 500 MeV protons from deuterium and lead targets in the quasielastic continuum. Since the

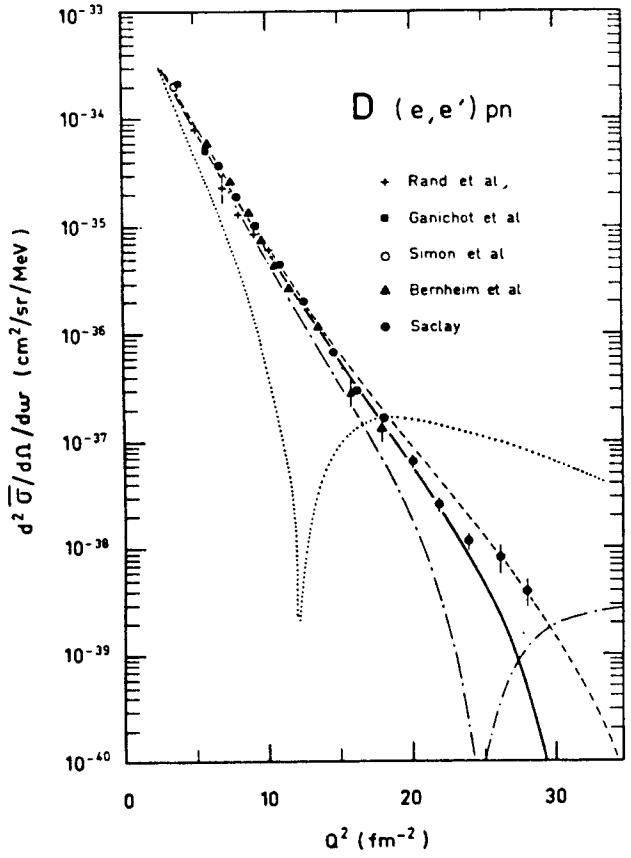


FIG. 2. Cross section for the electrodisintegration of the deuteron at threshold.[2] The dotted curve is for nucleons only, the dash-dotted curve includes one-pion exchange currents, and the dashed curve includes in addition $\rho$-meson exchange. The total result, indicated by the continuous curve, also takes into account the contribution of $\Delta$-isobars.

$\pi$-N coupling is strong, such experiments should be sensitive to any $A$-dependence of the pion field. Carey *et al.* isolated the axial-longitudinal coupling of the proton to the pion field from other interactions by measuring a complete set of polarization transfer variables. Within experimental errors, the results show the axial-longitudinal response functions for d and Pb to be equal, suggesting that there is no enhancement of the pion field in massive nuclei. Notwithstanding the significance of this result, the question of the $A$-dependence of the pion field is one of such importance that it should be explored by any means possible.

It is unlikely that any single experimental study can resolve the issue. For example, the momentum distribution of the virtual pions in deuterium may be somewhat different from that in heavy nuclei, and hence measurements at a single momentum transfer value, such as that of Carey *et al.*, cannot be entirely conclusive. The interpretation of the proton scattering measurements is also compromised by the inherent complexity of the proton-nucleus interaction; for example, the understanding of polarization transfer asymmetries measured for discrete nuclear states in $(\vec{p},\vec{p})$ has presented considerable difficulty. The means of probing the pion field to be discussed in this paper, the $(e,e'\pi)$ reaction, is also subject to uncertainty, particularly from the large final-state interaction effects.[7] For both reactions, there is theoretical debate regarding the interpretability of the data in terms of the nuclear pion field. In fact, on an even more basic level, the range of applicability of the meson field representation has yet to be defined.

## Pion Electroproduction in the Continuum

Güttner *et al.*[8] have suggested that the nuclear pion field can be investigated by longitudinal electroproduction of pions in the continuum region. Güttner *et al.* argue that if virtual pions can be interpreted as partons of nucleons and nuclei, the pion distribution function could be determined in a manner analogous to the determination of the quark distribution functions from deep inelastic scattering. For low squared momentum transfer $|t|$ onto the target nucleon, data for charged pion electroproduction have been reasonably described by the Born term model, the reaction diagrams for which are shown in Fig. 3. It is the t-channel diagram which is of relevance for the investigation of the nuclear pion field.

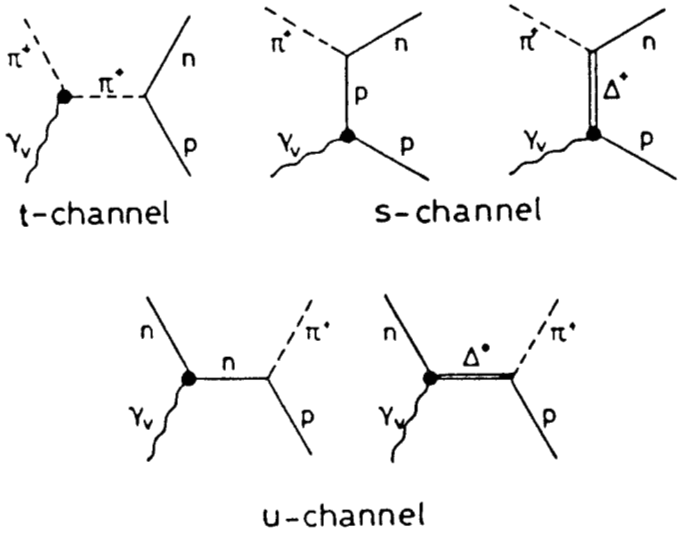


FIG. 3. Born term diagrams for the reaction $ep \to e'\pi^+ n$.

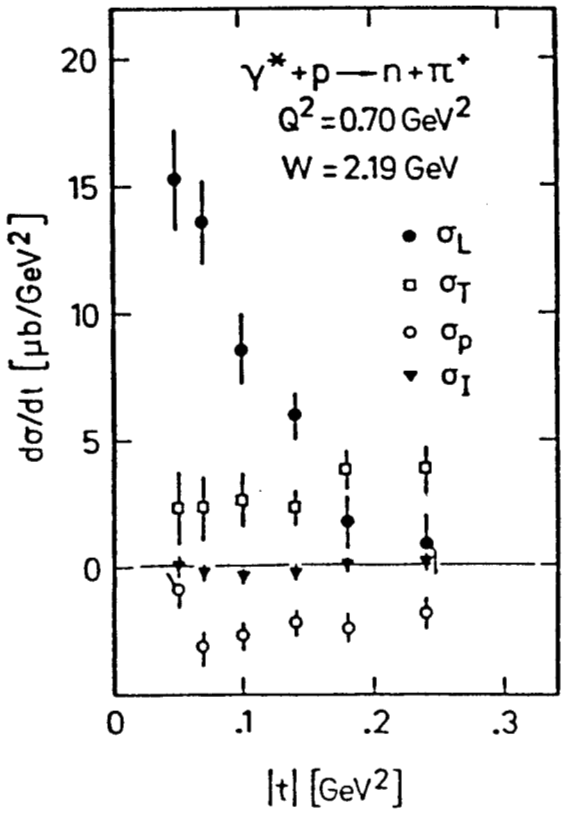


FIG. 4. Components of the cross section for $ep \to e'\pi^+ n$ as a function of the squared momentum transfer $|t|$ onto the target nucleon.[9]

Four separate terms contribute to the cross section obtained when the scattered electron and produced pion are measured in coincidence:[9]

$$2\pi\frac{d^2\sigma}{dtd\phi} = \frac{d\sigma_T}{dt} + \varepsilon\frac{d\sigma_L}{dt} + \varepsilon cos(2\phi)\frac{d\sigma_P}{dt} + \sqrt{2\varepsilon(\varepsilon+1)}cos\phi\frac{d\sigma_I}{dt}.$$

In this expression $\phi$ is the angle between the hadron production and electron scattering planes and $\varepsilon$ measures the polarization of the virtual photon. Due to the $J^\pi = 0^-$ spin of the pion, the t-channel diagram contributes mainly to the longitudinal component of the cross section $d\sigma_L/dt$, shown in Fig. 4. In fact, a crucial element in the argument of Güttner *et al.* is that the strong peaking observed at low $|t|$ in the longitudinal cross section arises almosts solely from the t-channel. The objective of the experimental procedure is therefore to perform measurements throughout a sufficiently comprehensive range of photon polarization parameters $\varepsilon$ and out-of-plane angles $\phi$ to permit the isolation of $d\sigma_L/dt$ from the transverse ($d\sigma_T/dt$ and $d\sigma_P/dt$) and interference ($d\sigma_I/dt$) components in the cross section.

Güttner *et al.* define the pion momentum distribution function $G_{\pi^*/N}(x,Q^2)$ to be the probability of finding a virtual pion $\pi^*$ in the nucleon with momentum fraction $x = P(\pi^*)/P(N)$, the familiar Bjorken scaling parameter. The distribution func-

tion $G_{\pi^*/N}(x,Q^2)$ is then extracted from the longitudinal component of the cross section at small $|t|$ by means of

$$\frac{d^2\sigma_L(eN \to e'\pi X)}{dxdQ^2} = G_{\pi^*/N}(x,Q^2)\frac{d\sigma_{el}(e\pi^* \to e'\pi)}{dQ^2},$$

with the elastic scattering $e\pi^* \to e'\pi$ cross section being calculated using a dipole form for the electromagnetic form factor of the pion.

Due to the lack of available data, Güttner *et al.* were able only to analyze the case of the $ep \to e'\pi^+ n$ reaction, for which the deduced distribution function had to be defined as the probability of finding a virtual $\pi^+$ with momentum fraction $x$ in state $\pi^+ n$. Values for $G_{\pi^+/p}$ were extracted for $x = 0.062, 0.123$, and 0.154, and, with an assumed functional dependence, the pion distribution function was integrated, yielding $(3.0 \pm 0.5)\%$ $\pi^+$ mesons in the proton. The unexpected smallness of this value has been attributed to various factors, some of which will be mentioned below. In practice, one would seek to assess the total pionic content of the nucleon by performing a semi-inclusive measurement for all possible final states $X$. Moreover, comprehensive measurements should be carried out for complex nuclei, to study the $A$-dependence of the number of virtual pions per nucleon.

## Experimental Considerations

The objectives of the measurement, namely, to isolate the longitudinal term in the cross section and check that it is dominated at low $|t|$ by the t-channel reaction diagram, demand rather comprehensive experimental capabilities and procedures:

1. The spectrometer(s) should have large out-of-plane angular acceptances in order to exploit the $\phi$-dependence of the cross section for separation of the $d\sigma_P/dt$ and $d\sigma_I/dt$ terms.

2. In order to separate $d\sigma_T/dt$ and $d\sigma_L/dt$ it is necessary to measure the cross section for different values of the virtual photon polarization parameter $\varepsilon$ with the kinematic parameters $Q^2, t$, and $s$, the squared invariant mass of the $\gamma^* N$ system, held constant. If $d\sigma_T/dt$ and $d\sigma_L/dt$ are to be extracted with reasonable precision, a range of incident electron energies are required. The operating range of the PEP storage ring at the Stanford Linear Accelerator Center (SLAC), extending from 18 GeV down to perhaps 4 GeV, appears to be well-suited to the needs of the $(e,e'\pi)$ experiment. Particularly for the higher incident energies, it is essential that the apparatus be capable of detecting scattered electrons and electroproduced pions at small angles with respect to the beam direction. The scattered electrons of interest will be primarily in the range $\theta_e = 10° - 40°$, and the corresponding pions between $\theta_\pi = 10°$ and 20°.

3. Because the experiment calls for a semi-inclusive measurement in the continuum region, fine resolution is not of primary importance.

4. The spectrometer(s) should have good particle identification capabilities. In particular, $\pi^+, \pi^-$, and $\pi^0$-mesons should be simultaneously detectable. Assuming a charge-symmetric nuclear force, and an isospin T=0 target, equality of the $\pi^-$ and $\pi^+$ production cross sections provides assurance that the dominant reaction mechanism is the t-channel diagram, for in this case, the ratio of the production cross sections is equal to the ratio of the squared pion charges:

$$\frac{\sigma(\pi^-)}{\sigma(\pi^+)} = \frac{(-1)^2}{(+1)^2} = 1.$$

Data taken at DESY[9] and elsewhere on the deuteron show that this is the case for $|t| < 0.15$ (GeV/c)$^2$, as indicated in Fig. 5. For high $|t|$ the cross section ratio is closer to 1/4, consistent with the result expected for hadronization after scattering from valence quarks of charge $\frac{1}{3}$ (for $\pi^-$ production) and $\frac{2}{3}$ (for $\pi^+$ production). Due to lack of charge for the $\pi^0$, neutral pions cannot be produced through the t-channel diagram. However, $\pi^0$ production does occur for the other diagrams, and hence measurement of the $\pi^0$ yield would provide information on the contribution from these background terms.

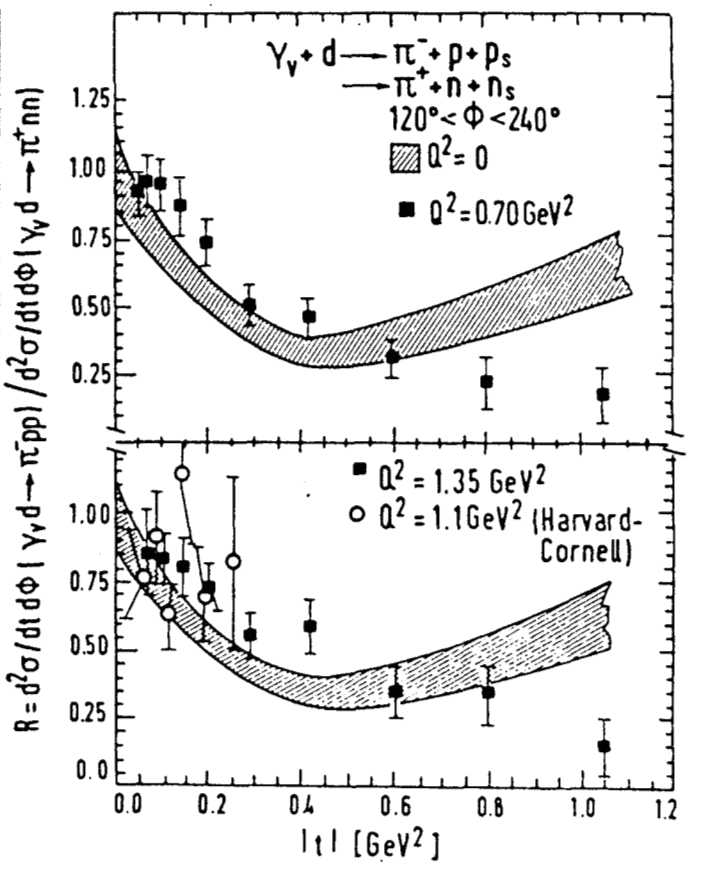


FIG. 5. Ratio of $\pi^-$ and $\pi^+$ production cross sections for deuterium.[9]

5. If it is the longitudinal t-channel mechanism which is dominant at low $|t|$, the struck pion should be ejected close to the direction of the momentum transfer and should carry energy fraction $z = E_\pi/\nu$ close to unity, where $\nu$ is the electron energy loss $E - E'$. The acceptance of the spectrometer(s) should be optimized to study such events.

6. Due to the smaller pion production cross sections at high $Q^2$, useful data will likely be confined to $Q^2 \leq 2$ (GeV/c)$^2$. As $Q^2$ increases so does the spatial resolution of the virtual photon, and the experiment becomes more sensitive to closely-bound virtual pions in the nucleon: What appears at low-$Q^2$ to be a bare nucleon, at high-$Q^2$ may be resolved into a nucleon and virtual pion. (The situation is directly analogous to the evolution of the deep inelastic structure functions with increasing $Q^2$.) The $ep \rightarrow e'\pi^+ n$ data analyzed by Güttner *et al.* had a maximum $Q^2$ of 0.70 (GeV/c)$^2$, inadequate to provide good sensitivity to these pions.[10] This, in part, explains the small $\pi^+$ admixture found in the proton. It should be noted, however, that as $Q^2$ increases the use of the Born term model represented in Fig. 3 becomes questionable as more and more reaction diagrams can contribute to pion electroproduction.

7. In order to avoid the strong final-state interaction between the nucleon and outgoing pion the energy transfer should be greater than 2.2 GeV, sufficient to put the pion above the resonance region. Nevertheless, even in this case, Monte Carlo calculations by Stoler[7] show that the cross sections measured for pion production from complex nuclei can be reduced by a factor of approximately 2 by final state interactions. Thus, even if one were to simply search for a possible $A$-dependence of the pion field, the conclusiveness of the results could well be obscured unless the large final-state interaction effects are understood. The neglect by Güttner *et al.* of rescattering of the pion from the nucleon also contributed to the small $\pi^+$ content found in the proton.[12]

8. The time structure of the incident beam should be consistent with low accidental-to-real coincidence count rate ratios. The standard 3-bunch mode of PEP, which provides a duty factor of less than 0.1%, is clearly far from optimum. The feasibility of performing $(e, e'\pi)$ studies at PEP would be greatly enhanced if future efforts to increase the number of stored bunches are successful.

Previous electroproduction measurements have utilized conventional magnetic spectrometers, one for the scattered electron, and the other to detect the pion ejected close to the momentum transfer direction. In the experiment of Brauel *et al.*,[9] for example, the two spectrometers each had an acceptance solid angle of 3.2 msr, with ± 100 mrad angular acceptance in the vertical direction. The good ~ 5% duty factor of the DESY synchrotron permitted Brauel *et al.* to use 10 cm long liquid hydrogen and deuterium targets and thereby achieve luminosities $\mathcal{L} \geq 10^{34}$ cm$^{-2}$ s$^{-1}$, despite the poor synchrotron beam current. With the anticipated luminosity at PEP being no better than $10^{33}$ cm$^{-2}$ s$^{-1}$, small acceptance spectrometers are out of the question.

One experimental possibility, proposed by van Bibber,[11] would be to use the septum magnets of the PEP-9 collaboration in a modified field configuration. In principle, such a spectrometer could provide acceptance angles close to ±20° in both the horizontal and vertical directions. Suitably instrumented with Čerenkov counters, time-of-flight hodoscopes, and a shower counter comprised of alternating layers of lead and liquid scintillator, the spectrometer could also have good particle identification properties. For this detector the estimated true electron-pion coincidence count rate is quite encouraging:[14] about 10 s$^{-1}$ for $\mathcal{L} = 10^{33}$ cm$^{-2}$ s$^{-1}$. The difficulty of using such a device in the standard low-duty factor PEP mode would be the high background singles rate from recoil hadrons, estimated to be about 4 per beam crossing.[15] Most of the recoil particles have momentum less than 2 GeV/c. Several measures may be taken to reject these particles, for example, the construction of highly-segmented detectors with multi-hit event processing capability, and the use of an event trigger which demands the production of a high-$z$ pion. Nevertheless, the range of practicable luminosities will be unavoidably compromised unless the PEP duty factor can be raised.

Another concern of the septum magnet spectrometer is the relatively low field strength of ≤ 0.3 T existing close to the transmitted beam path. The smallness of this field, incurred as a consequence of the mandate not to interfere with the steering of the stored beam, results in relatively poor momentum resolution for particles emerging at small angles. An alternative system, previously developed at SLAC for the measurement of inclusive hadron production cross sections, utilized a large-aperture dipole magnet traversed by a superconducting transport tube to expel the magnetic field, thereby providing a field-free region for the beam emerging from the target.[16] In this

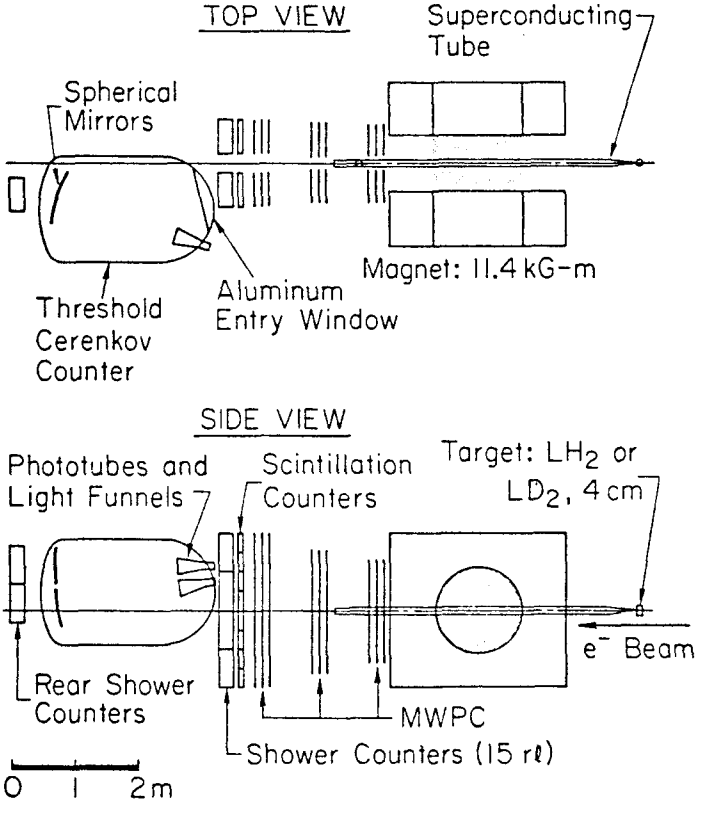


FIG. 6 Large-acceptance, forward-angle spectrometer used by Martin *et al.* for the measurement of inclusive hadron production cross sections.[16]

way, magnetic fields $\geq 1$ T could be applied only a few cm from the stored beam. A schematic representation of this apparatus is presented in Fig. 6.

## Summary

Preliminary studies indicate that the measurement of coincidence electropion production should be feasible at the PEP storage ring, especially if efforts to improve the duty factor by injecting more beam bunches are successful. The observation of peaking in the longitudinal cross section at small $|t|$, combined with a $\pi^+$ to $\pi^-$ production ratio close to one, suggests a reaction mechanism in which the longitudinally-polarized photon couples directly to a virtual pion. Whether or not the nuclear pion sea can be quantitatively determined from such measurements is rendered uncertain by the possible importance of other reaction mechanisms, as well as by the large final-state interaction effects. Nevertheless, measurements of this type may well help to define the region of applicability of the meson field representation.

This work was supported by the U.S. Department of Energy.

## References

1. D.O. Riska and G.E. Brown, Phys. Lett. 38B, 193 (1972).
2. S. Auffret *et al.*, Phys. Rev. Lett. 55, 1362 (1985).
3. J.M. Laget, Nucl. Phys. A312, 265 (1978).
4. E.L. Tomusiak *et al.*, Phys. Rev. C 32, 2075 (1985).
5. F.-P. Juster *et al.*, Phys. Rev. Lett. 55, 2261 (1985).
6. T.A. Carey *et al.*, Phys. Rev. Lett. 53, 144 (1984).
7. P. Stoler, Proceedings, this conference (1987).
8. F. Güttner *et al.*, Nucl. Phys. A429, 389 (1984).
9. P. Brauel *et al.*, Z. Physik C 3, 101 (1979).
10. E.L. Berger, A. Schafer, private communications (1987).
11. K. van Bibber, Proceedings, this conference (1987).
12. H.J. Pirner, private communication (1986).
13. J. Spencer, Proceedings, this conference (1987).
14. B. Fillipone, R. Milner, private communications (1987).
15. S. Rock, private communication (1987).
16. J.F. Martin *et al.*, Phys. Rev. D 20, 5 (1979).

# (e,e'$\pi$) AND THE PION NUCLEON FORMFACTOR

*Andreas Schäfer and Steven E. Koonin*

W.K.Kellogg Radiation Laboratory, CALTECH, Pasadena, CA 91125, USA

It has been claimed[1] that the reaction

$$e + p \rightarrow e' + \pi^+ + n \qquad (1)$$

tests directly the 'pion content of the nucleon'. Such a measurement would be very interesting as it could test some of the models[2] proposed to explain the EMC effect. We will argue that this claim is invalid and that the only information one can extract from such an experiment is the pion nucleon formfactor $F_{\pi NN}$ (and the electromagnetic formfactor of the pion).

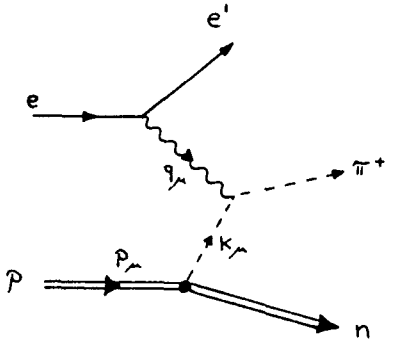


Fig.1 : The reaction ( e p , e' $\pi^+$ n )

An experiment of the type (1) was carried out by Brauel et al.[3] in 1979 at DESY. One might consider repeating this experiment at PEP and comparing the results for different target nuclei, e.g. for hydrogen and a heavy nucleus. Such an experiment should show some characteristic differences due to nuclear binding, i.e. due to the exchange of virtual pions between the nucleons of a nucleus. Brauel et al. isolated the graph of Figure 1 by doing a Rosenbluth separation (which guarantees that the photon is scattered off a spin zero particle) and by imposing a cut on the total momentum squared of the outgoing baryon state (Figure 2).

$$( p - k )_\mu ( p - k)^\mu \leq (1.2\ GeV)^2 \qquad (2)$$

For very large momenta $Q^2 = -q^2$ or, more precisely, for $x\sqrt{q^2} > 1\ GeV$ the longitudinal cross section can be simply written as

$$\frac{d^2\sigma_L(ep \rightarrow e'\pi^+n)}{dx\ dQ^2} = G_{\pi^+/p}(x)\ \frac{d\sigma_{elastic}(e\pi^+ \rightarrow e'\pi)}{dQ^2} \qquad (3)$$

where $G_{\pi^+/p}(x)$ is a $Q^2$ independent function, namely the probability to find a virtual $\pi^+$ with momentum fraction x associated with a proton. This interpretation holds only for large $Q^2$. For small values, i.e. for $x\sqrt{Q^2} \ll 1\ GeV$, the ratio of the two cross sections

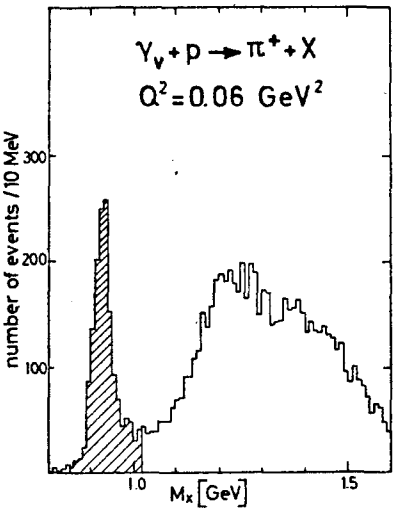


Fig.2 : The experimentally observed values for the square of the four-momentum of the outgoing baryon state. Only the shaded events were taken into account. The broad bump at 1.2 - 1.3 GeV is due to the reaction ( e p , e' $\pi$ $\Delta$ ) . ( From ref. 2)

$$\frac{d^2\sigma_L(ep \rightarrow e'\pi^+n)}{dx\ dQ^2} \Big/ \frac{d\sigma_{elastic}(e\pi^* \rightarrow e'\pi)}{dQ^2} = G(x,Q^2) \qquad (4)$$

becomes a strongly $Q^2$ dependent function with no simple physical interpretation. This is illustrated in Figure 3. The nucleus emits virtual pions with a momentum squared $t = -k^2$. The further these pions are off mass shell, i.e. the larger the value of $|t|$, the sooner they will be reabsorbed. Thus, strongly off shell pions can only be found close to the nucleus. Due to the pion

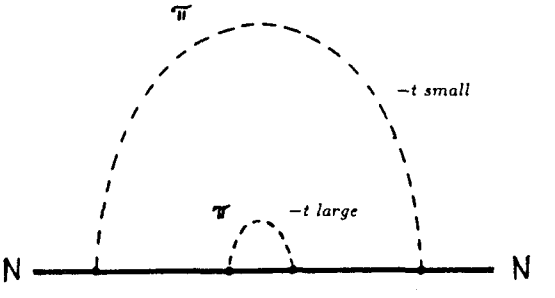


Fig.3 : The virtual pion cloud of a nucleon. Pions which are far off the mass shell are found close to the nucleus.

nucleon formfactor $F_{\pi NN}(t)$ there are no pions with arbitrarily large $|t|$. The strong decrease of $F_{\pi NN}$ with $t$ renders the total number of virtual pions finite. If one probes the virtual pion cloud of a nucleus with photons the response one gets depends on the resolution, i.e. on $Q^2$. For small $Q^2$ virtual pions with large t cannot be resolved. Consequently $G(x,Q^2)$ decreases with decreasing $Q^2$.

Now the problem with the reaction (1) is that the Rosenbluth separation can only be done for small values of $Q^2$, typically smaller than 1 $GeV^2$, because the longitudional cross section drops to zero. The question is therefore whether for such a low $Q^2$ the function $G(x,Q^2)$ is still a good approximation to $G_{\pi^+/p}(x) = \lim_{Q^2\to\infty} G(x,Q^2)$. We interpret the results of reference 1 as a proof that this is not the case, in complete disagreement with the authors of that paper.

They analyzed the data of ref. 2 under the assumption

$$G(x, Q^2 = 0.7\ GeV^2) \approx G_{\pi^+/p}(x) \qquad (5)$$

and claimed that there would be far less virtual pions associated with a nucleon than is usually assumed. Furthermore they concluded that the proton radius is

$$R = 1.5 \pm 0.1\ fm \qquad (6).$$

The latter result they got from the relation[3]

$$G_{\pi^+/p}(x) = \frac{g^2}{8\pi^2} \int_{\frac{x^2M^2}{1-x}}^{\infty} \frac{t\ F_{\pi NN}(t)}{(t+m_\pi^2)^2}\ dt \qquad (7)$$

where the pion nucleon form factor is related to the nucleon radius by

$$F_{\pi NN}(t) = e^{-0.106\ (t+m_\pi^2)\ R^2}. \qquad (8)$$

Because they got from the data very small values for $G(x, Q^2 = 0.7\ GeV^2)$ they had to postulate such an extremely large nuclear radius. The value in Eq.(6), however, is completely unacceptable. In Figure 4 we show the formfactor for $R = 0.7\ fm$ and $0.8\ fm$ which is the physically reasonable range[4] (dashed lines).

The exponential form of the $\pi NN$ formfactor (8) is motivated by the bag model. From a phenomenological point of view one can also advocate a dipole form[5]

$$F_{\pi NN}(t) = \left(\frac{\Lambda^2 - m_\pi^2}{\Lambda^2 + t}\right)^2, \qquad (9)$$

with $\Lambda = (4.8 - 7.0)\ fm^{-1}$ (dash-dotted lines) or even a monopole form[6] (dotted line)

$$F_{\pi NN}(t) = \frac{\Lambda^2 - m_\pi^2}{\Lambda^2 + t} \qquad (10)$$

with $\Lambda \approx 5\ fm^{-1}$.

In fact, $F_{\pi NN}$ is tested experimentally only for small values of $t$ ( $t \leq 0.2\ GeV^2$), where all of these functions coincide more or less, whereas the formfactor used by Güttner et al. is definitely ruled out.

Besides being incompatible with other experiments the analysis of ref.1 is also inconsistent with the analysis by Brauel et al.. By fitting an exponential t dependence to their data Brauel et al. got $R = (1 \pm 0.2)\ fm$. We thus conclude

$$G(x, Q^2 = 0.7\ GeV^2) \ll G_{\pi/p}(x) \qquad (11)$$

in agreement with our crude argument sketched in Figure 2. It is therefore not possible to measure directly the 'pion content of a nucleus'. One can only extract $F_{\pi NN}(t)$ for some limited $t$ range, as was done by Brauel et al.. The ratio in Eq.(3) becomes especially uninformative if the electrons are scattered off a nucleus instead of a proton. The final state interactions are important and they will blur the meaning of $G(x,Q^2)$ still further.

By doing an inclusive measurement as opposed to an exclusive one the problem that the Rosenbluth separation works only for too small values of $Q^2$ is not remedied. One just looses the possibility to extract $F_{\pi NN}$.

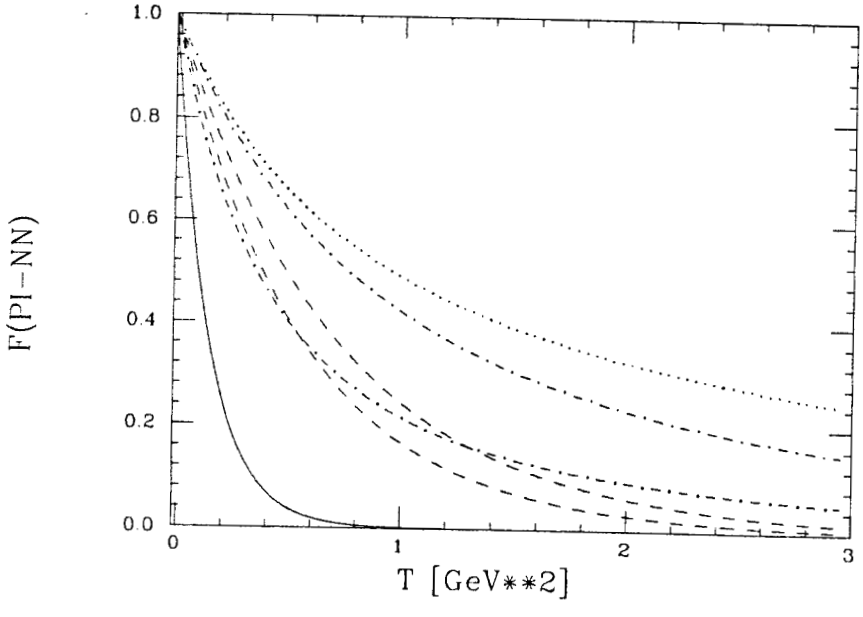


Fig.4 : Comparison of the different $F_{\pi NN}$ formfactors discussed in the literature. The two dashed lines sketch the range expected for an exponential formfactor (ref. 4). The dash-dotted line bounds the allowed range for a dipole formfactor according to ref. 5. The dotted line is the monopole formfactor used in ref. 6. The result of ref. 1 is the solid line.

REFERENCES :
[1] F. Güttner, G. Chanfray, H. J. Pirner, and B. Povh, Nucl.Phys. **A429** (1984) 389
[2] C. H. Llewellyn Smith, Phys.Lett. **128B** (1983) 107
M. Ericson and A.W.Thomas, Phys.Lett. **128B** (1983) 112
E. L. Berger, F. Coester, and R. B. Wiringa, Phys.Rev. **D29** (1984) 398
[3] P. Brauel et al., Z.Phys. **C3** (1979) 101
[4] A. W. Thomas in Advances in Nuclear Physics 13, eds. J. W. Negele and E. Vogt
[5] B. L. Friman, V. R. Pandharipande, and R. B. Wiringa, PRL **51** (1983) 763
[6] J. Cohen and J. M. Eisenberg, Phys.Rev. **C28** (1983) 1309

# MODIFICATION OF NUCLEON PROPERTIES IN NUCLEI

Carl M. Shakin
Department of Physics, Brooklyn College of the City University of New York
Brooklyn, New York 11210

Abstract: We interpret various nuclear physics experiments as providing evidence for modification of QCD order parameters in nuclei.

## Introduction

I would like to emphasize that three topics of current interest in nuclear physics: the EMC effect,[1] the quenching of the longitudinal response seen in inclusive (e,e') reactions,[2] and the use of the Dirac equation to describe nucleon motion in nuclei,[3-5] are all related to a single effect, the modification of the gluon condensate in nuclei.[6] We will argue that, in all three cases mentioned above, we are seeing the effects of a change of a QCD mass (or length) scale away from its vacuum value. The order parameter describing this scale change is an order parameter of the gluon condensate.[7] In the absence of current quark masses, there is only a single mass scale developed dynamically in QCD. It is possible to construct an effective Lagrangian for QCD[7] which only contains a single dimensional order parameter. A change in this parameter will lead to a corresponding change of all dimensional quantities. In particular, we have shown[6,7] how a length scale may be specified for QCD by making use of the gauge and Lorentz invariant parameter,

$$\langle \mathrm{vac} | \frac{g^2}{4\pi^2} G^a_{\mu\nu} G^{\mu\nu}_a | \mathrm{vac} \rangle = \frac{3}{52\pi^2} g^4 \phi_o^4 . \tag{1}$$

Here $g^2$ is the QCD coupling constant renormalized at the mass scale, $\mu^2$. (Equation (1) may be taken as a definition of the quantity $g^2\phi_o^2$.) We remark that a value of 0.012 $(\mathrm{GeV})^4$ has been obtained for the left-hand side of (1) in work on QCD sum rules. (Note that this quantity is a renormalization group invariant in a physical gauge.)

As we have seen in other works,[6,7] various dynamical masses are given in terms of the quantity, $g^2\phi_o^2$. We obtain a dynamical gluon mass,

$$m_G^2 = \frac{1}{4} g^2 \phi_o^2 , \tag{2}$$

and a dynamical quark mass,

$$(m_q^{G\ell})^2 = \frac{1}{6} g^2 \phi_o^2 , \tag{3}$$

as well as a number of other mass parameters, all of which are proportional to the same order parameter. The quark also obtains a dynamical mass via the formation of a chiral condensate, however, in our model the chiral condensate order parameters do not define an independent mass scale. Therefore, if we take the current quark mass to be zero for the up and down quarks, there is only a single mass scale in our effective Lagrangian, which we assume describes QCD at large length scales.[6,7]

Now the presence of quarks tends to break down the gluon condensate and in nuclear matter we claim that $\phi_o$ should be replaced by $\phi_{NM} < \phi_o$. Indeed, we want to show that if $\phi_o/\phi_{NM} \cong 1.25$, we can understand the various phenomena mentioned at the beginning of the introduction.

## The EMC Effect

There have been a very large number of theoretical papers which deal with the EMC effect.[9] The rescaling model of Close, Ross, Roberts and Jaffe[10] is quite interesting, although the physical basis of this model is obscure. (It has also been noted that the model really does not fully address the effects arising from a mechanical change in the size of the nucleon.[11]) In this model moments of structure functions are assumed to exhibit "rescaling". With A specifying a nucleus of mass number A, and N denoting the nucleon, it is assumed that moments are related by the following expression,[10]

$$M_A(Q^2) = M_N(\xi_{NA}(Q^2)Q^2), \tag{4}$$

where the quantity $\xi_{NA}(Q^2)$ evolves with $Q^2$ as follows,

$$\xi_{NA}(Q^2) = \xi_{NA}(Q_o^2)^{\alpha_s(Q_o^2)/\alpha_s(Q^2)} . \tag{5}$$

Here $\alpha_s(Q^2)$ is the running coupling constant and $Q_o^2$ is the momentum scale for which a valence quark model (such as the bag model) is supposed to give a good description of the nucleon structure function $Q_o^2 \leq 1\ \mathrm{GeV}^2$). The essential assumption is that $\xi_{NA}(Q_o^2)$ is given by a length scale modification,

$$\xi_{NA}(Q_o^2) = \left( \frac{\lambda_A}{\lambda_N} \right)^2 > 1. \tag{6}$$

Here $\lambda_N$ is a length scale appropriate to the nucleon in vacuum, and $\lambda_A$ is the length scale appropriate for the nucleus. In the papers dealing with the rescaling model one finds calculations of the ration $\lambda_A/\lambda_N$ based upon models of the nucleon-nucleon correlation functions.[10] We prefer to make the identification

$$\frac{\lambda_A}{\lambda_N} = \frac{\phi_o}{\langle \phi \rangle_A} , \tag{7}$$

where the brackets denote the average value of $\phi(r)$ in the nucleus. For example, we can write, using a local-density approximation,

$$\phi(r) \cong \phi_o \left( 1 - \frac{1}{5} \frac{\rho(r)}{\rho_{NM}} \right) , \tag{8}$$

where $\rho(r)$ is the matter density of a nucleus and $\rho_{NM}$ is the density of nuclear matter. Therefore, we have

$$\langle\phi\rangle_A \cong \phi_o\left(1 - \frac{1}{5}\,\frac{\langle\rho\rangle_A}{\rho_{NM}}\right) \tag{9}$$

and

$$\frac{\lambda_A}{\lambda_N} \cong \frac{1}{\left(1 - \frac{1}{5}\frac{\langle\rho\rangle_A}{\rho_{NM}}\right)} . \tag{10}$$

Thus, the A dependence of the ratio $\lambda_A/\lambda_N$ is here related to the fact that nuclei of different mass number have different percentages of surface nucleons. (A naive extrapolation of (10) higher densities would indicate a deconfining phase transition of about five times nuclear matter density.)

We have noted that in the effective Lagrangian we have suggested to model QCD at large length scales there is only a single dimensional quantity, if we neglect the small current masses of the up and down quarks.[7] Dimensional quantities will then scale with the value of this order parameter. For example, the radius of a nucleon in nuclear matter will be given by,

$$\frac{R_{NM}}{R_{vac}} = \frac{\phi_o}{\phi_{NM}} , \tag{11}$$

where $R_{vac}$ is the nucleon radius in vacuum. The average radius of a nucleon in a nucleus is then given by,

$$\frac{\langle R\rangle_A}{R_{vac}} = \frac{\phi_o}{\langle\phi\rangle_A} . \tag{12}$$

Thus, using (7), we can also identify

$$\frac{\lambda_A}{\lambda_N} = \frac{\langle R\rangle_A}{R_{vac}} . \tag{13}$$

This result is consistent with the fact that in the rescaling model one "rescales" the moments (or the structure function) of the nucleon itself.

While the rescaling model has some attractive features, we believe that further study is required. In particular, one should actually calculate the structure function of a nucleon, either in vacuum or in a nucleus using an appropriate model of nucleon structure.

## Modification of nucleon electromagnetic form factors in nuclei

Issues related to the effects of the nuclear medium in modifying nucleon properties have recently been reviewed by A. Gerard[12] and we refer the reader to that work for a more complete set of references.

We have published a number of papers on this topic and have shown that the momentum transfer dependence and the mass number dependence of the quenching of the longitudinal response in nuclei may be understood in terms of the medium-modified form factors we calculated in earlier work.[13] For example, consider the usual phenomenological expression for the electromagnetic form factor of the proton,

$$G_E^p(q^2) \cong \frac{1}{\left(1 - \frac{q^2}{a_{vac}^2}\right)^2} . \tag{14}$$

Here $a_{vac}^2 = 0.71\ \mathrm{GeV}^2$ is the value of this quantity in vacuum. In nuclear matter we have

$$\frac{a_{vac}}{a_{NM}} = \frac{\phi_o}{\phi_{NM}} , \tag{15}$$

or alternatively,

$$\frac{[r_p^2]^{\frac{1}{2}}_{NM}}{[r_p^2]^{\frac{1}{2}}_{vac}} = \frac{\phi_o}{\phi_{NM}} , \tag{16}$$

where $[r_p^2]^{\frac{1}{2}}$ is the r.m.s. radius of the proton calculated from the slope of the form factor at $q^2=0$. We have shown in an earlier work[14] that the ratio

$$\frac{\langle[r_p^2]^{\frac{1}{2}}\rangle_A}{[r_p^2]^{\frac{1}{2}}_{vac}} = \frac{\phi_o}{\langle\phi\rangle_A} , \tag{17}$$

which we have calculated using a soliton model of the nucleon,[13] reproduces the values of $(\lambda_A/\lambda_N)$ which are required to fit the EMC effect. That is, the electromagnetic radius of the nucleon (calculated using a soliton model of the nucleon) scales with the inverse of the dynamical quark mass and that dynamical mass scales as the ratio $\phi/\phi_o$.[6,7]

The medium-modified form factors obtained earlier[13] have been used to explain a large body of data dealing with the longitudinal response in nuclei[15-17] and the charge distribution of $^{208}Pb$.[18] The situation with respect to the transverse response is more complicated since there appears to be a large amplitude for two-nucleon processes which is important in the region of the quasi-elastic peak.[15] More theoretical and experimental work is needed to clarify the situation in the case of the transverse response.

Some attempts have been made to study the modification of nucleon properties in nuclei via y-scaling.[19] One can use the analysis of y-scaling to argue that there is little change of nucleon properties in nuclei[20]; however, we believe this conclusion is premature. For example, the analysis of y-scaling presupposes that one can use the impulse approximation to understand the data. However, as can be seen from the experimental data summarized in Ref. 12, the impulse approximation (with free-space nucleon form factors) cannot explain the data in the most recent (e,e') and (e,e'p) experiments.[21] Therefore, it is hard to understand why the impulse approximation should provide a satisfactory basis for the analysis of y-scaling. While y-scaling may be an experimental fact, it is not clear that one has identified the reaction mechanism correctly so that firm conclusions may be drawn. Again, further study is required.

## Dirac phenomenology and the relativistic Brueckner-Hartree-Fock theory

In the work of Noble[22] one finds the first attempt to relate the quenching of the longitudinal response to a change of nucleon size. Noble uses the scaling relation,

$$\frac{R_{NM}}{R_{vac}} = \frac{m_N}{m_{eff}} \quad , \tag{18}$$

where

$$m_{eff} = m_N + U_s . \tag{19}$$

Here $U_s$ is the scalar potential felt by a nucleon in nuclear matter. Dirac phenomenology[4,5] yields $U_s \cong 400$ MeV so that $R_{NM}/R_{vac} \cong 1.74$, or in $^{56}$Fe $\langle R\rangle/R_{vac} \cong 1.4$. This represents an increase of the average nucleon radius in $^{56}$Fe of about 40 percent, while to explain the EMC effect (or to explain the quenching of the longitudinal response) in iron, the radius increase needs to be only 15 percent.[10,16] At first sight there might appear to be a problem with the rescaling analysis; however, as we will discuss below, an understanding of the relativistic Brueckner-Hartree-Fock theory[3] allows us to clarify this situation and to see the applicability of the rescaling analysis.

The problem with the simple analysis of (18) and (19) is that $U_s$ contains a number of effects which have nothing to do with the change of mass scale. In particular the various contributions to $U_s$ include exchange (Fock) terms arising from the exchange of omega, rho and pi "mesons" between nucleons. We must remove these terms from $U_s$ before we calculate a value for the modified mass parameter, $\tilde{m}$. In our analysis we found $U_s \cong -350$ MeV; however, only about 60 percent of this scalar potential was due to sigma exchange. (This may be seen from inspections of Figs. (2.8) - (2.12) of [3], for example.) Therefore, $\tilde{m} \cong 938-210 = 728$ MeV, and

$$\frac{R_{NM}}{R_{vac}} = \frac{m_N}{\tilde{m}} \cong 1.29 \ . \tag{20}$$

There is certainly some theoretical error to be associated with the estimate in (20), but the result is quite close to that obtained from our previous analysis.

More precisely, we can see that in the theory of covariant soliton dynamics,[11] the mass and radius of a nontopological soliton are given by,[23]

$$m = f(g_\chi, \eta)\, m_q^{dyn} \ , \tag{21}$$

$$R = \frac{h(g_\chi, \eta)}{m_q^{dyn}} \ , \tag{22}$$

where $m_q^{dyn}$ is a dynamical quark mass arising from the coupling of the quark to the QCD condensates and f and h are dimensionless functions of a coupling constant, $g_\chi$, and a mass ratio, $\eta$. The mass ratio does not change upon rescaling, so that

$$\frac{R_{NM}}{R_{vac}} = \frac{m_q^{dyn}}{\tilde{m}_q^{dyn}} \ , \tag{23}$$

$$= \frac{\phi_o}{\phi_{NM}} \ , \tag{24}$$

as noted earlier.

## Summary

In summary, we can say that if we use the order parameter of the gluon condensate to set the mass and length scale both in vacuum and in nuclei, we can understand several interesting phenomena from a unified point of view. Either theoretical analysis or phenomenological considerations lead to the conclusion that the gluon consensate order parameter is reduced by about 25 percent in nuclear matter. This effect may be considered as a precursor of a deconfining phase transition.[24]

## References


1. J.J. Aubert et al. (EMC collaboration ) Phys. Lett. 123B, 275 (1981); A. Bodek et al., Phys. Rev. Lett. 50, 1431 (1984); 51, 534 (1984); R.D. Arnold et al., Phys. Rev. Lett. 52, 727 (1983). BCDMS Collaboration, Phys. Lett. 163B, 282 (1985).
2. Z.E. Meziani et al., Phys. Rev. Lett. 52, 2130 (1984).
3. M.R. Anastasio, L.S. Celenza, W.S. Pong, and C.M. Shakin, Phys. Rep. 100, 327 (1983).
4. L.S. Celenza and C.M. Shakin, Relativistic Nuclear Physics: Theories of Structure and Scattering (World Scientific, Singapore, 1986).
5. B.D. Serot and J.D. Walecka, in Advances in Nuclear Physics, Vol. 16, edited by J.W. Negele and E. Vogt (Plenum Press, New York, 1985).
6. L.S. Celenza and C.M. Shakin, Phys. Rev. D34, 1591 (1986).
7. L.S. Celenza and C.M. Shakin, Effective Lagrangian Methods in QCD, in Chiral Solitons, edited by K.F. Liu (World Scientific, Singapore, in press).
8. M.A. Shifman, Ann. Rev. Nucl. Part. Sci. 33, 199 (1983).
9. For a review see R.L. Jaffe, in Relativistic Dynamics and Quark-Nuclear Physics, edited by M.B. Johnson and A. Pickleseimer (Wiley, New York, 1985).
10. F.E. Close, R.J. Jaffe, R.G. Roberts and G.G. Ross, Phys. Rev. D31, 1004 (1985).
11. S. Brodsky, private communications.
12. A. Gerard, Saclay Report No. 2388 (Sept. 1986). To be published in the proceedings of the CEBAF Summer Workshop (Newport News, June 23-28, 1986).
13. L.S. Celenza, A. Rosenthal and C.M. Shakin, Phys. Rev. C32, 232 (1985).

14. L.S. Celenza, A. Rosenthal and C.M. Shakin, Phys. Rev. Lett. 53, 892 (1984).

15. L.S. Celenza, A. Harindranath and C.M. Shakin, Phys. Rev. C32, 248 (1985).

16. L.S. Celenza, A. Harindranath, C.M. Shakin and A. Rosenthal, Phys. Rev. C32, 650 (1985).

17. L.S. Celenza, A. Harindranath and C.M. Shakin, Phys. Rev. C33, 1012 (1986).

18. L.S. Celenza, A. Harindranath, C.M. Shakin and A. Rosenthal, Phys. Rev. C31, 1944 (1985).

19. G.B. West, Phys. Rep. 18C, 264 (1975).
I. Sick, Phys. Lett. 157B, 13 (1985).
R.D. McKeown, Phys. Rev. Lett. 56, 1452 (1986).

20. I. Sick, contribution to CEBAF Workshop - 1986 (to be published).

21. G. Van der Steerhoven et al., Phys. Rev. Lett. 57, 182 (1986).

22. J. Noble, Phys. Rev. Lett. 42, 412 (1981).

23. L.S. Celenza, V.K. Mishra, and C.M. Shakin, Mass scales in QCD and nuclear dynamics, Brooklyn College Report B.C.I.N.T. 86/051/155 (1986). Unpublished.

24. See for example, M. Satz, Ann. Rev. Nucl. Part. Sci. 35, 245 (1985).

# INFLUENCE OF SIX-QUARK BAGS ON ELECTRON SCATTERING

Gerald A. Miller

Institute for Nuclear Theory
Department of Physics, FM-15
University of Washington
Seattle, Washington 98195

## Abstract

Possible signatures of the presence of nuclear six-quark bags are discussed.

## I. Introduction

In the past few years, many workers have tried to use quarks and their interactions to compute nuclear properties. One way to include quarks is to postulate the existence of nuclear six-quark bags[1], and then predict the influence of such objects on various nuclear reactions. Information about how QCD determines nuclear properties may be obtained if a given reaction turns out to be very sensitive to the presence (or lack) of such objects. The purpose of this communication is to discuss some electronuclear reactions that might yield information about six-quark bags.

Let me begin with an outline. First, I discuss my conception of the term "six-quark bag", and the properties of such objects. Simple estimates show that copious numbers of such objects might exist in nuclear matter. Suppose 40 or 50% of the baryons in a heavy nucleus were six-quark bags. One might expect that this would contradict many observations. Consider one spectacular piece of evidence for nucleonic degrees of freedom: the measurement of the charge density difference between Pb and Tl.[2] I found[3] that including (more than about 50% of) six-quark bags does not affect the predicted cross section very much. No strong disagreement is found![3] One may even claim that including six-quark bags improves the comparison between theory and experiment. Kisslinger and Hoodbhoy[4] and others have argued that recent measurements of the He and H charge densities provide evidence for the existence of six-quark bags at the 15% level. But the main message is that elastic scattering is not extremely sensitive to the six-quark bag presence in nuclei. (I say this because six-quark (6q) bags are generally one among many "second order" effects yielding similar contributions.) Thus, my purpose here is to instead consider inelastic electron scattering and to examine regions of the $(Q^2\nu)$ plane where 6q bags might be found. P. Mulders[5] has already studied the role of 6q bags in the inclusive (e,e') process. He finds that six-quark bags could be responsible for the suppression of the longitudinal structure function and can fill in the "dip" region between the nucleon- and $\Delta$- quasielastic peaks. Furthermore, in the $\Delta$ production region ($\nu$ = 300 MeV), the contributions of six-quark bags to the transverse structure function are about equal to those of the $\Delta$. I reproduced Mulders' results and extended them to the case of a $^4$He target. Six-quark bags are indeed important numerically. However, their largest contributions occur near the $\Delta$ region, so it is difficult to tell a $\Delta$ from a six-quark bag. In the hope of obtaining more definitive information, I suggest experimental studies of the energy dependence of the angular distribution of protons emitted in the (e,e'p) or (e,e'pp) reactions.

## II. What and Why Six-quark Bags?

Learning how confinement works in nuclei is a fundamental issue. One way to make progress is to determine if quark effects (as opposed to nucleonic) effects) contribute to making the nucleus. Quarks may participate if they are confined occasionally in six-quark (6q) bags. To differentiate from "ordinary" effects we suppose that the 6q bag is orthogonal to simple product states of nucleonic wave functions. For present purposes we take the 6q bag to consist of six (antisymmetrized) quarks in the lowest ($\kappa$ = -1, L = 0) state of the MIT bag. Eigenfunctions and energy eigenvalues have been obtained in Ref. 6. Some relevant features are shown in Table 1, taken from Ref. 5.

Table 1. Six-quark Bag Properties

| I,S | Mass (GeV) |
|---|---|
| 0,1 | 2.16 |
| 1,0 | 2.24 |
| 1,2 | 2.36 |
| 2,1 | 2.52 |

The numbers I,S represent the isospin and spin of the 6q system. These states are expected to have a width of about 150 MeV, which is a bit larger than that of the $\Delta$. If one decomposes the 6q wave function into sums of products of baryon-baryon wave functions one finds that 80% of the probability is contained in components in which one of the "baryons" carry color. About 10% of the wavefunction occurs in nucleon-nucleon components, so there is some overcounting. However, this is smaller than other uncertainties.

One may view the six-quark bags as off-shell components in a generalized baryon-baryon wave function. From the table one sees that the typical energy denominators are about 0.3 to 0.6 GeV. One needs that amount of input energy to place these objects on the energy shell where they can be observed (under sufficiently lucky conditions).

Another property of six-quark bags is their size. In Ref. 6 the radius of a six-quark bag ($R_6$) is about $2^{1/3}$ times the radius of a nucleon. As discussed below, this assumption has a significant incluence on the location of the quasielastic peaks for 6q bag knockout. Lomon[7] assumes a smaller value of $R_6$.

## III. How Many Nuclear 6-quark Bags Are There?

I would really like to know the answer to the above question. Estimates range from zero to very many. Here I present a very simple estimate based on geometry. One wants to use 6q bags instead of nucleons to represent the short-distance baryon-baryon wave function. Our procedure[1] has been to replace a two-nucleon wave function by a 6q bag whenever the motion of the pair brings their centers closer than a distance, $r_0$. Probability conservation is maintained by taking the probability for the 6q bag as equal to the removed probability for the nucleons to be closer than $r_0$. The value of $r_0$ is then an important number, and $r_0$ ~ 1 fm often leads to

results in good agreement with experiment.[1] This separation occurs when the edge of one nucleon is at the center of the other, provided the radius of the nucleon is taken as about 1 fm. Then the volume of the overlap region is large. The 6q probability per nucleon pair turns out to be between about 3 and 6%, depending on the state.

In heavy nuclei there are many possible pairs and (in this picture) many 6q bags. Consider, for example, a nucleon in infinite nuclear matter of density $\rho_0$ (= 0.166 $Fm^{-3}$). The probability that another nucleon lies within $r_0$ is $\frac{4\pi}{3} r_0^3 \rho_0 \approx 0.7$. Although Pauli principle effects multiply this number by 3/4, this seems excessively large. I don't insist that there really are that many 6q bags in nuclei, but it is likely there are some. The most irritating feature of this is that existing data cannot be used to rule out such an enormous percentage.

## IV. $^{205}$Pb - $^{205}$Tl Charge Density Difference

This quantity is one of the best tests of the conventional nuclear picture. One observes the structure of the 3s proton wave function quite clearly.[2] Surely copious amounts of 6q bags should spoil this result. Calculation[3] shows that this is not so! The reason is that, in our treatment of elastic electron scattering, the dominant effect of 6q bags is that they are bigger than nucleons. But the difference between $R_6$ and a nucleon radius is very small compared to the size of the Pb nucleus. Thus no effect remains. The size is the only influence because six-quark bags are formed in the interior. There, the effective density of the center of mass of an NN pair is essentially the product of the 3s density by the approximately constant density of the nuclear interior.

## V. Using (e,e') to See 6 Quark Bags

We want to ask what are the appropriate values of the momentum transfer ($Q^2 = -q^2$) and energy loss ($\nu$) for 6q bags to be observable. Start with $Q^2$. We include processes in which the virtual photon knocks the 6q bag out of the nucleus. In this mechanism the 6q bag maintains its character. It is not blown to bits in the absorption of the virtual photon. In that case the 6q amplitude includes the appropriate form factor $G_6(Q^2)$. We follow Refs. 5 and 6 and assume that the six-quark bags are larger than nucleons. That means that the ratio of 6q to nucleon form factors: $G_6(Q^2)/G_3(Q^2)$ approaches zero as the momentum transfer Q increases, and it becomes harder to find 6q bags at higher momentum transfers. This does not mean that it is harder to observe the influence of quarks at higher values of $Q^2$. It is just that the coherent effects of the 6q bag acting as one particle go away at high momentum transfer.

If the radius of the six-quark bag were equal to or smaller than that of the nucleon, as implied in Ref. 7, the opposite conclusion could be drawn. The calculations discussed below follow Refs. 5 and 6.

What about the photon energy loss, $\nu$? The basic idea is that a 6q bag can be knocked out of the nucleus if it absorbs a photon of large enough energy $\nu$. These excitation energies are the masses of the six-quark bag minus the mass of two bound nucleons. From Table 1, this is about 0.3 to 0.6 GeV. Considering the expected width of the 6q systems, these values of $\nu$ are contiguous with those needed for production of the $\Delta$.

Thus 6q bags might be important at fairly low $Q^2$, but fairly high (by typical nuclear standards) values of $\nu$.

## VI. (e,e') Calculations

As mentioned in the introduction, I follow the work of Mulders.[5] The formulae necessary to make calculations of the cross sections are given in Mulders' paper.

It is necessary to discuss the basic assumptions of his model.

1. A photon strikes and knocks out either a three-quark (nucleon) (with probability $P_3$) or six-quark bag with probability $P_6$ given by $P_6 = 1 - P_3$. In this model, pionic components of nuclei do not contribute.

2. A plane wave approximation is used for all outgoing particles. The knocked out nucleons, 6q bags and produced $\Delta$'s are all on the mass-shell. Thus no final state interactions are included.

3. The final states are $|3q\rangle \times |A-1\rangle$ or $|6q\rangle \times |A-2\rangle$. These are treated as orthogonal states. Thus there is no interference between the two terms. This is a good approximation when $Q^2$ is large enough so that the one and two-baryon states are kinematically well-separated, but 6q bags have effects at values of $Q \lesssim 500$ MeV/c. Then (on average) each baryon of the 6q bag carries $\lesssim 250$ MeV/c, a value close to the Fermi momentum.

As Mulders remarks, the model is oversimplified but one can use it to determine the region of sensitivity to 6q effects in the (e,e') reaction. Furthermore, the model is consistent with data from Q = 400 to 500 MeV/c when natural values of the parameters ($P_6 \sim 0.4$) are used.

During the oral presentation I showed several figures from Ref. 5. These showed that the suppression of the longitudinal structure could be understood in terms of six-quark bags. This is because some 40% of the strength occurs at values of $\nu$ about .3 - .6 GeV ABOVE the quasi-elastic peak for nucleon knockout. There are also nice results for the transverse structure function. The six-quark bags fill in the dip region between the nucleon and delta peaks. In fact, the contributions of the six-quark bags are approximately equal to that of the delta. These results of Mulders are for the $^{12}$C nucleus. I showed also calculations (but no data) for the $^4$He nucleus. The values q and $\nu$ for which 6q bags are important are roughly the same as for the $^{12}$C target.

The contributions of the individual six-quark bag states exhibit interesting peaks as a function of $\nu$ for fixed $Q^2$). However, these peaks are not directly observable since they occur in the $\Delta$ region.

The result of all of this is that there are large 6q bag effects seemingly in agreement with the data. However, we encounter the problem of too many competing mechanisms one more time.

## VII. Better Identification of 6q Bags?

The six-quark bags of interest here are made of quarks in L = 0 states. Therefore, the angular distribution for the decay into two nucleons is isotropic, in the 6q rest frame. This is very different than the decay $\Delta \to N\pi$ ($3\cos^2\theta + 1$). I propose to use this idea to separate the contributions of 6q bags and delta decays.

Consider, for example, measurements of the angular distributions of protons emitted in the (e,e') reaction. One can look for a resonant enhancement of isotropic correlations. The isotropy is to be with

respect to the direction of the photon momentum. If the 6q bags I discuss are relevant there could be a 150 MeV wide region of energy ($\nu \approx 0.3$-$0.6$ GeV/c or higher depending on the model) in which the angular distributions of high energy protons are isotropic. The restriction to high energy protons enters since we want the products of the decay $6q \to NN$, not $6q \to \Delta N$ or $6q \to \Delta\Delta$.

One could apply the rapidity analysis of McKeown et al.[8] to identify the isotropic distribution. Ref. 8 dealt with pion absorption on a cluster of nucleons. After absorption, the cluster spews out nucleons. They[8] found the velocity (essentially the rapidity y) of the coordinate frame in which the emitted nucleons have an isotropic angular distribution. The same technique should work for the photon absorption under consideration here. In that case $y \sim \tanh^{-1} |\vec{q}|/M_{6q}$ is the rapidity of the 6q bag that absorbed the photon. In the frame of rapidity y, the nucleons from the $6q \to NN$ decay are emitted isotropically.

Another possibility is to look for a resonant enhancement of the isotropic angular distribution of two protons emitted in the (e,e'pp) reaction. This could be done with a $4\pi$ detector.

This hope for identifying the 6q effects lies in combining two distinct effects: an isotropic angular distribution (in the appropriate coordinate system) and a resonant energy behavior. Combining these two separate pieces of information may allow the separation of 6q bag effects from the background of ordinary two-nucleon processes which are not expected to have those two features.

## VIII. Summary

The Summary is given in the Introduction.

## References


1. G.A. Miller, Workshop on Nuclear Chromodynamics, ed. S. Brodsky and E. Moniz, World Scientific Publishing, Singapore, 1986, p. 343.
2. G.A. Miller, Int. Rev. of Nucl. Phys, ed. W. Weise, World Scientific Publications, Singapore (1984), p. 189.
3. G.A. Miller, Phys. Lett. 174B, 229 (1986).
4. P. Hoodbhoy and L.S. Kisslinger, Phys. Lett. 146B, 163 (1984).
5. P. Mulders, Nucl. Phys. 459A, 525 (1986).
6. R.L. Jaffe, Phys. Rev. Lett. 38, 195 (1972); A.T. Aerts et al., Phys. Rev. D 17, 260 (1978).
7. E.L. Lomon, AIP Conf. 97, 78 (1983).
8. R. McKeown, Phys. Rev. Lett. 49, 1033 (1980).

# NUCLEAR FRAGMENTATION, PART I
# PROTON-NUCLEUS COLLISIONS AT HIGH ENERGIES

Andrew S. Hirsch, Purdue University,
West Lafayette, IN 47907
John Molitoris, Lawrence Livermore National Laboratory
Livermore, CA 94550

Abstract: The features of p-nucleus collisions leading to the production of nuclear fragments are briefly reviewed. Emphasis is placed on what is known and what is unknown experimentally.

When a proton of incident energy exceeding about 1 GeV collides with a large target nucleus, such as xenon, nuclei of up to about 1/3 the target mass ($A_T$) become likely reaction products. This has been known for over three decades[1] and has been studied extensively using both emulsions[2] and radiochemical techniques.[3] Counter experiments have made detailed and comprehensive examinations of these nuclear fragments[5,6,7,8] although the vast majority of these have been inclusive in nature. It has been clearly established that fragmentation is a high energy process with a threshold of about 1 GeV for incident protons[8] (fig. 1), and a high charged particle multiplicity indicative of a central collision. Above about 10 GeV, the typical fragment cross section enters the limiting fragmentation region where it is independent of energy up to the highest energies studied, 350 GeV.[7] Despite the great body of experimental data that now exists, the production mechanism of nuclear fragments by high energy protons remains unclear. Processes such as evaporation[9], cold fracturing[10], and a phase transition (gas to liquid) near the critical point[7] have been proposed to account for the systematics of the data.

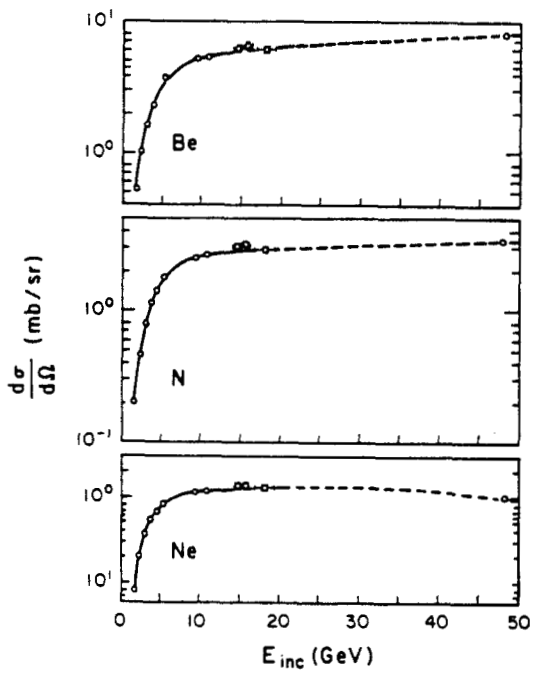


Fig. 1: Fragment cross section vs. incident energy. Solid curve is fit to the data from 1-20 GeV (AGS data). The point at 48 GeV was obtained at Fermilab, Ref. 7.

Fragment kinetic energy spectra are characterized by a Maxwell-Boltzmann like shape, although they tend to be broader than a single MB spectrum (fig. 2). The peak in the kinetic energy spectrum for a fragment such as carbon produced from p-xenon collisions occurs at about 2 MeV per nucleon, and thus a significant number of fragments emerge with very small kinetic energies. Studies of the spectra indicate that the Coulomb energies involved are small when compared to the tangent sphere value of the fragment and the target minus fragment system. A possible interpretation of this fact is that fragmentation is a multibody breakup involving the entire volume of the disassembling system. This is in contrast to a system undergoing sequential evaporation. We know from a recently completed experiment at the AGS[8] that the slope characterizing the high energy tail of the spectrum is independent of incident energy from 1 to 350 GeV, but the shape of the spectrum changes dramatically between 1 and 6 GeV. The high energy tails also indicate that all of the fragments come from a common system which has been reduced in nucleon number over the initial target.[6,7] For a xenon target, this 'remnant' sytem is some 20 nucleons lighter. By detecting fragments at both forward and backward scattering angles, the speed of the emitting system has been found to be very small, $\beta \sim .002$ for xenon. Thus, the remnant system is practically at rest in the laboratory.

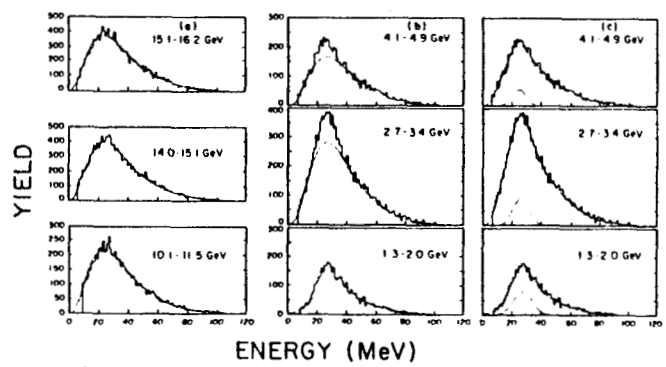


Fig. 2: Kinetic energy spectra obtained at the AGS.
a) Solid curve is the total fit
b) Fragmentation component
c) Gaussian component, Ref. 8.

The fragment mass yields have a power law fall off with fragment mass number (fig. 3). It has been shown that fragment multiplicities and cross sections for fragments in the range $2 \leq Z_f \leq 12$ are essentially the same whether these events are observed with a fragment trigger ($A_f$ =20-40) or not.[11] Thus the inclusive and coincident data are evidently the same, reinforcing the notion of a multibody breakup. Assuming that fragmentation is a multibody breakup, we can estimate that the total energy in the remnant system must have been on the order of 1 GeV.[8]

The above paragraphs summarize some of the 'facts' concerning fragmentation. Experiments have also been performed with high energy protons incident on nuclear targets with the focus on the outgoing

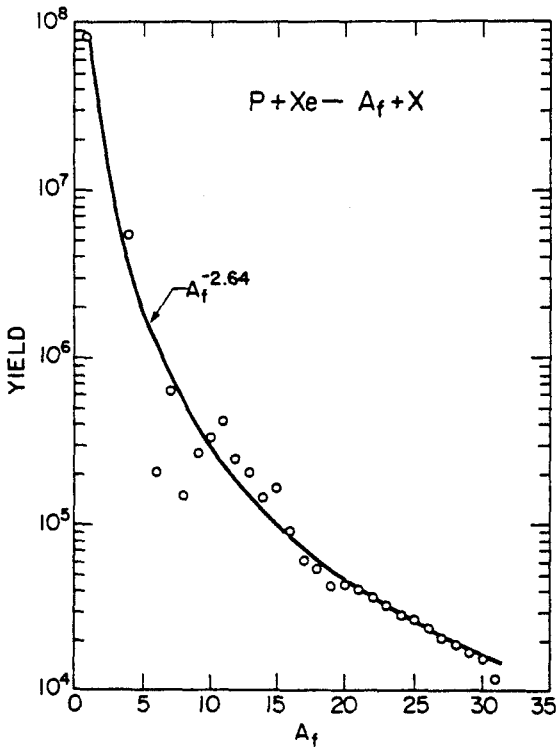


Fig. 3: Mass yield vs. fragment mass obtained at FNAL (Ref. 7).

nucleons.[12] These studies show that the incident proton produces a fast moving source of nucleons ($\beta$ ~.1-.2) which, when fully developed contains (3-5) x $A_T^{1/3}$ nucleons. We note that for a xenon nucleus, this is in good agreement with size of the remnant system. Thus, there is a hint that fragments may be produced when a moving source containing a substantial fraction of the nucleons in the original target is formed. A 4 GeV proton incident on a heavy target was found 30% of the time to produce a moving source which carried away about 75% of the incident energy. One might conjecture that the remaining 25% was left in the surviving nuclear system. This happens to agree with the estimate made above for the energy in the remnant.

A $4\pi$ experiment capable of measuring the kinetic energies of protons and heavy fragments, with charge and perhaps mass identification, could resolve many of the issues raised above. How much energy is in the remnant system? Is the decay sequential or simultaneous? Is fragment production correlated with the formation of a moving source of nucleons? These questions and many others may be addressed when exclusive experiments are performed with high energy probes on heavy nuclear targets.

## References


1. N. A. Perfilov et al., Fiz. Nauk 60, 3 (1960) [Sov. Phys.-Usp. 3, 1 (1960)].
2. J. Hudis, Nuclear Chemistry, edited by L. Yaffe (Academic, New York, 1968), Vol. 1, Chap. 3.
3. R. Wolfgang et al., Phys. Rev. 103, 394 (1956); O. Scheidemann and N. T. Porile, Phys. Rev. C 14, 1534 (1976).
4. A. M. Poskanzer et al., Phys. Rev. C 3, 882 (1971).
5. G. D. Westfall et al., Phys. Rev. C 17, 1368 (1978).
6. J. A. Gaidos et al., Phys. Rev. Lett., 42, 82 (1979).
7. A. S. Hirsch et al., Phys. Rev. C 29, 508 (1984).
8. T. C. Sangster, Ph. D. thesis, Purdue University (1986); M. Mahi, Ph. D. thesis, Purdue University (1986).
9. W. A. Friedman and W. G. Lynch, Phys. Rev. C 28, 950 (1983).
10. J. Aichelin et al., Phys. Rev. C 30, 107 (1984).
11. A. I. Warwick et al., Phys. Rev. C 27, 1083 (1983).
12. K. Nakai et al., Phys. Lett. 121B, 373 (1983); T.-A. Shibata et al., University of Tokyo Report UTPN-195 (1983).

# Nuclear Fragmentation, Part II
## Electron-Nucleus Collisions at High Energies

John D. Molitoris
Lawrence Livermore National Laboratory
Livermore, CA 94550

Andrew S. Hirsch
Purdue University
West Lafayette, IN 47907

Some observed features of $e^{\pm}$-nucleus collisions are discussed and similiarities with high energy p-nucleus collisions are outlined. A search for massive nuclear fragments ($A \geq 4$) produced in these $e^{\pm}$-nucleus collisions is proposed.

In February 1986 an exploratory experiment[1] was conducted at PEP using the TPC/2γ facility, where the Time Projection Chamber (TPC) provided the primary particle identification in electron-nucleus collisions. A small quantity of gas was bled into the beam pipe inside the TPC at the interaction region. This increased the pressure in the interaction region about two orders of magnitude and was sufficient to increase the incidence of target beam gas events well above that of the residual gas. Although deuterium, argon, and xenon were used, only some features of the $e^{\pm}$+Xe collisions will be discussed here. The analysis of this data is still in a very preliminary state.

The $e^{\pm}$+Xe data had a significant number of events with large proton and deuteron multiplicities. The energy deposition (ν) in these events typically ranges from about 6 to 10 GeV with $Q^2<0.1$ GeV$^2$ and $x<0.01$. Figure 1 shows one of the most spectacular events in the $e^{\pm}$+Xe data. The left hand side of the figure shows an end-cap projection of the charged particle tracks and the right hand side shows the same tracks folded in φ. This event has 4 deuterons and 9 protons in the TPC and the highest deuteron and proton multiplicities of all the data. The kinematic variables take on the values: $Q^2=0.07$, $x=0.003$, and $\nu=10$ GeV. A plot of the rapidity (y) vs transverse momentum ($p_\perp$) is shown in figure 2, where $\langle y\rangle=0.146$ and $\langle p_\perp\rangle=0.55$.

These high multiplicity events leave such questions unanswered as the source of the deuteron production and the mechanism which produces the many fast protons. Such questions may be answered by further analysis of the TPC data, but that data cannot determine what happens to the remainder of the nucleus. The energetic protons and deuterons account for up to 13% of the target mass, which leaves most of the nucleus behind. A complete experiment should record the energetic protons and deuterons as well as the subsequent decay of the target remnant. This could not be done in the exploratory run at PEP as any massive nuclear fragments were stopped in the thick beam pipe and vertex detector of the TPC. In addition to the relationship between the remnant and the observed high energy nucleon and deuteron yields, it is important to understand how the energy deposited by the incident electron in the nucleus affects the target remnant. This requires that the incident electron also be detected.

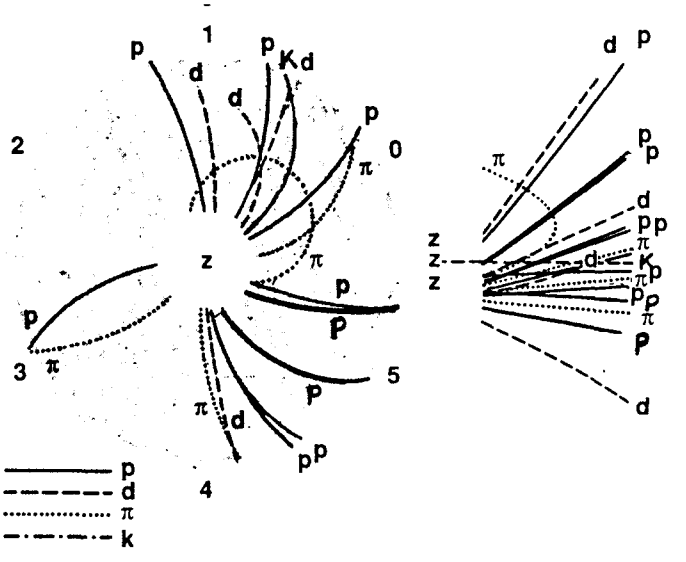


**Figure 1. 14.5 GeV $e^{\pm}$ + Xe (run 422, event 169)**

A situation similiar to the above has been noted in high energy p+A collisons. Here, Nakai et al[2] have observed energetic nucleon emission much like that

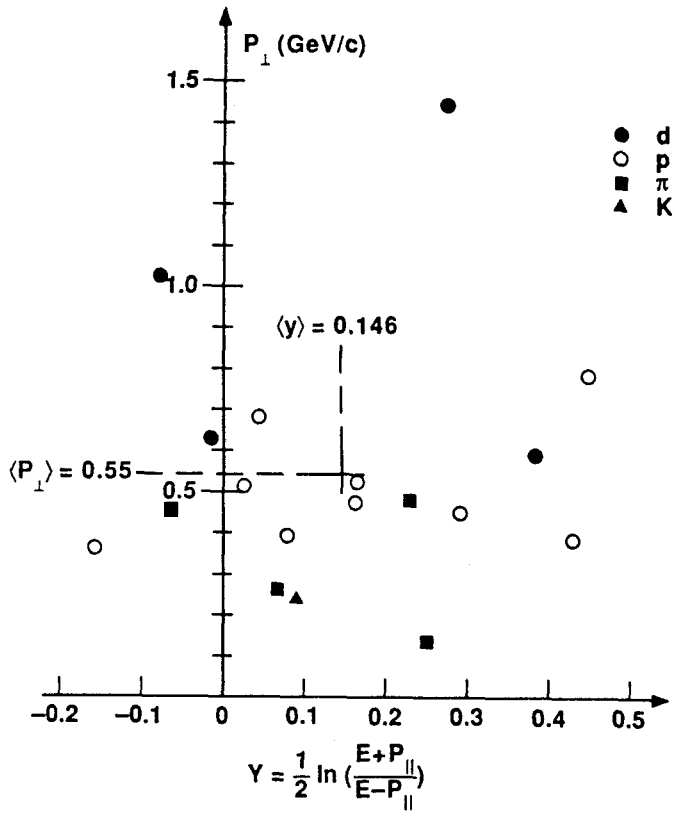


**Figure 2. $e^{\pm}$ + Xe at 14.5 GeV**

seen in the TPC data and estimate there to be about (3-5) x $A_T^{1/3}$ energetic nucleons produced per collision. This estimate is in agreement with the higher multiplicity proton events (proton multiplicity $\geq 7$) in our $e^{\pm}$+Xe data assuming that the proton and neutron multiplicities are equal and summing in the nucleons bound up as deuterons. Furthermore, Hirsch et al[3] have studied massive fragment production in p+A collisions (see Part I of this presentation) and were able to estimate the mass loss between the initial target nucleus and the remnant from the kinetic energy spectra of the fragments. The mass difference determined by Hirsch et al is also in good agreement with the total mass of the fast nucleons observed by Nakai. This and other common features of the two p+A measurements allowed Hirsch to draw a connection between high multiplicity energetic nucleon emission and massive fragment production[3].

As Nakai et al[2] only measured the fast nucleon component and Hirsch et al[3] only measured the fragmentation of the remnant system, a definitive experiment detecting both processes in coincidence has yet to be performed. Furthermore, neither measurement detected the incident proton, so the energy deposited in the nucleus was not well known. Whether or not the energetic nucleons observed in $e^{\pm}$+Xe collisions at PEP are related to massive fragmentation of the remnant nucleus has yet to be determined. Presently, such a study would be unique to PEP due to the projectile and bombarding energy. Also, the proposed detector scheme at a PEP nuclear physics interaction region[4] would allow an exclusive measurement to be performed (described below).

Independent of any results in p+A collisions, one would like to study the behavior of the remnant nucleus in $e^{\pm}$+A collisions and its dependence on the various kinematic variables. Assuming that the remnant does break up into massive fragments, it would be interesting to determine fragment production as a function of $\nu$ for fixed values of $Q^2$. While it is most probable that the characteristics of target fragmentation are only functions of $\nu$, one should keep an open mind concerning the dependence on other kinematic variables, i.e. $Q^2$. For example, one might conceive that the later stages of fragmentation might "remember" the mode of initial energy deposition. Very low $Q^2$ events where the virtual photon appears hadron-like to the nucleus might be different from true deep-inelastic events ($Q^2>1$) where one pictures the formation of a string whose length scale may be comparable to nuclear dimensions.

We can make a rough estimate of the coincident counting rate by taking the deep inelastic cross section per nucleon $d^2\sigma/d\Omega_e dE'$ from the parametrized structure functions, and making the usual assumption that the nuclear cross section is the incoherent sum over the nucleons. This gives the inclusive cross section for a given energy deposition $\nu$, and $Q^2$. To get the coincident cross section where one also measures a fragment with $A\geq 4$, we note that in the p+A work (ref. 3), the fragment cross section ($A\geq 4$) was ≈0.3 of the geometric cross section. Thus, taking the factor of 0.3, a total heavy-ion telescope coverage of 0.5 sr, and assuming isotropy of fragment emission, we find rates of >3Hz for $0.001\leq Q^2\leq 1$ and <1 Hz for $1\leq Q^2\leq 5$. This results from integrating over the electron scattering angle range $0°<\theta<11°$ (realizable with the proposed septum spectrometer for the nuclear physics region at PEP[4]) and $\nu$=5.5-14.5 GeV. We have assumed a luminosity of 1.5 x $10^{29}$ cm² $sec^{-1}$ for Xe.

This is a multifaceted experiment and can be performed in three phases. Central to the experiment is the implementation of a warm gas jet target in PEP with the capability of using heavier gases (i.e. Ar, Kr and Xe). It is also important that the target allow solid state detector arrays to be placed in close

proximity to the gas jet with no obstructions. Solid state detector telescopes have excellent Z and energy resolution and have been used successfully by Hirsch et al[3] to detect heavy fragments from p+A collisions. It would be advantageous to have the solid state detector arrays subtend a reasonably large solid angle, as the fragmentation cross section is not known and difficult to estimate theoretically. With just the solid state detector telescopes, one could perform an inclusive measurement similiar to the one for p+A collisions.

A more interesting measurement and an improvement on the above would be to include a small angle spectrometer to tag the incident electron and determine $\nu$ and $Q^2$. Then any dependence of the fragment production on $\nu$ and $Q^2$ could be observed.

Finally, the addition of a $4\pi$ detector centered on the target would enable us to observe the energetic protons and deuterons seen at TPC and ascertain if there is a connection between these and fragment production.

Presently we are studying the feasibility of solid state detectors in the PEP environment. The electromagnetic field of the circulating beam is intense enough to render these detectors useless if they are placed too close to the beam or not shielded properly. Furthermore, they are susceptable to radiation damage which will continually degrade their energy resolution and (again) if not shielded properly, the signal can be swamped by synchrotron radiation. We hope to test some of these effects on the solid state detectors in fall 1987, when PEP will be operated for high energy physics. A simple apparatus could be incorporated into the beam line which could move the detector array toward and away from the beam. The effectiveness of various foils to block the electromagnetic field could also be investigated. Before this is done, a study of the solid state detectors' outgassing properties in high vacuum must be performed as they will be coupled directly to the PEP vacuum.

## References


1. F. S. Dietrich, S. O. Melnikoff, and K. A. Van Bibber, "An Exploratory Gas-Target Experiment at PEP using the TPC/2γ Facility," UCRL preprint 94764, June 1986.

2. K. Nakai et al, Phys. Lett. 121B, 373 (1983); T.-A. Shibata et al., University of Tokyo Report UTPN-195 (1983).

3. A. S. Hirsch et al, Phys. Rev. C 29, 508 (1984)

4. K. A. Van Bibber, (contribution to this workshop).

# A FRESH LOOK AT BOSE-EINSTEIN CORRELATIONS

Werner Hofmann
Lawrence Berkeley Laboratory, University of California, Berkeley, California

Recent experimental data on Bose-Einstein (BE) correlations between identical bosons are reviewed, and new results concerning the interpretation of the BE enhancement are discussed. In particular, it is emphasized that the classical interpretation of the correlation function in terms of the space-time distribution of particle sources cannot be directly applied to particle production in high energy reactions.

Bose-Einstein (BE) correlations between like-sign pions, also known as the GGLP effect, have first been observed over 25 years ago and have been of continued interest since[1]. In this paper, I will summarize recent progress in our understanding of the BE effect. First the "classical" BE effect and its interpretation is summarized. Next, I will show that the classical description is not appropriate for high-energy reactions, and will point out where modifications are required. Following is a review a experimental data and a discussion of experimental problems which complicate the study of BE correlations, and some concluding remarks.

The classical "setup" to study BE correlations is indicated in Fig. 1: given a (large) number of fixed, identical, incoherent ("chaotic") pion emitters with lifetime $\tau$ and a spatial distribution $\rho(\mathbf{r})$ (with a characteristic width R), plus two distant detectors looking for the simultaneous emission of two identical pions with four-momenta $p_1 = (E_1,\mathbf{p}_1)$ and $p_2 = (E_2,\mathbf{p}_2)$. For any pair of emitters, there are two ways for the particles to propagate to the detectors, and those two amplitudes interfere.

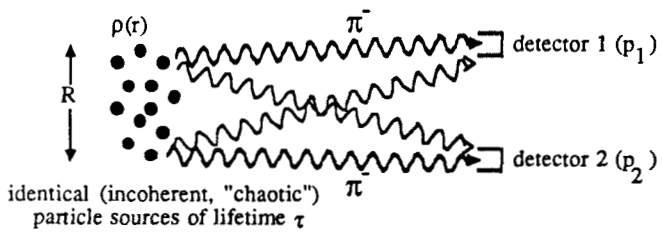


Fig. 1. Amplitudes interfering in the creation of the Bose-Einstein enhancement for identical bosons

Summing over all pairs of emitters, it is easy to show that the resulting two-particle correlation function C is essentially the square of the four-dimensional Fourier transform of the (normalized) distribution $\rho(r) = \rho(\mathbf{r},t)$ of emission points[2,3]:

$$C = \sigma^{(2)}(p_1,p_2) / \sigma_0^{(2)}(p_1,p_2) = 1 + \{\int d^4r\, \rho(r) e^{iqr}\}^2 \qquad (1)$$

with

$$q = p_1 - p_2 = (q_0,\mathbf{q})$$

Here $\sigma^{(2)}(p_1,p_2)$ denotes the measured two-particle cross section, and $\sigma_0^{(2)}(p_1,p_2)$ stands for the two-particle cross section in the absence of BE symmetrization. Since all sources are assumed to have identical lifetimes, the Fourier transform factors into a term depending only on $q_0 = E_1 - E_2$ and a term depending on three-momentum difference $\mathbf{q} = \mathbf{p}_1 - \mathbf{p}_2$: $C = 1 + |f(\mathbf{q})g(q_0)|^2$. For large $\mathbf{q}$ or $q_0$ the integral vanishes and we obtain C = 1; for small momentum differences C rises and reaches C = 2 for $\mathbf{q} = q_0 = 0$. In other words, BE statistics predict that identical bosons will be preferentially emitted in the same quantum state, i.e. $|q|\,R < 1$ and $q_0\,\tau < 1$ (we use $\hbar = c = 1$ everywhere). Since the correlation function C(q) is rather insensitive to details of the distribution $\rho(r)$ — it is e.g. virtually impossible to distinguish a gaussian distribution in space from a group of emitters arranged on the surface of a sphere — experiments are typically limited to the determination of R and $\tau$. In case the events exhibit a preferred axis, such as in $e^+e^-$ annihilation into jets of hadrons, one can make futherstatements concerning the shape of the distribution of emitters ("spherical" or "cigar-like" or "pancake-like") by studying the effective size as a function of the angle between $\mathbf{q}$ and the event axis.

At a first glance, the interpretation given by eqn. (1) works extremely well: considering e.g. two rather different pion sources, namely heavy ion collisions at 1.8 GeV/nucleon[4] and $e^+e^-$ annihilations at 29 GeV cms energy[5], we find in both cases a two-pion correlation function which is constant for large momentum transfers, and rises for small momentum differences (Fig. 2). For the heavy-ion system, the correlation length of about 70 MeV/c translates into a characteristic source size of ≈3 fm — just about the size of the composite nuclear system — whereas for $e^+e^-$ annihilation the enhancement extends over a larger range in $\mathbf{q}$, resulting in an effective source size of about 0.7 fm, consistent with the expected range of the confinement forces responsible for particle production.

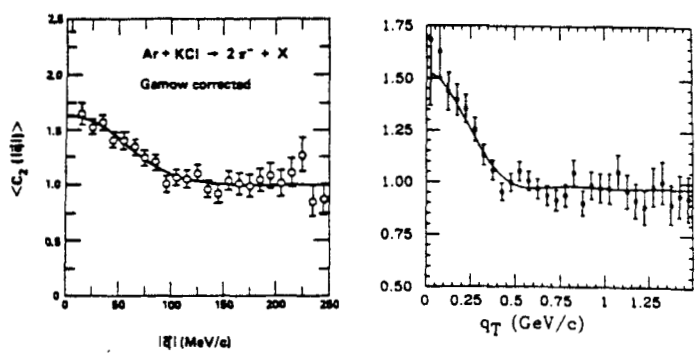


Fig. 2. (a) Two-pion correlation function measured in Ar + KCl collisions at 1.8 GeV/Nucl, as a function of the momentum difference |q| [4]. (b) Two-pion correlation function obtained in $e^+e^-$ annihilation at 29 GeV cms energy[5], as a function of $q_T$, the component of $\mathbf{q}$ perpendicular to the total momentum of the pion pair.

However, several authors[2,6,7] have recently pointed out that eqn. (1) is not appropriate to describe BE correlations among particles produced in high energy reactions. As we shall see, several of the basic assumptions are violated: 1) particle sources are typically not

at rest, but move with high velocity with respect to each other; 2) because of this motion, the spectra of different emitters (as observed in a common frame, such as the lab frame) will not be identical; 3) for eqn. (1) to hold, the spectra should be approximately constant over a range $|q| \approx 1/R$; however momentum spectra in $e^+e^-$ reactions, e.g., show strong variation over a range of a few 100 MeV. Finally one may question if the different emitters are actually incoherent.

In order motivate these statements and to show how the interpretation of BE correlations has to be modified to suit high-energy reactions, I need to discuss the present model of the space-time evolution of particle production in high-energy reactions[8], as it has evolved over the last decade or so. I will use $e^+e^-$ annihilation as the simplest example. At t=0, a quark and an antiquark are created from a virtual photon (Fig. 3). They recede from each other at close to the speed of light, feeding energy into the color force field which builds up between them. At early times, corresponding to short gluon wavelengths, perturbative QCD can be used to describe the structure of this color field; at later times, large coupling constants cause any perturbative treatment to break down, and we have to resort to the phenomenological picture of a color flux tube ("string"[9]) spanned from quark to antiquark. Such a string provides a linear confinement potential, in agreement with measurements and consistent with results obtained using QCD on discrete space-time lattices. The energy stored in this color field is ultimately released through the production of new quark-antiquark pairs, which screen the color field and which recombine to form colorless hadrons. Since the decay of the color field will occur on a typical time scale $\tau_0$ in the rest frame of the corresponding string segment, particle production points will scatter about the hyperbola $t^2 - z^2 = \tau_0^2$. On average, the primary quarks will propagate over a distance $\gamma\tau_0 = (\sqrt{s}/2m)\,\tau_0$ before they are confined to a hadron. We expect $\tau_0$ to be of the order of typical hadron sizes; m is a typical hadronic mass scale, $O(m_\rho)$. At PEP energies — $\sqrt{s}$ = 29 GeV — this picture implies a longitudinal extent of the distribution of particle sources of about 30 fm, as compared to a transverse extent of order 1 fm (the diameter of a flux tube).

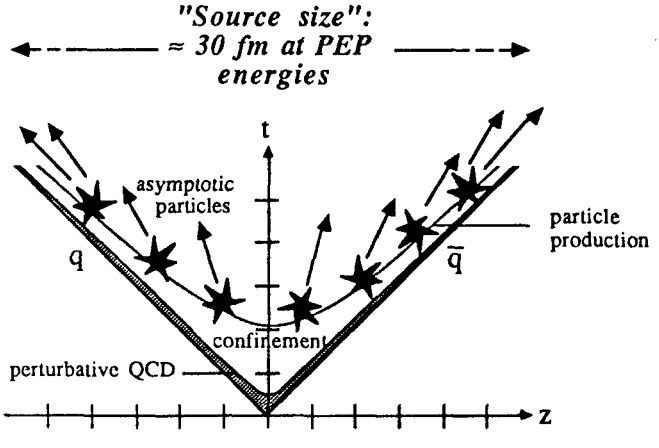


Fig. 3. Space-time evolution of particle production in $e^+e^-$ annihilation into hadrons

Since this general model relies mainly on invariance arguments, and since all models with specific dynamics constructed so far agree with it[9,10], there is considerable confidence in this picture. Why, then, is this large source size not observed experimentally ?

The key to the answer lies in the observation that for such a space-time evolution source position in space and momentum of the emitted particles are highly correlated. A source moving along the z-axis with a velocity $\beta$ will typically decay at a distance $z_{lab} \approx \beta\gamma c\tau_0$ from the origin, and the average z-component of momentum of one of its daughters will be $\langle p_{z\,lab}\rangle \approx \beta\gamma E_0$, where $E_0$ is its average energy in the rest frame of the emitter; hence $\langle p_{z\,lab}\rangle \propto z_{lab}$. This correlation implies the particles created at opposite "ends" of the event are never closeby in phase space. As a consequence, BE correlations will show no evidence of a large source size. This is most easily demonstrated in the example of two decaying "fireballs" of radius R and lifetime $\tau$ moving rapidly in opposite directions (Fig. 4). BE statistics enhances two-particle production near the diagonal $p_{z1} \approx p_{z2}$ (neglecting transverse momenta, for simplicity). We note that regions where the enhancement occurs are populated by particle pairs originating from the same fireball, never from opposite fireballs. The BE correlation length is therefore determined by the fireball size $R/\gamma$ (as seen in the lab), and not by the two-fireball separation $D \approx \gamma t$!

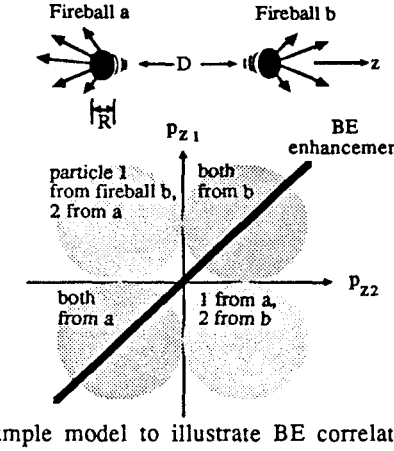


Fig. 4. Simple model to illustrate BE correlations for moving sources with $\beta \approx 1$. Lorentz boosts result in $p_z > 0$ for most particles emitted from 'b', and in $p_z < 0$ for most particles from 'a'. The lower plot indicates the resulting two-particle density. In the region of the BE enhancement, $p_{z1} \approx p_{z2}$ (indicated by the black band), both particles tend to stem from the same fireball.

For the more general case of $e^+e^-$ jets, it is easy to show that each of the emitters indicated in Fig. 3 will spread particles over approximately $\pm 0.7$ units in rapidity $y = (1/2)\log(1+\beta_z/1-\beta_z)$, centered at the rapidity of the emitter[11] (assuming isotropic emission in its rest frame). Particle distributions from different emitters will overlap in momentum space provided that the rapidity difference $\Delta y$ of the emitters is of the order of one unit or less. In a comoving frame, this in turn implies a maximum separation of the emitters $\Delta z \approx \tau_0 \sinh(\Delta y) \approx \tau_0$. In such frame, the BE correlation length both in longitudinal momentum difference and in energy difference is therefore of order $1/\tau_0$. The equality of space and time scales is a natural consequence of the covariant description. The correlation length in transverse direction is determined by the flux tube diameter, which is of the same order as $\tau_0$. Since the BE correlation length thus is similar for q-vectors parallel and

perpendicular to the jet (= z) axis, we would thus expect the distribution of particle sources to appear roughly spherical, and no cigarlike with a large ratio of major to minor axes, as one might naively expect based on Fig. 3.

More detailed studies[2,6] confirm these features: one finds that

- the correlation function C depends mainly on the (invariant) square of the four-momentum transfer $Q^2 = -q^2 = (p_1-p_2)^2$, and hence cannot be represented in the form $C = 1 + |f(q)g(q_0)|^2$
- the apparent source size, determined from the correlation length in $Q^2$, is of order $\tau_0$
- the source appears essentially spherical
- the measured source size is almost independent of the cms energy and the momentum of the pion pair

Let me briefly discuss one explicit implementation of BE effects - a modification of the Lund hadronization model[9] proposed first by Andersson and myself[6], and later studied in detail by Artru and Bowler[12]. The basic idea is simple: consider a typical space-time diagram à la Lund[9] for particle production via string decay into quark-antiquark pairs (top diagram in Fig. 5). In this scheme, break-up points of the string uniquely determine particle momenta; the energy of particle is proportional to the distance between the production points of its quarks, and its momentum is proportional to the difference in quark production times. It is plausible that the matrix element M describing the decay of the color string is given by $M \approx e^{i\xi A}$, where $\xi = \kappa + iP/2$. A denotes the (invariant) space-time area spanned by the string. The real part of $\xi A$, $\kappa A$, is essentially the classical string action ($\kappa$ denotes the energy per unit length, $\kappa \approx 1$ GeV/fm). The imaginary part, $PA/2$, describes the breaking of the string by quark-antiquark production at a constant rate P per unit length. In order to properly symmetrize production amplitudes for final states containing several identical bosons, we need to sum over all diagrams corresponding to permutations of those particles. In the context of BE correlations between two given pions, let us consider the effect of exchanging those two pions. Swapping two particles will change the space-time area swept by the string, and hence both the amplitude and phase of $e^{i\xi A}$ (bottom diagram in Fig. 5). Given the known magnitudes of $\kappa$ and P [9], it is easy to see that the interference pattern between the amplitudes corresponding to Fig. 5 is dominated by the phase change of order $\Delta\phi \approx Q^2/2\kappa$. As a result, amplitudes interfere constructively for $Q^2 < \kappa \approx (0.4\ \text{GeV})^2$ and cause a BE enhancement at low $Q^2$, compared to an effectively incoherent superposition for larger $Q^2$. As in the classical case, C(q) reaches a limiting value $C = 2$ for $q = q_0 = 0$, indicative of complete chaoticity of the source. However, whereas in the classical case the chaoticity is built in via the assumption that emission phases vary randomly from emitter to emitter and from event to event, here the strong momentum dependence of the amplitude $e^{i\xi A}$ guarantees virtually random phases between amplitudes corresponding to different permutations of particles, unless the final state contains two pions with almost identical momenta.

I should point out here that much of our revived interest in BE correlations results from this point of view — BE correlations as a measure of multiparticle production amplitudes and their phases — as opposed to the classical geometrical interpretation, which suffers from conceptual difficulties for systems with dimensions of the order of the wavelength of the emitted particles.

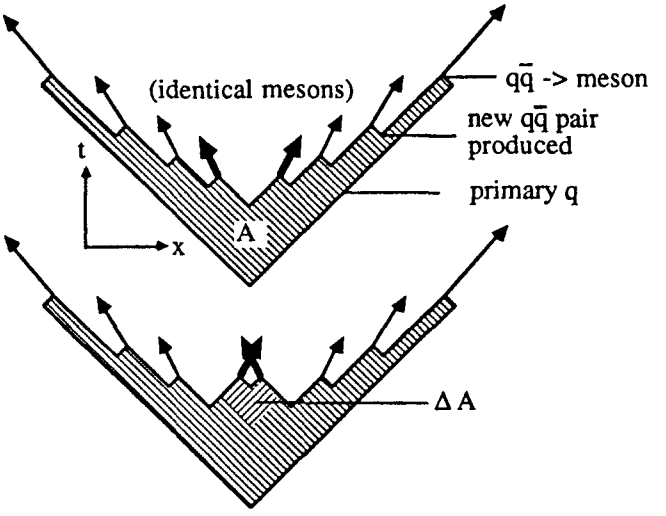


Fig. 5. Space-time structure of quark fragmentation in $e^+e^-$ annihilation, as predicted in the Lund string model. The space-time area swept by the color field is denoted by A and gives rise to the production amplitude $M \approx e^{i\xi A}$. An exchange of the two central particles results in a change of that area by $\Delta A$, with a corresponding change in amplitude and phase.

In the remainder of this paper, I will summarize relevant experimental data (with some emphasis on results from $e^+e^-$ colliders) and discuss potential drawbacks in the experimental procedures. To begin, let us see if there is indeed evidence that BE correlations depend only on $Q^2$, and not on q and $q_0$ in a factorizable fashion.

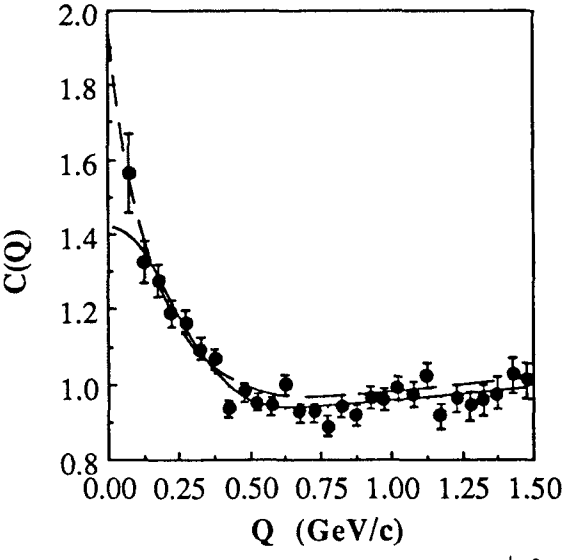


Fig. 6.Correlation coefficient C as a function of $Q = \sqrt{-q^2}$, measured in $e^+e^-$ annihilation at 29 GeV cms energy[5]. Full line: fit to the data based on eqn. (3). Dashed line: prediction of the model of ref. 6. Possible dilution of the BE correlation due to long-lived resonances is not included in the model curves. Predictions of the model of ref. 2 exhibit a very similar shape.

Fig. 6 demonstrates the that BE enhancement is certainly seen in the variable $Q = \sqrt{Q^2}$. A clean distinction between the classical form

$$C = 1 + \alpha \exp(-R_3^2 q^2) \exp(-\tau^2 q_0^2) \quad (2)$$

(where we have for simplicity used a gaussian space-time distribution of emission points; the "fudge" factor $\alpha$ will be discussed later) and the relativistically invariant form (note the different sign of the $q_0$ term)

$$C = 1 + \alpha \exp(-R^2 q^2) = 1 + \alpha \exp(-R^2 q^2) \exp(+\tau^2 q_0^2) \quad (3)$$

however turns out to be rather difficult, since $\mathbf{q}$ and $q_0$ are of course highly correlated. Basically, the distinction boils down to the question of whether there is a positive correlation for large and approximately equal $|\mathbf{q}|$ and $q_0$. Both the TASSO[13] and CLEO[14] groups claim evidence in favor of eqn.(3). For the TASSO data, the evidence is based on a global fit of the measured $C(\mathbf{q},q_0)$, which prefers eqn.(3) over eqn.(2). However, their statistical errors on the large $|\mathbf{q}|$, large $q_0$ data are such that the evidence, though statistically significant, is by no means striking. In the CLEO paper, the main conclusion — absence of a $\exp(-\tau^2 q_0^2)$ dependence, as displayed in their Fig. 3 — depends strongly on the maximum $\mathbf{q}$ (or, to be specific, $q_T$) allowed; Fig. 6 of the same paper indicates a significant $q_0$ dependence. In any case, higher statistics data would certainly be welcomed!

An essential prediction of the new class of models is that the BE correlation length is virtually independent of the reaction energy, the dipion momentum, and the angle between $\mathbf{q}$ and the event axis. Fig. 7 shows a summary of effective radii R determined using eqn. (3) for different reaction types over a wide range of cms energies; given the systematic problems to be discussed later, the data are consistent with each other and point to an effective radius of about 0.7 - 1 fm. The source shape is consistent with approximate spherical symmetry[5,13,14] (Fig. 8) and independent of the $\gamma$-factor of the pion pair (Fig. 9).

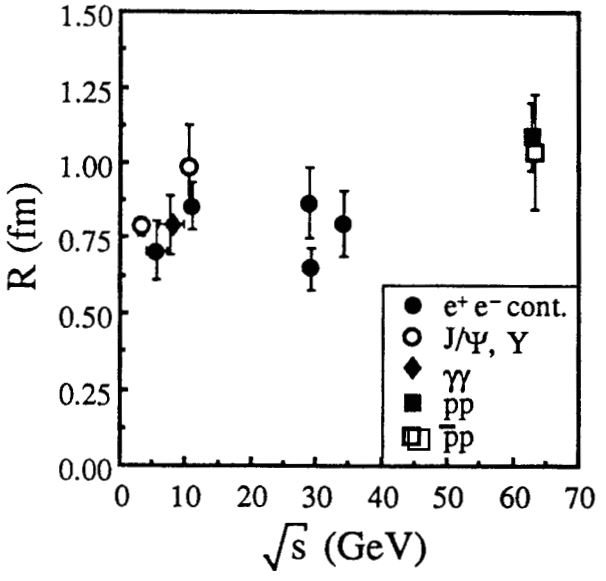


Fig. 7. Size parameter R of the pion source, determined according to eqn. (3) in various reactions, as a function of the cms energy[1,5,13,14,15].

Both in Figs. 2 and 6 we note that C does not seem to reach the predicted value C = 2 for vanishing momentum difference q of the two pions. Parameterization of the BE enhancement in terms of a gaussian (egn.(3)) typically yields $\alpha \approx 0.5$ - 0.6 instead of $\alpha \approx 1$ (after correction for particle misidentification, detection efficiency etc.); see Fig. 10. The two exceptions are BE correlations in J/Ψ decays and in two-photon collisions, for which $\alpha$ near 1 is measured. Several explanations have been put forward for the deviation of $\alpha$ from 1: BE correlations are absent for coherent particle sources[2,3], hence $\alpha < 1$ could be evidence for a partial coherence of the source.

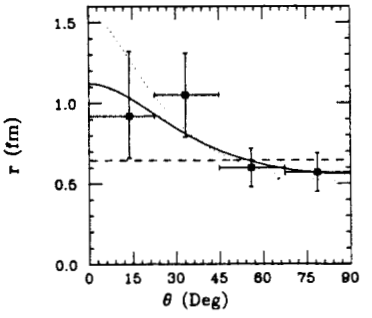


Fig. 8. Apparent size of the pion source in $e^+e^-$ annihilation at 29 GeV, determined using eqn. 3, as a function of the viewing angle with respect to the jet axis[5]. Curves are based on the assumption the the pion emitting region is a three-dimensional ellipsoid, with a transverse size $R_0$ and a longitudinal extent $cR_0$, for c=1 (dashed), c=2 (solid) and c=3 (dotted).

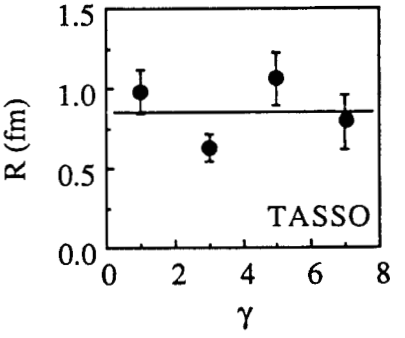


Fig. 9. Size parameter R of the pion source in high-energy $e^+e^-$ annihilation, as a function of the boost $\gamma = E_{\pi\pi}/m_{pp}$ of the pion pair[13].

A much simpler explanation is that the measured value of $\alpha$ is usually obtained from an extrapolation of data at finite $Q^2$ to $Q^2 = 0$ and is therefore sensitive to the assumptions concerning the $Q^2$-dependence of the BE enhancement. The usual gaussian shape is used mainly for convenience and has no strong theoretical motivation. In fact, the recent models discussed above[2,6] predict shapes which are much more peaked for $Q \to 0$. As shown in Fig. 6, the models are in reasonable agreement with data in the range typically covered by experiments, $Q > 50$ MeV, and nevertheless extrapolate to $C \approx 2$ for $Q \to 0$. Another reason for a non-gaussian shape is pion production by long-lived resonances such as $\omega$, $\eta$, and $\eta'$. For pions created in such decays, the effective source size is of the order $1/\Gamma_{resonance} > 20$ fm. Correspondingly, such pions contribute[16] to the BE enhancement only for small $Q < 10$ MeV/c - a region not covered by experimental data, resulting in an underestimate of $\alpha$ (Fig. 11). The absence of detectable BE

correlations for pion daughters from long-lived particles has been demonstrated experimentally using pions from $K_0^s$ decays[5].

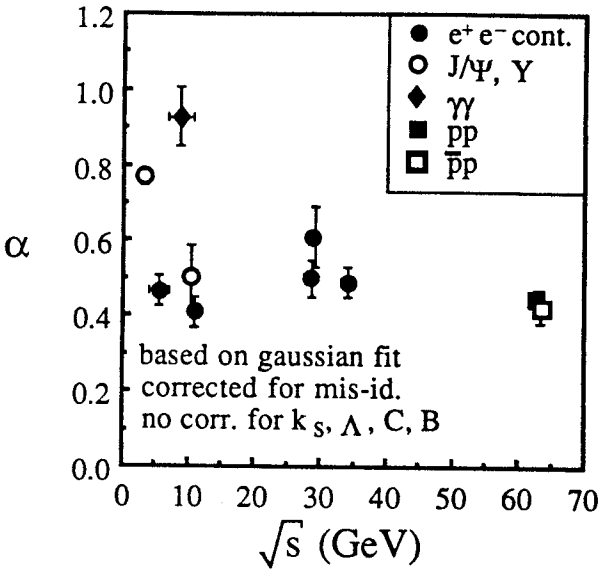


Fig. 10. Parameter a determined from fits of $C(Q^2)$ according to eqn. (3), for different reaction types as a function of cms energy[1,5,13,14,15]. Data points are corrected for particle misidentification (except for the ISR data), but are not corrected for the reduction in $\alpha$ due to pions from decays of long-lived particles.

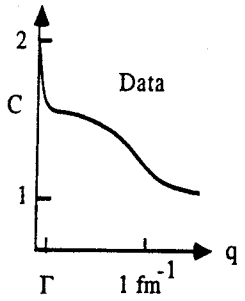


Fig. 11. Expected Q-dependence of the two-pion correlation function C, assuming that 50% of all pairs contain at least one decay product of a long-lived resonance of decay width $\Gamma$. The dotted region indicates the region typically covered by data points.

The CLEO group has attempted to correct their data for resonance effects and obtain $\alpha \approx 1$ after correction (Fig. 12). The problem there is, however, that the decrease in the effective $\alpha$ is very sensitive to the rates of $\eta$ and $\eta'$ production[17], which are not well measured and probably overestimated in current fragmentation models. It is therefore very difficult to draw any clear-cut conclusion at this point. Obviously, there are several mechanisms which explain $\alpha_{measured} < 1$ in a rather natural fashion; its seems premature to invoke partially coherent sources at this point. Clearly, more detailed data is needed.

However, major technical problems stand in the way of more precise measurements. Let us first consider the $\sigma^{(2)}(p_1,p_2)$ term in the definition of C (eqn. (1)): particle pairs in the interesting region $p_1 \approx p_2$ tend to overlap in the detector and create pattern recognition problems.

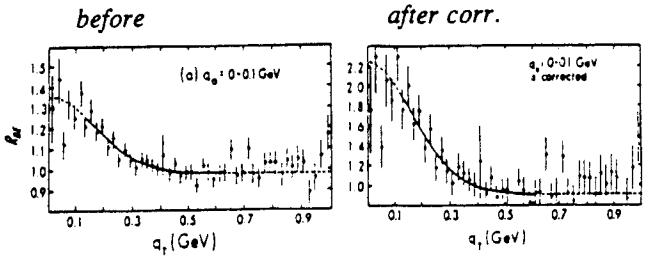


Fig. 12. Two-pion correlation function C as a function of $q_T$ (see Fig. 2), for $q_0 < 0.1$ GeV. (a) uncorrected data, (b) corrected for the fraction of non-interfering pion pairs from decays of long-lived particles. From CLEO[14]

Furthermore, since the BE effects occurs only for identical particles, some particle identification is required, otherwise the data has to be corrected for a (typically 30%) contamination from other species. Finally, one needs to remove (or correct for) pions from very long-lived particles such as $K_0^S$ or $\Lambda$, and ideally one would want to reject pions from particles with C or B quarks. These corrections introduce additional uncertainties. Finally, the rate of pairs at low Q decreases rapidly with Q, since the available phase space goes like $Q^2$. Even worse, however, are the problems caused by the $\sigma_0^{(2)}(p_1,p_2)$ term in eqn. (1). Obviously, BE effects cannot simply be "switched off" in the experiment in order to determine $\sigma_0^{(2)}$. One technique is to approximate $\sigma_0^{(2)}(p_1,p_2)$ by the product of single particle densities $\sigma^{(1)}(p_1)\sigma^{(1)}(p_2)$. This procedure removes the BE enhancement, but it also removes correlations caused e.g. by phase space constraints, superposition of different event types etc., and can result in a serious overestimate of $C(q\approx 0)$. Another solution is to use unlike particles, i.e. unlike-sign pion pairs, to derive $\sigma_0^{(2)}$. The problem here is that while natural correlations due to phase space etc. are taken into account, the unlike-sign pion sample shows many additional correlations due to resonance decays and local charge conservation. Furthermore, acceptance corrections will usually not cancel when comparing like-sign to unlike-sign pion pairs. Even if great care is taken in handling all these problems, one is typically left with a O(10%) systematic uncertainty on the parameter R for "easy" data samples - such as global BE correlations in e+e- annihilation. For more difficult samples such as pions produced in $\nu$N reactions[18] (where event characteristics such as the hadronic mass W vary from event to event) or for specific phase space region in $e^+e^-$ events, systematic errors due to the $\sigma_0^{(2)}$ determination can easily reach 50%; the systematic problems in the determination of $\alpha$ are even worse.

Let me summarize: I feel that BE correlations provide a rather interesting way to study multiparticle production dynamics; however, given our limited understanding of even the simplest cases ($e^+e^-$) and the experimental problems discussed above, I don't view BE correlations at this moment as a powerful diagnostic tool for such complicated processes as electron scattering off nuclei. Topics I would like to see studied (most likely in $e^+e^-$)

include: the precise shape at low $Q^2$, the detailed dependence on **q** and $q_0$ (or similar variables, see ref. 13), and the effect (and rates) of resonances. As to applications in nuclear physics, I feel that one first needs to understand results from simple ($e^+e^-$) systems in a quantitative way. Nevertheless, it is certainly interesting to see effective source radii measured in the current and target fragmentation region, and for different values of Bjorken x - there is always hope for a surprise!

This work was supported by the US Department of Energy under contract number DE-AC03-76SF00098. The author wants to thank M.G. Bowler and X. Artru for valuable correspondence, and acknowledges interesting and helpful discussions with G. Goldhaber, I. Juricic and M. Suzuki.

References

1. For recent reviews, see: G. Goldhaber, LESIP I Workshop, Bad Honnef, Germany (1984), and LBL-19417 (1985); G. Goldhaber and I. Juricic, LESIP II Workshop, Santa Fe, NM, 1986, and LBL-21531 (1986); and references given there.
2. M.G. Bowler, Z. Phys. C29, 617 (1985). This reference contains a very pedagogical introduction to theory of BE correlations; a more rigorous treatment is given in ref. 3.
3. M. Gyulassy at el., Phys. Rev. C20, 2267 (1979), and references given there.
4. W.A. Zajc et al., Phys. Rev. C29, 2173 (1984)
5. TPC Collaboration, H. Aihara et al., Phys. Rev. D31, 996 (1985)
6. B. Andersson and W. Hofmann, Phys. Lett. 169B, 364 (1986)
7. M. Gyulassy and K. Kolehmainen, Presented at Conf. on Ultrarelativistic Nucleus-Nucleus Collisions, Asilomar, Pacific Grove, CA, 1986
8. J.D. Bjorken, Int. Conf. on Physics in Collision, Stockholm, Sweden, 1982, and FERMILAB-Conf-82/42-THY (1982)
9. B. Andersson et al., Phys. Rep. 97, 33 (1983); X. Artru, Phys. Rep. 97, 1 (1983)
10. G. Marchesini et al., Nucl. Phys. B181, 335 (1981)
11. E.L. Berger, Nucl. Phys. B85, 61 (1975)
12. X. Artru, M.G. Bowler, Oxford-NP 79/86 (1986), submitted to Z. Phys. C
13. Tasso Collaboration, M. Althoff et al., Z. Phys. C30, 355 (1986)
14. CLEO Collaboration, P. Avery et al., Phys. Rev. D32, 2294 (1985)
15. AFM Collaboration, T. Akesson et al., Phys. Lett. 129B, 269 (1983)
16. P. Grassberger, Nucl. Phys. B120, 231 (1977)
17. M.G. Bowler, Phys. Lett. 180B, 299 (1986)
18. EMC Collaboration, M. Arneodo et al., Z. Phys. C32, 1 (1986)

# Development of a Warm Gas Jet Target for PEP

John D. Molitoris and Karl A. Van Bibber
Lawrence Livermore National Laboratory
Livermore, CA 94550

## Abstract

We are presently involved in a feasibility and design study of a warm gas jet target system for PEP. Our aim is to construct a low throughput system which will produce a target of dimensions less than 1 $cm^3$ with areal densities in the range $\sim 10^{-8} - 10^{-10}$ $g/cm^2$.

## Introduction

Warm gas jet targets (WGJT) have been used successfully in experiments at Fermi National Accelerator Laboratory (FNAL) and Brookhaven National Laboratory (BNL)[1,2] and have been found to be reliable for long periods of time. In fact, the implementation of a WGJT at FNAL was motivated by the previous use of an unreliable cold target system[2]. WGJT's work well for a wide range of gases and cost much less than a cold target system due to the lack of a liquid nitrogen handling mechanism. In view of this, we are using the Purdue WGJT system[1] as a model for an internal target for PEP.

The PEP base vacuum is typically $\sim 3 \times 10^{-9}$ torr and is maintained by ion pumps built into the PEP beam line. Any internal target system implemented in PEP must be able to locally confine the gas to a high degree and recover the PEP base pressure in as short a distance as possible both upstream and downstream from the target. Such increases in the base pressure not only do not add to the effective target thickness, but serve to decrease the lifetime of the recirculating beam. A schematic of such a system is shown in fig. 1. Here the flow is directed through a nozzle into a receiver vessel which pumps out most of the gas. A well defined jet matched to a tight orifice on the receiver volume keeps backstreaming from the receiver into the target volume to a minimum. Most of the gas that does not make it into the receiver is pumped out by the first evacuation stage. This section is conductance limited from a second stage which incorporates more pumps and is further conductance limited from the main ring of PEP. Beyond the second pumping stage the PEP evacuation system must be able to maintain an acceptable vacuum.

Very stringent conditions are imposed on any target system coupled directly to the PEP beam line. One

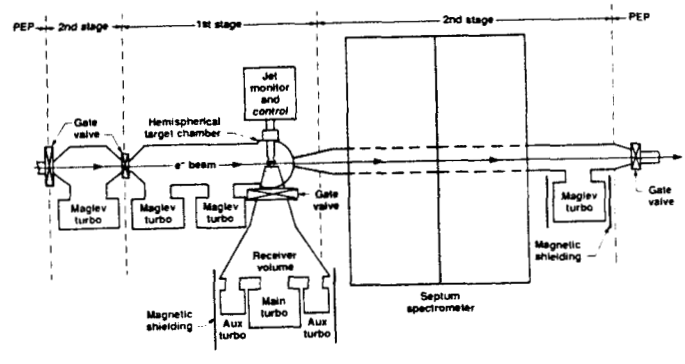


Figure 1. Schematic of a gas jet target system. The gas flows from some inlet volume through a nozzle and into the receiver. Most of the gas is pumped out through the reciever.

major criteria is that the outgassing of heavy hydrocarbons (A>50) be negligible. Figure 2 is a spectrum from our residual gas studies of the PEP vacuum which shows that for A>50 there are only three mass peaks (even on the most sensitive scale). These peaks represent benzene ($C_6H_6$) and two other trace gases (in the 50 to 60 a.m.u. mass region). For A<50 a.m.u. similiar scans show carbon monoxide (CO), carbon dioxide ($CO_2$), nitrogen ($N_2$), water vapor ($H_2O$), hydrogen ($H_2$) and argon (Ar) to be present in the ring. The condition on heavy hydrocarbons makes it difficult to use most conventional high throughput pumps in the target chamber, so we are presently investigating the possibility of using specially modified magnetically levitated turbomolecular pumps which are backed by a dry pumping system to maintain the vacuum in the target chamber. Pumps in the receiver volume (see fig. 1) are highly conductance limited from the PEP vacuum (by the receiver oriface) and can be sectioned off by two gate valves (one close to the oriface and one at the throat of each pump). Therefore these pumps may be

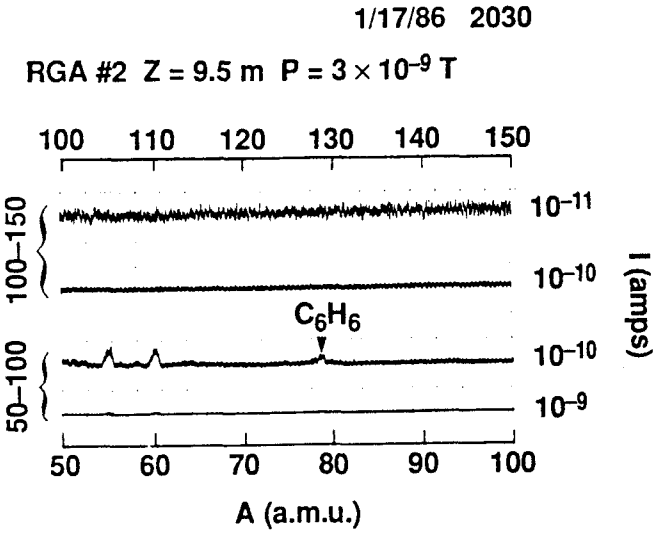


Figure 2. Mass spectrum of the PEP vacuum taken with a Residual Gas Analyzer (RGA). Scans are shown on two sensitivity scales for the mass ranges 50-100 a.m.u. and 100-150 a.m.u.

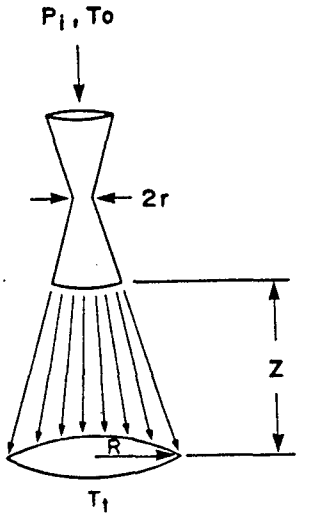


Figure 3. Schematic of a de Laval nozzle and jet. $P_i$ and $T_o$ are the input pressure and temperature in °K of the target gas. Z is the length of the jet and R is its radius at beam intersection. ( From ref. 1).

conventional turbo molecular pumps, but with some modifications and a coldtrapped backing system.

Operation of a WGJT in PEP requires areal densities ≈ $10^{-8}$ - $10^{-10}$ g/cm² with as low a throughput as is feasible. Low throughputs (<0.01 torr-ℓ/sec) simplify the pumping scheme and reduce the overall cost of the system.

Although an actual WGJT system will incorporate the features of this schematic, it will probably look much different due to detector placement and other factors. Crucial to the design of any such system is the nozzle which produces the gas jet target.

## Nozzle Considerations

A gas jet is usually produced by an axially symmetric converging-diverging nozzle, where the gas passes through a converging entry section and a diverging exhaust section (see figure 3). The constriction where these sections meet is the orifice which governs the throughput and density of the jet. This is a de Laval nozzle and its properties are well known[3]. In particular, for the correct conditions, a subsonic flow in the entry section on passing through the orifice will change into a supersonic flow in the exhaust section. Here the flow becomes sonic at the orifice. For this to occur the receiver pressure must be below a certain critical pressure[1], but this is always true for jets flowing into a high vacuum region. On the exhaust end of the nozzle there develop rarefaction waves tending to lower the pressure of the jet to that of the receiver. Somewhere on the outer border of these waves a shock front cuts across and intercepts them (see figure 4). If the receiver pressure remains lower than that of the exhaust, these shock fronts emanate from somewhere within the nozzle. The pressure decreases across the rarefaction wave towards the interior of the jet, consequently there is a pressure gradient acting from the boundary toward the interior which makes the jet boundary curve inward. The adjustment to receiver pressure occurs via this intercepting shock outside the nozzle and is the desirable regime for operation of the target system. Within the

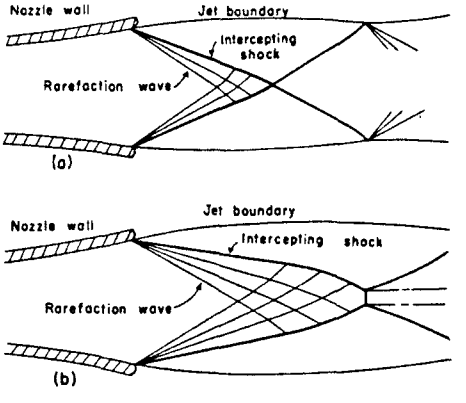


Figure 4. Shock patterns which may result in a diverging jet emitted with a pressure greater than the receiver pressure. (a) Here no shock disc is formed, while (b) illustrates the shock front being cut off by a disc perpendicular to the axis. (From ref. 3).

nozzle the boundary is defined by the diverging section. After the gas exits there is a free boundary due to the axially directed layer of subsonic gas and the low pressure region of the target vessel. As the boundary layer disperses into the target vessel, the jet gradually loses its structure and any pattern fades.

Figure 3 is a schematic of a converging-diverging nozzle and the jet it produces. Mantsch and Turkot[2] approximated the flow through such a nozzle by a one-dimensional gas-dynamics model assuming an ideal gas in steady state, isentropic flow. This model takes the actual shape of the gas jet to be known. Using the quantities defined in fig. 3, the density of gas (where the shock interfaces with the vacuum) is

$$\rho = \left(\frac{r}{R}\right)^2 \left(\frac{P_i M}{C T_0}\right) \left(\frac{2}{\gamma+1}\right)^{(1/(\gamma-1))} \left(\frac{\gamma-1}{\gamma+1}\right)^{1/2},$$

and the throughput of the nozzle is given by

$$Q = \pi r^2 P_i \left(\frac{2}{\gamma+1}\right)^{(1/(\gamma-1))} \left(\frac{2\gamma}{\gamma+1}\right)^{1/2} \left(\frac{C}{M T_0}\right)^{1/2} T_t,$$

where M is the molecular weight of the gas, C the molar gas constant (83 mbar- ℓ-mole$^{-1}$ °K$^{-1}$)and $\gamma$ is the ratio of the specific heats ($\gamma_{monoatomic}$=5/3 and $\gamma_{diatomic}$=7/5). Here r is the radius of the throat, R the radius of the jet profile, $P_i$ the inlet pressure of the gas, $T_0$ the inlet temperature, and $T_t$ the temperature of the jet. Stringfellow et al have measured the throughput and density profile of jets produced with 0.004" and 0.006" orifice nozzles, they find agreement with the above equations to be quite good[1]. However, these workers were not able to obtain a narrow jet below inlet pressures of 25 psig, which implies that they may have approached the lower limit of viscous flow for their nozzles (small Reynolds numbers, before the onset of Stokes flow) or that other effects due to the nozzle construction set in. As both of the above equations are quadratic in r and linear in $P_i$, it is wise to reduce the orifice diameter and, if necessary, accept a smaller increase in the pressure to gain a net reduction in target density and throughput.

Figure 5 shows the He gas throughput as a function of inlet pressure for various orifice sizes <0.004". For a 0.000125" nozzle one can obtain throughputs less than 0.01 torr-ℓ/sec for $P_i$<40 psi. Here we have assumed that $T_t$ is equal to $T_0$, and neglected the cooling which occurs in the exhaust region of the nozzle. As the increase of the Mach number from the throat to the exhaust port will lower $T_t$, the curves

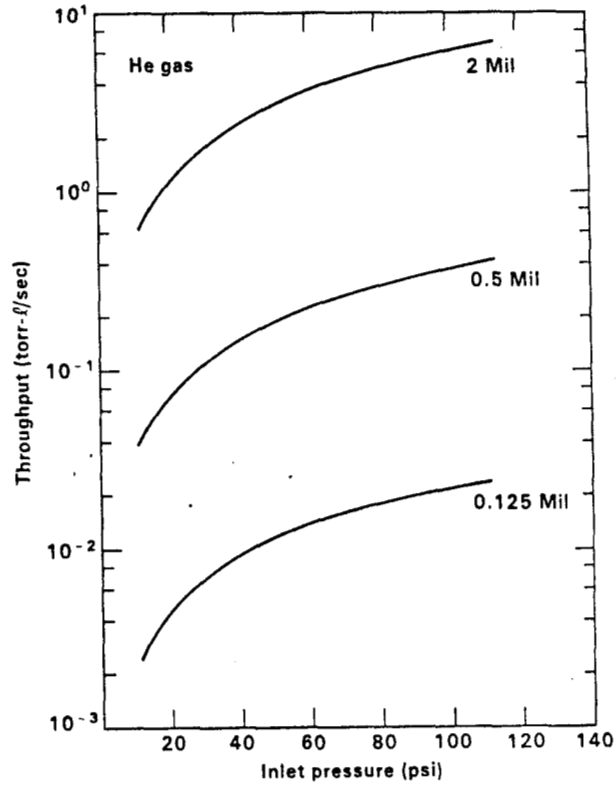


Figure 5. Throughput as a function of inlet pressure for small orifice nozzles.

in figure 5 represent upper limits on the throughput.

As figure 5 is only for He gas, fig. 6 shows how the throughput varies as a function of the mass for a fixed inlet pressure of two atmospheres. Here the throughput is shown to decrease with increasing target mass ($A_{tgt}$), so a target system which can handle the throughput of the lighter gases, should have enough pumping speed for the heavier gases. It should be noted that the pumping speed does decrease as $A_{tgt}$ increases, which tends to make the design throughput a constant.

One is constrained to use a gas target in particle storage rings by the fact that the beam is recirculated. A thicker solid target will scatter the entire beam in a few fractions of a second, hence gas targets have been explored extensively for storage rings. The density of a target should be such that the beam has a reasonable lifetime in the ring. The solid curve in fig. 7 is the maximal density allowable in PEP for a two hour lifetime of a circulating 14.5 GeV $e^-$ beam. The dashed lines are the calculated target densities for gas jets produced by an inlet pressure of two atmospheres with various small diameter orifice nozzles. Only the 0.000125" nozzle is below the allowable densities for all target masses. One would like to increase the density of the lower mass targets so

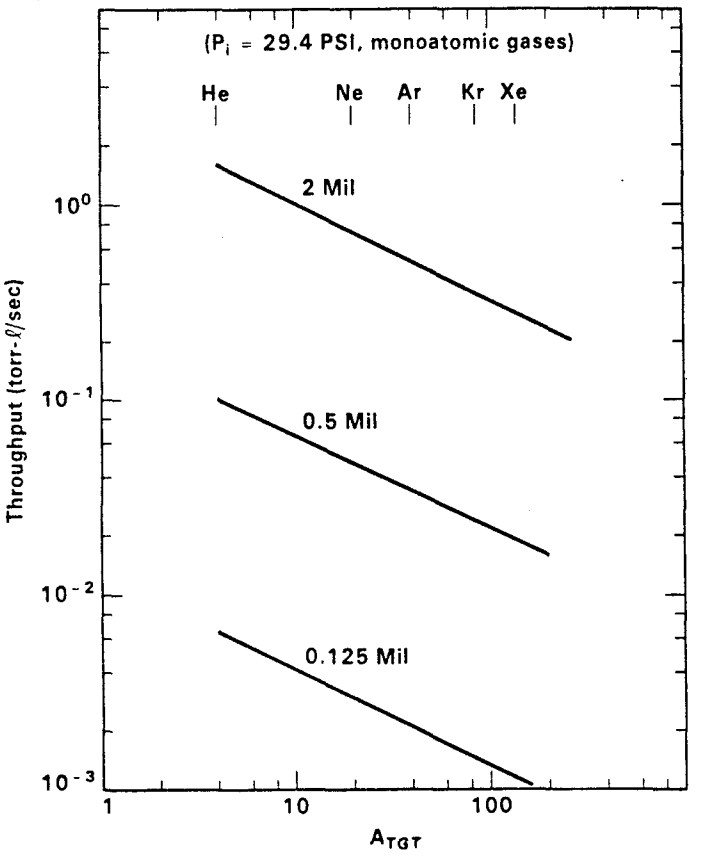


Figure 6. Throughput as a function of target mass for small orifice nozzles.

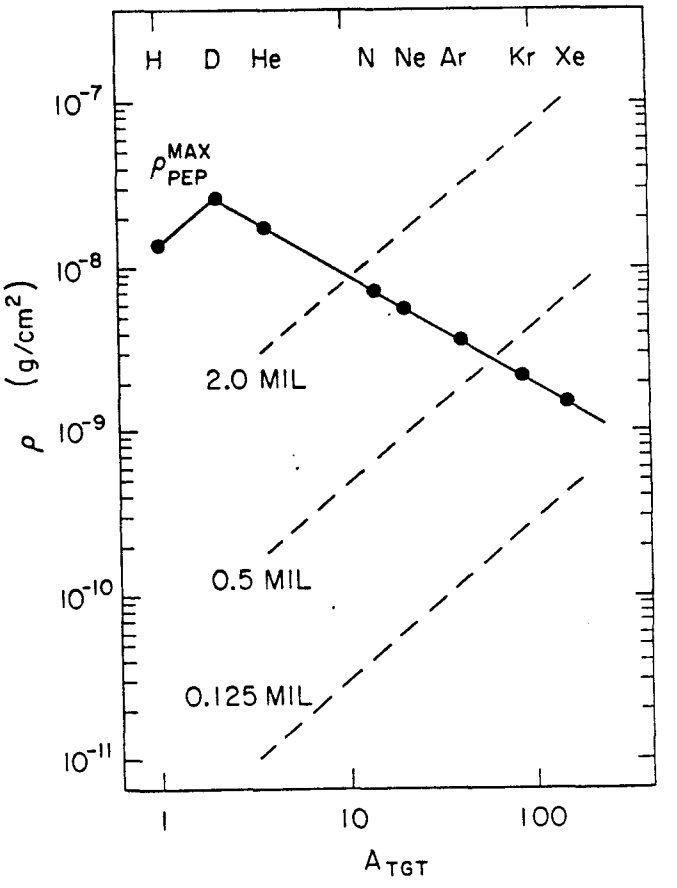


Figure 7. Allowable target densities in PEP as a function of target mass (solid line). The dotted lines are the densities provided by a fixed orifice nozzles under a constant inlet pressure of 29.4 psi.

that a higher luminosity could be obtained. This could be done by increasing the inlet pressure for low $A_{tgt}$, but for a fixed orifice $P_i$ must be increased about three orders of magnitude to track the allowable density for PEP. If one could switch to a larger orifice nozzle, $P_i$ could be varied within a more reasonable range. It must be kept in mind that by increasing the densities by either of these methods, one also increases the throughput.

## Nozzle Design and Fabrication

In order to achieve the desired throughputs and densities a nozzle with an orifice ≈ 0.000125" is required. It is not possible to bore such small diameter holes with conventional techniques, although holes as small as 0.001" can be obtained with special drills. For holes <0.001" one must use electron, ion or laser beam techniques. We are presently pursuing a laser method to obtain orifices of the desired diameter. Figure 8a shows a 0.00015" hole which was obtained with laser techniques. A cross sectional side view of the hole is shown in fig. 8b. This shape is actually ideal for a nozzle throat as it diverges smoothly after the minimum constriction.

There are various ways to construct the rest of the nozzle. One would like to guarantee the shape and surface finish of the final piece through the orifice. As it is not possible to inspect the interior of the nozzle down to the orifice, we are pursuing an electrodeposition method. Here a mandrel is carefully machined to the specifications of the interior of the nozzle. The mandrel is easily inspected and the quality of the mandrel's shape and surface finish guarantees that of the final piece ar long as the etching process is well known. The mandrel is electroplated with a thick layer of material and the exterior is machined to specifications. Finally the mandrel is etched out. As the converging section of the nozzle is typically less than a third the length of the diverging section and is less critical, it can be made by standard high precision machining techniques. Figure 9 shows conical mandrels which will be used to produce nozzle exhaust sections. These mandrels are aluminum and will be electrodeposited with nickel.

(a)

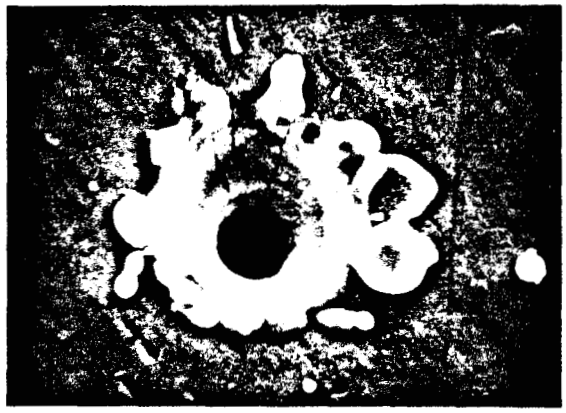

(b)

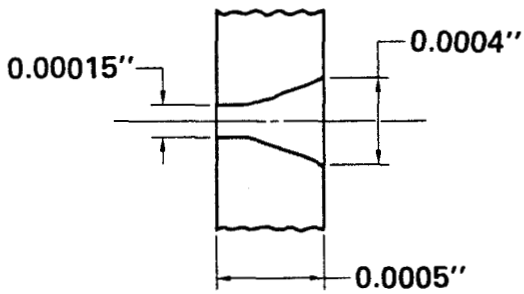


**(a) Laser drilled 0.00015" diameter orifice. Detail in (b) shows shape of interior and dimensions.**

Figure 8. (a) Photograph taken with a scanning electron microscope of a 0.00015" dia. hole bored with a Neodymium YAG laser. (b) Cross sectional view of hole.

By using the techniques described above, the converging and diverging sections of the nozzle are built separately and joined via a laser weld. The initial nozzles have orifice diameters down to 0.001". This configuration can be decoupled and smaller orifices inserted. An orifice of the type shown in figure 8a can be mated to the converging section via a circular laser weld of 0.004" to 0.005" dia and the sections rejoined. Ideally the orifice should join smoothly with the converging and diverging sections, but for these small constrictions that is not possible. This design will have a discontinuity where the orifice section mates to the converging and diverging sections of the nozzle. The effect that this 'step' will have on the flow through the nozzle should be small considering the dimensions involved to the overall length of the nozzle and exhaust port area (although this is still under study). The step should act to slightly increase the boundary layer (the subsonic flow layer which interacts with the wall of the nozzle exit) and perhaps create stream lines and a stable shock front within the nozzle itself. As the shock pattern repeats itself, the diverging section will act to control the expansion of the gas and reproduce the shock front outside the nozzle.

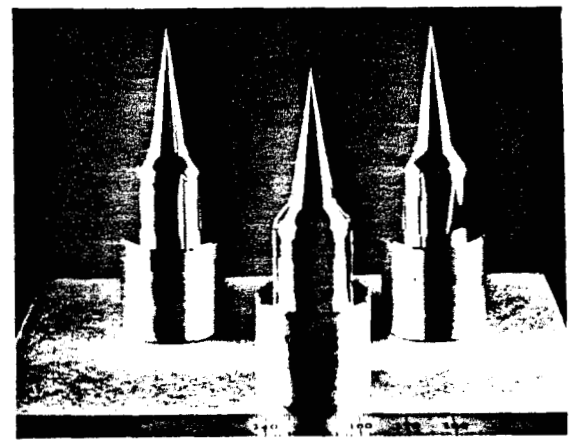

**Finish is 1L down to 0.008" dia pin. Material is electro deposited on mandrel which is etched out.**

Figure 9. Conical aluminum mandrels.

The other variables in the nozzle design are the overall length of the diverging section, the area of the exhaust duct and the shape of the diverging section. The length and the area define the geometric opening angle of the nozzle, which must be chosen as to not interfere with the flow from the orifice. The actual shape of the nozzle not only controls the expansion of the jet in a specific manner, but it should match the flow lines from the orifice and allow sufficient room for a boundary layer. Some of the shapes the diverging section can take on are shown in fig. 10. Although for axially symmetric flow a parabolic nozzle should be preferred, the conical and trumpet shapes are those mainly used in gas target systems[1,4,5,6]. In profiling studies of nozzles with the same orifice diameters and diverging section lengths, the trumpet shaped nozzle has been shown to have a slightly narrower density distribution than the conical one[4].

## Profiling Studies

At LLNL we are presently constructing nozzles using the methods described above. Our first set of de Laval nozzles will have conical exhaust sections with throat diameters of 0.001" and 0.002". These nozzles will be evaluated by studying the jets they produce and their operation in a WGJT system on loan from Purdue University. The density profile of the gas jet will be measured by deuteron elastic scattering at the LLNL 30" cyclotron. In the present set up the beam

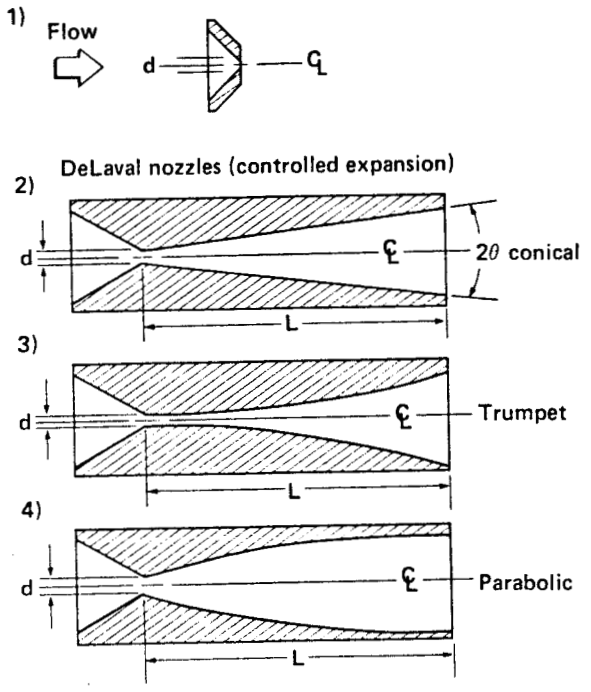


Figure 10. Axial cross sectional view of nozzles showing the various interior shapes.

and detector are kept fixed and the jet is moved perpendicular to the beam. We are interested in the density profile across the jet and how this profile changes as a function of the distance from the nozzle.

The effect of the $P_i$ on the jet will also be studied. In principle one should be able to produce a jet at input pressures lower than that used by Stringfellow et al[1]. In practice other factors may be preventing this.

Using the above profiling studies we can attempt to match the jet to the receiver opening such that the amount of gas flowing into the target vessel is a minimum. Ideally one would like to direct all of the gas jet into the receiver and leave the target chamber vacuum unaffected, but in practice this is impossible as the boundary layer begins to diffuse as soon as the jet exits the nozzle. The Purdue WGJT only directed about 80% of its throughput into the receiver. This was due mainly to the distance between the nozzle and receiver opening and the fact that they pulsed their jet. Pulsing cuts down on the overall throughput, but the jet is not well formed at the beginning and end of the pulse. Consequently, less of the gas is directed into the receiver then.

Our goal is a continuous operation WGJT that meets the above density and throughput criteria and has a nozzle receiver mating which directs >95% of the throughput into the receiver. The above studies will enable us to model and ultimately design a WGJT system for PEP.

The authors would like to thank Prof. Daniel Burshader of Stanford University and Dr. Alfred Buckingham of LLNL for enlightening discussions. We are grateful to Prof. Andrew Hirsch of Purdue University for the loan of their WGJT system and to Norman Dean and the SLAC Vacuum Group for their help and advice.

REFERENCES

1. B. C. Stringfellow et al., Nucl. Inst. and Meth. A251, 242-253 (1986).

2. D. Gross, P. Mantsch and F. Turkot, FNAL Report TM-534-0710.000 (January 1975); P. Mantsch and F. Turkot, FNAL Report TM-582-0710.000 (June 1975); P. Mantsch and F. Turkot, FNAL Report TM-586-0710.000 (June 1975).

3. R. Courant and K.O. Friedrichs, "Supersonic Flow and Shock Waves (New York Interscience, New York, 1948).

4. W. Obert, "Properties of Cluster Beams Formed with Supersonic Nozzles", 11th Symposium on Rarified Gas Dynamics, Cannes, 1978 (CEA, Paris 1978), p 1181.

5. M. Macri, "A Clustered $H_2$ Beam", in Physics with Low Energy Cooled Antiprotons (Plenum, New York, 1983) p 432.

6. J. F. Brolley, IEEE Trans. Nucl. Sci. 20 (3), 475 (1973).

# EXCLUSIVE AND INCLUSIVE REACTIONS WITH REAL AND VIRTUAL PHOTONS TO PROBE MULTI-QUARK EFFECTS

K. E. Lassila

Ames Laboratory-DOE and Physics Department, Iowa State University
Ames, Iowa 50011

and

A. Harindranath* and J. P. Vary*

Physics Department, California Institute of Technology, Pasadena CA 91125

## Abstract

We have examined many exclusive and inclusive reactions to conclude it best to project real or virtual photons on partons in a nucleus to probe the mechanism responsible for the EMC effect. Such reactions could be triggered on particles produced beyond usual (nucleon target) kinematical limits from quarks in, e.g., multi-quark color singlet structures. We show that the multi-quark fragmentation function may be measurable in the quark (QCD or real) Compton effect.

## Introduction

Deep inelastic scattering experiments on nucleons and nuclei have unambiguously established that the partons of QCD behave differently in nuclear matter than they do in an isolated nucleon.[1] To established what these differences are and the sources of these differences is an objective of future experiments for which predictions can only be made from model calculations at the present time. A specific model which has been remarkably successful in explaining this anomalous behavior is the quark cluster model (QCM).[2] In the QCM the quarks (q) in a nucleus are organized into multi-quark color singlet clusters involving groups of i = 3, 6, 9, etc., quarks. For a 3-q cluster, a critical radius $R_c$ is assumed such that clusters of 6 or more quarks are defined by the number of 3-q clusters joined by the center of mass separations $d \leq 2R_c$. This definition allows one to calculate probabilities for cluster existence and to calculate the momentum fraction x distribution for quarks in a cluster with reasonable facility and reliability.[3] One of the striking and compelling features of the QCM is the prediction of x values beyond those possible for quarks in free nucleons, i.e., $0 \leq x \leq i/3$, for an i quark cluster. Calculations have yielded excellent descriptions of deep inelastic lepton scattering (DIS) data, of the EMC effect, and of the elastic charge form factor of $^3He$.[2] Predictions have likewise been made for the Drell-Yan process and electroproduction on nuclei.[4,5] The high momentum components of quarks in clusters make unique contributions to these processes, and particularly in pre-threshold production of particles in high energy collisions with nuclear targets.[6]

From an experimental study viewpoint, the injection of nuclei into high energy electron beams or in some other way colliding nuclei with electrons and photons appears to be one of the best possible ways to study and to probe for partons with high momentum components within the nucleus. Though hadron reactions would yield larger statistics on events originating from $x \geq 1$ partons, the background problems would be horrendous. Of all reactions examined, the cleanest seems as if they will be those done with a real or virtual photon probe into the nuclear interior. Further DIS experiments are well worth doing but would, most likely, not shed new light on the source of the EMC effect. In Ref. 3, we pointed out that the QCM makes rather unique predictions for ratios of DIS experiments from different nuclear targets. If one takes the DIS cross section times the energy transfer $\nu$ divided by the Mott cross section to get the nuclear structure function $\nu W_2$ and takes data for two targets of nucleon number A and B, the ratio $V = [\nu W_2(A)/A]/[\nu W_2(B)/B]$ will show a sequence of unique steps in the $x > 1$ region. The size of these steps is predicted by the calculable probabilities for clusters, as mentioned above. Events in the region $1 < x < 2$ in the QCM will be most sensitive to 6-q clusters while events in the region $2 < x < 3$ will be most sensitive to 9-q clusters, etc. For each increase in x by unity, the ratio V will increase. Preliminary results of an experiment at SLAC apparently confirm this behavior.[7] This is the strongest possible motivation, then, for performing more sophisticated calculations for exclusive reactions to encourage more direct study of high momentum quarks in nuclei.

## Multi-Quark Fragmentation

We shall pursue the possibility that (I) the QCD Compton process and (II) Compton scattering from quarks may be the best probes for location high momentum quarks besides providing information on an interesting, previously unmeasured physical quantity, the multi-quark fragmentation function.

In Fig. 1, we depict the collision between a photon ($\gamma$) and a nucleon, with the microscopic $\gamma$-q collision enlarged within the circle. In the head-on $\gamma$-q collision, as drawn in the center of momentum (cm) frame for (I) the QCD Compton process, the final state quark $q_f$ and the gluon G go back-to-back and produce jets as

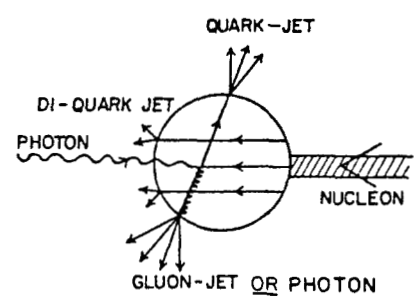


Fig. 1. The photon-nucleon (three quark cluster) collision. The photon-quark interaction is shown in the center of momentum frame with the final state quark, gluon, and diquark jets for the QCD Compton process. For the QED Compton process, the final state gluon is relabelled as the final state photon (with or without originating an EM shower).

labelled by the parent parton.[8] For (II), usual Compton scattering, as also indicated in the magnified region of Fig. 1, the final state gluon and its jet are replaced by a photon (and its resultant electromagnetic shower, if present). The dynamical part of the calculation is done in terms of the three basic QCD or QED diagrams for (I) or (II) which are shown in combined form in Fig. 2. Here, the label $\hat{s}$, $\hat{t}$, and $\hat{u}$ show the familiar s,t, and u Mandelstam channel for the $\gamma$-q interaction. With a nucleon, or 3-q cluster,

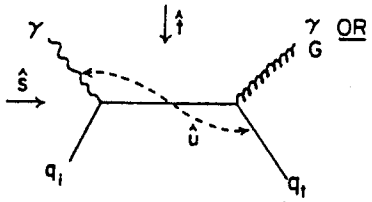


Fig. 2. The QCD Compton effect (I) for photon + quark → gluon + quark and the QED Compton effect (II) for photon + quark → photon + quark with the subprocess kinematical variables as labelled.

target the remainder of the event consists of two quarks, or a di-quark, breaking up in the target fragmentation region. The 'di-quark' (two quarks which need not be in a bound state) is still an interesting object for study because of the basic QCD information it contains. Its behavior when probed with different real and virtual photons will give $Q^2$ evolution data which is nonexistent to date.

The process in Fig. 1 is used to describe the photon-3 quark cluster interaction when the nucleon target is inside a nucleus. There is also a relatively large probability that the photon will interact with color singlet clusters of 6, 9, etc., quarks. The interaction of the photon with a 6-q cluster is depicted in Fig. 3 for (I) the QCD Compton process and (II) the QED Compton effect. Two main differences from the 3-q

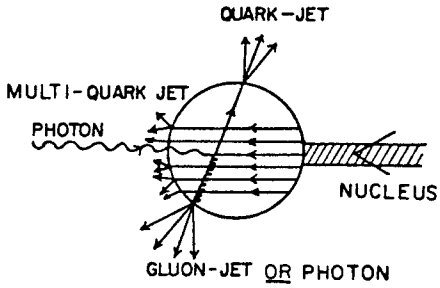


Fig. 3. The photon-nucleus collision with quark cluster structure in the nucleus. The enlarged interaction region sketched inside the circle shows the photon interacting with a six quark cluster. In (I), the QCD Compton effect, the quark and gluon go out back-to-back; in (II), the QED Compton process, the quark and photon go out back-to-back. The remainder of the six-quark cluster after the photon-quark reaction continues in the direction opposite to the incident photon and fragments as the multi-quark jet (in the case drawn, as a five-quark jet).

cluster target, as pictured in Fig. 1, stand out: The kinematic range of x is 0 to 2, and the diquark fragmentation region is replaced by five-quark break-up. This type of experiment , (I) and (II), thus offers the unique possibility of measuring multiquark fragmentation functions. Furthermore, backgrounds can be drastically reduced by selecting events coming from those quarks with large x. These events could have abnormally large total energy in the jets or a hadron in a jet with abnormally large momentum. Since the incident photon disappears completely, the projectile fragment region is very clean. Therefore, the back-to-back quark and gluon jets in (I) or quark jet with a recoil final photon in (II) can provide a trigger to tag photon-quark events with unusually high cm energy, indicating a reaction with a cluster. These events should provide a good sample of multi-quark fragmentation.

It may be possible in the future to obtain data relevant to the Q-squared evolution behavior of this multiquark fragmentation function. The five-quark recoiling object has many ways in which gluons might interact and be emitted so it is possible to have deviation from the most naive type of Altarelli-Parisi behavior.

## Calculation

Detailed mathematical expressions will not be given here nor details of the Monte Carlo procedure used for the program, some of the output of which will be discussed. An effort to mainly sketch the physics involved will be done to aid experimenters with thoughts along these lines.

Calculations involving the multi-quark portion of this investigation are highly preliminary, but the results given on photon-3 quark cluster interactions are reliable. These were done by Monte Carlo methods to produce the complete QCD Compton event in the photon-nucleon cm frame. The QED Compton results follow by changing gluon variables into photon variables and removing the fragmentation aspect of the photon, gluon.

The dynamical input is described by the three diagrams in Fig. 2. This input is supplemented by the addition of fragmentation functions appropriate for the quark, gluon, and diquark in the final state. In typical, present day experiments, the photon energy will probably be so low that the jets overlap considerably. This is no real limitation on the use or validity of the calculation unless the cm energy is so low that there is less than about 2.5 GeV available for each jet. The photon-3q cluster calculation at any rate must be done to get a reliable estimate of the background with which photon-6q cluster reactions are to be compared.

To study three color systems in reaction (I) moving separately in the cm frame, we essentially use the Field-Feynman prescription for the fragmentation of each color system. The diquark, for present purposes, is approximated as a color anti-triplet system and treated accordingly. The radiated gluon is treated as a quark-antiquark pair of definite flavor. A cascade chain or string is generated via Monte Carlo between the quark of this pair and the diquark. Also, a string of primary mesons is created between the antiquark of this pair and the original final state quark labelled $q_f$ in Fig. 2. The Q-squared dependent fractional momentum distributions for quarks in the nucleons in the target nucleus are those of Buras and Gaemers.[9] The momentum of partons created along the chain transverse to the fragmentation axis is taken as Gaussian with width 350 MeV/c. An appropriate suppression factor for strange quarks created along the chain is used. Then,

the final distributions in the lab system for the fully generated events are obtained by a Lorentz transformation along the photon direction to the laboratory system.

Probably the dominant effect of the large x parton component in the nucleus will show up in the increased cross section at large transverse momentum ($p_t$). The ratio of positive to negative pions will increase with $p_t$ also. At high $p_t$, roughly bigger than 3.5 GeV/c, the processes under discussion should dominate the old fashioned vector meson dominance terms. In Fig. 4, we show plotted the invariant cross section as a function of the transverse momentum of the gluon jet for a number of photon energies. These curves are for real photons, but the general trend stays similar for virtual photons. The gluon is produced with low rapidity

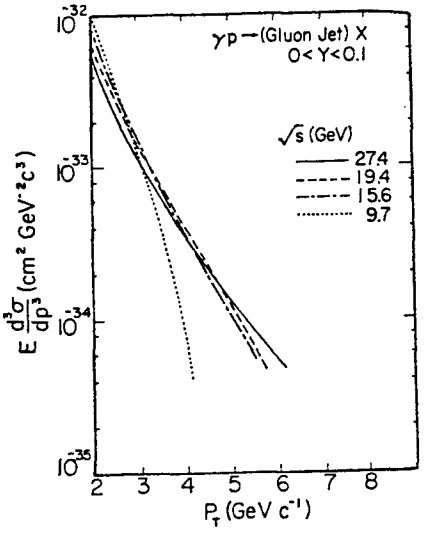


Fig. 4. Calculated invariant gluon jet production cross section as a function of transverse momentum for the QCD Compton effect on a three quark cluster. The curves are labelled by the cm energy 9.7, 15.6, 19.4, and 27.4 GeV in the photon-nucleon cm system and correspond to photon laboratory momentum values of 50, 150, 200, and 400 GeV/c, respectively.

$0 < Y < 0.1$ for each of photon energies as labelled by 9.7, 15.6, 19.4, and 27.4 GeV cm energy. These correspond to photon momentum of values 50, 150, 200, and 400 Gev/c, respectively, incident upon a nucleon. The curves can be reinterpreted in terms of expectations for collision of the photon with a six quark cluster, nine quark cluster, etc. Suppose the incident momentum is 50 GeV/c; the dotted curve will be produced in collisions with quarks that have $0 < x < 1$. The dot-dashed curve then gives the general $p_t$ dependence for events produced from quarks with $2 < x < 3$, possible in 9-q clusters; the dashed curve for events produced from quarks with $3 < x < 4$, possible for quarks in 12-q clusters; and, the solid curve corresponds in trend to the result for $4 < x < 5$. The events produced off quarks in 6-q clusters with $1 < x < 2$ would lie intermediate betweer the dotted and the dot-dash curves. The relative normalization of these curves would fall as photon energy increases, but the general trend with a longer tail in $p_t$ should be a reasonable result to expect from photon reactions with nuclei when clusters are present. The detailed calculations explicitly for these various big clusters should be completed soon because they now appear relevant since the recent SLAC NE3 experiment found events out to x values near 6.[7] For and incident photon beam of 25 GeV/c, the dotted curve gives the relative $p_t$ dependence for reactions off 6-q clusters and the dot-dash curve correspondingly off 12-q clusters.

## Discussion and Conclusions

The Quark Cluster Model has achieved considerable success in describing the ways that quarks seem to behave differently in nuclei than they do in free nucleons. Detailed comparisons and calculations now appear needed for significant further progress. To reach this goal we have begun complete Monte Carlo calculations of events expected to be produced by photons interacting with the quark clusters in nuclei. The QCM predicts more large transverse momentum events then could occur from a nucleus made of independent nucleons. We also find that the ratio of positive to negative pions will be larger if the photon is indeed interacting with clusters in a nuclear target. These predictions are a consequence of high momentum quarks in the clusters. This leads to the occurence of events well beyond the kinematic limits for photo reactions with free nucleons. Triggering an experiment on such events leads to the possibility of studying and measuring a new physical quantity, the multi-quark fragmentation function. On a free nucleon, a photon interaction with a quark leaves behind a diquark which is an interesting and legitimate object for QCD study.[10] The object left behind when a photon interacts with a quark in a six quark cluster will be five quarks rather than a diquark. An interesting reason for looking at the 5-q system is to find out to what extent it behaves as a single entity. If it does, then when it fragments as shown in Fig. 3, the QCD activity between quarks is complicated and one can enhance a sample for study by triggering on events from large x quarks. From the counting rules, then, one might expect to find a target fragmentation z distribution that is concentrated near $z = 0$ with a very high power of $(z - 1)$. Such a sample would contrast markedly with those from the diquark fragmenting when a free nucleon interacts.


## Acknowledgment

This work was supported by the U.S. Department of Energy Contract No. W-7405-Eng-82, Office of Energy Research (KA-01-01), Division of High Energy and Nuclear Physics.

## References


* On leave from Iowa State University, Ames, Iowa.

1. D. Day et al., Phys. Rev. Lett. 43, 1143 (1979); J. J. Aubert et al. (European Muon Collaboration abbreviated EMC) Phys. Lett. 123B, 275 (1983); A. Bodek et al., Phys. Rev. Lett. 50, 143 (1983).

2. H. Pirner and J. P. Vary, Phys. Rev. Lett. 46 1376 (1981); H. J. Pirner, Progress in Particle and Nuclear Physics Ed. A. Faessler (Pergamon, Oxford, 1985) p. 361; J. P. Vary, Nucl. Phys. A418, 195 (1984); C. E. Carlson and T. J. Havens, Phys. Rev. Lett., 51, 261 (1983); J. P. Vary, S. A. Coon and H. J. Pirner, Proceedings of the International Conference on Hadronic Probes and Nuclear Interactions (AIP, New York, 1985) p. 83.

3. J. P. Vary, A. Harindranath and K. E. Lassila, International Conference and Symposium on Unified Concepts of Many-Body Problems, Eds. Kuo and Speth (North-Holland, Amsterdam, 1987).

4. A. Harindranath and J. P. Vary, Phys. Rev. D, in press.

5. A. Harindranath, K. E. Lassila and J. P. Vary, "Electroproduction of hadrons from Nuclei," Phys. Rev. D, submitted for publication.

6. K. E. Lassila and J. P. Vary, "Pre-Threshold Production of the W Intermediate Boson," Proceedings of the International Conference on Neutrino Physics, Ed. E. Fowler (Purdue University, IN, 1978) p. 435.

7. University of Virginia-Cal Tech experiment, SLAC-NE3.

8. A. Ng, R. Orava and K. E. Lassila, Z. Phys. C 14 313 (1982).

9. A. J. Buras and K. J. F. Gaemers, Nucl. Phys. B 132 249 (1978).

10. U. P. Sukhatme, K. E. Lassila and R. Orava, Phys. Rev. D25 2975 (1982) and XII International Symposium on Multiparticle Dynamics, Ed. W. D. Shephard and V. P. Kenney (World Scientific, Singapore, 1982) p. 465.

# PION ELECTROPRODUCTION FROM NUCLEI AND QUARK-PION NUCLEAR INTERACTIONS

Paul Stoler
Physics Department, Rensselaer Polytechnic Institute, Troy, NY 12181*

The theory of pion photo and electroproduction is closely related to our understanding of fundamental processes involving elementary particles. At excitations below 2 GeV these reactions have provided much of our information about baryon resonances (Do-78). At higher excitations, in the scaling region they are directly related to the processes by which quarks hadronize. The study of these reactions are interesting in nuclei where one would like to learn about the influence of the nuclear environment on the elementary processes.

In the past electro and photoproduction experiments on nuclei have been strongly limitated by the parameters of existing electron accelerators, the most important of which are low energy and duty factor. The new generation nuclear physics facilities at CEBAF and PEP will complement each other in making possible programs of pion electroproduction not previously possible. CEBAF, with an eventual maximum energy of ~ 6 GeV, will cover the nucleon resonance region, through the transition to x scaling. PEP with a maximum energy of ~ 14 GeV is well suited for experiments in the x scaling and higher $Q^2$ region.

The main features of both kinematic regions which can be addressed by CEBAF and PEP are seen in Figure 1, which shows inclusive electron scattering data from SLAC.

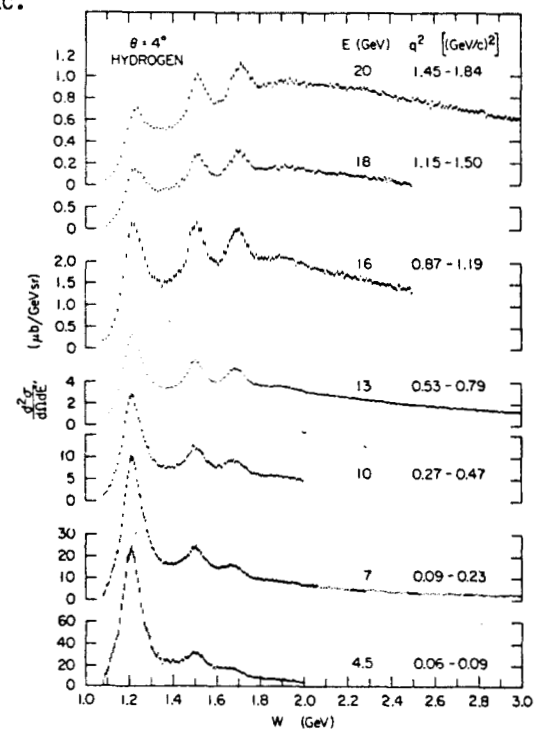


Figure 1 Inelastic electron scattering data obtained at SLAC (St-75) as a function of W for various values of Q.

In the resonance region only the delta is free from the interference of other resonances, whereas above the delta there are about 20 known resonances, all of which overlap strongly with each other. The properties of these resonances can be disentangled only from exclusive experiments involving pion electroproduction. An active program to study the properties of resonances is planned for CEBAF (Bu-87, Mu-87).

Photoproduction data on nuclei is sparse in comparison with that for the nucleon. In the resonance region nuclear programs have concentrated only on real photon experiments in the delta energy region (see e.g. St-87), and even in this energy region there have been no exclusive electroproduction experiments on nuclei. This situation will certainly change in the next several years with the arrival first of MAMI-III at Mainz, and later CW accelerators at Bates and Saclay. However only CEBAF and PEP will have enough energy to cover the entire resonance region.

Because the delta is the lowest energy nucleon excitation, is very strongly excited at low $Q^2$, and plays an important role in medium energy nuclear phenomena, one of the most actively studied subjects in nuclear physics during the past decade concerns the production and propagation of the delta in nuclei, including the absorption of the delta by the medium (Ge-83). The propagation of the pions in the nucleus is part of the problem of the propagation of the delta through the successive decay and formation of the delta due to the strong pion-nucleus final state interaction (FSI).

In the future there will be a strong interest in studying some of these problems for the higher excitation resonances. However, the problem of overlaping resonances will add to the complications in interpreting the data. A favorable energy to study may be in the region of excitation near W = 1520 MeV, where the $S_{11}$ and $D_{13}$ stand out clearly, and behave differently as a function of $Q^2$.

For example, it will be interesting to see how the width of this peak is affected by the nuclear medium as it is for the delta. Pion FSI play an important role at all excitation energies. This also will complicate the interpretation of experiments where the motivation is to learn about the initial interaction process in the nuclear medium. Examples at low and high energies respectively are the effects of medium polarization on the spin-isospin operators (Dy-86, Mu-79), and the modifications of the pion distribution involved in t-channel electroproduction in nuclei compared to the case of the nucleon (Hi-79).

Figure 2 shows the mean pion interaction length in a nucleus, obtained by a simple convolution of the elementary pion nucleon interaction with a uniform nucleon density. At the peak of the delta this length is about 0.5 fm, increasing to 2 to 3 fm at higher energies.

A more realistic picture emerges from experiments on pion nucleus scattering in the delta region performed at LAMPF (As-81). Figure 3 shows the various components of the pion-nucleus interaction which they obtained for $^{12}C$. In addition to quasi-free scattering, nuclear effects such as coherent scattering and true absorption are important at the delta peak, but decrease relative to quasi-free scattering at higher energies. It would be interesting to see how these effects evolve with increasing energy.

The effects of pion FSI in photo and electroduction are most important at the peak of the delta. They also depend upon the nuclear radius, being smallest for light nuclei. This is illustrated in Figures 4 and 5, which show the effect of final

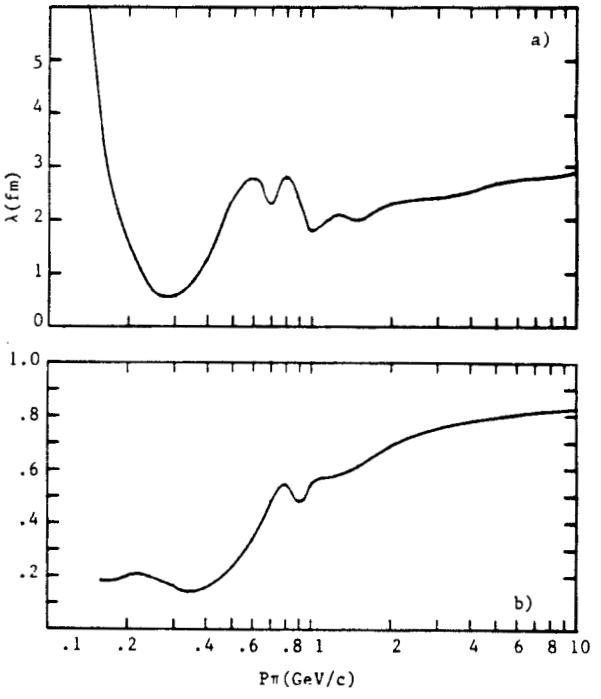


Figure 2 a) Charged pion mean path in nuclei obtained by convoluting the elementary pion nucleon interaction cross section with a uniform nuclear density. b) Fraction of pion nucleon interactions resulting in inelastic events.

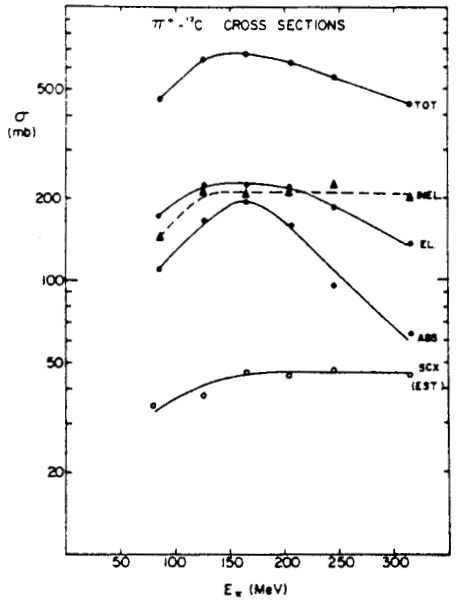


Figure 3 The various components of the pion nucleus interaction for $^{12}C$ from AS-81.

state interactions on charged pion photoproduction from $^{2}H$, and $^{12}C$ at energies corresponding to the peak of the free nucleon delta. The $^{2}H$ data, taken at Saclay (Fa-84), show only a small effect of pion FSI. (There is a large enhancement at the highest momenta in the spectrum of Figure 4, due to the large interaction between the p-p pair emerging in a relative s state). The $^{12}C$ (Ar-82) data indicate a large reduction in the quasi free production peak, which can be explained by the cascading and true absorpiton of the pions interacting strongly with the other nucleons.

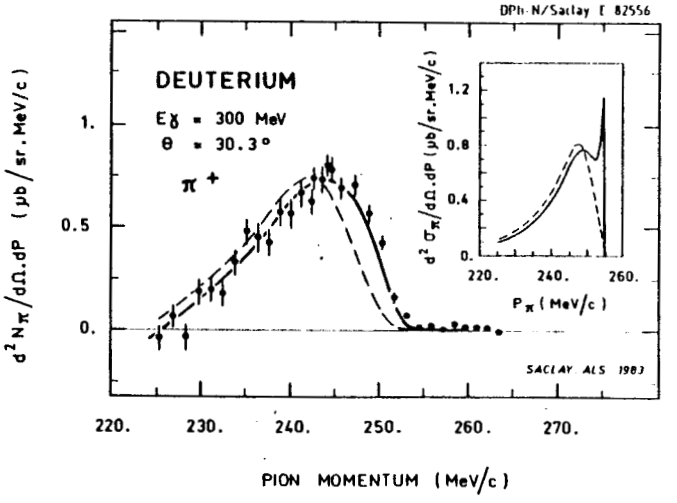


Figure 4 Momentum spectrum of positive pions due to the reaction $^{2}H(\gamma,\pi^{+})X$ for E = 300 MeV, obtained at Saclay (Fa-84). The dashed curve, due to a calculation by J.M. Laget, is a simple quasifree process with no pion FSI. The solid curve includes FSI. The enhancement at the high momentum part of the spectrum is due to scattering of two protons emerging in a relative s-state.

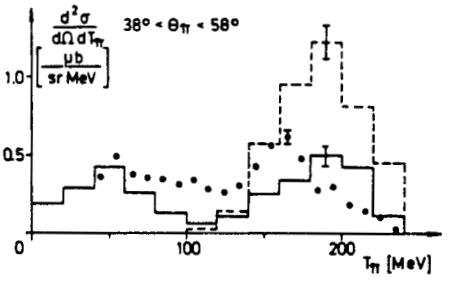


Figure 5 Energy spectrum of positive pions from the reaction $^{12}C(\gamma,\pi^{+})X$ obtained at Bonn (Ar-82). The dashed curve is due to a Monte-Carlo cascade simulation with no pion FSI. The full curve includes pion FSI.

At high energy, above the resonances, the cross section for the reaction $^{1}H(e,e'\pi^{+})n$ is much smaller than that for more inelastic processes. Also, pions may be the secondary result of the decay of primary hadrons. Within the framework of mesons and baryons, the pion electroproduction cross section at forward angles can be reproduced by the t channel Born diagram shown below.

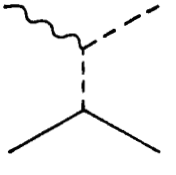

For unpolarized electrons the cross section can be written as follows:

$$\frac{d\sigma}{dE_e\, d\Omega_e\, d\Omega_\pi} = \Gamma \left\{ \frac{d\sigma_T}{d\Omega_\pi} + \varepsilon \frac{d\sigma_L}{d\Omega_\pi} + \varepsilon \frac{d\sigma_P}{d\Omega_\pi} \cos 2\phi_\pi \right. \quad (1)$$

$$\left. + \sqrt{2\varepsilon(\varepsilon+1)} \frac{d\sigma_I}{d\Omega_\pi} \cos \phi_\pi \right\}$$

Because of the longitudinal coupling of the photon to the pion, the longitudinal term $\sigma_L$ dominates at forward angle, and approximately follows the form exp(At), which is characteristic of a high energy diffractive process. In fact at high energies the same function fits diverse high energy diffractive processes such as Compton scattering, vector meson production and proton scattering (Le-78). Figure 6 shows the result of an experiment separating the four cross sections of equation 1. The t dependence of $\sigma_L$ is typical of t channel dominance.

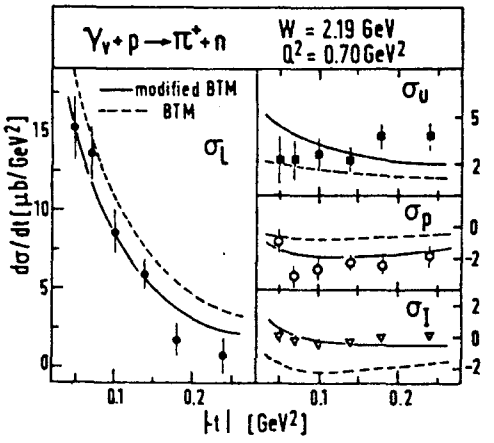


Figure 6 The separation of the various components of equation 1 for kinematics corresponding to Table Ia. The curves are the result of Lagrangian calculations based on Born term diagrams. Data and figure from Br-78.

From the quark-gluon point of view an interesting question is how to describe the evolution of the initial struck quark, which carries the virtual photon's energy and momentum, to the final hardronic state. This subject was discussed in ample detail in this workshop, and the reader is referred to other sources in these proceedings and elsewhere (e.g. Di-87). One of the most successful phenomenological approaches to this problem has been the Lund hadronization code (An-83), which is a Monte-Carlo simulation of the evolution of a string as it successively dissipates the initial quark energy by fragmenting into the final hadrons via the creation of quark-antiquark pairs. Figure 7 shows an example of the kind of results obtained by (Ch-87) using this code for charged pion production. The figure illustrates the distribution of charged pions as a function of the variable Z ($=E_\pi/\nu$), the fraction of the initial quark's energy carried by the pion. Here, $\nu$ is the virtual photon energy absorbed by the quark. Only near Z = 1 are the pions mainly primary, i.e., not the result of the decay of stable primary hadrons.

When this reaction is imbedded in a nucleus, in the simplest model the pions are produced on free nucleons having a Fermi momentum distribution. The emerging pion distribution will be strongly modified by strong FSI. For example, Figure 8 shows a Monte-Carlo simulation of the momentum distribution of pions due to the reaction p(e,e'$\pi^+$)n from a uniform Fermi gas. The pion FSI consists of multiple elastic diffraction scattering, with inelastic events simply absorbed. At energies considered here, only about ten to fifteen percent of the high Z interacting pions are elastically scattered.

Due to the strong FSI, the modification of the primary electroproduction process by the nuclear environment is just one part of, and cannot be separated from the overall problem of electro-

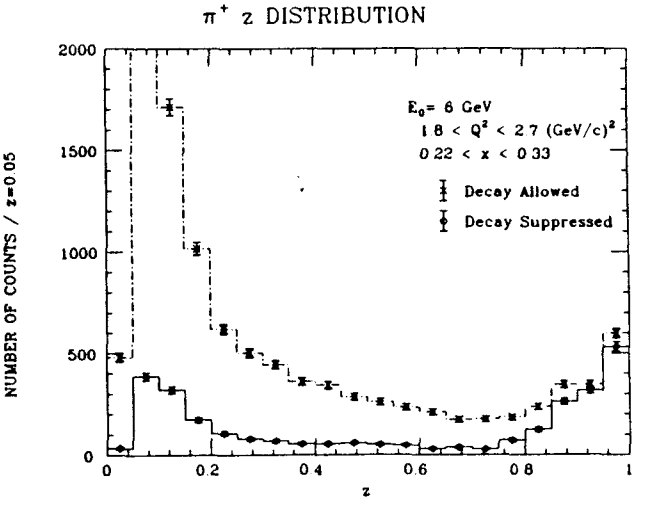


Figure 7 Spectrum of charged pions obtained by C.C. Chang using the Lund hadronization code (An-83). The lower curve is the spectrum of primary pions. The upper curve includes pions resulting from unstable primary hadrons.

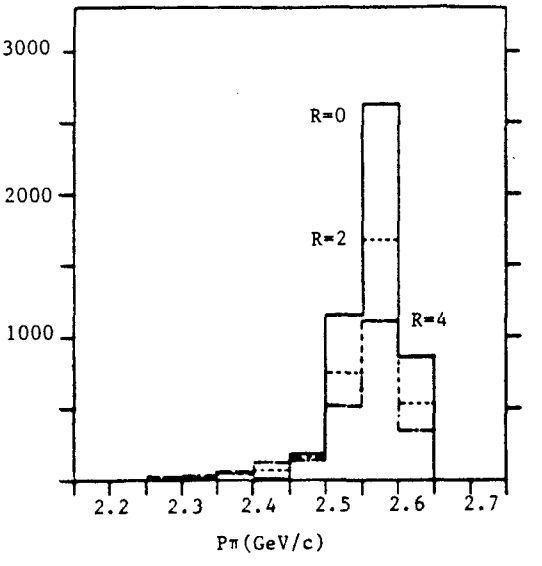


Figure 8 Simulated pion momentum spectra for the reaction A(e,e'$\pi^+$)X corresponding to the quasifree kinematics and spectrometer acceptances of Table I-a. The three curves denote a)no FSI, b)$R_A$ = 2.0 fm., c)$R_A$ = 4.0 fm.

production from nuclei, in which the uncertainty of the FSI must be taken into account.

During the workshop, the utility of using the pion electroproduction reaction to learn about the pion distribution in nuclei was disucssed, with some

doubts expressed. However, some very interesting points were raised (Br-87) about the effect of the nuclear medium on the quark hadronization process and the pion FSI.

The distance over which the hadronization occurs in a nucleus is throught to be related to the momentum of the hadron through the uncertainty principle and relativistic time dilation effects (see Ar-84, Bj-76, Ni-81, Bi-80). The higher momentum hadrons, corresponding to $Z > 0.5$ are produced furthest from the initial interaction site, according to the approximate relationship $r = E/m^2$, where E is the hardron energy and m it's mass.

When the electroproduction reaction is imbedded in a nucleus an interesting question is how the quark interacts with the nuclear environment prior to hadronization, and the subsequent evolution into the final hadron state, including the FSI of the hadrons themselves. It may be that the cross sections in nuclear matter for the quarks is rather small (Bi-80), so that at high enough energies the high Z hadrons may actually be produced at the edge of the nucleus, and the final hadron spectrum may be relatively independent of nuclear radius.

This effect has also been predicted from QCD considerations (Be-81). From the QCD point of view the high energy probe selects closely spaced valence quark-antiquark pairs. The diffractive interaction of the produced high energy hadron with the nucleus results in a longer interaction length in nuclear matter than would be expected from ordinary multiple scattering of mesons from nucleons in the nucleus. This effect should also result in an altered jet transverse momentum spectrum Z.

The transparency effects are expected to become apparent when $E >> R_A m^2$, where $R_A$ is the nuclear radius. They have been observed in moun scattering in the deep inelastic scaling region, by the EMC group (Ar-84), involving moun energy transfers of several tens of GeV. It was found that the production of hadrons with $Z > 0.5$ is independent of $R_A$. In electron scattering experiments at SLAC (Os-78) at lower energy transfer the number of hadrons per nucleon produced at high Z was observed to diminish with increasing nuclear radius indicating the presence of FSI. However, due to poor statistics the data were averaged over an energy transfer interval 3 -17 GeV, and a Z interval 0.5 - 1.0. From these two sets of results Ar-84 conclude that $r \sim 0.1$ fm/GeV within a broad statistical range. However, using $E > R_A m^2$ as a cutoff, one expects a hadronization length for pions on the order of several fm. Another possibility is that the quark FSI in nuclear matter is increasing at lower energy transfer.

Pion electroproduction on nuclei may be the best way to study the effects of nuclear matter on quark hadronization because of the $1/m^2$ dependence of the hadronization length. Experiments should be carried out at high Z, where the observed hadrons carry most of the virtual photon energy, and are not likely to be the result of more complicated or secondary processes. Also, at small t the nucleus is minimally disrupted, and the diffractive properties of the pion interaction are preserved.

Example of a Specific Experiment

An experimental measurement of the cross section for pion electroproduction from nuclei at small $\Theta_\pi$ and large Z was simulated using the Monte-Carlo code mentioned above (St-87a). Two kinematic settings and kinematic conditions, given in Table I, were chosen to conform to parameters likely to be available at PEP.

Kinematics I

$W = 2.3$ GeV $Q^2 = 0.6$ GeV$^2/c^2$
$E = 6$ GeV $E' = 3.4$ GeV $\Theta_e = 10°$ $P_\pi = 2.6$ GeV/c

Kinematics II

$W = 4.0$ GeV $Q^2 = 2.0$ GeV$^2/c^2$
$E = 17$ GeV $E' = 8.0$ GeV $\Theta_e = 7°$ $P_\pi = 9.0$ GeV/c

Table I

The pion angular acceptance, $\Delta\Theta_\pi = \Delta\phi = \pm 20°$ is in accordance with a possible design discussed at this workshop, and the pion momentum acceptance of 10% selects the highest interval of Z. The solid angle for electrons coincident with the detected pions was taken as 100 mr, with an energy acceptance of 1 GeV. The luminosity was taken as $1 \times 10^{33}$.

The resulting pion momentum spectra for the lower energy kinematics, for nuclei with $R_A = 2.0$ fm and $R_A = 4.0$ fm are shown in Figure 8. Also shown is the spectrum with no FSI. Although FSI are important, with considerable depletion in the quasi-free peak, the pions observed in the spectrometer would have undergone very little FSI, since those pions which would have interacted are either scattered elastically or inelastically out of the range of the spectrometer acceptance, or they are absorbed.

To estimate the effect of a finite hadronization length, a simple model was constructed, in which the hadronization length distribution is given by $N(L) = N(0)\exp(-L/H)$, where $H = E \times H_0$. The hadronization parameter $H_0$ is in units of fm/GeV. The ratio of the simulated cross section relative to that for the proton as a function of nuclear radius, for two values of the parameter $H_0$; 0 fm and 1 fm is given in Figure 9.

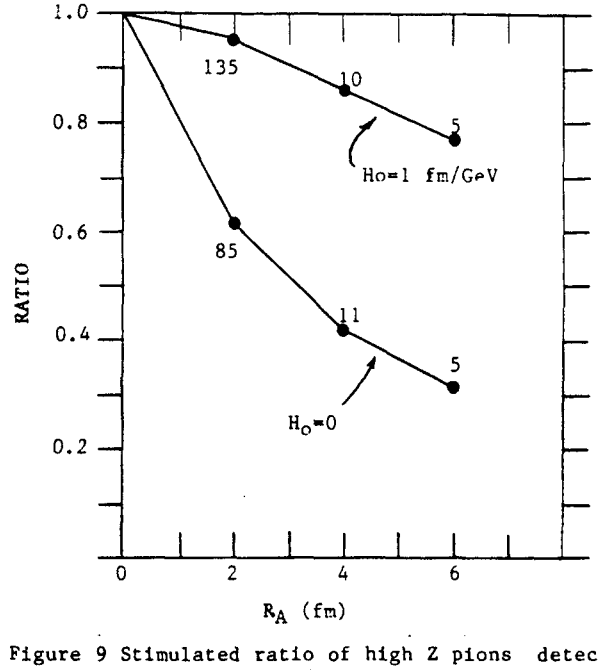


Figure 9 Stimulated ratio of high Z pions detected from nuclei as a function of $R_A$, for two values of the parameter $H_0$ defined in the text, corresponding to kinematics-b of Table I. The estimated number of hours of beam on target necessary to obtain the ratio to a statistical accuracy of 2% is shown for various points.

The elementary cross sections of Br-79 was used to estimate counting rates at the lower energy kinematics, and for the higher energy the extrapolation $1/(W^2-M^2)^2$ was used. Counting rates vary from about 30 per hr. to more than 1000 per hr., depending on atomic number and kinematic conditions. The number of hours with beam on target needed to obtain a statistical precision of 2% are also shown in Figure 9.

In conclusion, it seems that pion electroproduction from nuclei may be an excellent way of learning about the quark hadronization in nuclei, and that such experiments may be quite feasible at PEP with the appropriately designed experimental equipment.

*Work supported in part by the National Science Foundation, Grant no. PHY-8601006.

References

(An-83) B. Anderson et al., Physics Reports, 97, 31 (1983).
(As-81) D. Ashery et al., Phys. Rev. C 23, 2173 (1981).
(Ar-82) J. Arends et al., Z. Phys. A, 305, 205 (1982).
(Ar-84) A. Arvidson et al., Nucl. Phys. B246, 381 (1984).
(Be-81) G. Bertsch, S.J. Brodky, A.S. Goldhaber, Phys. Rev. Lett. 47, 297 (1981).
(Bi-80) A. Bialas and E. Bialas, Phys. Rev. D, 675 (1980).
(Bj-76) J.D. Bjorken, SLAC-PUB-1756 (1976).
(Br-79) P. Brauel et al., Z. Phys. C, 101 (1979).
(Br-87) S.J. Brodsky, comments during the present workshop and private communication.
(Bu-87) V. Burkert et al., Report of the CEBAF Steering Committee on Nucleon Resonances, CEBAF PAC Meeting Feb. 1987.
(Ch-87) C.C. Chang, private communication.
(Di-87) F. Dietrich and C. Johnson, Research Program at CEBAF (II), p. 389, SURA 1987.
(Do-78) 'Electromagnetic Interactions of Hadrons, Vol. I', A Donnachie and G. Shaw ed., Plenum, New York (1978).
(Dy-86) S. Dytman and F. Tabakin, Phys. Rev. C 33, 1699 (1986).
(Fa-84) J.L. Faure et al., Nucl. Phys. A424, 383 (1984).
(Ge-83) 'Proceedings of the Symposium of Delta-Nucleus Dynamics' D.F. Geesaman et al., eds. Argonne National Laboratory Report ANL-PHY-83-1.
(Hi-87) R. Hicks, Talk presented at this workshop.
(Le-78) 'Electromagnetic Interactions of Hadrons, Vol. I', A. Donnachie and G. Shaw eds., Plenum, New York (1978), p. 345.
(Mu-79) N. Mukhopadhyay, N. Toki and W. Weise, Phys. Lett., 84B, 35 (1979).
(Mu-87) N. Mukhopadhyay, Proceedings of the CEBAF Summer Workshop - 1986, SURA (1987) p. 451. p. 491.
(Ni-81) N.N. Nikolaev, Sov. Phys. Usp. 24, 531 (1981).
(Os-78) L.S. Osborne et al, Phys. Rev. Lett., 40, 1624 (1978).
(St-75) S. Stein et al., Phys. Rev. D 12, 1884 (1975).
(St-87) P. Stoler, Research Program at CEBAF (II), p. 261, SURA (1987).
(St-87a) P. Stoler, report circulated at PEP collaboration meeting Feb. 1987.

# ELECTROMAGNETIC PHYSICS WITH A POLARIZED $^3$HE INTERNAL TARGET

R.G. Milner
W.K. Kellogg Radiation Laboratory,
California Institute of Technology,
Pasadena,
California 91125

Polarization observables provide one method of extracting small components of wave-functions and reaction mechanisms. Examples are the measurements of the D-state admixture in the ground state wave-functions of $^3$He [1] and $^4$He [2] ; measurement of $t_{20}$ in $\pi$-deuteron elastic scattering[3]; measurement of $t_{20}$ in e-deuteron elastic scattering[4]; deep inelastic asymmetry measurements on the nucleon[5]; parity measurements in electron-deuteron elastic scattering[6]. A program of measurements of polarization observables on the proton, deuteron, and $^3$He would provide a very strict constraint for any model of nucleons in the nucleus.

To date, the only targets of polarized nuclei considered in detail for polarization studies in electromagnetic physics have been the proton, the deuteron, and $^{165}$Ho [7]. The targets require both cryogenics and intense magnetic fields to produce polarizations of order 50%. These intense magnetic fields are a likely source of systematic error for measurement of small asymmetries in that they will deflect both the incident and scattered beams. Also, the proton and deuteron targets are based on the method of dynamic nuclear polarization and hence the polarized nucleus is part of a large molecule, e.g. butanol, ammonia. This can dilute the measured asymmetry by typically an order of magnitude. Luminosities are limited to $\approx 10^{35}\text{cm}^{-2}\text{s}^{-1}$ by depolarization of the target.

A promising idea, which would eliminate many of the above problems, is to use an internal target of density $2 \times 10^{15}\text{cm}^{-2}$ of polarized atoms in an electron storage ring with a stored current of 100 mA. This would provide a luminosity of $10^{33}\text{cm}^{-2}\text{s}^{-1}$ and would use a new generation of polarized few-nucleon targets based on the method of optical pumping. These targets, if feasible, have the advantages of requiring only few gauss holding fields and do not give rise to any dilution of the measured asymmetry in that the polarized atoms are pure atomic species. At Argonne National Laboratory, Dr. Roy Holt is working on the development of a polarized deuterium target using direct optical pumping of an alkali followed by spin-exchange to a deuterium atom[8]. Such a technique would also work for a hydrogen atom. At Caltech, we have been working on the development of a polarized $^3$He target. $^3$He has the advantages that a direct optical pumping technique exists and also that its interaction with containment walls is very weak.

## I. Target technology

It is important to note initially that in inclusive electron scattering from a spin-$\frac{1}{2}$ particle, it is necessary to have both beam and target polarized to obtain additional information beyond unpolarized measurements[9]. Thus, it is imperative for measurements on the nucleon or $^3$He that there be the capability to deliver longitudinally polarized electrons at the interaction region in the ring.

The method used to polarize $^3$He nuclei is an optical pumping technique developed by Colegrove, Schearer, and Walters[10]. Experimentally one requires a source of 1.083$\mu$m light to excite the $^3S_1$–$^3P_0$ transition. Until recently, one was limited to discharge lamps which because of Doppler broadening were not very efficient at pumping. A French group [11] has developed a high power infra-red laser which reliably emits 300mW of 1.083$\mu$m light. This laser yields polarizations of 70% in a sample of $^3$He of density $10^{16}\text{cm}^{-3}$ and a feed rate of $3 \times 10^{16}$ polarized $^3$He per second. With higher power lasers now under development[12], feed rates of $10^{17}$ polarized $^3$He per second look reasonable. It is important to note that the small holding magnetic field ($\approx$ 5 gauss) required to maintain the polarization of the $^3$He, allows easy orientation of the target spins. As will be evident below, this is very important for maximizing sensitivity to particular interesting pieces of the cross-section.

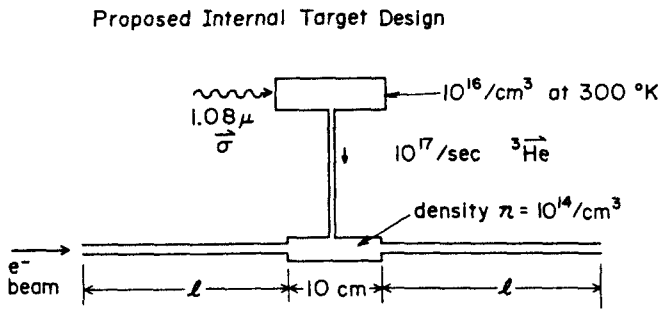


**Fig.1** This figure is a schematic diagram of the proposed internal target design.

A schematic diagram of the proposed polarized $^3$He internal target is shown in Fig. 1. A high power infra-red laser optically pumps a sample of $^3$He at a density of $10^{16}$atoms cm$^{-3}$ contained in a pyrex cell. This cell is connected through a narrow tube to a 10 cm long "bottle". This "bottle" has a long narrow tube of length 30 cm and i.d. 7 mm at each end to act as an impedance for the gas flow. It may be necessary to arrange the end tubes in a clam-shell configuration so that they have a large i.d. when tuning the electron beam and collapse to a 7 mm i.d. when running the internal target. A few gauss holding magnetic field is required for the optical pumping process.

However, a possible problem is depolarization of the target by the intense beam. At Caltech, we have investigated the depolarization mechanism in the region of a few torr and for beams of several microamperes of 3 MeV protons[13]. The depolarization rate due to the charged particle beam is found to be consistent with a model based on the formation of the $He_2^+$ diatomic molecule. This molecule is formed in 3 body collisions and so the formation rate increases as the square of the pressure. Extrapolation of this model to the low pressures and high currents of an internal target indicate that target depolarization is a problem for luminosities in excess of $10^{34}\text{cm}^{-2}\text{s}^{-1}$.

I shall consider two interesting experiments that become possible with such a target. One is a measurement of the neutron electric form factor up to $Q^2 = 0.8$ (GeV/c)$^2$ with the proposed 1 GeV pulse stretcher ring at the Bates laboratory at MIT. The second is a measurement of the deep inelastic spin structure function for the neutron at the PEP storage ring at SLAC. In both experiments I shall assume a luminosity

of $10^{33}\mathrm{cm}^{-2}\mathrm{s}^{-1}$ and a longitudinally polarized electron beam of polarization 0.4.

## II. Quasielastic electron scattering

An impulse approximation calculation [14] with a wave function obtained by solving the Faddeev equation with the Reid soft-core potential, has been performed in the quasi-elastic region for longitudinally polarized electrons incident on a polarized $^3$He target. It is found that near the quasi-elastic peak the contribution of the two protons to the asymmetry is small, and so a polarization measurement can extract the contribution from elastically scattering from the neutron in $^3$He. As one moves out into the tail of the quasi-elastic peak, the contribution of the two protons to the asymmetry increases. For example, at incident energies of a few hundred MeV and at low energy transfer, the asymmetry is large, and mainly due to D-state admixture in the wave function. It is clear one needs more realistic calculations that include effects like distortion and meson-exchange currents, but it is certain that measurement of the asymmetry in the tail of the quasi-elastic peak would provide a direct test of the small components of the $^3$He wave function.

Consider the measurement of the asymmetry on the quasi-elastic peak as a measurement of the electric form-factor of the neutron ($G_E^n$) in $^3$He. Our present knowledge of $G_E^n$ [15], extracted from e-d elastic measurements, is quite poor. Clearly it is important to improve our knowledge of this fundamental quantity. The existing data has been parametrized as

$$G_E^n(Q^2) = \frac{-\tau\mu_n}{(1+\eta\tau)(1+Q^2/B)^2}$$

where $B = 0.71$ GeV/c$^2$, $\mu_n$ is the neutron magnetic moment and $\tau = Q^2/4M^2$. Present indications are that $1 \leq \eta \leq 10$; however, the entire range $0 \leq \eta \leq \infty$ cannot really be excluded. We have taken $\eta = 5$.

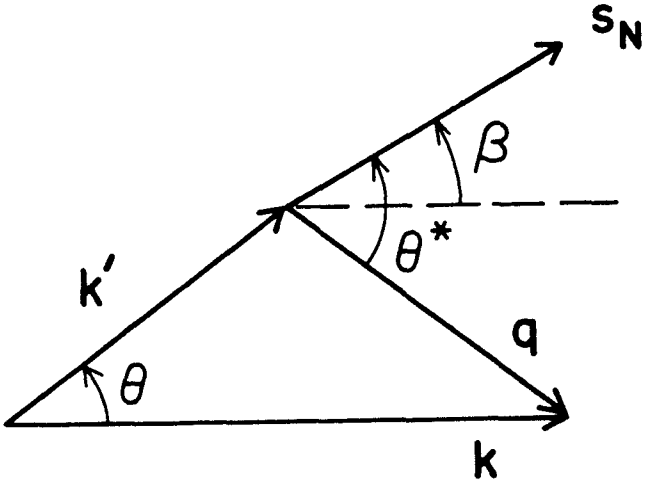


**Fig.2** This defines the angles $\beta$, which is the angle between the nuclear spin vector, $\mathbf{S}_N$, and the incident electron momentum, $\mathbf{k}$ ; and $\theta^*$, which is the angle between $\mathbf{S}_N$ and $\mathbf{q}$, the 3-momentum transfer.

The measurement of $G_E^n$ is basically a measurement of the asymmetry

$$A = \frac{\sigma(\theta,\theta^*,+) - \sigma(\theta,\theta^*,-)}{\sigma(\theta,\theta^*,+) + \sigma(\theta,\theta^*,-)} \qquad (1)$$

where $\sigma(\theta,\theta^*,+)$ is the cross section for quasielastic scattering of longitudinally polarized electrons with positive helicity off a polarized $^3$He target whose polarization lies in the scattering plane and where the angle $\theta^*$ is defined in Fig. 2.

In the case of a free neutron the asymmetry is[6]

$$A_{en} = \frac{2\tau {G_M^n}^2 \cos\theta^* v_T' + 2\sqrt{2\tau(1+\tau)} G_M^n G_E^n \sin\theta^* \cos\phi^* v_{TL}'}{v_L(1+\tau){G_E^n}^2 + v_T 2\tau {G_M^n}^2}$$

where

$$v_L = (\frac{Q^2}{q^2})^2$$

$$v_T = \frac{Q^2}{2q^2} + \tan^2\frac{\theta}{2}$$

$$v_T' = \tan\frac{\theta}{2}\sqrt{\tan^2\frac{\theta}{2} + \frac{Q^2}{q^2}}$$

$$v_{TL}' = \frac{Q^2}{q^2}\frac{\tan\frac{\theta}{2}}{\sqrt{2}}$$

Here $q^2 = Q^2 + \nu^2$ in conventional notation .

To a good approximation the asymmetry due to quasielastic scattering off polarized $^3$He is given by

$$A = \frac{A_{en}\sigma_n}{\sigma_n + 2\sigma_p}$$

where $A_{en}$ is the asymmetry for the free neutron. The validity of this approximation was demonstrated by Blankleider and Woloshyn in their Faddeev calculation. One can see that by varying $\theta^*$, i.e. the angle between the nuclear spin and the direction of momentum transfer, it is possible to pick out the longitudinal and transverse pieces of the quasielastic spin-dependent cross-section. In particular, if $\theta^* = \frac{\pi}{2}$, then the asymmetry is proportional to $G_E^n$; if $\theta^* = 0$, it is sensitive only to $G_M^n$. Also note that for a given $Q^2$, the asymmetry on the quasielastic peak vanishes at a value of $\theta_0^*$ given by

$$\frac{G_E^n}{G_M^n} = -\frac{\cot\theta_0^*}{\cos\phi^*}\sqrt{\tau + \tau(1+\tau)\tan^2\frac{\theta}{2}}$$

In what follows we assume that $\phi^* = 0 \pm 8°$, and so $\cos\phi^*$ is always within 1% of unity. This provides an elegant way of determining the ratio of $\frac{G_E^n}{G_M^n}$ as a function of $Q^2$, independent of the beam and target polarizations. The cross-section is obtained from a y-scaling model of quasielastic scattering from $^3$He. This model is in excellent agreement with existing unpolarized data.

Running times for a $\pm 20\%$ measurement of $G_E^n$ are then calculated using the following experimental parameters. We assume a luminosity of $L = 10^{33}\mathrm{cm}^{-2}\mathrm{s}^{-1}$. The polarizations of the $^3$He target and incident electron beam are taken to be $p_T = 50\%$ and $p_e = 40\%$ respectively. We assume a solid angle of $\mathrm{d}\Omega = 25$ msr for the spectrometer and take half the total yield of $(d\sigma/dE')\Delta E'$ over the quasielastic peak. All measured asymmetries are greater than $10^{-3}$. The running time in terms of these parameters is then

$$t = \left[\frac{d^2\sigma}{d\Omega dE'}\Delta E'\Delta\Omega L(p_e p_T \Delta A)^2\right]^{-1} \qquad (2)$$

where $\Delta A$ is the required statistical uncertainty in the asymmetry.

The resulting running times for a ±20% measurement of $G_E^n$ and a 1 GeV incident electron beam for $Q^2$ = 0.2, 0.4, 0.6, 0.8 $(GeV/c)^2$ are shown in Table 1. It is to be noted that the direction of **q** varies as a function of energy loss and $\theta$ and so $\theta^*$ will vary over the spectrometer acceptance. A large acceptance spectrometer would allow simultaneous measurement of the $\theta^*$ and $\phi^*$ dependence of the asymmetry. Measurements with $\theta^* = \frac{\pi}{2}$ provide information on $G_M^n$.

**Table 1. Running times for a ±20% measurement of $G_E^n$**

incident energy = 1 GeV
luminosity = $10^{33}\,cm^{-2}s^{-1}$
$P_T = 0.5$
$P_e = 0.4$
$d\Omega = 25$ msr

| $\frac{Q^2}{(GeV/c)^2)}$ | $\frac{\theta}{deg.}$ | $A_{meas}$ | $\frac{T}{days}$ |
|---|---|---|---|
| 0.2 | 27.4 | $1.9 \times 10^{-3}$ | 4.5 |
| 0.4 | 41.8 | $6.8 \times 10^{-3}$ | 4 |
| 0.6 | 56.0 | $1.3 \times 10^{-2}$ | 6 |
| 0.8 | 72.4 | $2.1 \times 10^{-2}$ | 12 |

## III. Deep inelastic electron scattering

In the deep inelastic region, it is possible to measure the spin- dependent structure functions of the neutron in the $^3$He nucleus[16]. The internal spin structure of the nucleon is important as a constraint on the development and testing of theories and models of nucleon structure. For a comprehensive review of this subject, see reference 5.

One considers the case of deep inelastic scattering of parallel and antiparallel spins for the polarized electron and polarized nucleon. Then one measures the asymmetry of eqn. (1) with $\beta = 0$, where

$$\frac{d^2\sigma}{d\Omega dE'} = \frac{\alpha^2 \cos^2\frac{\theta}{2}}{4E^2 \sin^4\frac{\theta}{2}}\Big[W_2 + 2W_1 \tan^2\frac{\theta}{2}$$

$$\pm 2\tan^2\frac{\theta}{2}(E + E'\cos\theta)MG_1 \pm 8EE'\tan^2\frac{\theta}{2}\sin^2\frac{\theta}{2}G_2\Big].$$

$W_1$ and $W_2$ are the well-known unpolarized structure functions and $G_1$ and $G_2$ are two new spin-dependent structure functions. From considerations of the total photoabsorbtion cross-sections, it is found convenient to write $A$ as follows:

$$A = D(A_1 + \eta A_2)$$

where

$$A_1 = \frac{M\nu G_1 - Q^2 G_2}{W_1}\ ; A_2 = \frac{\sqrt{Q^2}}{W_1}(MG_1 + \nu G_2)$$

$$D = \frac{1 - E'/E\epsilon}{1 + \epsilon R}\ ; \eta = \frac{\epsilon\sqrt{Q^2}}{E - \epsilon E'}$$

$$\epsilon = \left[1 + 2(1 + \frac{\nu^2}{Q^2})\tan^2\theta/2\right]^{-1}.$$

Here $E$ and $E'$ are respectively the incident and final electron energies; $Q^2$ is the four-momentum transfer squared; $\nu$ is the energy transfer; $R$ is the ratio of longitudinal to transverse cross-sections.

In the Bjorken scaling limit

$$M^2\nu G_1(Q^2,\nu) \to g_1(x)\ ; M\nu^2 G_2(Q^2,\nu) \to g_2(x)$$

i.e., the spin-dependent structure functions scale. $A_1$ and $A_2$ can be readily expressed in terms of the quark spin distribution functions. It can be shown that the asymmetry $A_2$ vanishes for massless quarks. The asymmetry $A_1$ is the dominant term in deep inelastic scattering with longitudinal polarization.

Bjorken has derived[18] a sum rule for spin-dependent deep inelastic electron-nucleon scattering. This sum rule may be written as

$$\int_0^1 [g_1^p(x) - g_1^n(x)]dx = \frac{1}{6}\left|\frac{g_A}{g_V}\right| = 0.209 \pm 0.001$$

where $g_A/g_V$ is the ratio of axial to vector weak coupling constants in nuclear beta-decay. This may also be written in the scaling limit as

$$\int_0^1 \frac{dx}{x}\left[\frac{A_1^p(x)F_2^p(x)}{1 + R^p} - \frac{A_1^n(x)F_2^n(x)}{1 + R^n}\right] = \frac{1}{3}\left|\frac{g_A}{g_V}\right|.$$

This form is convenient for experimental comparison. The scaling function $F_2(x)$ is the scaling limit of $\nu W_2$. Separate sum rules for the neutron and proton have been derived[17] using quark light-cone algebra and under the additional assumption that the net spin polarization of strange sea quarks is zero. These are

$$\int_0^1 g_1^p(x)dx = \int_0^1 \frac{dx}{x}\frac{A_1^p(x)F_2^p(x)}{1 + R^p} = \left|\frac{g_A}{g_V}\right|\frac{1.78}{12}$$

and

$$\int_0^1 g_1^n(x)dx = \int_0^1 \frac{dx}{x}\frac{A_1^n(x)F_2^n(x)}{1 + R^n} = \left|\frac{g_A}{g_V}\right|\frac{-0.22}{12}.$$

Recently, Jaffe has reconsidered these sum rules in light of the non-conservation of the U(1) axial current in QCD[19]. He derives inequalities at large $Q^2$

$$\int_0^1 g_1^p(x)dx = \int_0^1 \frac{dx}{x}\frac{A_1^p(x)F_2^p(x)}{1 + R^p} \le \left|\frac{g_A}{g_V}\right|\frac{1.18}{12}\Big(1 - \frac{\alpha_s(Q^2)}{\pi}\Big)$$

and

$$\int_0^1 g_1^n(x)dx = \int_0^1 \frac{dx}{x}\frac{A_1^n(x)F_2^n(x)}{1 + R^n} \le \left|\frac{g_A}{g_V}\right|\frac{-0.82}{12}\Big(1 - \frac{\alpha_s(Q^2)}{\pi}\Big).$$

These are derived assuming the validity of the Bjorken sum-rule and imply that the neutron sum-rule is bigger than the SU(3) picture by of order a factor of four.

Data has been obtained on polarized $e - p$ scattering. In a series of measurements performed at SLAC by the Yale-SLAC collaboration in the late seventies[5], the spin-dependent asymmetry $A_1$ has been measured for the proton over the deep

inelastic kinematic range $0.1 \leq x \leq 0.7$ and $1 \leq Q^2 \leq 10$ $(\mathrm{GeV/c})^2$ with an accuracy of 15-30%. The experimental data confirm the Bjorken polarization sum rule under the assumption that the neutron contribution is zero. The quality of the SLAC data on the proton is not sufficient to distinguish between the SU(3) and QCD sum-rules for each nucleon isospin state. New, as yet unpublished, data from EMC should have sufficient precision to do this[20]. The SLAC data also verify the scaling behaviour of $A_1^p$ within their limited accuracy. Furthermore, the data successfully distinguished the phenomenological models of the spin structure of the proton and support the prediction of perturbative QCD that $A_1(x) \to 1$ as $x \to 1$ for the nucleon.

The prediction for $A_1^n(x)$ of the unsymmetrical quark model[5], which fits well the measured $A_1^p$ data, is shown in Fig.3. We see that $A_1^n(x) \to 1$ as $x \to 1$ and that it is negative at small x. The bulk of the contribution to the sum-rule comes from the low x region. Thus, a sensitive test of the QCD model of the nucleon would be a measurement of $A_1^n(\mathrm{x})$ at low x as a function of $Q^2$. Fig.4 shows the statistical precision with which one can measure $A_1^n$ as a function of x and $Q^2$ with a 15 GeV polarized electron beam incident on a polarized $^3$He target at PEP. In the above notation I assume $p_e = 0.4$, $p_T = 0.5$, and luminosity $= 10^{33}\mathrm{cm}^{-2}\mathrm{s}^{-1}$. Also I take $\mathrm{R}(\mathrm{x},Q^2) = 0.25$, an assumption which may be modified by the results of experiment E140 at SLAC. The statistical precision obtained in a 16 day run in a bin $\Delta\theta = 10$ mrad and $\Delta\nu = 200$ MeV is shown in the $Q^2$ vs. $\nu$ plane. The cross-section is taken from the Bodek fit

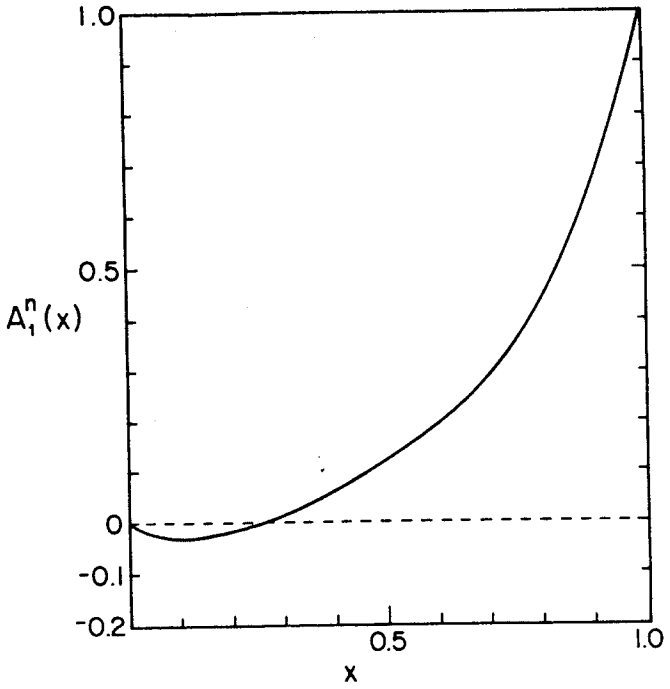


**Fig.3** This figure shows the prediction of the unsymmetrical quark model for $A_1^n(\mathrm{x})$. It is taken from reference 5.

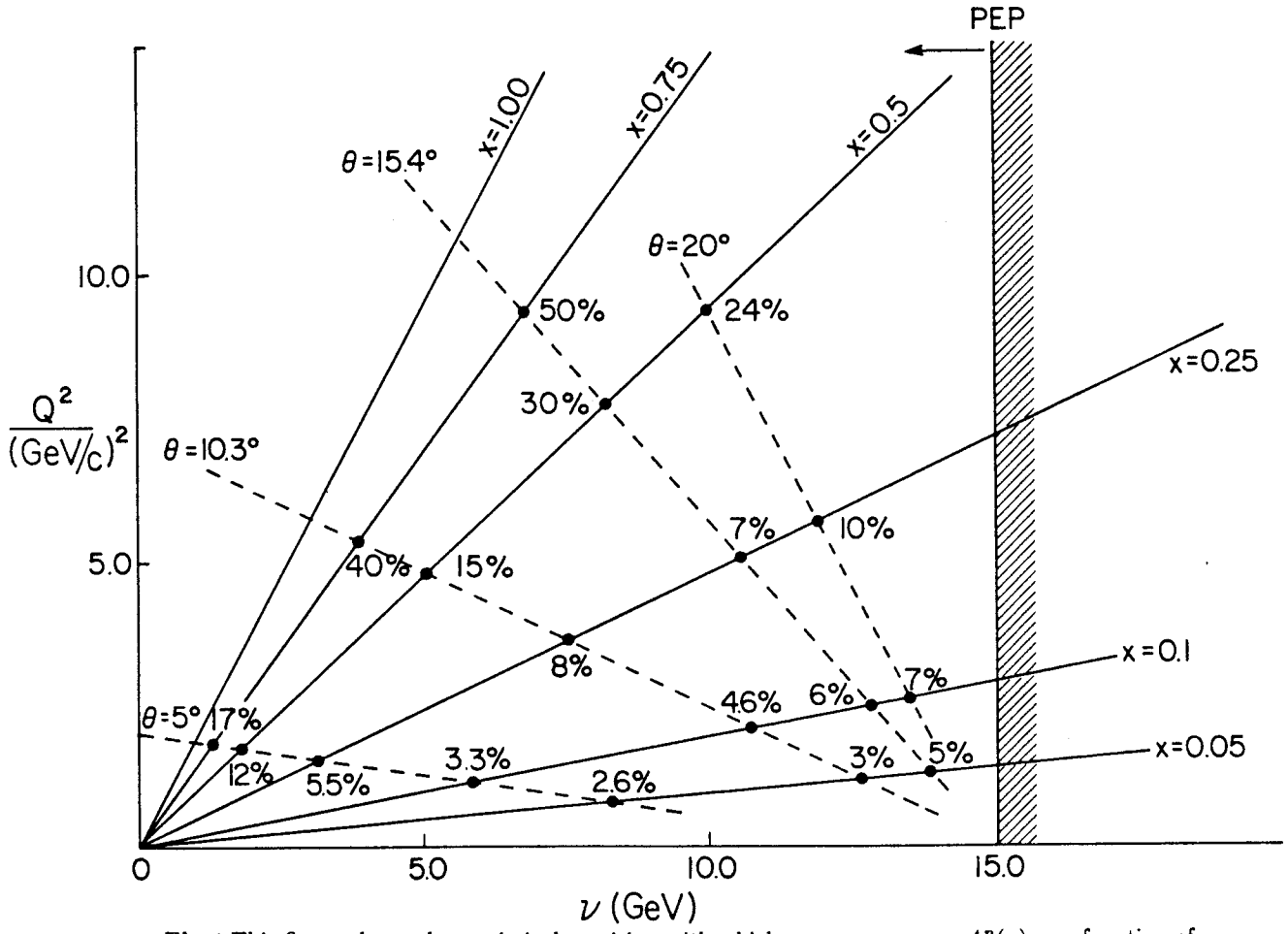


**Fig.4** This figure shows the statistical precision with which one can measure $A_1^n(\mathrm{x})$ as a function of x and $Q^2$ in bins of $\Delta\theta = 10$ mrad and $\Delta\nu = 200$ MeV in a 16 day run with a 100 mA beam of 15 GeV 40% longitudinally polarized electrons incident on a $2 \times 10^{15}\mathrm{cm}^{-2}\mathrm{s}^{-1}$ 50% polarized $^3$He target.

to the deep-inelastic region and no Fermi-motion is included. The dilution of the asymmetry because of the two protons in $^3$He is included.

## V. Summary

With a luminosity of $10^{33}\mathrm{cm}^{-2}\mathrm{s}^{-1}$ of polarized electrons incident on a polarized $^3$He internal target, one could undertake very fundamental measurements on the neutron in $^3$He. In the quasielastic region, one could measure the charge distribution of the neutron up to $Q^2$ of 0.8 $(\mathrm{GeV/c})^2$ at the proposed 1 GeV pulse stretcher ring at MIT. In the deep inelastic region, measurements on the spin structure of the neutron become possible at PEP if longitudinally polarized electrons become available at one of the interaction regions . It is strongly urged that a design study be carried out to determine feasibility and cost of implementing this. Using a reasonable choice of running parameters, the running time for an interesting series of measurements in each of these kinematic regions is of the order of 30 days. At Caltech an effort is underway to construct high density, high polarization targets of polarized $^3$He which would permit these measurements.

This research was supported by the National Science Foundation under Grants PHY85-05682 and PHY-8351737.

References

[1] J.Jourdan *et al.*, Phys. Lett. **162B**, 269 (1985)
[2] B.C.Karp *et al.*, Phys. Rev. Lett. **53**, 1619 (1984)
[3] E.Ungricht *et al.*, Phys. Rev. Lett. **52**, 333 (1984)
[4] M.E.Schulze *et al.*, Phys. Rev. Lett., **52**, 597 (1984)
[5] V.W.Hughes and Julius Kuti, Ann. Rev. Nucl. Sc. **33**, 611 (1983)
[6] C.Y.Prescott *et al.*, Phys. Lett. **77B**, 347 (1978)
[7] F.J.Uhrhane, J.S.McCarthy, and M.R.Yearian, Phys. Rev. Lett. **26**, 578 (1971)
[8] R.J.Holt, Proceedings of Workshop on Polarized Targets in Storage Rings, Argonne National Laboratory (ANL-84-50), p.103 (May 1984)
[9] T.W.Donnelly and A.S.Raskin, Annals of Physics **169**, 247 (1986)
[10] F.D.Colegrove, L.D.Schearer, and G.K.Walters, Phys. Rev. **132**, 2561 (1963)
[11] M.Leduc *et al.*, "A new infra-red tunable laser (LNA) for optical pumping of helium", contribution to CLEO, June 1986, San Francisco
[12] L.D.Schearer *et al.*, IEEE **QE-22**, No. 5, 713 (1986)
[13] R.G.Milner, R.D.McKeown, and C.E.Woodward, Nucl. Instr. and Meth. *in press*
[14] B.Blankleider and R.M.Woloshyn, Phys. Rev. **C29**, 538 (1984)
[15] S.Galster *et al.*, Nucl. Phys. **B32**, 221 (1971)
[16] R.G.Milner, Proceedings of Workshop on Polarized $^3$He Beams and Targets, Princeton NJ, October 1984 p. 186 (AIP Conference Proceedings No. 131)
[17] J.D.Bjorken, Phys. Rev. **148**, 1467 (1966)
[18] J.Ellis and R.Jaffe, Phys. Rev. **D9**, 1444 (1974)
[19] R.L.Jaffe, MIT CTP preprint No. 1445, submitted to Phys. Rev. Lett. Jan. 1987
[20] Private communication, T.Sloan

# (e,e'N) REACTIONS WITH POLARIZED BEAMS AND POLARIZED TARGETS

S.Boffi, C.Giusti and F.D.Pacati

Dipartimento di Fisica Nucleare e Teorica dell'Universita', Pavia,
Istituto Nazionale di Fisica Nucleare, Sezione di Pavia, Italy

Abstract: The quasi-free nucleon knockout by the electron is studied in the general case of both polarized beams and polarized targets. The general formalism provides nine structure functions, four of which appear only when the target nucleus is polarized. Results obtained in a nonrelativistic DWIA framework on $^7$Li and $^{39}$K for cross sections, asymmetries and electron polarization ratios are presented. The particular case is also considered of a nucleon ejected along the direction of the momentum transfer from a target with spin oriented in the same direction where only three structure functions survive and can be simply separated.

In the one-photon exchange approximation and neglecting the electron mass and the nuclear recoil factor, the six-fold differential coincidence cross section for quasi-free nucleon knockout from a polarized target nucleus by an incident polarized electron may be written as follows [1]

$$\frac{d\sigma^h}{d\vec{p}_o'\, d\vec{p}'} = \alpha^2 \frac{1}{q_\nu^2\, p_o\, p_o'\, (\epsilon-1)} (\Sigma + h\,\Delta) \quad , \qquad (1)$$

where $\alpha = e^2/4\pi = 1/137$ is the fine structure constant and the ultrarelativistic electron with initial helicity h and momentum $\vec{p}_o$ is scattered to a final momentum $\vec{p}_o'$ while a nucleon is knocked out with final momentum $\vec{p}'$. Then, the four-momentum transfer is $q_\nu^2 = \omega^2 - q^2$, with $\omega = p_o - p_o'$ and $\vec{q} = \vec{p}_o - \vec{p}_o'$. In eq. (1)

$$\Sigma = 2\,\epsilon_L\, F_{oo} + F_{11} + [\epsilon_L\,(1+\epsilon)]^{1/2}\, F_{o1} - \epsilon\, F_{1-1} \quad , \qquad (2)$$

$$\Delta = (1-\epsilon^2)^{1/2}\, F_{11}' + [\epsilon_L\,(1-\epsilon)]^{1/2}\, F_{o1}' \quad . \qquad (3)$$

The quantity

$$\epsilon = [1 - 2\,(q^2/q_\nu^2)\,\tan^2\theta/2]^{-1} \qquad (4)$$

measures the transverse linear polarization of the virtual photon exchanged by the electron scattered at an angle $\theta$, and

$$\epsilon_L = (-q_\nu^2/q^2)\,\epsilon \quad . \qquad (5)$$

In the laboratory frame, where the nucleon is ejected at an angle $\gamma \neq 0$ with respect to the momentum transfer $\vec{q}$ and the initial nucleus is assumed to be at rest and with a polarization direction specified by the zenithal angle $\theta^*$ and the azimuthal angle $\phi^*$, the six structure functions in eqs. (2) and (3) depend on the seven variables ($\omega$, q, p', $\gamma$, $\alpha$, $\theta^*$, $\phi^*$), where $\alpha$ is the angle between the hadron and the electron planes. One has

$$\begin{aligned}
F_{oo} &= f_{oo} \quad , \\
F_{11} &= f_{11} \quad , \\
F_{o1} &= f_{o1}\cos\alpha + \bar{f}_{o1}\sin\alpha \quad , \\
F_{1-1} &= f_{1-1}\cos 2\alpha + \bar{f}_{1-1}\sin 2\alpha \quad , \\
F_{11}' &= f_{11}' \quad , \\
F_{o1}' &= f_{o1}'\sin\alpha + \bar{f}_{o1}'\cos\alpha \quad . \qquad (6)
\end{aligned}$$

where

$$\begin{aligned}
f_{oo} &= |J_o|^2 \quad , \\
f_{11} &= |J_1|^2 + |J_{-1}|^2 \quad , \\
f_{o1} &= 2\,\mathrm{Re}\,(J_1\, J_o^* - J_o\, J_{-1}^*) \quad , \\
f_{1-1} &= 2\,\mathrm{Re}\,(J_1\, J_{-1}^*) \quad , \\
f_{11}' &= |J_1|^2 - |J_{-1}|^2 \quad , \\
f_{o1}' &= -2\,\mathrm{Im}\,(J_1\, J_o^* + J_o\, J_{-1}^*) \quad , \\
\bar{f}_{o1} &= -2\,\mathrm{Im}\,(J_1\, J_o^* - J_o\, J_{-1}^*) \quad , \\
\bar{f}_{1-1} &= -2\,\mathrm{Im}\,(J_1\, J_{-1}^*) \quad , \\
\bar{f}_{o1}' &= 2\,\mathrm{Re}\,(J_1\, J_o^* + J_o\, J_{-1}^*) \quad . \qquad (7)
\end{aligned}$$

In eq. (7) an average over initial states and a sum over final undetected states of products of matrix elements $J_\mu$ are understood, where

$$J_\mu = \int d\vec{r}\, e^{i\vec{q}\vec{r}} \langle \Psi_f |\; j_\mu(\vec{r})\; | \Psi_i \rangle \qquad (8)$$

are matrix elements of the nuclear charge-current operator $j_\mu$ taken between the initial ($|\Psi_i\rangle$) and final ($|\Psi_f\rangle$) nuclear states.

For an unpolarized target nucleus the barred structure functions $\bar{f}_{o1}$, $\bar{f}_{1-1}$ and $\bar{f}_{o1}'$ vanish identically. In addition, $|J_1|^2 = |J_{-1}|^2$, i.e. $f_{11}' \equiv 0$. Therefore, in this case one recovers the expression of the cross section in terms of five structure functions already studied in ref. 2 with incident polarized

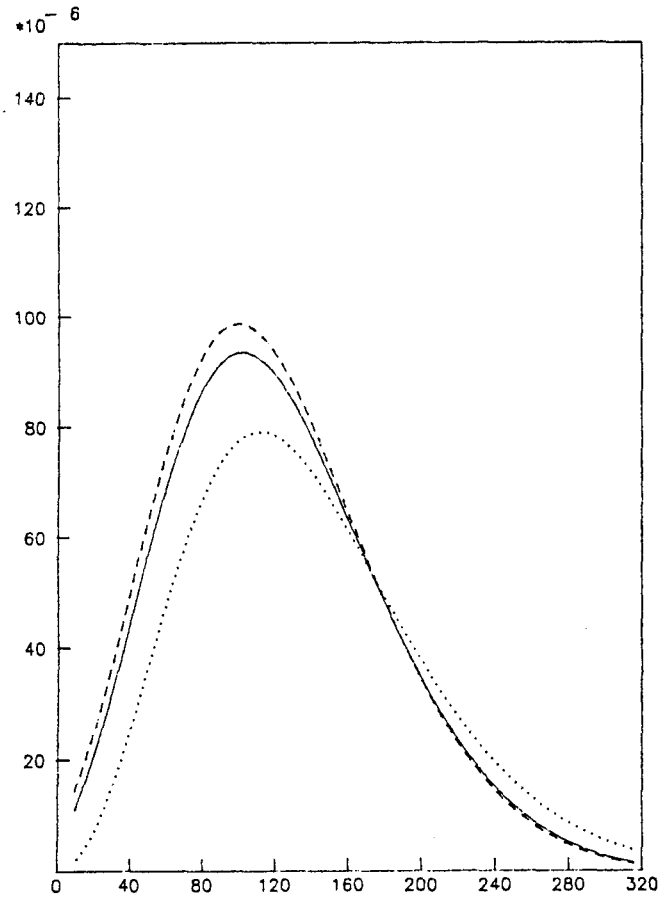


Fig. 1. Cross section ($fm^3$ $sr^{-2}$) vs. recoil momentum (MeV/c) for $p_{3/2}$ proton knockout from N-polarized $^7Li$ by unpolarized electrons of 700 MeV energy. The final proton energy is 144 MeV and q=2.6 $fm^{-1}$. Bound state from ref. 7, optical model from ref. 5 (solid line) and from ref. 6 (dashed line); dotted line for PWIA.

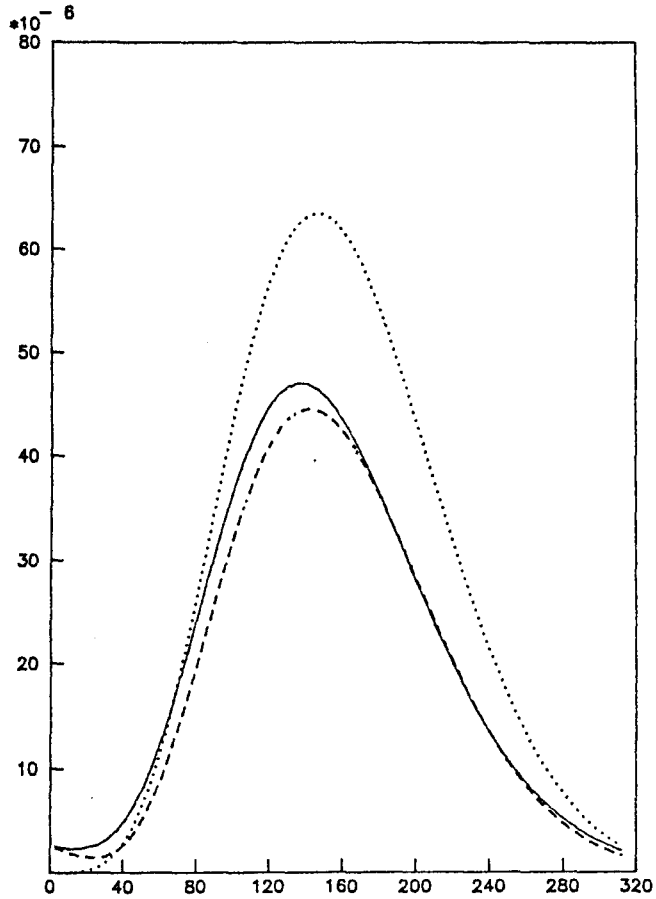


Fig. 2. Cross section ($fm^3$ $sr^{-2}$) vs. recoil momentum (MeV/c) for $d_{3/2}$ proton knockout from N-polarized $^{39}K$ by unpolarized electron of 500 MeV energy. The final proton energy is 100 MeV and q=2.2 $fm^{-1}$. Bound state from ref. 7 and optical model from ref. 8 for the solid line, bound and scattering states with the hamiltonian of ref. 9 for the dashed line; PWIA for the dotted line.

electrons. The same situation occurs when the target polarization is perpendicular to the hadron plane, because in this case $J_{-\lambda}\, J^*_{-\lambda'} = (-)^{\lambda+\lambda'}\, J_\lambda\, J^*_{\lambda'}$.

The primed structure functions $f'_{11}$, $f'_{01}$ and $\tilde{f}'_{01}$ contribute only in the presence of polarized electrons. If in addition to an unpolarized electron beam also an unpolarized target is used, the familiar form in terms of only four structure functions, $f_{\lambda\lambda'}$, is obtained.[3]

When $\gamma = 0$, the decomposition (6) in terms of nine structure functions is not possible because the angle $\alpha$ is no more defined. However, $\Sigma$ and $\Delta$ can still be expressed in the form of eqs. (2) and (3) in terms of six F-responses. This means that in the socalled parallel kinematics ($\gamma = 0$) six responses enter in the cross section contrary to what happens in the case with unpolarized targets where only two structure functions survive.

In the particular case of parallel kinematics and orientation of the target polarization along $\vec{q}$, i.e. of what can be called a superparallel kinematics, for symmetry reasons only $F_{00}$, $F_{11}$ and $F'_{11}$ survive in general, whereas the interference responses $F_{01}$, $F_{1-1}$ and $F'_{01}$ vanish.

The relevant quantity containing all the necessary ingredients for describing the knockout process is the matrix element in eq. (8).

The results presented in this paper are obtained with the nonrelativistic charge-current operator along the lines of previous work.[2,3]

The general formalism is here applied to the case of proton knockout by an electron of positive helicity from a polarized target. For each target polarization the nine structure functions depend on $\omega$, q, p' and $\gamma$. Specific cases can be studied with 100% target

polarization (m = j) oriented longitudinally (L), normally (N) and sideways (S) with respect to the incident electron direction.[4] For symmetry reasons the N-polarization reduces the number of nonvanishing structure functions to five: only $f_{00}$, $f_{11}$, $f_{01}$, $f_{1-1}$ and $f'_{01}$ survive. Without final state interactions $f'_{01} = \overline{f}_{01} = \overline{f}_{1-1} = 0$ for L- and S-polarization of the target.

In ref. 1 figures are given for the different structure functions in $^{7}$Li and $^{39}$K under standard kinematical conditions. Their separation requires out-of-plane experiments with a high degree of precision.

As a first step one can measure cross sections which do not necessarily require out-of-plane kinematics nor such a high precision as do structure functions. In fact a measurement of the cross section with coplanar kinematics either with or without polarized incident electrons would be extremely useful to give access to new information. The numerical calculations indicate that peak values are obtained of the same order of magnitude as the ones with unpolarized targets. As an example to set the scale and to show the sensitivity to final state interactions in figs. 1 and 2 the cross section obtained with unpolarized electrons for N-polarized $^{7}$Li and $^{39}$K is reported.

With coplanar kinematics one can also measure asymmetries, i.e.

$$(\Sigma^N - \Sigma^S)/\Sigma_0 \ , \ (\Sigma^L - \Sigma^N)/\Sigma_0 \ , \ (\Sigma^S - \Sigma^L)/\Sigma_0 \ , \qquad (9)$$

where $\Sigma_0$ is the cross section with unpolarized target and unpolarized electron. These asymmetries are determined by the behaviour of the usual four structure functions $f_{00}$, $f_{11}$, $f_{01}$ and $f_{1-1}$ with different orientations of the target polarization. Only two of them are independent. In fig. 3 the N-S and the L-N asymmetries are given for $p_{3/2}$ hole in $^{39}$K as a function of the recoil momentum $p_R$ under the same kinematic conditions of fig. 2. These asymmetries are not vanishing as an indication that different results are expected for different orientation of the target polarization. Moreover, the size of the asymmetry is measurable and is increased by final state interactions.

Another measurable quantity with coplanar kinematics is the electron polarization ratio $\Delta/\Sigma$ with L- and S-polarization of the target. For N-polarization, $\Delta/\Sigma = 0$ as already noticed in ref. 4. In fig. 4 $(\Delta/\Sigma)_L$ is plotted for the $p_{3/2}$ hole in $^{7}$Li. This result shows that the electron polarization ratio is large and can be measured, e.g., on top of the $p_{3/2}$ momentum distribution ($p_R \simeq 100$ MeV/c) with a weak dependence on final state distortion.

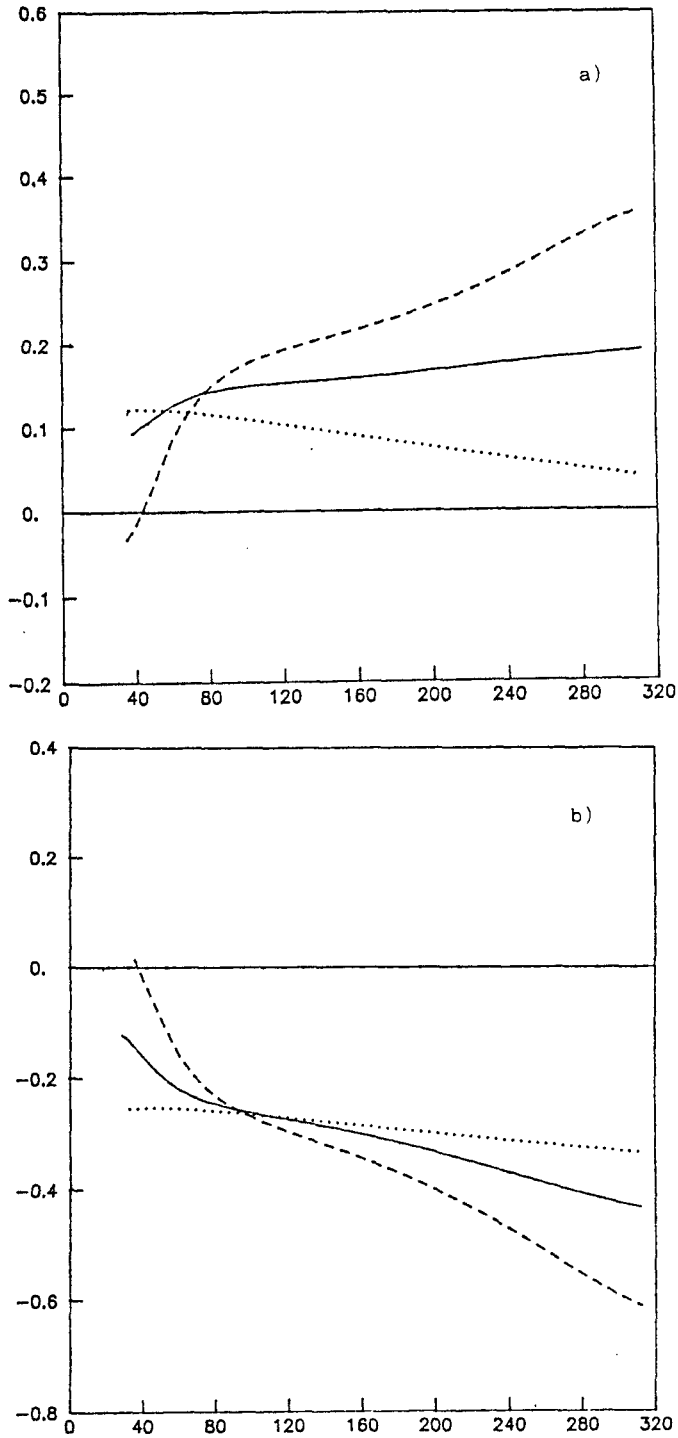


Fig. 3. Asymmetries a) $(\Sigma^N-\Sigma^S)/\Sigma_0$ and b) $(\Sigma^L-\Sigma^N)/\Sigma_0$ vs. recoil momentum (MeV/c) for $d_{3/2}$ hole in $^{39}$K under the same conditions as in fig. 2.

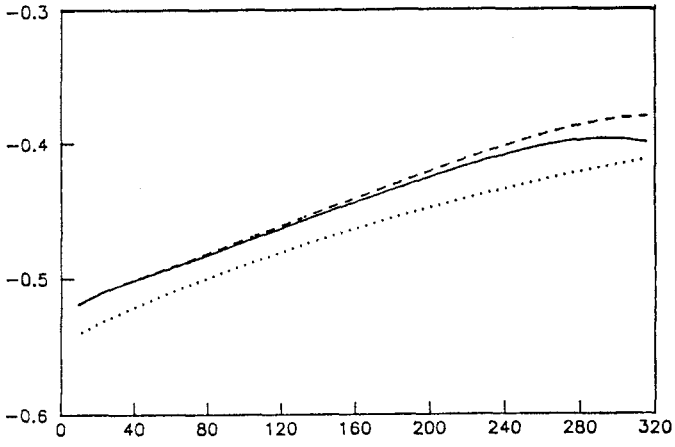


Fig. 4. The electron polarization ratio $\Delta/\Sigma$ vs. recoil momentum (MeV/c) with L-polarization of the $^7$Li target nucleus for $p_{3/2}$ hole under the same conditions as in fig. 1.

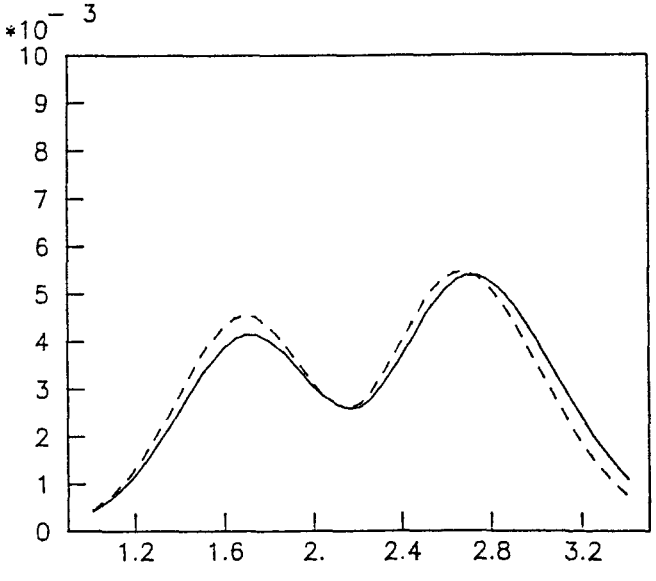


Fig. 5. The response $F_{11}$ (fm$^3$) vs. momentum transfer q (fm$^{-1}$) for $d_{3/2}$ hole in $^{39}$K polarized along $\vec{q}$ under parallel kinematic conditions. The other conditions are as in fig. 2.

The superparallel kinematics a priori involving only three nuclear responses is in principle interesting in order to achieve their separation. In fact, $F'_{11}$ is simply determined by flipping the electron helicity. Then a Rosenbluth separation determines $F_{00}$ and $F_{11}$. In addition, in the present model based on the impulse approximation, $F_{00}$ vanishes for a target spin $j > 3/2$ ($m = j$) and $F_{11} = \pm F'_{11}$.

In fig. 5 $F_{11}$ is plotted for the $d_{3/2}$ hole in $^{39}$K. It appears that the maximum corresponding to $p'<q$ is higher by $\sim$ 20% than the one corresponding to $p'>q$. This large asymmetry as well as the whole response itself is entirely due to the final state interaction because in PWIA $F_{11} = 0$.

## References


1. S.Boffi, C.Giusti and F.D.Pacati, to be published; S.Boffi, C.Giusti, F.D.Pacati and M.Radici, Proc. of CEBAF 1986 Summer Workshop, eds. F.Gross and J. Mougey (to be published).
2. S.Boffi, C.Giusti and F.D.Pacati, Nucl. Phys. A435, 697 (1985).
3. S.Boffi, C.Giusti and F.D.Pacati, Nucl. Phys. A386, 599 (1982).
4. T.W.Donnelly, in Perspectives in Nuclear Physics at Intermediate Energies, ed. S.Boffi, C.Ciofi degli Atti and M.M.Giannini (World Scientific, Singapore, 1984) p. 244; T.W.Donnelly and A.S.Raskin, Ann. of Phys. 169, 247 (1986).
5. A.K.Kerman, H.McManus and R.M.Thaler, Ann. of Phys. 8, 551 (1959).
6. O.N.Jarvis, C.Whitehead and M.Shal, Nucl. Phys. A184, 615 (1972).
7. L.R.B.Elton and A.Swift, Nucl. Phys. A94, 52 (1967).
8. P.Schwandt, H.O.Meyer, W.W.Jacobs, A.D.Bacher, S.E. Vigdor, M.D.Kaitchuck and T.R.Donoghue, Phys. Rev. C 26, 55 (1982).
9. M.M.Giannini and G.Ricco, Ann. of Phys. 102, 458 (1976).

# SPIN DEGREES OF FREEDOM IN ELECTRON NUCLEON SCATTERING IN THE RESONANCE REGION

Volker D. Burkert
CEBAF
12070 Jefferson Avenue
Newport News, VA 23606, USA

## Abstract

Some aspects of using polarized electrons and/or polarized targets in electron-nucleon scattering experiments are discussed. Polarization measurements can be used to extend the knowledge of nucleon formfactor measurements to higher $Q^2$ and are indispensable for a model-independent extraction of the helicity amplitudes of exclusive meson production. Measurements of polarization asymmetries may also help in revealing the excitation of weaker resonances.

## I. Introduction

The study of the electromagnetic couplings of the ground state nucleon and its excited states should be an essential part of any research program to investigate electroweak interactions with nuclei. The ultimate goal in studying the 'elementary' process is to obtain information on the $\gamma_v NN^*$ vertex. Detailed knowledge of this transition provides the data base which is necessary for the interpretation of electron nucleus scattering at high momentum and high energy transfer. The understanding of nucleon-nucleon correlation, e.g., will depend essentially upon our understanding of the role played by nucleon resonances in nuclei. Studying nucleon resonance transition is, on the other hand, very important in itself. The knowledge of the $Q^2$ dependence of the $\gamma_v NN^*$ transition appears crucial for the development of more realistic, QCD based, interquark potentials for light quarks, and finally for the definite implementation of QCD to hadrons at intermediate distances where non perturbative effects have to be taken into account.

## II. The Electric Formfactor of the Neutron and the Proton

The hadronic current in elastic electron nucleon scattering is specified by the electric and magnetic formfactors $G_E(Q^2)$ and $G_M(Q^2)$. The knowledge of these quantities up to the highest possible $Q^2$ is not only of fundamental importance for testing microscopic models of the nucleon and its electromagnetic coupling, but has strong impact on the interpretation of electron nucleus scattering in general. Our present knowledge is practically limited to the magnetic formfactors $|G_{Mp}|$ and $|G_{Mn}|$ which have been measured for $Q^2$ up to 30 and 20 GeV$^2$, respectively. $G_{Ep}$ has been measured up to 3GeV$^2$ with uncertainties between 10% and 30% at $Q^2$>1GeV$^2$. Little is known about the electric formfactor of the neutron. In fact, our only solid knowledge comes from scattering of thermal neutrons off electrons from atoms, showing that $dG_{En}/dQ^2 > 0.$ at $Q^2 \to 0$. There is some information on $G_{En}$ at $Q^2 < 1.\text{GeV}^2$, extracted from elastic eD scattering[1]. These results, however, are necessarily model dependent in that they depend on the specific deuteron wavefunction assumed in the analysis. Attempts to measure $|G_{En}|$ from quasielastic eD scattering have not yielded satisfactory results[2]. A model independent measurement of $G_{En}$ is urgently needed. Studying quark effects in nuclei at large $Q^2$ will bear heavily on the knowledge of the nucleon formfactors, since new effects will reveal themselves as deviations from the "conventional" picture of the nucleus.

Several ways of measuring this fundamental quantity have been proposed. One way is to measure $G_{En}$ in scattering of polarized electrons from unpolarized neutrons and to study the neutron recoil polarization in a second scattering experiment[3]. An alternative method is to use quasielastic scattering of polarized electrons from vector polarized deuterium[4]. I will briefly discuss this latter method which may be of interest not only for use in storage rings but for external beam experiments at Bates and CEBAF as well.

For an orientation of the neutron spin in the electron scattering plane perpendicular to the direction of $\gamma_v$, the elastic electron neutron cross section is given by:

$$\frac{d\sigma}{d\Omega} = \left(\frac{d\sigma}{d\Omega}\right)_o \left[1 + P_e P_n A^n(Q^2)\right]$$

($P_e$=electron polarization, $P_n$=effective neutron polarization, $(d\sigma/d\Omega)_o$=unpolarized cross section).
The asymmetry is given by:

$$A^n(\theta^2) = \frac{2\, G_{En}\, G_{Mn}\, \sqrt{\tau(1+\tau)}\, \text{tg}\,\frac{\theta e}{2}}{G_{En}^2 + \tau G_{Mn}^2 + 2\tau^2(1+\tau) G_{Mn}^2\, \text{tg}^2\,\frac{\theta e}{2}} \; ; \; \tau = \frac{Q^2}{4M_n^2}$$

The appearance of the interference term allows the measurement of $G_{En}$ if $G_{Mn}$ is known, without Rosenbluth separation. This is advantageous in determining the electric formfactor because $G_{En}$ is expected to be small[5], and its contribution to the elastic cross section at large $Q^2$ is negligible. Fig. 1 shows the expected asymmetry for $G_{En}=0$ and $G_{En}=-\tau G_{Mn}/\mu_n$, both of which are consistent with present data at not too small $Q^2$.

### 1. An Experiment to Measure $G_{En}$ in $\vec{d}(\vec{e},e'n)p$

Using a polarized $ND_3$ solid state target with an approximately 20mW cooling power at a temperature of ≃270mK, luminosities of ≃$0.6\cdot10^{32}$ cm$^{-2}$sec$^{-1}$ have been obtained (only neutrons in deuterium are counted)[6]. A cooling power of ≃500mW was achieved at ≃270mK in a dilution refrigerator[7]. This would allow measurements to be performed with effective luminosities in excess of $10^{33}$cm$^{-2}$sec$^{-1}$. Neutron polarizations of ≃45% were obtained in a 3.5T magnetic field[8]. With a 5T field, neutron polarizations of 60% can be anticipated. Using appropriate kinematical cuts on the scattered electron and the recoil neutron angle, background contributions from neutrons in the nitrogen nucleus can largely be suppressed, and effective polarizations of ≃40% should be achievable[9]. The expected running time of a measurement of $G_{En}$ is shown in Fig. 2 for a specific experimental setup. It is perhaps worthwhile noting that the use of polarized deuterium as target material has the advantage of allowing the same measurement to be carried out with protons (from the deuterons). A comparison of proton measurements with $ND_3$ and $NH_3$ as target materials would allow the testing of effects which may result from the binding of the proton in the deuteron. This information provides a sensitive mean in correcting the neutron data for nuclear effects.

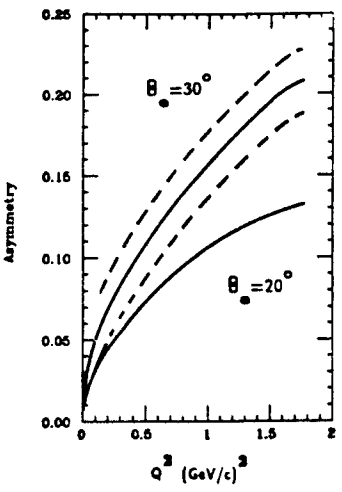


Fig. 1 Polarization asymmetry $\vec{n}(\vec{e},en)$ for electron scattering angles. $G_{En}=-\tau G_{Mn}/\mu_n$ has been assumed. $A_n=0$ if $G_{En}=0$. The dashed lines indicate an uncertainty $\delta A = \pm 0.02$.

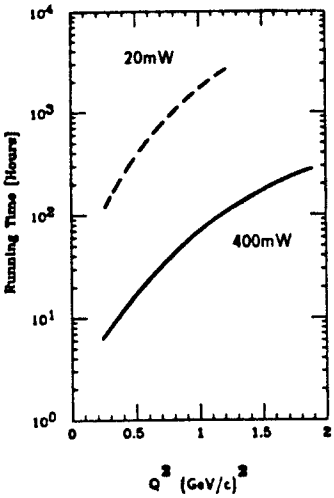


Fig. 2 Running time for an experiment to measure the neutron asymmetry with $\delta A = \pm 0.02$, for polarized target cryostats with different cooling power.

## 2. An Experiment to Measure $G_{Ep}$ in $\vec{p}(\vec{e},e'p)$

The method outlined above can also be used to measure the polarized proton asymmetry using $NH_3$ as polarized target material. Hence the electric formfactor $G_{Ep}$ of the proton can be measured. Since protons can be polarized to a higher degree than deuterons at higher temperatures, polarized proton targets can be operated at much higher cooling powers and therefore can be used with higher electron currents. With a $^4$He cryostate of ≃10 Watts of cooling power at 1 Kelvin, luminosities of $5\cdot10^{34}$ cm$^{-2}$sec$^{-1}$ (only free protons count) can be achieved[18]. The polarization asymmetry as predicted by QCD sum rule calculations[5] is shown in Fig. 3. The expected running time of an experiment to measure $G_{Ep}$ is displayed in Fig. 4. Measurements of $G_{Ep}$ for $Q^2_{Ep}$ up to 6 GeV$^2$ appear feasible using existing polarized target technology.

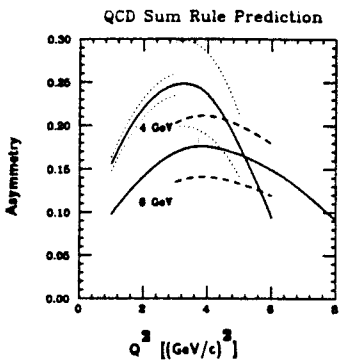


Fig. 3 QCD sum rule prediction of the polarized $\vec{p}(\vec{e},ep)$ asymmetry.

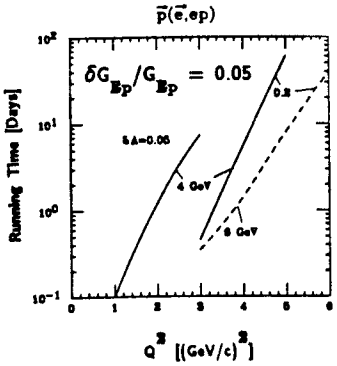


Fig. 4 Expected running time for an experiment to measure $G_{Ep}$ with ±5% and ±20%, respectively.

In summary, it appears that with presently available polarized solid state target technology, considerably higher $Q^2$ values can be reached in measuring the electric proton and neutron formfactors than has been possible with the usual Rosenbluth separation.

## III. Electroproduction of Nucleon Resonances

Studying the $Q^2$ dependence of the $\gamma NN^*$ transition for the nucleon resonances gives us many details of the wavefunction of the excited states. This knowledge is essential in developing more realistic interquark potentials which are based on the fundamentals of QCD[11]. It appears important to obtain as much information as possible to probe the full electromagnetic structure of the transition, including its spin structure. Before discussing exclusive measurements in some detail, it is perhaps instructive to recall some features of the inclusive cross section in the resonance region.

### 1. The Inclusive Cross Section p(e,e')X

It is widely assumed that the cross section for electroproduction of nucleon resonances would decrease faster with increasing $Q^2$ than the nonresonant part does. This, however, turns out not to be the case, as can be inferred from Fig. 5, where the total photoabsorption cross section in the mass region up to W≃2GeV is shown for small and large values of $Q^2$[12]. I want to point out several interesting features in the $Q^2$ dependence of the cross section:

- -- The strong enhancement in the region of the Δ(1232) disappears quickly at large $Q^2$.
- -- The enhancements near W≃1.5GeV and W≃1.7GeV remain prominent up to the highest $Q^2$. The signal/background ratio does not appear to decrease at all over the entire $Q^2$ range.
- -- The shoulder near W≃1.45GeV in the $Q^2$=0 data, which is generally attributed to the excitation of the Roper $P_{11}(1440)$, disappears very quickly with $Q^2$. Already at $Q^2$=0.1GeV$^2$ there are no indications of an excitation of this resonance any more.
- -- At $Q^2$>3GeV$^2$ a resonant structure near W≃1.4 GeV seems to emerge which may even become dominant over the Δ(1232) at the highest $Q^2$.

In conclusion, the total photoabsorption cross section indicates very different $Q^2$ dependences for the various resonant parts of the cross section. The fast decrease of the Δ(1232) excitation strength offers the possibility to study the lower mass region at large $Q^2$ in detail, where the cross section is no longer dominated by the higher mass tail of the Δ(1232). This may prove especially important for studying the excitation of the $P_{11}(1440)$ and possible other $P_{11}$ partners nearby.

It is obvious that due to the large widths and large number of resonances (approximately 20 with masses below 2 GeV) individual resonances can in general not be isolated[13]. A program to separate and study details of single resonances requires studying spin and isospin structure of the intermediate state which can only be done by measuring the resonance decay products in exclusive experiments.

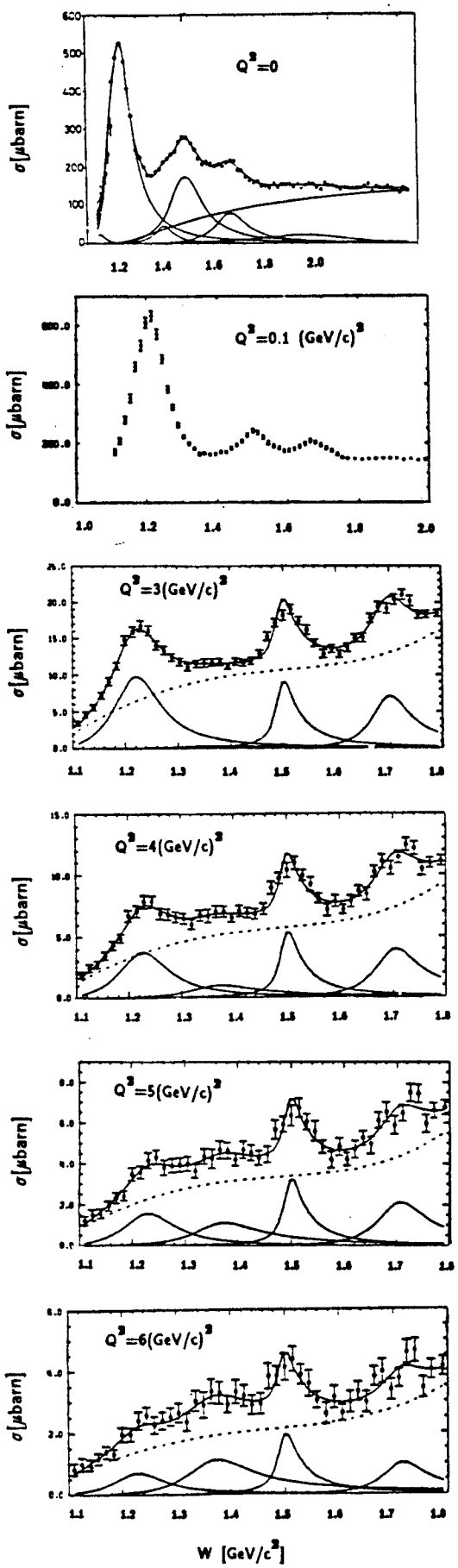


Fig. 5 Inclusive cross section for p(e,e′)x at fixed $Q^2$.

## 2. Exclusive Reactions for Resonance Studies

Many of the lower lying resonances have a strong single $\pi$ or $\eta$ decay channel. The reactions $p(e,e'p)\pi^0(\eta)$, $p(e,e'\pi^+)n$ and $n(e,e'\pi^-)p$ are therefore most suitable for studying resonance properties. The unpolarized coincidence cross section is given by

$$\frac{d\sigma}{dE_e' d\Omega_e d\Omega_\pi} = \Gamma_T\left[\sigma_T + \epsilon\sigma_L + \epsilon\sigma_{TT}\cos 2\phi + \sqrt{\epsilon(1+\epsilon)/2}\,\sigma_{TL}\cos\phi\right]$$

The first and third term depend on the transverse unpolarized and polarized coupling of the photon, the second term depends on the the longitudinal part and the last term is a transverse/longitudinal interference term. These quantities are functions of $Q^2$, W, $\theta^*$ and can be expressed in terms of 6 complex, parity conserving helicity amplitudes[14]:

$$\sigma_T = P/2K\left[|H_1|^2 + |H_2|^2 + |H_3|^2 + |H_4|^2\right]$$
$$\sigma_L = P/2K\left[|H_5|^2 + |H_6|^2\right]$$
$$\sigma_{TT} = P/K\ \mathrm{Re}\left(H_2 H_3^* - H_1 H_4^*\right)$$
$$\sigma_{TL} = 2P/K\ \mathrm{Re}\left[H_5^*(H_1 - H_4) + H_6^*(H_2 + H_3)\right]$$

A complete and model independent determination of these amplitudes requires at least 11 independent measurements at each kinematical point. Unpolarized experiments allow four independent measurements only. With a polarized beam one additional combination of these amplitudes can be measured. A polarized nucleon target allows eight sensible measurements, and experiments with polarized beams and polarized target allow measurement of five more combinations of amplitudes[15]. If one can measure the recoil polarization, e.g., if the final state nucleon is a proton, one can obtain the same number of combinations as with a polarized target, four of which are different from the polarized target case[16].

A separation of the various terms requires detailed out-of-plane measurements. In addition to the $\cos\phi$ and $\cos 2\phi$ terms of the unpolarized cross section $\sin\phi$ and $\sin 2\phi$ terms appear in the polarization dependent terms. Also, measurements with different orientations of the target spin will be necessary.

## 3. Existing Data

Although such a detailed experimental program has not been conducted so far, some information, in particular on the most prominent resonances, has been obtained from measuring the angular dependence of the unpolarized coincidence cross section. From experiments performed at the BONN, DESY, NINA synchrotrons[12,9] we have limited information on the transverse helicity amplitudes $A_{1/2}$ and $A_{3/2}$ for the $P_{33}(1232)$, $S_{11}(1535)$, $D_{13}(1520)$ and the $F_{15}(1688)$ proton resonances. It is well known that the $\gamma_v pP_{33}(1232)$ transition amplitudes drop faster with $Q^2$ than the elastic formfactor. As can be inferred from Fig. 6, the other resonances show quite a different behaviour.

The $S_{11}(1535)$ which can only be excited by helicity 1/2 in the $\gamma_v p$ initial state exhibits a strikingly weak $Q^2$ dependence. At $Q^2$=3 GeV$^2$, the $A_{1/2}$ has decreased by only 50% of its value at $Q^2$=0. For the $D_{13}(1520)$ and the $F_{15}(1688)$ the helicity-3/2 dominance at $Q^2$=0 switches to a helicity-1/2 dominance at large $Q^2$, a behaviour that is qualitatively in accordance with quark model predictions[11], as well as with expectations

from helicity conservation in perturbative QCD[17]. The transition to helicity 1/2 dominance seems to be a general feature at high $Q^2$. It is the details, however, of how this transition occurs that would give us insight into the dynamics of the multiquark-gluon system. Very little information is available for resonances other than the ones mentioned above, and practically no data exist for neutron resonances.

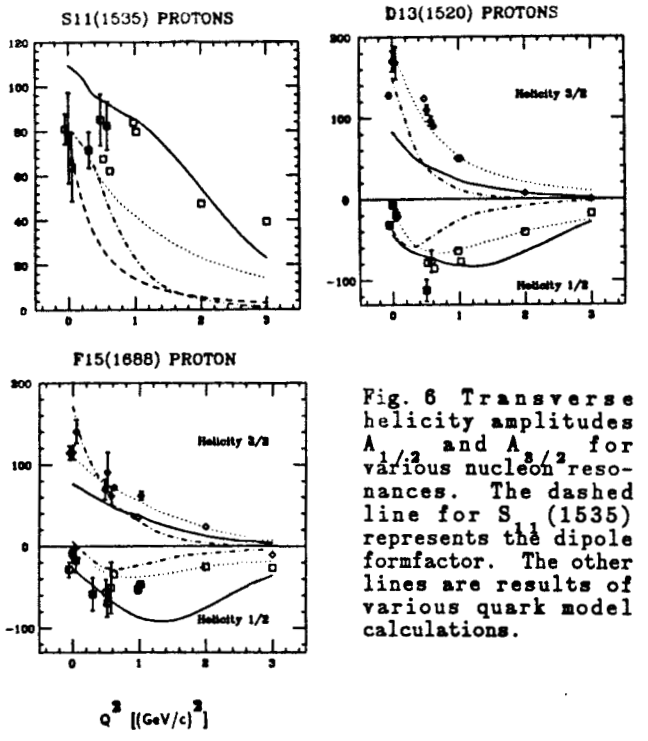


Fig. 6 Transverse helicity amplitudes $A_{1/2}$ and $A_{3/2}$ for various nucleon resonances. The dashed line for $S_{11}(1535)$ represents the dipole formfactor. The other lines are results of various quark model calculations.

It should be noted that the data points in Fig. 6 are subject to systematic uncertainties, largely due to the limited experimental information that could be used in the data analysis. Also, there are uncertainties in the description of the nonresonant part of the cross section[12].

An experimental program to study electroproduction of nucleon resonances should be able to combine very high statistics unpolarized cross section measurements and detailed polarization measurements of the relevant asymmetries, going up to the highest possible $Q^2$. Polarization asymmetries contain interference terms of amplitudes. They are therefore especially sensitive to small amplitudes and to relative phases between amplitudes. Already information of limited statistical accuracy will prove extremely sensitive in determining signs and absolute values of the less prominent amplitudes. In the following chapter we give two examples to illustrate the sensitivity of polarization asymmetries to small amplitudes.

## 4. The Scalar Amplitude $S_{1+}$ in the $\gamma_v p\Delta(1232)$ Transition

Quark models with SU(6) symmetry yield $S_{1+} \equiv 0$ for the scalar (longitudinal) multipole as a consequence of the assumed pure magnetic dipole transition between two states with angular momentum $L_{qq}=0$ of the 3 quark system. The inclusion of a hyperfine color magnetic interaction arising from the QCD motivated one gluon exchange between the valence quarks[18] leads to a finite longitudinal coupling, reflecting the (SU(6) forbidden) L=2 state of the multiquark wavefunction[19]. Our present knowledge on $S_{1+}$ for the $\Delta(1232)$ comes from studying $p(e,e'p)\pi^0$. Assuming s and p wave contributions only, and $M_{1+}$ dominance (only terms with $M_{1+}$ are retained), the unpolarized cross section can be written as:

$$\frac{d\sigma}{d\Omega_\pi^*} \simeq \left[\frac{5}{2}|M_{1+}|^2 - 3\,\mathrm{Re}\left(M_{1+}E_{1+}^*\right) + \mathrm{Re}\left(M_{1+}M_{1-}^*\right)\right]$$
$$+ \cos\theta_\pi^*\left[2\mathrm{Re}\left(E_{0+}M_{1+}^*\right)\right]$$
$$+ \cos^2\theta_\pi^*\left[-\frac{3}{2}|M_{1+}|^2 + 9\mathrm{Re}\left(M_{1+}E_{1+}^*\right) - 3\mathrm{Re}\left(M_{1-}M_{1+}^*\right)\right]$$
$$+ \epsilon\cdot\sin^2\theta_\pi^*\cdot\cos 2\phi\left[-\frac{3}{2}|M_{1+}|^2 - 3\mathrm{Re}\left(M_{1+}E_{1+}^*\right)\right]$$
$$+ \sqrt{2\epsilon(1+\epsilon)}\cdot\sin\theta_\pi^*\cdot\cos\phi\left[-\mathrm{Re}\left(S_{0+}M_{1+}^*\right) - 6\cos\theta_\pi^*\cdot\mathrm{Re}\left(S_{1+}M_{1+}^*\right)\right]$$

From studying the $\phi$ and $\theta_\pi^*$ dependence of the cross section one can separate the term $\mathrm{Re}(S_{1+}M_{1+}^*)$, which is most sensitive to $S_{1+}$. Fig. 7 shows results of previous measurements. The accuracy of existing data is clearly not sufficient to separate resonant and nonresonant parts. Note that the quantity $\mathrm{Re}(S_{1+}M_{1+}^*)/|M_{1+}|^2$ is displayed. A resonance-like behaviour of $S_{1+}$ would result in a flat distribution in this quantity. The $Q^2$=1GeV$^2$ data show some W dependence which may indicate that the measured quantity contains nonresonant contributions. In order to enable a full determination of the resonant and nonresonant contribution to $(S_{1+}M_{1+}^*)$, a measurement of the term $\mathrm{Im}(S_{1+}M_{1+}^*)$ is required as well. This term is particularly sensitive to nonresonant contributions. If only $S_{1+}$ and $M_{1+}$ amplitudes of the resonance contribute, having the same phases, the term $\mathrm{Im}(S_{1+}M_{1+}^*)$ would vanish identically. According to fixed and dispersion relation calculations the nonresonant contribution $\mathrm{Re}S_{1+}(I=1/2)$ may be of the same order of magnitude as $\mathrm{Re}S_{1+}(I=3/2)$. This would result in quite different phases for $M_{1+}$ and $S_{1+}$, which consequently give rise to a sizeable polarization asymmetry in the vicinity of the resonance.

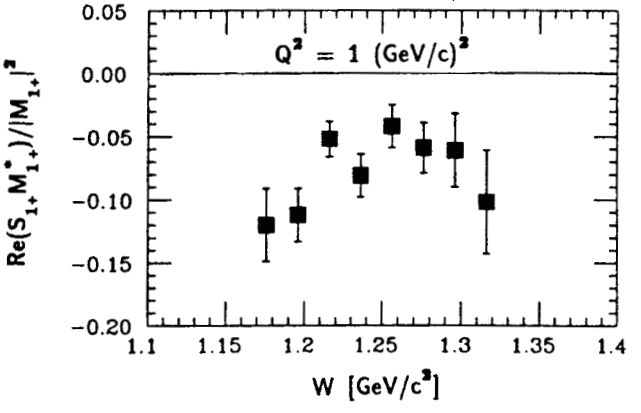


Fig. 7 The quantity $\mathrm{Re}(S_{1+}M_{1+}^*)/|M_{1+}|^2$ in the $\Delta(1232)$ region. Data from DESY[27].

The quantity $\mathrm{Im}(S_{1+}M_{1+}^*)$ can be measured by using a longitudinally polarized electron beam and measuring the cross section asymmetry[28].

$$A_e \simeq \sqrt{2\epsilon(1-\epsilon)}\cdot\sin\phi\cdot\sin\theta_\pi^*\left[\mathrm{Im}\left(S_{0+}M_{1+}^*\right) + 6\cos\theta_\pi^*\mathrm{Im}\left(S_{1+}M_{1+}^*\right)\right]$$

In this expression the same approximation as in the unpolarized cross section has been assumed. This experiment requires a measurement of the $\theta_\pi^*$ distribution of one of the outgoing hadrons at large $\phi$ (out of the scattering plane). Measuring the $\theta_\pi^*$ dependence of $A_e$ at fixed $\sin\phi$ enables a separation of $\mathrm{Im}(S_{0+}M_{1+}^*)$ and $\mathrm{Im}(S_{1+}M_{1+}^*)$. Asymmetries of 5 to 10% can be expected[19].

## 5. Polarized Target Asymmetry in the Region of the $P_{11}(1440)$

There is an ongoing controversy as to whether or not the $P_{11}(1440)$ is actually composed of two $P_{11}$ resonances as a recent analysis indicates[12]. In electroproduction, however, only weak indications of a resonant structure in this particular mass region have been seen in unpolarized electroproduction experiments. Single pion photoproduction data have on the other hand revealed a rather strong resonance excitation[22]. Pion electroproduction may help solve the above controversy because of the additional kinematical degree of freedom given by $Q^2$. The various resonances may exhibit very different $Q^2$ dependence.

Measurements of asymmetries with polarized targets appear quite sensitive to the strength of the $P_{11}(1440)$ excitation. Fig. 8 shows the sensitivity of the target asymmetry in $\pi^0$ production to the excitation of the $P_{11}(1440)$. By choosing a suitable orientation of the target polarization and by carefully selecting the kinematics of the decay particles, interference effects may become large and exhibit sizable effects even from weak resonances. In this example the amplitudes which have been obtained in an analysis[22] of the world data at $Q^2$=1 GeV$^2$ were used. In the analysis, a sizable longitudinal amplitude $S_{1-}$ was found for the $P_{11}(1440)$. This gives rise to strong effects in $T_x$ which contains transverse-longitudinal interference terms.

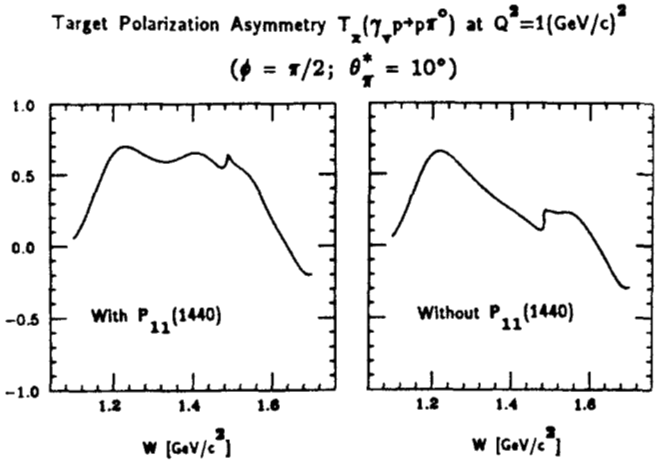


Fig. 8 Polarized target asymmetry $T_x(\gamma_v p\to p\pi^0)$ for a specific kinematical situation. The target protons are polarized perpendicular to the virtual photon direction, in the electron scattering plane. Results of a recent analysis[22] have been used to predict the asymmetry (l.h.s.). To illustrate the sensitivity to the longitudinal coupling of the $P_{11}$, the expected asymmetry is shown if the $P_{11}$ were not excited (r.h.s.).

## 6. Double Polarization Asymmetry

With a polarized beam and a polarized nucleon target, one can measure double polarization asymmetries which require flipping the spin of the electron as well as of the target nucleons. Of particular interest is the asymmetry $D_z$

$$D_z = \frac{\sigma(P_z{=}1,P_e{=}1)-\sigma(P_z{=}1,P_e{=}-1)-\sigma(P_z{=}-1,P_e{=}1)+\sigma(P_z{=}-1,P_e{=}-1)}{\sigma(P_z{=}1,P_e{=}1)+\sigma(P_z{=}1,P_e{=}-1)+\sigma(P_z{=}-1,P_e{=}1)+\sigma(P_z{=}-1,P_e{=}-1)}$$

where the nucleon spin is aligned parallel and antiparallel to the direction of the virtual photon. Fig. 9 shows that this asymmetry can be large. $D_z$ measures directly the helicity asymmetry

$$\frac{1}{2\pi}\int D_z\left(Q^2,W,\theta^*_\pi,\phi\right)d\phi = \frac{\sigma^T_{1/2}-\sigma^T_{3/2}}{2\sigma_0}$$

for the transverse cross section. The partial wave analysis of this quantity at fixed $Q^2$ and W yields the helicity asymmetry for single partial waves. Unpolarized measurements allow the determination of $\sigma^T_{1/2}+\sigma^T_{3/2}$ for single partial waves. The two measurements combined allow determination of $\sigma^T_{1/2}\sim|\sigma A_{1/2}|^2$ and $\sigma^T_{3/2}\sim|A_{3/2}|^2$ for specific resonances (after subtracting the nonresonant background). $A_{1/2}$ and $A_{3/2}$ have been predicted by microscopic models of the nucleon and provide tests of the helicity structure of the resonance transition. In view of the quark model and QCD predictions, e.g., that $\sigma_{3/2}$ should vanish at large $Q^2$, measurements of this type provide immediate tests of essential aspects of theoretical approaches in the nonperturbative regime. In Fig. 9 examples of predictions for $D_z$ are shown.

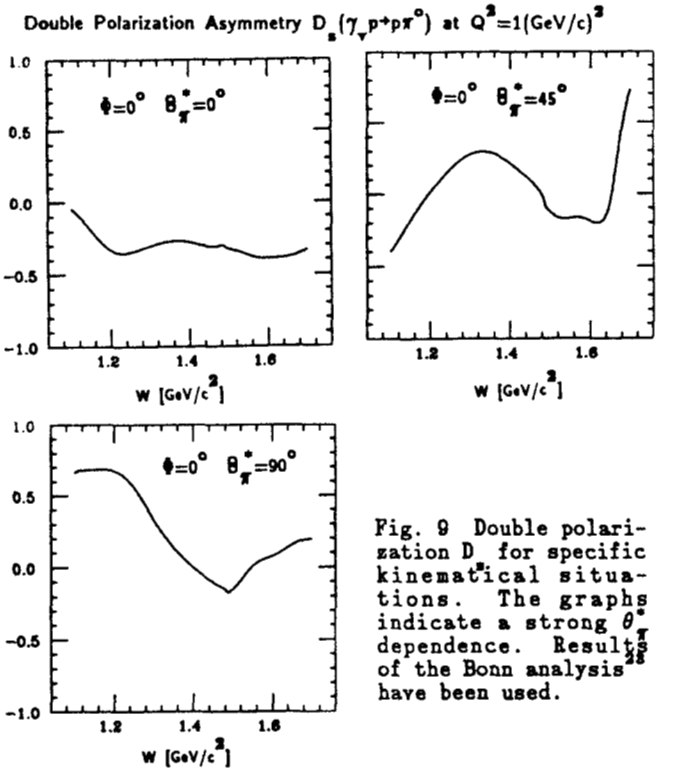


Fig. 9 Double polarization $D_z$ for specific kinematical situations. The graphs indicate a strong $\theta^*_\pi$ dependence. Results of the Bonn analysis[23] have been used.

## IV. Parity Violation Measurement in the Δ(1232) Region

In low energy ($Q^2 \ll M_Z^2$) neutral current interactions, the parity violating contribution arises from the interference between the one-photon exchange ann the neutral weak boson (Z°) exchange graphs. In electron scattering, the interaction contains an isoscalar as well as an isovector piece in both the vector ($V_\mu$) and axial vector ($A_\mu$) coupling. The effective Lagrangian which describes the parity non-conserving )PNC) part of the interaction for electron hadron scattering is given by[24]

$$L^{PNC}_{eff} = -\frac{G_F}{\sqrt{2}}\cdot\left[\bar e\gamma_\mu\gamma_5 e\left(\tilde\alpha V^3_\mu+\tilde\gamma V^0_\mu\right) + \bar e\gamma_\mu e\left(\tilde\beta A^3_\mu+\tilde\delta A^0_\mu\right)\right]$$

The $\tilde\alpha$, $\tilde\beta$, $\tilde\delta$, $\tilde\gamma$ denote the respective coupling constants which have to be determined experimentally. In the

Glashow-Salam-Weinberg Model (GSW) of electroweak interaction, these coupling constants can be expressed in terms of a single parameter, the weak mixing angle $\theta_W$. By choosing appropriate kinematical conditions for electron scattering from nucleons and nuclear targets, one can determine the couplings by a set of four linearly independent measurements.

The SLAC/Yale $D(\vec{e},e')X$ scattering experiment[25], in conjunction with atomic physics experiments[26], enabled a model independent determination of $\alpha$, $\gamma$. The Mainz experiment[27] measures a different combination of the four coupling constants and allows the extraction of a combination of $\beta$ and $\delta$, using the previously obtained results as an input. It should, however, be noted that this experiment measures quasielastic electron scattering from $^9$Be rather than elastic electron nucleon scattering. This fact could be of importance if the data are used for a determination of the weak angle. The Bates experiment[28], which has recently become operational, simply measures $\gamma$.

From this brief survey of existing measurements it is obvious that for a complete determination of the coupling constants additional measurements are needed. One should also attempt to measure a possible $Q^2$ dependence of these couplings. Deviations from the GSW model may occur at the level of one percent[29]. High precision measurements are therefore needed.

Various arguments have been made for measureing parity violation in elastic electron-proton scattering[30,32]. A precise measurement of the $\Delta$-excitation seems equally important. We summarize here some arguments for measuring this process.

- $\Delta(1232)$ excitation separates the isovector part $(\alpha, \beta)$.
- It is an almost pure magnetic resonance with a dominant magnetic dipole ($M_{1+}$) excitation. The scalar coupling ($S_{1+}$) and the electric coupling ($E_{1+}$) are both small.
- At low $Q^2$ (<0.6 GeV$^2$) the nonresonant background is small. Its effects on the PNC asymmetry should be reliably calculable[32]. In order to understand the PNC effects of the nonresonant part at the one percent level, more precise electroproduction data in different isospin channels will presumably be needed as well.
- The asymmetry is predicted to be large in the GSW model[31,34].

$$A_{\Delta(1232)} = \left[\frac{G_F}{\sqrt{2}}\right]\left[\frac{Q^2}{2\pi\alpha}\right]\left[\tilde{\alpha} + F(Q^2,E)\beta\right]$$

and has a strong sensitivity to $\sin^2\theta_W$.

The factor $F(Q^2,E)$ in the above formula is close to 1 in the energy range of interest. Assuming a weak angle of $\sin^2\theta_W = 0.225$, one obtains $A_{\Delta(1232)} \sim -1.17\times10^{-4}Q^2$.

## V. Conclusions

Polarization experiments open up a large variety of possibilities to study electromagnetic properties of the nucleon and its excited states with increased sensitivity compared to unpolarized measurements. The numerical examples chosen assumed an external target situation at CEBAF energies. Most of the experiments can, of course, be done with gas targets in storage rings, if high enough luminosities can be achieved. "High enough" translates as $\geq10^{32}$cm$^{-2}$sec$^{-1}$ for the measurement of the neutron electric formfactor and $\geq10^{34}$cm$^{-2}$sec$^{-1}$ for the proton electric formfactor. The nucleon resonance program would also need luminosities in excess of $10^{34}$cm$^{-2}$sec$^{-1}$ for a substantial improvement of previous work, if full solid angle coverage is provided.

Precision experiments for studying parity violation in electron scattering require measurements with very high luminosity ($L>10^{38}$cm$^{-2}$se c$^{-1}$) and large acceptance detectors[35,36]. Because of the luminosity requirements, these experiments will have to employ thick targets in an external beam line.

## References


1) S. Galster et al., Nucl. Phys. B32 (1971) 221.
2) W. Bartel et al., Nucl. Phys. B58 (1973) 429.
3) R. Arnold, C. Carlson, F. Gross, Phys. Rev. C23 (1981) 363.
4) V. Burkert, Lect. Notes in Phys. 234 (1984) 228.
5) W. A. Nesterenko, A. V. Radyushkin, Phys. Lett. 115B (1982) 410.
6) K. H. Althoff et al., Europhysics Conf. on Nuclear Physics with Electromagnetic probes, Paris (1985).
7) T. O. Niinikoski, Proc. 4th Workshop on Polarized Target Materials and Techniques, ed. W. Meyer, Bonn (1984).
8) W. Meyer et al., Nucl. Instr. Methods A244 (1986) 574.
9) V. Burkert, CEBAF Reports CR-86-002, CR-86-003, CR-86-011.
10) U. Hartfiel et al., Proc. 4th Workshop on Polarized Target Materials and Techniques, Bonn (1984).
11) W. Pfeil, Report of the 1986 Summer Study Group, CEBAF, Newport News, Virginia, 219.
12) F. Foster and G. Hughes, Rep. Prog. Phys. 46 (1983) 1445.
13) D. Walecka, Acta Physica Polonica B3 (1972) 117.
14) R. Walker, Phys. Rev. 182 (1969) 1729.
15) A. Bartl, W. Majeotto, Nucl. Phys., B62 (1973) 267.
16) H. Funsten, Report of the 1986 Summer Study Group, CEBAF, Newport News, Virginia, 183.
17) C. Carlson, Phys. Rev. D34 (1980) 2704.
18) N. Isgur, G. Karl, Phys. Rev. D19 (1979) 7653; Phys. Rev. D23 (1981) 817.
19) M. Bourdeau, N. C. Mukhopadhyay, Phys. Rev. Lett. 58 (1987) 976.
20) G. V. Gehlen, Nucl. Phys. B26 (1971) 141.
21) R. Arndt, J. Ford, D. Roper, Phys. Rev. D32 (1985) 1085.
22) R. L. Crawford, W. T. Morton, Nucl. Phys. B211 (1983) 1.
23) B. Boden and G. Kroesen, Report of the 1986 Summer Study Group, CEBAF, Newport News, Virginia.
24) P. Q. Hung, J. J. Sakurai, Phys. Lett. 63B (1976) 295.
25) C. Y. Prescott et al., Phys. Lett. 77B (1978) 347; Phys. Lett., 84B (1979) 524.
26) P. Q. Hung, J. J. Sakurai, Annual Rev. of Nucl. & Part. Science 31.
27) W. Achenbach et al., Presented at the Int. Symp. on High Energy Spin Physics, Protvino, Sept. 1986.
28) Proceedings of CEBAF Workshop on Parity Violation, Newport News, VA, Dec. 1986, ed. R. Siegel.
29) S. Kowalski, in (28).
30) P. Langacker, in (28).
31) D. Walecka, in (28); see also D. Walecka, Argonne Lecture Notes ANL-83-50 (1983).
32) S. Pollock, in (28).
33) S. Pollock, private communications.
34) D. Jones, S. Petcov, Phys. Lett. 91B (1980) 137.
35) V. Burkert, in (28).
36) B. Mecking, in (28).
37) J. C. Alder et al., Nucl. Phys. B46 (1972) 573.

# A TAGGED PHOTON BEAM FROM BREMSSTRAHLUNG ON AN ARGON JET TARGET

M. Anghinolfi[2], A. Bertocchi[3], N. Bianchi[1], G.P. Capitani[1], P. Corvisiero[2], E. De Sanctis[1], S. Frullani[3], F. Garibaldi[3], C. Guaraldo[1], P. Levi Sandri[1], V. Lucherini[1], L. Mattera[2], V. Muccifora[1], E. Polli[1], A.R. Reolon[1], G. Ricco[2], P. Rossi[1], M. Sanzone[2], M. Taiuti[2], G.M. Urciuoli[3], U. Valbusa[2] and A. Zucchiatti[2]

(1) I.N.F.N. - Laboratori Nazionali di Frascati, P.O.Box 13, I-00044 Frascati, Italy.

(2) Dipartimento di Fisica dell'Università di Genova o I.N.F.N. - Sezione di Genova, I-16146, Genova, Italy.

(3) Laboratorio di Fisica dell'Istituto Superiore di Sanità and I.N.F.N. - Sezione Sanità, I-00185, Roma, Italy.

Abstract. A proposed monochromatic photon beam produced by the tagging technique is described. The radiator is a condensed molecular beam of argon (thickness $10^{-8}$ g/cm$^2$) installed in a straight section of the Adone storage ring. The recoil electron counters are placed in the magnetic field of the next dipole ring. The tagging system defines 80 channels (each 1% resolution) covering the photon energy range (0.4 - 0.8 $E_0$. The total photon intensity is about $10^8$ sec$^{-1}$.

In view of the great interest in nuclear physics studies with electromagnetic probes, at Frascati it is foreseen to install an internal jet target on the electron storage ring Adone to produce a monochromatic high energy (up to 1.2 GeV) photon beam by the tagging technique.

The use of internal target in circulating beams antedates the availability of external beam from circular machines. In recent years, with improved understanding of beam dynamics and the contruction of high energy synchrotron and storage rings, there have been a renewed interest in this option and growing activity in the development of suitable targets. The target which gives the largest luminosity is a type of condensed molecular beam(1) which provides a flow of gas at supersonic speed (hence the name of gas "jet" target) due to the expansion of gas from a vessel at high pressure and low temperature into the vacuum through a nozzle of very small aperture (10 ÷ 150 μm) and special geometry. The molecular jet flies forward along the axis of expansion and it is absorbed after having crossed the accelerator vacuum pipe. Only the core of the jet reaches the ultra-high vacuum of the ring via several differential pumping stages where almost all the uncondensed residual gas is pumped off.

Fig. 1 shows the schematic view of the jet target proposed for Adone. The argon jet is produced in the chamber 1 (installed on top of the Adone vacuum pipe) where the gas expansion take place. The injector is a converging-diverging nozzle with special trumpet-shaped end part. Then the jet moves across the machine vacuum pipe to the sink system, installed below the storage ring.

We have interposed three differential pumping stages (each equipped with a 360 l/sec turbo-pump) to separate both the expansion and the sink chambers from the vacuum pipe in order to minimize the pressure rise in the interaction region ($\lesssim 10^{-8}$ torr). An additional pumping system (two 1000 l/sec turbo-pumps) is acting on the straight section of the ring where the jet target will be mounted, in order to reduce this rise pressure and limit the length of the region where the pressure is $\simeq 10^{-8}$ torr. Two fast acting UHV valves separate the production and sink chambers from the Adone vacuum pipe to easy the jet on/off operations and to prevent the possible contamination of the ring in case of a large pressure bump due to breakdown of the target system. The operating conditions are inlet pressure and temperature 6 bar and 150 °K respectively, nozzle throat diameter 87 μm and semiaperture 3.5°. From a total flux of $10^{20}$ Ar-atoms/sec expanding from

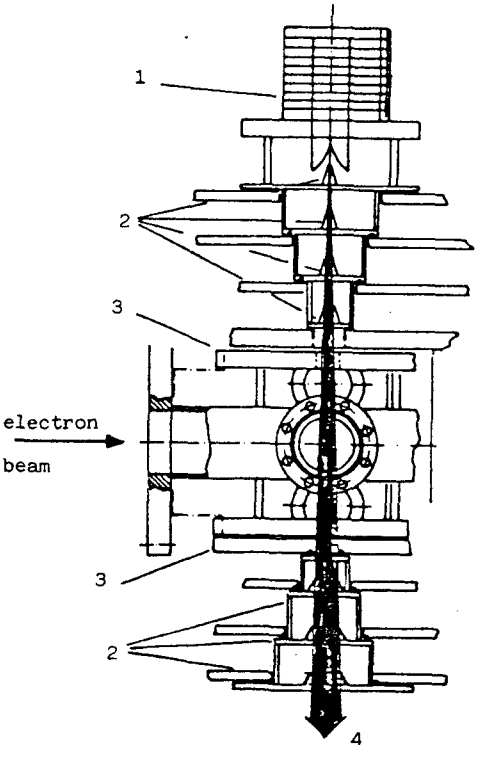


Fig. 1 - Side view of the argon jet target proposed for Adone: 1 gas expansion chamber; 2 collimators; 3 valves; 4 sink chamber.

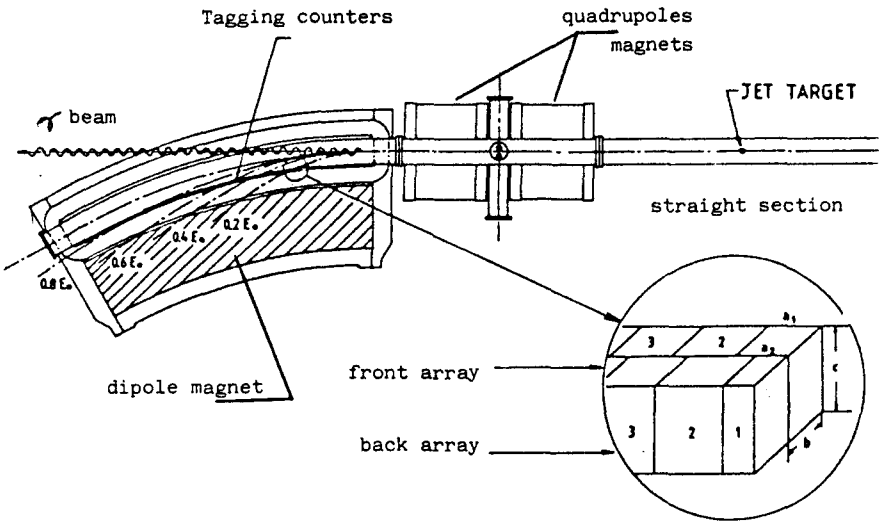


Fig. 2 - Schematic view of the tagging system

the nozzle the collimator system selects 5 $10^{18}$ atoms/s, which corresponds to a target thickness of $\simeq 10^{-8}$ g/cm$^2$ ($\emptyset$ = 1 cm) on the path of the electron beam (that is a distance of $\simeq$ 25 cm from the nozzle).

The circumference of the Adone ring is approximately 105 m, so that a bunch of ultrarelativistic electrons takes about $T_0$ = 351 nsec to make a round. The ring is divided into twelve identical lattice elements each consisting of a straight section, a bending magnet (dipole) and a couple of defocusing-focusing magnets (quadrupoles).

Electrons are injected into the storage ring at an energy of 300 MeV (a few-turn injection will result in about 100 mA current circulating in the ring) and then accelerated to the desired energy by rising the magnetic field of the guiding magnets (this operation requires about 20 sec). The 51.4 MHz RF-cavity groups the circulating electrons into 18 bunches, each 1 nsec wide and 20 nsec apart.

After the rise in energy the argon jet will be fired into the vacuum pipe and the electron beam lifetime $\tau = T_0/(\sigma_\varepsilon x)$ cut down to about 130 sec ($T_0$ is the revolution period, $\sigma_\varepsilon$ the removal cross section and x the jet target thickness). Then the cycle is ended by lowering the field of the magnets to the injection value. The removal cross section involves only that process of bremsstrahlung in which the energy loss places the electron outside the acceptance band-width of the ring ($\varepsilon = 0.01\ E_0$, $E_0$ being the machine energy). In fact the target thickness is so small that neither the multiple scattering nor the ionization losses contribute to the lifetime, being the RF-cavity able to compensate for both the growth in divergency and the mean energy losses.

In fig. 2 is sketched a lay-out of the apparatus: the argon jet will be placed in a straight section (2.58 m long) between consecutive lattice elements and the recoil electron is bended by the dipole magnet and detected by a two-array scintillator counter hodoscope. This hodoscope will be placed between the ring vacuum pipe and the dipole magnet flux return joke. The scintillators have different sizes to give the same photon energy resolution (= 1% at $E_0$ = 1.5 GeV and = 2.7% at $E_0$ = 500 MeV) over the whole tagging range. The complete tagging system defines 80 energy channels covering the photon energy range $k = (0.4 \div 0.8)E_0$. This implies an extensive array of tagger detectors covering a side 1 m long of the bending magnet pole.

Since the determination of the photon energy relies on a coincidence between the tagging counters and the detector for the photoejected particles, the tagging method is limited by the random coincidences. In the normal operating mode the facility produce $\simeq 10^8$ photons/sec in the whole tagging range. To use the tagged photon beam at the maximum intensity it is foreseen the installation of a new 350 MHz RF-cavity which makes the beam almost continuous in time (126 bunches 2.86 nsec apart).

To compensate for the relatively low intensity of the tagged photon beam, the detection apparatus for photoejected particles has to cover a large solid angle and energy range simultaneously. In our case this apparatus will be a $4\pi$ BGO crystal ball (whose design is presently going on), consisting of 300 ÷ 400 crystals, each coupled to a photomultiplier. A 20 cm bore along a diameter of the sphere will allow the passage of the beam.

A partial list of experiments which will be carried out with this beam are:

- measurement of the total hadronic cross section through both the transmission method and the uranium photofission;
- deuteron photodisintegration;
- photo-exitation of nucleon resonances;
- particle correlation and resonance propagation in nuclei.

References

1. O.F. Hagena and W. Obert, J.Chem.Phys. 56,1793(1972)

# SCATTERING OF POLARIZED ELECTRONS FROM ORIENTED ROTATIONAL NUCLEI

E. MOYA DE GUERRA

and

P. SARRIGUREN

I.E.M., C.S.I.C., Serrano 123. 28006-MADRID. (Spain)

ABSTRACT

The interest of using polarized beam and target to extract information on current distributions in rotational nuclei is pointed out. The differential cross section for elastic and inelastic scattering of longitudinally polarized electrons from oriented nuclei is analyzed in detail focusing on the case of K=½ ground state bands.

## 1. Introduction

The study of nuclear ground state rotational bands by means of electron scattering experiments has been a subject of interest for many years. So far, a substantial amount of experimental information is available concerning longitudinal form factors for transitions within the ground state band of many deformed nuclei[1]. However, little is known yet about the more interesting transverse form factors[2] that carry the information on the nuclear current distribution, and hence, on the nature of the rotational mode. This is mainly due to the fact that in ordinary electron scattering on deformed nuclei (i.e., with unpolarized beam and target) the differential cross section is dominated by the longitudinal form factor and, therefore, extracting information on transverse multipoles is hard, specially at low q values. In this brief communication we wish to point out that the best way to obtain information on transverse multipoles is to use oriented targets and, or polarized beam and target.

The differential cross section for scattering of linearly polarized electrons from an oriented nuclear target is given in first Born approximation by[3,4]

$$\frac{d\sigma}{d\Omega} = \frac{4\pi\ \sigma_M}{f_{rec.}}\ \sigma(h;\ \theta',\ \varphi') \qquad (1)$$

where $\sigma_M$ and $f_{rec.}$ are the standard[5] Mott cross section and recoil factor, respectively, h is the incoming electron helicity and $(\theta',\varphi')$ is the target polarization direction with respect to the direction of the momentum transfer. The dependence on h and $(\theta',\varphi')$ in eq. (1) can be written as

$$\sigma(h;\ \theta',\ \varphi') = \sigma_o + \sigma_{al.}(\theta',\varphi') + h\ \sigma_{pol.}(\theta',\varphi') \qquad (2)$$

where $\sigma_o$ is the usual combination of longitudinal and transverse form factors occurring in ordinary electron scattering, and $\sigma_{al.}$, $\sigma_{pol.}$ are, respectively, the alignment and polarization cross section that depend on the target polarization direction. While in ordinary scattering the different multipoles occurring in a given transition within the band appear allways in the combination[5]

$$\sigma_o \equiv V_L|F_L|^2 + V_T|F_T|^2 \qquad (3)$$

with

$$|F_L|^2 = \sum_{\lambda=\text{even}\geq 0} |F^{C\lambda}|^2,$$

$$|F_T|^2 = \sum_{\lambda=\text{odd}} |F^{M\lambda}|^2 + \sum_{\lambda=\text{even}\geq 2} |F^{E\lambda}|^2, \qquad (4)$$

$\sigma_{al.}$ and $\sigma_{pol.}$ contain in general many different combinations of the longitudinal and transverse multipoles, some of which are interference terms between coulomb and transverse multipoles. Each of these combinations can be separeted by appropriate choices of the target polarization direction, as well as using the dependence on the target

orientation along a fixed polarization direction, on the electron helicity and on the scattering angle.

To make this presentation as short as possible only a specific case, that bears many interesting physical features, will be discussed in detail. This is the case of K=½ bands with level sequence I=½, $\frac{3}{2}$, $\frac{5}{2}$, $\frac{7}{2}$, ... In this case aligment of the target is not possible (ground state spin is I=½) and to get additional information to that contained in $\sigma_o$, experiments with polarized projectile and target have to be done.

## 2. Application to K=½ ground state bands

As it is well known[6] the level sequence of K=½ bands depends on the value of the decoupling parameter a. For $-1<a<1$ the spin sequence is I=½, 3/2, 5/2, ... this is for instance the case of the ground state bands of $^{29}Si$, $^{183}W$ and $^{239}Pu$. Polarization considerations are greatly simplified for spin ½ targets and the discusion here will be restricted to this kind of K=½ bands. When the target is prepared with its magnetic substates M=±½ propulated with different probabilities, P(M), the polarization cross section for transition to any state within the band is given by[4]

$$\sigma_{pol.} = \alpha_1^{1/2}(\sin\theta'\cos\varphi' V'_{TL} F^1_{TL} + \cos\theta' V'_T F^1_T) \qquad (5)$$

where $\alpha_1^{1/2} = \frac{1}{\sqrt{3}}(1-2P(M=-½))$, $V'_{TL}$, $V'_T$ are electron kinematic factors and $F^1_{TL}$, $F^1_T$ are the q-dependent form factors that carry the information on the nuclear structure. $F^1_{TL}$ contains interference terms betwen longitudinal (Cλ) and transverse (Eλ,Mλ) multipoles, while $F^1_T$ contains only transverse multipoles.

In ordinary scattering $|F_T|$ can be separated from $|F_L|$ by the usual Rosenbluth sparation method and ussually scattering at 180° is required. As said before, if $|F_T|^2 << |F_L|^2$ it is hard to extract information on $|F_T|$ from ordinary electron scattering.

With polarized beam and target the different terms in $\sigma_{pol.}$ can be easily separated, since for instance one has that

$$F^1_{TL} \propto ½(\sigma(h;\theta'=\tfrac{\pi}{2},\varphi'=0) - \sigma(h;\theta'=\tfrac{\pi}{2},\varphi'=\pi)) =$$

$$= ½(\sigma(h;\theta'=\tfrac{\pi}{2},\varphi'=0) - \sigma(-h;\theta'=\tfrac{\pi}{2},\varphi'=o)$$

$$F^1_T \propto ½(\sigma(h,\theta'=o) - \sigma(h,\theta'=\pi)) =$$

$$= ½(\sigma(h,\theta'=o) - \sigma(-h,\theta'=o))$$

Restricting ourselves to elastic and inelastic scattering to the two first excited states, the measurable form factors $|F_{L_{I_f}}|^2$, $|F_{T_{I_f}}|^2$, $F^1_{TL_{I_f}}$, $F^1_{T_{I_f}}$ are given in terms of the transition multipoles $F^{\sigma\lambda}_{I_f}$ by the following relations[4] (where σ = C,E,M.; the index $I_f$ is used to distinguish transitions to different states in the band, and a convention is used in which the $F^{\sigma\lambda}$'s are real).

For elastic scattering ($I_f$=½):

$$|F_{L_{½}}|^2 = |F^{CO}_{½}|^2,\ |F^{T}_{½}|^2 = |F^{M1}_{½}|^2,\ F^1_{TL_{½}} =$$

$$= \sqrt{3/2}\, F^{CO}_{½} F^{M1}_{½},\ F^1_T = -\sqrt{3}\,|F_{T_{½}}|^2 \qquad (6)$$

For scattering to the first excited state ($I_f$=3/2):

$$|F_{L_{3/2}}|^2 = |F^{C2}_{3/2}|^2, |F_{T_{3/2}}|^2 = |F^{M1}_{3/2}|^2 + |F^{E2}_{3/2}|^2$$

$$F^1_{TL_{3/2}} = \sqrt{3/8}\, F^{C2}_{3/2}\,(\sqrt{3}\, F^{E2}_{3/2} - F^{M1}_{3/2}) \qquad (7)$$

$$F^1_{T_{3/2}} = \sqrt{3}/2(|F^{M1}_{3/2}|^2 - |F^{E2}_{3/2}|^2 + 2\sqrt{3}\, F^{M1}_{3/2} F^{E2}_{3/2})$$

For scattering to the second excited state ($I_f$=5/2):

$$|F_{L_{5/2}}|^2 = |F^{C2}_{5/2}|^2, |F_{T_{5/2}}|^2 = |F^{E2}_{5/2}|^2 + |F^{M3}_{5/2}|^2$$

$$F^1_{TL_{5/2}} = F^{C2}_{5/2}\,(F^{M3}_{5/2} - 1/\sqrt{2}\, F^{E2}_{5/2}) \qquad (8)$$

$$F^1_{T_{5/2}} = 1/\sqrt{3}(|F^{E2}_{5/2}|^2 - |F^{M3}_{5/2}|^2 + 4\sqrt{2}\, F^{M3}_{5/2} F^{E2}_{5/2})$$

Then, for every transition, one has four measurable form factors to determine at most three independent transition multipoles. Furthermore, in the q-regions where transverse multipoles are much smaller than longitudinal ones, the combined information on $|F_{L_{I_f}}|$ and $F^{1}_{TL_{I_f}}$ can be used to extract information on the transverse multipoles.

On the other hand, since the transition multipoles can be parametrized in terms of intrinsic multipoles that are common to all the transitions[4,7] (i.e., that are independent of inicital and final spins), the information on multipoles corresponding to different transitions can be combined to extract information on the intrinsic structure of the rotational band and on the nature of the rotational mode. For instance, the Ml multipoles of the intrinsic single particle ($\mathcal{F}^{Ml}_{k}$, $\mathcal{F}^{Ml}_{2K}$) and collective ($\mathcal{F}^{Ml}_{R}$) currents can be obtained from[4,7]:

$$\mathcal{F}^{Ml}_{K} = 1/\sqrt{3}\ (F^{Ml}_{1/2} + \sqrt{2}\ F^{Ml}_{3/2})$$

$$(\mathcal{F}^{Ml}_{R} - \sqrt{2}\mathcal{F}^{Ml}_{2K}) = 2/\sqrt{3}\ (F^{Ml}_{1/2} - 1/\sqrt{2}\ F^{Ml}_{3/2}) \qquad (9)$$

Similarly the E2 multipoles of the intrinsic single particle ($\mathcal{F}^{E2}_{2K}$) and collective ($\mathcal{F}^{E2}_{R}$) currents can be obtained from

$$\mathcal{F}^{E2}_{R} = (1/6\sqrt{5})(\sqrt{2}\ F^{E2}_{3/2} + \sqrt{3}\ F^{E2}_{5/2})$$

$$\mathcal{F}^{E2}_{2K} = 1/\sqrt{30}\ (\sqrt{3}\ F^{E2}_{5/2} - 4\sqrt{2}\ F^{E2}_{3/2}) \qquad (10)$$

Also, the C2 multipole of the intrinsic charge distribution ($\mathcal{F}^{C2}$) is obtained, to lowest order in angular momentum, from

$$|\mathcal{F}^{C2}| = \sqrt{5/2}\ |F_{L_{3/2}}| = \sqrt{5/3}\ |F_{L_{5/2}}| \qquad (11)$$

Note that relation (11) is characteristic of the K=½ bands considered here, and provides the most direct test of band mixing effects in the charge distribution of rotational states. Departures from this relation in measured longitudinal form factors would give a direct measure of the above mentioned band mixing effects.

## References


1. W. Bertozzi; Nucl. Phys. A374 (1982) 109C.
2. T.W. Donnelly and I. Sick; Rev. of Mod. Phys., 56 (1984) 461.
3. L.J. Weigert and M.E. Rose; Nucl. Phys., 51 (1964) 529.
   T.W. Donnelly and A.S. Raskin; An. Phys. (N.Y.) 169 (1986) 247,
4. E. Moya de Guerra; Phys. Rep. 138 (1986) No. 6, 293.
5. T. de Forest, Jr. and J.D. Walecka; Adv. in Phys., 15 (1966) 1.
   H. Ubeerall; "Electron Scattering from complex Nuclei", Parts A and B (Academic Press, 1971).
6. A. Bohr and B. Mottelson; "Nuclear Structure", v. II (Benjamin Inc., 1975).
7. E. Moya de Guerra; Ann. Phys. (N.Y.) 128 (1980) 286.